eman ta zabal zazu

Universidad del País Vasco
Euskal Herriko Unibertsitatea

UNIVERSITY OF THE BASQUE COUNTRY
(UPV/EHU)

DEPARTMENT OF CHEMICAL ENGINEERING

CFD-DEM modeling of spouted beds with internal devices using PTV

DOCTORAL THESIS

Aitor Atxutegi
2020

eman ta zabal zazu

Universidad del País Vasco
Euskal Herriko Unibertsitatea

UNIVERSITY OF THE BASQUE COUNTRY
(UPV/EHU)

DEPARTMENT OF CHEMICAL ENGINEERING

CFD-DEM modeling of spouted beds with internal devices using PTV

Author:
Aitor Atxutegi

Supervisors:
Prof. Martin Olazar
Prof. Roberto Aguado

A thesis submitted in fulfillment of the requirements for the degree of Doctor in Chemical Engineering

Abstract

This thesis is mainly focused on the development and validation of computational models for the simulation of spouted beds in a range of operating conditions and configurations. To that end, experimental runs have been performed in order to determine the hydrodynamic behavior of various materials ranging from spheres to ellipsoids and pseudo-cylindrical pellets.

The hydrodynamic analysis with these materials has been conducted in contactors of different configuration, either without any internal device or with different types of internal devices, as are draft tubes and fountain confiners. The study is based on the classical procedure of monitoring bed pressure drop with air velocity. The parameters specifically determined are operating pressure drop, minimum spouting velocity and fountain height, which roughly characterize the overall behavior of the spouting bed. Furthermore, pressure fluctuations have also been analyzed in the power spectral domain by FFT, as they are mainly stemmed from the solid incorporation from the annular zone into the spout. In addition, as the validation of the numerical simulations required acquisition of local dynamic data, they have been achieved by building an in-house particle velocimetry technique based on borescopes and high speed cameras. Subsequently, this experimental raw data have been processed with an algorithm that has been specifically tailored to track all the image shapes monitored throughout this thesis. The implementation of the velocimetry technique with the algorithm has allowed obtaining local solid velocity data from the monitoring of the images acquired for each configuration.

This data has been used to run and validate *CFD-DEM* simulations for regular and irregular particles. In the former case, the most precise drag model and frictional terms have been chosen for the different draft tubes used in this study. Simulation data, such as pressure drop, fountain height and solid velocities have been

compared with the experimental values and the main differences and effects of hydrodynamic variables have been ascertained. These simulations have enabled obtaining data that are experimentally cumbersome to obtain, such as void fractions and gas residence times. In addition, certain essential macroscopic parameters, such as the solid circulation flow rate, have been reproduced, which involves a significant step in the designing and scaling of these contactors.

Furthermore, the non-resolved *CFD-DEM* simulation of superquadric particles has also been approached in this thesis. This approach enables a relatively efficient way of introducing irregularity to the solids being treated in this systems, as most applications require the simulation of particles that generally deviate from the spherical shape. To that end, an efficient void fraction model for irregular particles has been implemented in order to capture the correct solid fraction that must be fed into all the governing equation and forces. The main force playing an essential role in these types of particles is the drag one, and therefore the correct drag force for superquadric particles has to be chosen. This force accounts for the solid irregularity and, in some instances, its orientation towards the fluid. In addition to this force, other secondary, but non-negligible forces, such as the lift and torque ones, have been implemented. As with the regular shape particles, once these simulations have been validated with the hydrodynamic data, valuable information has been extracted, such as solid and gas residence times. The effect of internal devices, such as draft tubes and fountain confiners, has also been studied, which provides essential information for the correct configuration to choose in a spouted bed contactor with a set of given design requirements.

Spray coating has been chosen as the applications that can build upon all the aforementioned information. A model for spray injection has been introduced in the *CFD-DEM* code and a solid-droplet collision detection has been implemented. This algorithm enables determining the homogeneity and/or deviation throughout the tablet coating process when spherical and superquadric particles are used.

Finally , a profiling of the current implementation has been run in order to determine the penalties that the addition of this droplet phase model would inflict in the overall code performance. Once an acceptable level of code performance has been reached, a set of coating test cases have been devised, which prove the capability of the overall model to ascertain the influence contactor geometry and tablet shape have on the final product.

ACKNOWLEDGEMENTS

A mis directores, Prof. Martin Olazar y Prof. Roberto Aguado. Gracias por confiar en mí, y darme la libertad y confianza para desarrollar esta tesis con una temática alternativa a las desarrolladas en el grupo.

A los otros miembros del grupo *CPWV* que han aportado directa o indirectamente al trabajo, especialmente al Prof. Javier Bilbao y al Prof. Andrés T. Aguayo. Y a las personas, sin cuya aportación la realización de esta tesis no hubiera sido posible. A Edu, Txema y Quim, administradores del cluster de la UPV/EHU, por su paciencia y flexibilidad.

I would like to thank Prof. Heinrich for supervising my research stay at *SPE* (TUHH), Dr. Pietsch for the warm welcome and specially to Paul for your invaluable help on *CFD-DEM* simulations and for allowing me to work on superquadrics, without which, this thesis would lack much of its weight.

A los compañeros con la que he tenido el gusto de compartir laboratorio durante estos años. En primer lugar a la gente del 0.7 que me acogieron, particularmente a Juan, Mikel e Idoia Estiati. No puedo olvidarme de agradecer a mi compañera de spinning y mesa en el *KCC*, Idoia Hita, por su ayuda en la estancia.

Especialmente, quiero agradecer a las personas con las que he pasado más tiempo dentro y fuera del laboratorio. Arandia, Pablo y Tomas, por las noches en Bilbao. A mis compañeros de piso, por ser como una familia y como tal, horrorizarse de mi talento culinario. Especialmente, a Tomas, por las conversaciones sobre ingeniería, ciencia y deporte que han amenizado confinamientos y estancias.

Finalmente, a mi familia. A mi hermano, Eneko, por esa competencia fraternal que me otorgó las herramientas, sin las cuales este trabajo no sería posible. Como me han repetido innumerables veces, no hay duda de que eres el Atxutegi bueno. A mi aita, Joseba, porque pese a que me duela admitirlo, he heredado tu personalidad, gustos y forma de afrontar las cosas. Finalmente a mi ama, Tere, por haber invertido incontables tardes en mi educación, cosa que nunca olvido. Eskerrik asko a ambos por el hogar y la educación que nos habéis dado tanto a mi hermano como a mí.

Aitor Atxutegi

Contents

Objectives

The main objective of this thesis is to develop the tools required for the acquisition of accurate internal hydrodynamic data in spouted beds and propose *CFD-DEM* simulation models for the most common configurations. Thus, these models will allow understanding the internal behavior of the systems, and therefore simplify the steps for the addition of new internal devices or solid shapes, without having to change the core relationships that govern this type of gas-solid contact.

Regarding the acquisition of internal data in the various configurations, the following objectives are set:

- Monitor the more traditional parameters in spouted beds, as are pressure drop, minimum spouting velocity and fountain height, in order to determine their ranges for operating in the different configurations (with and without internal devices) to be analyzed in this thesis.

- Develop a reasonably fast and efficient particle velocimetry technique to be applied in a fully $3D$ conical spouted bed in order to accurately measure local internal properties. This data will allow ascertaining the effect internal devices have on the internal flow structure, and will also be used to validate the proposed simulations models.

Once all the required hydrodynamic data have been acquired, a *CFD-DEM* simulation model will be built and run with different internal devices, contactor geometries and solid shapes, with the specific objectives being as follows:

- Determine the main forces acting upon spherical and non-spherical particles, mainly drag, lift and torque ones. Special emphasis will be place on the drag force, as is the dominant one in spouted beds. Efficiency will be

considered an essential point in the implementation of the models in order to avoid unreasonable penalties in the overall code performance.

- Validate the magnitude of these forces and friction terms using the aforementioned experimental data in order to obtain a reasonably accurate model that is able to predict the behavior of the various internal devices.

- Analyze the influence internal devices and solid types have on the spouting regime, as well as predict particle cycle times and gas residence times for any configuration, as this information is crucial in the design of any chemical contactor for both chemical and physical processes.

Based on all this knowledge, the simulation of spray coating will be implemented in spouted beds, with the objectives being as follows:

- Study the effect different contactor geometries and solid shapes have on the final product quality and the process time required to attain it.

- Check implementation efficiency and correct scaling up capability of the model in order to ensure its plausible use for the simulation of industrial spray coating processes. This will be performed based on a given number of droplets present in a realistic industrial scale environment.

1 Introduction

Fluidization is the operation in which a fluid is passed through a bed of particles in order to exert an erratic force on said particles and give them a fluidlike behavior. Therefore, buoyant forces and advective displacement play a relevant role. The fluid can be either gas or liquid, but this work is specially focused on gas-solid fluidization, as it is the most common and of greater significance in industry. Within the gas-solid fluidization technologies the design of the equipment greatly changes depending on the type of solid circulation to be achieved and the process in which it is involved. When particles are desired to put in contact with the gas at low flow rates, a bubbling fluidized bed (Figure 1.1a) is the usual variant. Certain applications require shorter contact times with a faster regime, for which fast fluidized beds are applicable (Figure 1.1b).

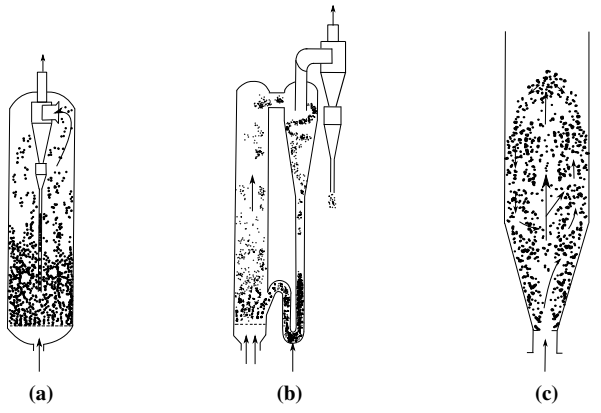

Figure 1.1. Diagrams of gas-solid fluidization technologies; (a) bubbling fluidized bed, (b) fast fluidized bed and (c) spouted bed [1].

However, depending on the solid size and density, the gas-solid interaction might not allow operating in a regular fluidized bed reactor as those previously mentioned. Thus, for solids of large mean particle diameter, $\bar{d}_p$, the air tends to create preferential paths resulting in slugging bed and unstable fluidization. In these cases, Geldart classification shown in Figure 1.2 clearly shows that stable bed circulation is only achieved through spouting. In such reactors (Figure 1.1c), a preferential path is opened at the bed axis and particles are dragged along a region called spout, which leads to a cyclic particle circulation in the bed. Aspects related to these beds have already been reported in the literature [2] due to their great operational flexibility in applications such as combustion [3], pyrolysis [4], gasification [5], spray coating [6], polymerization [7] and production of nuclear fuels [8]. Nonetheless, the complexity of the gas-solid interaction in the bed, along with the heterogeneity of the multiphase system, has hindered the development of this technology on an industrial scale.

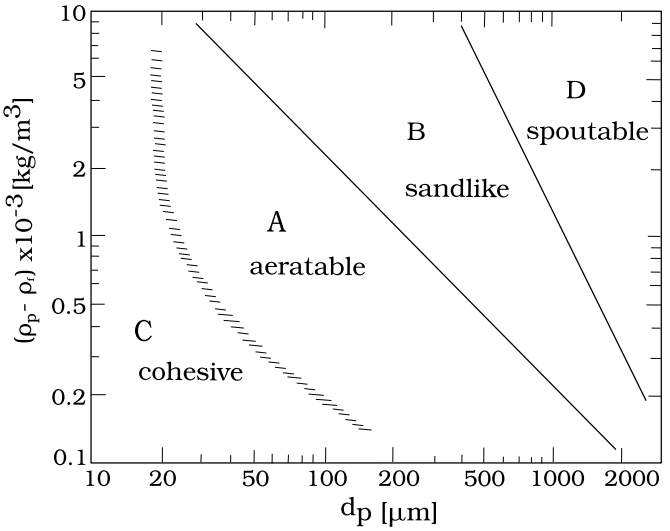

Figure 1.2. Geldart classification of particles and their fluidization type [9].

A variety of invasive and non-invasive techniques have been proposed in the last decades in order to study the internal gas-solid interaction, which are extensively reviewed elsewhere [10]. Among the former, those based on particle optical monitoring [11], X-ray volume tomography [12, 13], capacitive volume tomography [14], ultrafast X-ray computed tomography [15], gamma ray computed tomography [16], radioactive particle tracking [17, 18] and magnetic particle tracking [19, 20] are worth mentioning.

However, invasive techniques allow obtaining data at the measuring point itself, while the disturbance may be reduced by decreasing the probe volume relative

to the system [21]. These techniques provide critical information, such as the dynamic solid velocity that governs the behavior of the system. Previous approaches have already been made in conical spouted beds through the use of optical fiber probes [22], but a detailed calibration for each material is needed. Another common way to study the solid velocity and structure is through particle tracking velocimetry (PTV), which makes use of high speed cameras to track the location and velocity of each particle. In terms of the PTV implementation in a conical spouted bed, a borescopic PTV [23] is required to study the internal structure of the bed, as opposed to the more common external PTV [24, 25], which only tracks particles for pseudo $2D$ systems, and is therefore of limited application.

PTV is concerned with the tracking of individual particles in the Lagrangian framework in contrast to particle image velocimetry (PIV), which measures the averaged flow field of a region commonly used for turbulence analysis and model validation [26]. Both techniques make use of high speed cameras, but PTV enables tracking individual particles for long trajectories [25]. The study of long trajectories and velocities gives local information to improve reactor design through model validation.

The design of multiphase chemical reactors is closely linked to the discovery of heterogeneous catalysts for the petrochemical and pharmaceutical industry [27]. Although Chemical Engineering research focuses on the improvement of these and other catalysts, optimization of yield and selectivity in a given process involves a suitable balance between the catalyst kinetics and transport phenomena [28], especially when such a process is to be scaled up. This intertwined relationship is being approached in Chemical Reaction Engineering, in which the use of models for the study of reaction kinetics through cascade lumping [29], neural network approach [30], single event micro-kinetics [31] and monte carlo simulations [32] are being coupled with fluid dynamic models, such as CFD-DEM [33], two-fluid model (TFM) [34], multiphase particle in cell ($MPPIC$) [35] and lattice Boltzman (LB) [36] models, with the objective being a balanced solution of both phenomena in order to ease the transition of a technology from the laboratory test stand to an industrial scale application.

Fluid dynamic models have been used since the early works in the $70s$ [37–39] and nowadays cover a wide range of researching areas in chemical industry, from combustion and turbulence analysis to fluidized bed simulation in a variety of scales. The always growing need for spatial and temporal resolution, along with tightly couple chemical reactions has made the search for increased computational resources of uttermost importance in order to obtain relevant information from CFD-DEM simulations in a reasonable time.

With the stalling or arguable death of Moore's law and the ubiquity of multipro-

cessor *CPU* architectures becoming more apparent, the use of *MPI* [40] in any of its flavors (*OpenMPI*, *MPICH*, *IntelMPI*) is of prime importance in order to exploit the concurrences in *CFD-DEM* simulations and solve a given case in a distributed manner. This implies that simulations have to be written by bearing the architecture shown in Figure 1.3 in mind, i.e., trying to increase data locality and reducing inter processor communication and data latency.

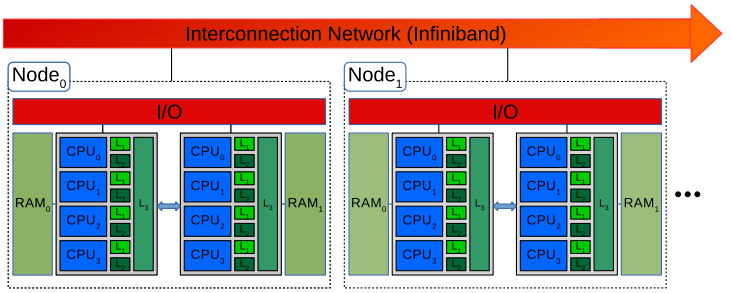

Figure 1.3. Simplified architecture of distributed memory and computing nodes.

In the following sections, the basics of *CFD-DEM* simulations will be explained, and more details on OpenFOAM® are reported by Moukalled et al. [41] and on *CFD-DEM* coupling by Norouzi et al. [42].

1.1 CFD modeling

OpenFOAM® is the open source library used to solve fluid domains due to its great flexibility and scalability [43]. In fact, it is increasingly used in industry. As with any other *CFD* code, the main set of equations to be solved accounts for mass and momentum conservation equations, which are commonly known as Navier-Stokes equations. The mass conservation equation is as follows:

$$\frac{\partial \rho}{\partial t} + \nabla \cdot (\rho \mathbf{u}) = 0 \tag{1.1}$$

with ρ being the fluid density and $\mathbf{u}$ the fluid velocity vector. This equation represents the conservation of the mass of a given component in a finite volume. However, when air compression is assumed insignificant, density may be considered constant and Equation 1.1 can be reduced to the following one:

$$\nabla \cdot \mathbf{u} = 0 \tag{1.2}$$

As already stated, the equation for momentum conservation has to be solved with the mass conservation (Equation 1.2). A common expression for the former when an incompressible, viscous and isothermic fluid is assumed, with the temporal and advective terms on the left-hand side and the diffusive, hydrostatic and gravity force terms on the right-hand side, is as follows .

$$\frac{\partial(\rho \mathbf{u})}{\partial t} + \nabla(\rho \mathbf{u}\mathbf{u}) = \nabla(\mu \nabla \mathbf{u}) - \nabla p + \rho \mathbf{g} \tag{1.3}$$

CFD in its current form works by using either a fixed or a moving finite volume mesh, Figure 1.4. Therefore, the Gauss divergence theorem shown in the following equation can be used to approximate the integration of a vector field in any finite volume to the summation of all vector fluxes through all the walls of the cell.

$$\iiint_V (\nabla \cdot \mathbf{F}) dV = \oiint_S (\mathbf{F} \cdot \mathbf{n}) dS \sim \sum_{i=0}^{n} \mathbf{F_i} \cdot \mathbf{S_i} \tag{1.4}$$

where $\mathbf{F}$ is the vector field to be integrated over the cell volume V, which is reduced to the sum of all vector fluxes through the i faces by using the surface vectors $\mathbf{S_i}$.

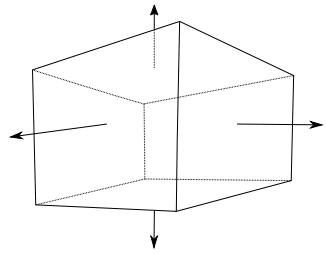

Figure 1.4. Diagram of the flow in a finite volume cell.

The main problem to couple velocity and pressure fields is the absence of pairs of algebraic equations containing the fields of both pressure and velocity. However, by splitting the momentum balance into the following two equations:

$$\rho \frac{u'' - u^n}{\Delta t} = -\nabla(\rho \mathbf{u}\mathbf{u}) + \nabla(\mu \nabla \mathbf{u}) \tag{1.5}$$

$$\rho \frac{u^{n+1} - u''}{\Delta t} = -\nabla p \tag{1.6}$$

and inserting the mass balance into Equation 1.6, the following expression con-

taining implicitly the mass balance is obtained:

$$\nabla^2 p = \frac{1}{\Delta t} \nabla \mathbf{u}'' \tag{1.7}$$

With this set of equations; i.e., Equations 1.5-1.7, both pressure and velocity fields can be solved in an iterative manner, as shown in the diagram in Figure 1.5. At each time step (Δt_{CFD}), the fluid velocity u and pressure field p are initialized. Using the momentum balance in Equation 1.5, the intermediate fluid velocity is obtained u'', which is used in Equation 1.7 to obtain the new pressure field. Given that most meshes contain some non-orthogonality, i.e., the cell face center $F_{1,e}$ does not line up with the centroids $F_{1,2}$ (Figure 1.6), the resulting fluxes have to be corrected through explicit terms once the new pressure and velocity fields have been obtained. These corrections allow attaining convergence of both fields. Considering that the velocity field is stored at the cell center, these values are interpolated to the center of each face, and subsequently used to obtain the face fluxes by multiplying with the face normal unit vectors S_i (Equation 1.4).

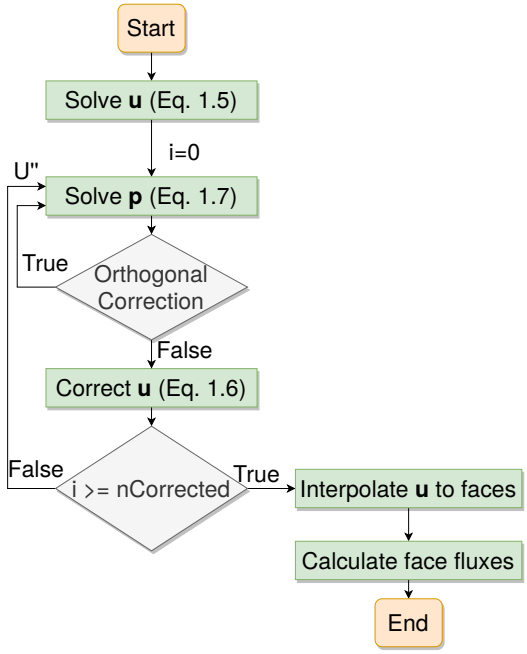

Figure 1.5. Pressure-implicit with Splitting of Operators (*PISO*) algorithm description.

Even though OpenFOAM® contains three main algorithms to solve the pressure-velocity coupling, namely, *SIMPLE*, *PISO* and *PIMPLE* (mixture of the previous two), this work only uses *PISO* (*PisoFoam* in OpenFOAM®) as *SIMPLE* is a steady

state solver and fluidized beds are inherently transient systems.

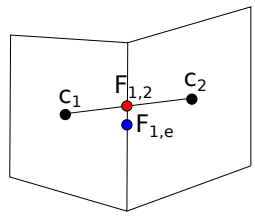

Figure 1.6. Face flux correction required for non-orthogonal meshes.

Once pressure and velocity fields have been coupled, the turbulence equations are solved together with any scalar transport equation, such as those for chemical components, passive scalars and phase coupling forces. Only two equations will be used in this work for turbulence closure; mainly, $\kappa-\varepsilon$ (Equation 1.8- 1.9) and $\kappa-\omega\,SST$. The aim of this study is to use non-resolved *CFD-DEM* simulations, for which a coarse mesh is required, which in turn removes the possibility of using complex turbulence models, such as *RSM* or *LES* [44].

$$\frac{\partial(\rho\kappa)}{\partial t}+\frac{\partial(\rho\kappa\mathbf{u_i})}{\partial x_i}=\frac{\partial}{\partial x_j}\left[\frac{\mu_t}{\sigma_\kappa}\frac{\partial\kappa}{\partial x_j}\right]+2\mu_t E_{ij}E_{ij}-\rho\varepsilon_t \tag{1.8}$$

$$\frac{\partial(\rho\varepsilon_t)}{\partial t}+\frac{\partial(\rho\varepsilon_t\mathbf{u_i})}{\partial x_i}=\frac{\partial}{\partial x_j}\left[\frac{\mu_t}{\sigma_{\varepsilon_t}}\frac{\partial\varepsilon_t}{\partial x_j}\right]+C_1\frac{\varepsilon_t}{\kappa}2\mu_t E_{ij}E_{ij}-C_2\rho\frac{\varepsilon_t^2}{\kappa} \tag{1.9}$$

Once all the fields have been solved for this time step, the treatment of temporal terms is executed by the implicit first order discretization shown in Equation 1.10 in order to guarantee a stable solution.

$$\frac{\partial\theta}{\partial t}\simeq\frac{\theta^{n+1}-\theta^n}{\Delta t}=f(\theta^{n+1}) \tag{1.10}$$

Given that the problem encountered in this work is a highly advective one ($Pe>>1$), at least a second order discretization scheme is required to keep the direction of the flow, thus giving more weight to the cells located upstream in the calculation of the face fluxes. This way, the second order upwind scheme is the most commonly used for the treatment of the advective term in Equation 1.3. In case higher order schemes are used (*QUICK* in Figure 1.7), the scalar boundedness might not be guaranteed due to the overshooting that these types of high order discretization schemes create. Thus, for those fields where low diffusion and solution boundedness has to be guaranteed, OpenFOAM® is provided with flux limiting schemes (*TVD* schemes) ensuring these requirements, albeit at a lower convergence speed.

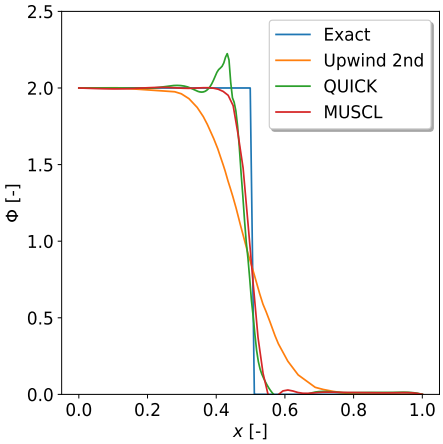

Figure 1.7. Result of different discretization schemes for a step increase in a scalar between cells.

Once all the fields have been discretized and all the source terms computed, the system of linear algebraic equations is solved for most fields through the preconditioned bi-conjugated gradient algorithm, except in some cases where this approach does not converge fast enough. In these cases, a geometric algebraic multigrid (*GAMG*) solver is used. This approach employs a hierarchical mesh where a coarsen mesh is solved first and its result initializes the finer level mesh [45]. This approach can save some computational time when the matrix converges slowly and is widely in other softwares, such as StarCCM+® and Ansys-Fluent® .

1.2 DEM modeling

The simulation and modeling of the discrete phase is accomplished through *DEM* with the use of LIGGGHTS®(an open source library written in C++ derived from LAMMMPS®), which enables the implementation of new models and applications. Instead of using a TFM approach base on the $KTGF$ in eulerian-eulerian simulations, $CFD\text{-}DEM$ simulations track the discrete phase in a Lagrangian reference frame. This entails that rigid solid properties, such as location, velocity, angular momentum and orientation, are tracked for every particle in the domain, while solid-solid collisions are computed for every pair of particles. Solid dynamics is governed by Newton's second law, whose expression for rigid bodies with uniform solid density is as follows:

$$\frac{\partial \mathbf{v_i}}{\partial t} = \frac{\beta_{f,s}(\mathbf{u}-\mathbf{v_i})}{\rho_s \varepsilon_s} + \mathbf{g} + \frac{\mathbf{f_s}}{m_i} - \frac{1}{\rho_s}\nabla p \tag{1.11}$$

where $\beta_{f,s}$ is the solid-fluid coupling term, $\mathbf{u}$ is the fluid velocity vector, $\mathbf{v}$ is the solid velocity vector, ρ_s is the solid density, ε_s is the solid volume fraction and f_s is the sum of all the remaining external forces on the solid. In addition to the translation equation, the conservation of angular momentum describes the relationship between torque and solid angular velocity:

$$\mathbf{T_i} = \mathbf{I_i}\frac{d\omega_\mathbf{i}}{dt} \tag{1.12}$$

where $\mathbf{I_i}$ is the moment of inertia tensor, $\omega_\mathbf{i}$ is the angular velocity and $\mathbf{T_i}$ is the sum of all the torques applied to a particle.

Solid-solid interactions have to be described in order to close Equations 1.11-1.12. The most common way to model this interaction in granular materials is through the smooth sphere Hertz dashpot-spring model [46] shown in Figure 1.8. When two particles (say i and j) are in contact, they slightly overlap each other and a counteracting force is applied to both particles depending on the overlapping volume and the spring stiffness (k).

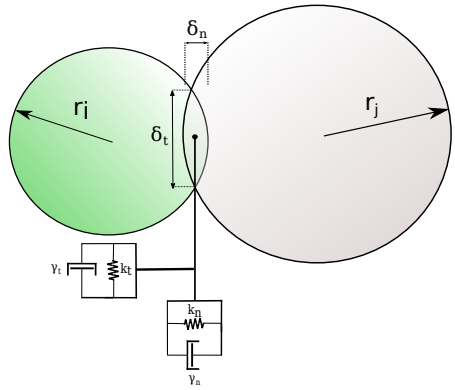

Figure 1.8. Depiction of the spring dash-pot plastic Hertz contact model.

These collisions are rarely purely elastic, and therefore an amount of the collision energy is dissipated through the viscoelastic damping coefficient (γ) represented by a dashpot. The normal and tangential forces are computed depending on the relative location and velocity following Table 1.1

These equations are combined to compute the total solid-solid interaction force between a pair of particles through Equation 1.19

Table 1.1. Dashpot and spring coefficient derivation from mechanical properties.

Normal	Tangential
$k_n = \frac{4}{3}E^*\sqrt{R^*\delta_n}$ (1.13)	$k_t = 8G^*\sqrt{R^*\delta_t}$ (1.14)
$\gamma_n = -2\sqrt{\frac{5}{6}}\beta\sqrt{S_n m^*}$ (1.15)	$\gamma_t = -2\sqrt{\frac{5}{6}}\beta\sqrt{S_t m^*}$ (1.16)
$S_n = 2E^*\sqrt{R^*\delta_n}$ (1.17)	$S_t = 8G^*\sqrt{R^*\delta_t}$ (1.18)

$$\mathbf{F} = (k_n \delta \mathbf{n}_{i,j} - \gamma_n \mathbf{v}_{n_{i,j}}) + (k_t \delta \mathbf{t}_{i,j} - \gamma_t \mathbf{v}_{t_{i,j}}) \tag{1.19}$$

where **F** is the rebounding force, k_n and k_t are the normal and the tangential stiffness coefficients, γ_n and γ_t are the normal and tangential damping coefficients, δ values are the overlapping volumes in the normal and tangential direction and $\mathbf{v_{i,j}}$ stands for the solid relative velocity in each direction.

The binary Young modulus E^*, binary shear modulus G^*, radius R^* and mass m^* are arithmetical averages following Equations 1.20-1.23:

$$\frac{1}{E^*} = \frac{(1-\nu_i^2)}{E_i} + \frac{(1-\nu_j^2)}{E_j} \tag{1.20}$$

$$\frac{1}{G^*} = \frac{2(2-\nu_i)(1+\nu_i))}{E_i} + \frac{2(2-\nu_j)(1+\nu_j)}{E_j} \tag{1.21}$$

$$\frac{1}{R^*} = \frac{1}{r_i} + \frac{1}{r_j} \tag{1.22}$$

$$\frac{1}{m^*} = \frac{1}{m_i} + \frac{1}{m_j} \tag{1.23}$$

with ν_i being the Poisson ratio of particle i.

Beyond the torque applied to the particles through tangential solid-solid interac-

tion, an additional term is usually included to account for the rotational dampening resulting from normal solid-solid interactions, which is given as follows [47–49]:

$$\mathbf{T_{r,i}} = \mu_r r_i |\mathbf{F_n}| \omega_\mathbf{i} \tag{1.24}$$

where $\mathbf{T_r}, \mathbf{i}$ is the rolling friction torque, $\mu_\mathbf{r}$ is the rolling friction coefficient and $\mathbf{F_n}$ is the normal force calculated from the first term on the right-hand side in Equation 1.19.

Once all the contacting granular pairs have been assigned and interaction forces have been applied, the solution is advanced and new particle positions are calculated by integrating Equation 1.25, with the number of particles, volume and temperature being assumed constant between steps (NVE condition).

$$\frac{d\mathbf{x}}{dt} = \mathbf{v} \tag{1.25}$$

The DEM time step, Δt_{DEM}, is chosen in the simulation as function of the particle relaxation time, which follows the Rayleigh time defined by Equation 1.26. Usually, the Δt_{DEM} chosen is below $20\% \Delta t_{crit}$, with its values being around $\sim 1\text{x}10^{-5}\, s$ [42].

$$\Delta t_{crit} = \frac{\pi R^*}{0.1631\nu + 0.8766}\sqrt{\frac{\rho_p}{G^*}} \tag{1.26}$$

1.2.1 Contact detection and neighbor lists

Before any binary force is applied to a given set of particles, a significant time is spent on the neighbor list building and the contact detection of solids [50]. Based on a naive approach with N particles, the time taken to check the distances between all particles is $\mathbf{O}(N^2)$, which is clearly a prohibitive computing cost for a reasonably sized simulation. Thus, it is generally assumed that a particle will not move more than its radial distance in a single time step, and therefore the positions of neighbor particles and potential contact candidates will not change much either. Henceforth, a Verlet neighbor list [51] of said particles is used and the contact detection is performed with only the particles within this list. In order to build it, LIGGGHTS®uses a binning process, where the whole domain is decomposed into bounding boxes with a preset bin size (l_{Bin}), as shown in Figure 1.9a, and only those particles in the same or neighboring bins are checked in the list build-

ing process. Of these particles, only those within a couple of particle radii from a given particle are included in the neighbor list, (Figure 1.9b). This whole process reduces the time complexity to $\mathbf{O}(Nlog(N))$ for most cases and to $\mathbf{O}(N/P)$ for the best cases, with P being the number of processors used to solve the problem.

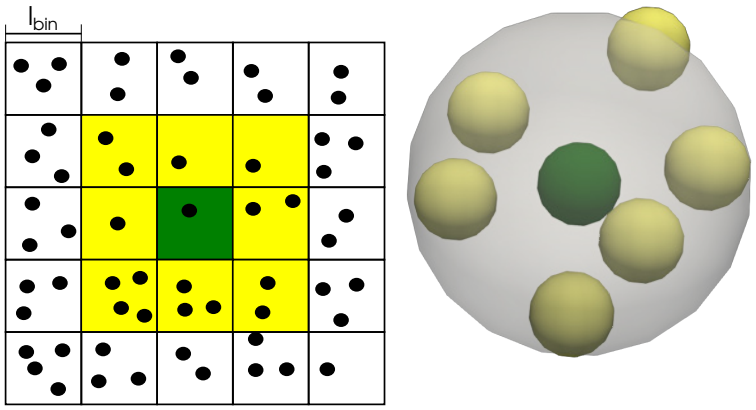

Figure 1.9. Graphical description of (a) the coarse binning process and (b) the particles included (yellow) into the target (gree) neighbor list.

Once the neighbor list building is completed, the contact detection of spherical particles shown in Figure 1.9b is straightforward, as the isotropic shape of spheres enables determining whether a contact between neighboring particles is underway, by means of the following equation:

$$|\mathbf{c}_i - \mathbf{c}_j| \leq r_i + r_j \tag{1.27}$$

where c_i is the location of the centroid of particle i. The contact detection procedure is speed up by using the contact history of a given particle, in order to build the neighbor list in a way that particles with the highest likelihood of contact are accessed first.

In the case of irregular particles, there are a number of approaches that can be taken in order to define the shape of a particle and, especially, to implement a robust and reasonably fast contact detection algorithm. One of the first ways to define the shape of an irregular particle is the multisphere (MS) approach, Figure 1.10a, where a number of spherical particles are merged together in a clump of particles whose surface resembles that of the irregular one [52]. The implementation of this approach lies on applying the procedure explained for spherical

particles to all the particles in the clump. This approach becomes costly as the number and types of spheres required to from the particle increases. There has been some progress in order to speed up the contact detection process [53, 54], but a significant number of spheres are still required in order to accurately represent the behavior of realistic irregular particles [55].

Another approach to capture particle irregularities, specially when flat faces are present in the modeled solids, is the polyhedral approach in Figure 1.10b. The contact detection between these particles is generally accomplished through the Gilbert–Johnson–Keerthi (*GJK*) approach[56] which has been proven to achieve a good scaling to solved sizable systems [57, 58]. However, this contact detection is purely limited to flat faced solids, which limits its use.

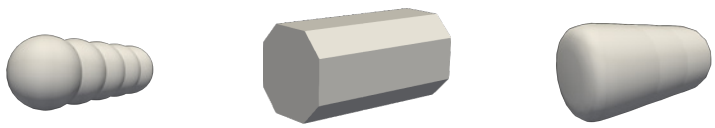

(a) (b) (c)

Figure 1.10. Representation of (a) multispherical particle, (b) polygonal particle and (c) superquadric particle to describe a cylinder.

The approach used in this work is that of superquadric (*SQ*) particles, shown in Figure 1.10c. *SQ* particles are described in their local coordinate system according to the following equation:

$$\left(\left|\frac{x}{r_x}\right|\right)^{n_1} + \left(\left|\frac{y}{r_y}\right|\right)^{n_2} + \left(\left|\frac{z}{r_z}\right|\right)^{n_3} = 1 \tag{1.28}$$

where x, y, z are the coordinates of a point in a local coordinate system based at the *SQ* particle centroid, r_x, r_y and r_z are the local shape parameters and n_1 and n_2 are the blockiness values. When blockiness values are close to 2, an spherical particle (Figure 1.11a) is formed, whereas an increase in this value results in sharper edges in particular dimensions, Figure 1.11b. *SQ* particles are more commonly described in a local reference frame following Barr et al. approach [59], by means of the following equation:

$$\left(\left|\frac{x}{r_x}\right|^{n_2} + \left|\frac{y}{r_y}\right|^{n_2}\right)^{n_1/n_2} + \left|\frac{z}{r_z}\right|^{n_1} = 1 \tag{1.29}$$

The contact detection for *SQ* particles follows a different procedure depending on whether they are ellipsoid ($n_1 = n_2 = 2$) or non-ellipsoid ones ($\exists x, n_x \neq 2$). Ellipsoid

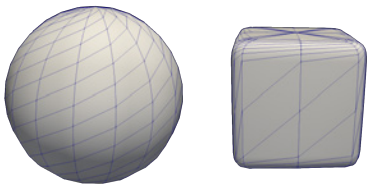

(a) (b)

Figure 1.11. Local description of a *SQ* particle with (a) spherical blockiness values and (b) high blockiness values.

particle contact detection has already being approached by means of the geometric potential (*GP*) method [60], but this procedure may fail to detect the correct contact point when the derivative of the normals of both particles are not completely parallel [61]. Another approach lies in using the common normal (*CN*) method, in which the *GP* method tries to find a point on the surface of each particle whose common line is perpendicular to both particles, but unlike the *GP* method their normal vectors are forced to be parallel to each other through Equation 1.31[62]. The set of equations for the contact detection first states that the contact points must be on the surfaces of the particles, Equation 1.30, then forces points a and b in Figure 1.12 to be parallel to each other (Equation 1.31), and finally makes the centroid connecting lines be parallel to both normal vectors, according to Equation 1.32.

$$\Gamma_i(x_i,y_i,z_i) = \Gamma_j(x_j,y_j,z_j) = 0 \tag{1.30}$$

$$\frac{\nabla\Gamma_i(x_i,y_i,z_i)}{|\nabla\Gamma_i(x_i,y_i,z_i)|} + \frac{\nabla\Gamma_j(x_j,y_j,z_j)}{|\nabla\Gamma_j(x_j,y_j,z_j)|} = 0 \tag{1.31}$$

where Γ_x is the potential of a given point relative to the particle surface.

$$(\mathbf{r}_i - \mathbf{r}_j) \times \nabla\Gamma_i(x_i,y_i,z_i) = 0 \tag{1.32}$$

Thus, when a set of points satisfying Equations 1.30-1.32 are found, they may be either the mininimum distance points (Figure 1.12a) or the maximum penetration points (Figure 1.12b), which is determined by the sign in Equation 1.33. In either case, the obtained values are stored as either contact points for the maximum penetration case or as initialization points for the minimum distance case.

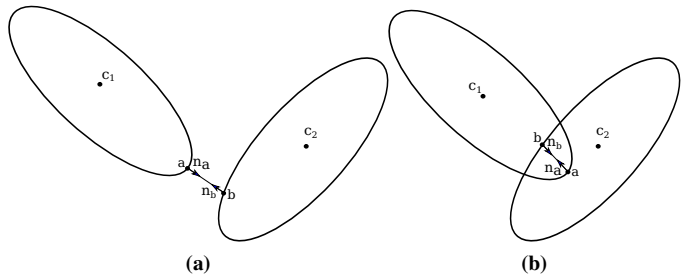

Figure 1.12. Detection of (a) convex shape minimum distance and (b) maximum penetration point.

$$\mathbf{r}_{i,j} \cdot \mathbf{n}_i = \mathbf{r}_{i,j} \cdot \frac{\nabla \Gamma_i(\mathbf{X})}{|\nabla \Gamma_i(\mathbf{X})|} \tag{1.33}$$

Once explained how *CFD* and *DEM* are independently solved, the next step is to explain the way these two techniques are coupled in order to conduct *CFD-DEM* simulations.

1.3 CFD-DEM coupling

CFD-DEM coupling encompasses the relationship between the continuous and the discrete phases and the effects on each other. When particles are suspended in low concentration and have low particle density they can be assumed to move at the same velocity as the surrounding fluid (Figure 1.13a), which is termed as a one way coupling scheme. When particle volume fractions are still low ($< 0.1\,\%$), but the particles are dense enough so as to have a significant effect on the fluid around them, this effect has to be taken into account through what is termed a two-way coupling, Figure 1.13b. Finally, when solid volume fractions are high and particles are of considerable size and density, particles not only affect the fluid velocity, but they are also affected by solid-fluid-solid collisions and by the fluid turbulence created by other particles, according to a four way coupling scheme (Figure 1.13c).

In this work the communication between LIGGGHTS®(*DEM*) and OpenFOAM® (*CFD*) is performed through CFDEM®Coupling , which, as inferred from the already explained governing equations, results in a four-way coupling scheme.

However, *CFD* and *DEM* approaches are base on two different reference frames (eulerian and lagrangian), and information must be exchanged in an efficient fash-

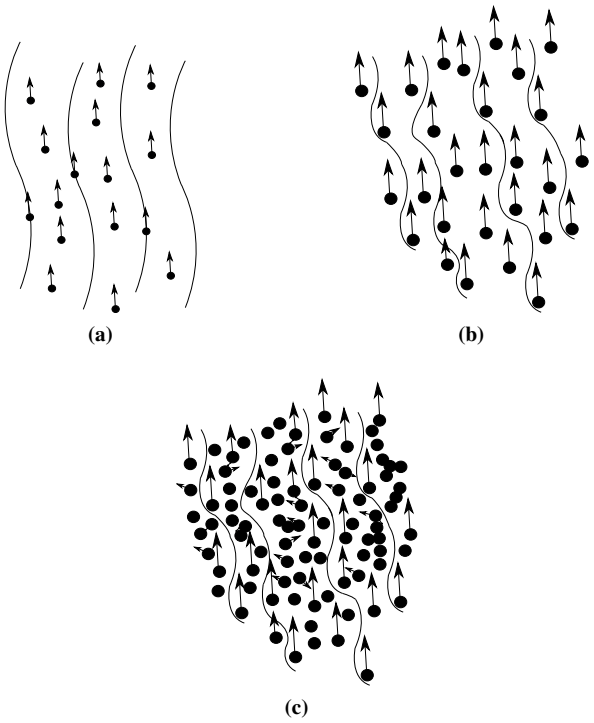

Figure 1.13. Representation of (a) a one way coupling, (b) two way coupling and (c) four way coupling schemes.

ion. In addition, from an implementation point of view, the location of a given particle in the memory is probably different depending whether the *CFD* or the *DEM* code is accessed. Henceforth, a mapping of the different critical properties, such as particle position, velocity and angular velocity, has to be conducted. The way this mapping and subsequent property communication is achieved depends on whether the system is solved in a centralized or distributed manner and, specially, on the scale of the problem [63].

There are two main *CFD-DEM* simulation paradigms, namely, resolved and unresolved simulations, Figure 1.14. The resolved *CFD-DEM* simulations (Figure 1.14a) [64, 65] require a fluid mesh that is much smaller than the average particle size, whereas the unresolved simulations (Figure 1.14b) use a cell volume that is at least a couple of times bigger than the average particle size.

Each approach has certain advantages and drawbacks. On the one hand, the former approach entails high computational requirements to solve fine meshes, but provides finer granularity of inter-particle properties and eases fluid-solid force

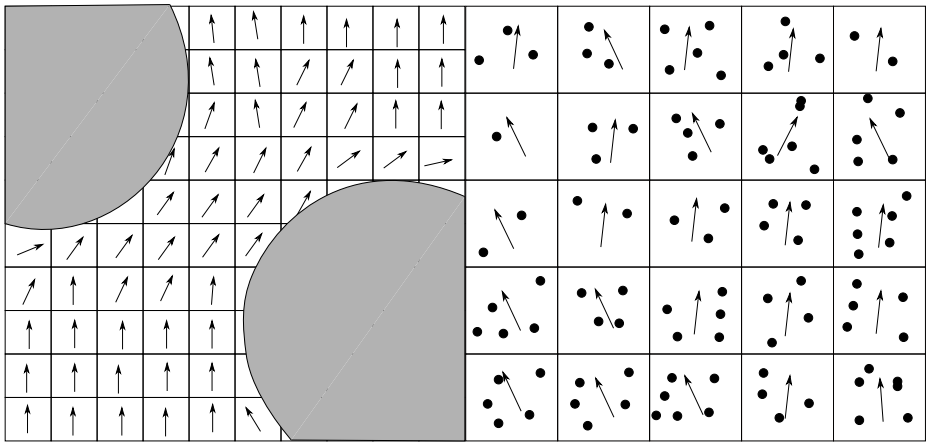

Figure 1.14. Main differences between the (a) resolved and (b) unresolved *CFD-DEM* approaches.

prediction, as each cell only contains information of a single particle. On the other hand, the unresolved *CFD-DEM* simulations lead to high simulation speeds for flows with low gas-solid coupling due to the coarser mesh. However the use of this approach does not give information about inter-particle properties and the swarm effect has to be taken into account when forces are applied to more than one particle per cell [64]. In this thesis, all the simulations have been run under the unresolved paradigm, as spouted beds do not involve severe fluid shear forces and, furthermore, simulation time and implementation procedure are considerably reduced.

In addition, it is also noteworthy that the temporal resolution of *CFD-DEM* can vary from concurrent coupling to partial or weakly coupled. The choice of with procedure to used depends on the strength of the coupling between phases. For those system where both phases operate under similar time scales and a heavy interaction between phases is present, both *CFD* and *DEM* times have to advance at the same pace.

However, the solid collision time scales are usually much sorter ($1x10^{-7}\,s$) than the fluid time scales ($1x10^{-5}\,s$)[66]. This feature enables *CFD* to advance at a different pace than its *DEM* counterpart. As shown in Figure 1.15, the *DEM* field advances a preset number of *DEM* time steps (Δt_{DEM}), while keeping the *CFD* field constant, before it gets updated at the coupling step. At this point, all the accumulated effect of the solid on the fluid phase is sent to the *CFD* field, along with all the new particle properties in order to advance the solution by a *CFD* time step (Δt_{CFD}).

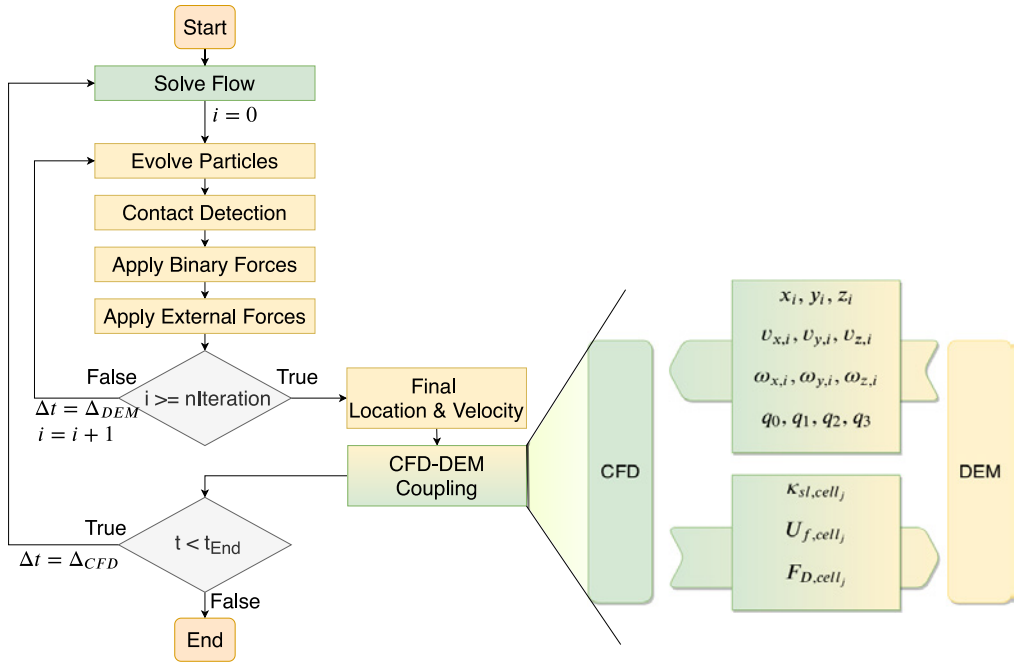

Figure 1.15. *CFD-DEM* algorithm flow diagram with *CFD* (green), *DEM* (yellow) and coupling step (color transition) with the exchanged parameters.

1.3.1 Domain decomposition and communication

As aforementioned, the domain has to be split between processors in order to take advantage of multicore processors and reduce the wall time required to solve a case. However, the way this decomposition is done can considerably affect the performance of the *CFD-DEM* code. In case of OpenFOAM® , there are two main ways to decompose a given domain:

- Simple: Split the domain into uniformly spaced bounding boxes, Figure 1.16a.
- Graph: Using a graph based library to decompose a non-uniform mesh by keeping a balanced cell count in all processors, while preserving cell locality, Figure 1.16b.

Considering that the mesh employed in this work is stationary and no dynamic refinement has been used, one of the most effective and easy ways to decompose a non-uniform and non-structured mesh is by means of the *Scotch* mesh partitioning library, as every processor in the simulation is given a matrix of similar size

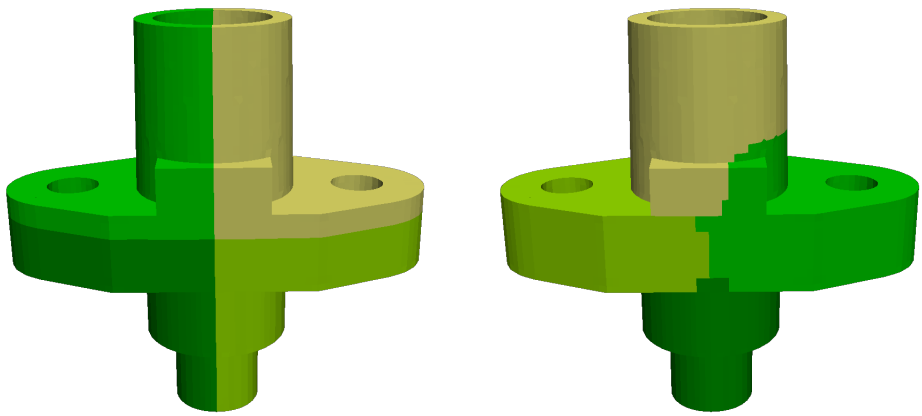

(a) (b)

Figure 1.16. Cell decomposition of a non-structured mesh with (a) simple decomposition and (b) graph decomposition.

to solve, thus minimizing the time each processor is idle. However, given that the fluid solution (*CFD*) is generally not the most expensive step, as the solid-solid *DEM* collisions takes the majority of the computational time, it is reasonable to try to optimize the decomposition to solve the *DEM* algorithm. Thus, it is common practice to try to use the same decomposition in the *CFD* side so as to increase data locality (data that is close in the system memory). Therefore, given that LIGGGHTS®uses a bounding box domain decomposition, the same processor splitting will be kept for the *CFD* side, accepting some cell imbalance between processors in exchange for a faster *CFD-DEM* communication. In order to balance the load between processors, instead of splitting the domain in uniform volume sets, the domain is split so as to assign the same amount of particles to each processor. Nonetheless, particle locations, and therefore their distribution, is not stationary, as these move through the domain, and hence a dynamic load balancing technique is required.

Most authors use the bounding box contraction and expansion approach [67, 68], where the particle count in each domain is computed at a preset number of *DEM* steps and a load imbalance value is calculated. In case this imbalance surpasses a preset threshold, the *DEM* subdomain is expanded or contracted and particle data is transferred between processors accordingly. This is the standard *MPI* decomposition implemented in LAMMMPS® , but, as few authors have suggested, the domain decomposition does not guaranty a homogeneous distribution of the workload, as this parameter is not sorely influenced by the number of particles,

but rather, the neighbor list building and solid-solid contacts. Henceforth, some authors have implemented hybrid schemes, in which, in addition to said *MPI* decomposition, the load within each processor is split into threads depending on the number of contacts in each subdomain by using thread/processor pinning for the *MPI* decomposition and recursive coordinate bisection (*RCB*) for the thread decomposition [67].

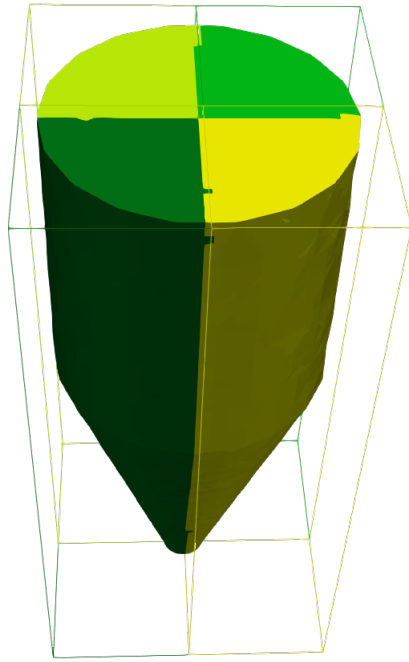

Figure 1.17. Comparison of a regular cell decomposition (*CFD*) and domain bounding box decomposition (*DEM*).

On the whole, the main objective of *DEM* is to split dense regions with many particles as many times as reasonably possible, whereas *CFD* requires to split the domain in a uniform group of cells. Unfortunately, this usually causes *CFD* and *DEM* decompositions to differ considerably, Figure 1.17. However, a balance must be struck between the two to keep both domains as similar as possible in order to reduce interprocessor communication and keep data locality.

Taking into account all the communication that has to be made for a *CFD-DEM* simulation and considering that some information might not be in the same processor or node, it is always recommended to minimize data exchange. When a multi-threaded workload as the one explained in this work is employed, a problem arises from particles that might interact or collide with particles belonging to another processor, as shown in Figure 1.18. In this case, the location, size and ori-

entation (irregular materials) has to be known in order to run the required contact detection algorithm. A dummy approach would be to store all the particles and locations in a global array that is subsequently broadcasted and updated. This approach is called an *all-to-all* communication [63] and works fairly well for a small number of particles and processors. When a significant number of processors are used, this approach does not properly scale, as every processor has to open an *MPI* communication with the remaining processors, thereby increasing the communication overhead and crippling the simulation performance.

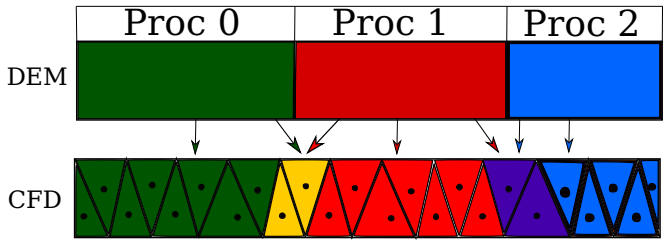

Figure 1.18. *CFD-DEM* data mapping and communication pattern in a 2D case.

A smarter way of building communication streams is to store only the particles that belong to a given processor and those of the neighbouring processors in an approach dubbed *few-to-few* [69], which has been used in this thesis. Considering that LIGGGHTS®splits the whole domain in cubic bounding boxes, the maximum number of partners a processors might have, ranges from 1 to 8, which is still a considerably high number of particles to track, but a significant improvement over the previous case, thus enabling the simulation of reasonably sized problems.

1.4 State-of-the-art in spouted bed simulation

Gas-solid contacts and spouted beds have been already modeled and simulated under varying conditions [70, 71]. Some early simulations derived from fluidized bed simulations employed Eulerian-Eulerian $3D\ TFM$ [72], along with specific closure equations in order to generalize the binary collisions in the $KTGF$ model. Most studies have been carried out in a configuration without draft tube (WDT) [73–76], but some authors have reported simulations with different internal devices, such as those equipped with a solid draft tube (SDT) [77, 78], porous draft tube [79] and draft plates [6]. Most studies rely on the Gidaspow drag model [80] and focus on the fitting of the closure parameters for each material or application, such as pyrolysis [81] and combustion [82].

In the search for more detailed simulations and to avoid assumptions made in

TFM, most authors have resorted to Eulerian-Lagrangian approaches, such as *MPPIC* [35, 83], and more commonly to non-resolved *CFD-DEM*. The latter simulation technique allows for a more granular result [50, 84] and a better matching of simulation properties to those obtained in the experimental setup. However, the use of *CFD-DEM* requires solving the solid-solid collisions, which considerably increases the computational cost of an industrial scale simulation. In order to cope with that restriction, some authors have used statistical methods [69] based on the recurrent behavior of the bed or coarse graining, where particles are considered to be moving in clusters and only collisions between these clusters are solved [85–88]. As a consequence, all the interaction forces, and specially the drag forces, need to be scaled up in order to account for this approximation, by either using the parcel properties [89] or the mean particle properties within the parcel [90].

Luckily, for a medium size problem, i.e., below one million elements, a fully non-resolved *CFD-DEM* simulation performs well within the reach of the current computation capabilities and a number of studies have been recently conducted for conical [91] and prismatic spouted beds [92]. Some studies also approached the effect of the internal devices [83, 91], along with some applications, such as coating [93], biomass gasification [94] and combustion [95]. In addition, attention has also been paid to the closure drag model in specific applications [96] and to the way *CFD-DEM* closure parameters are measured experimentally in order to attain reproducible results [36, 97].

Regarding irregular solid simulation, Liu et al. [98] conducted simulations in spouted beds with cylindrical particles and Zhong et al. [99] reviewed the basic approaches for irregular solid fluidized bed simulation. Most simulation approaches in the literature use data from previous studies by other others, such as the one by Zhou et al. [100], and so they rely on a specific flow rate and configuration, which widely limits their application to other systems. Therefore, given the low availability of local experimental data for regular and irregular particles, as well as the limited number of simulations at varying flow rates and internal devices, it becomes apparent the need for conducting a study to gain knowledge in the understanding of these systems and their prediction capabilities.

2 Experimental

2.1 Bed materials

Table 2.1 shows the physical properties of the bed materials used in this study, which vary mainly on density and shape, but all fit the description of superquadric particles. Even though their shape varies considerably, their volume is of the same order so as to avoid this variable in the analysis.

Apart from the main physical properties shown in Table 2.1, a few variables ought to be estimated for the simulations, such as restitution coefficients and frictional parameters. To this end, an approach similar to the one used by Rackl et al. [101] has been implemented. Thus, a given amount of particles has been poured into a cylinder, which has been lifted in order to allow the particles to settle under gravity. These particles form a heap, whose angle of repose is measured experimentally through image treatment and compared against the value obtained in a simulation of this process, thereby adjusting the frictional parameters accordingly.

2.2 Equipment

Two types of spouted bed technologies have been used in order to study the influence each geometry has on the fluidization of varying shape particles. Even though these two geometries belong to the same type of spouted bed, their sizes, operating modes and data gathering differ considerably and will be separately explained in the following sections.

Table 2.1. Physical properties of bed materials.

Material	ρ_s [kg/m^3]	$\bar{d_p}$ [mm]		
		d_x	d_y	d_z
Conical Spouted bed				
Glass beads	2500	2, 4	2, 4	2, 4
Lentils	850.50	4.1	4.1	2.12
Prismatic spouted bed				
Glass beads	2500	2, 4	2, 4	2, 4
ABS pellets	2100	2.2	3.4	2.7
Lentils	811.50	4.5	4.5	2.54

2.2.1 Conical spouted bed

The conical spouted bed is a pilot scale plant that allows for a wide range of fluidodynamic studies and operating modes. Figure 2.1 shows a simplified diagram of the equipment, where a 5.5 kW blower feeds air into the system with a maximum flow rate of 600 $m^3\,h^{-1}$. This flow rate is measured by means of a thermal mass flow meter (ValueMass^{TM} 400 Thermal Mass Flow Meter, Eldridge Products, United States) with a measuring resolution of 1% of the total flow rate of 800 $m^3\,h^{-1}$. Air passes through a three way valve that diverts a fraction of the blower output to the environment and the remaining air is directed through a pipe to a polyethylene terephtalate (*PET*) contactor. The differential pressure is measured between the inlet point and the contactor outlet by means of a high frequency pressure transducer (PD-23, Keller, Switzerland) with a sampling frequency of 1 kHz.

Once the air has passed through the contactor, the stream is directed to the filtering system where the solids are retained before releasing the stream to the environment. Figure 2.1 shows that the unit is provided with four manual butterfly valves, which allow treating the whole range of flow rates. Thus, when low flow rates are used ($< 125\ m^3\,h^{-1}$) a bag filter is able to treat the stream, but high flow rates require an air cyclone for coarse filtering, as the capacity of the bag filter is exceeded.

System monitoring and data acquisition is accomplished through a *PLC* (MFXEU, Mitsubishi, Japan) and its analog-digital expansion blocks, while the operator introduces new set points and displays the data by means of a touch screen. There are two options for the flow rate controlling loop, a coarse flow rate setting by a three way valve, which is set through a 0-10 V signal, whereas the flow rate fine tunning is completed by adjusting the rotational speed of the blower with a variable frequency drive, whose set point may be changed by a 4-20 mA signal. This

set-up allows to keep a constant flow rate, that is finely adjusted to changes in bed due to bubbling or pressure fluctuations, as they may affect the amount of air passing through the system.

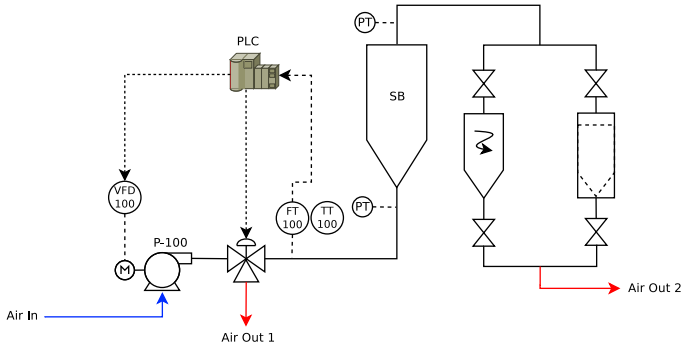

Figure 2.1. Simplified diagram of the experimental pilot scale plant.

As already mentioned, the most important piece of equipment in the whole set up is the transparent conical spouted bed, where the bed is place for the hydrodynamic experiments. The design of the pilot scale plant eases changing contactors and their geometrical parameters in order to achieve a fluidization (spouting) similar to that shown in Figure 2.2a. Thus, the solids are dragged trough the spout region and, once they have reached the bed surface height (H_o), they follow a parabolic trajectory (fountain zone) to land onto the surface of the annular zone. They then go downwards in a moving bed to finally complete a cycle. The fluidization regime is heavily dependent on the interaction of the bed material and the contactor geometry, Figure 2.2b. In this study, the dimensions of the contactor are as follows: diameter of the upper cylindrical section, D_c, 0.36 cm; conical height, H_c, 45.5 cm; angle, γ, 36^o and base diameter, D_i, 6.2 cm. Although the inlet diameter D_o can be modified, it has been kept at 0.4 cm following previous works that showed that this inlet diameter is highly stable under a wide rage of operating conditions [102–104].

In addition to the contactor geometry, there is also the possibility of using internal devices to increase the stability of the fluidization and the operational range of the conical spouted bed. The main types of internal devices have traditionally been draft tubes [105], but fountain confiners [106] have lately been used. In fact, the latter are essential devices not only for stabilizing the fluidization but also for reducing bed elutriation and extending greatly the operating range [107, 108]. This work has been specially devoted to the study of two draft tube types, namely, the solid draft tube (SDT) and the open-sided draft tube ($OSDT$), whose geometric parameters are described in Figure 2.3 [103, 109]. The open-sided draft tube has an aperture ratio ω_T of 56%, total length L_T of 0.22m and diameter D_T of 0.05m.

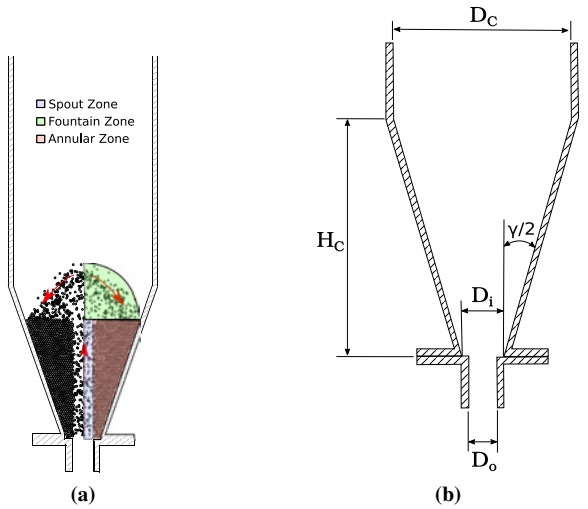

Figure 2.2. Diagram of (a) the expected solid movement within the bed, and (b) cross section of a conical spouted bed with the main geometrical parameters.

The reason to use this draft tube lies in the stability provided by this device to the system, as well as the fact that it ensures a suitable gas-solid contact by means of the wall aperture. In the case of the solid draft tube, the total length is the same as that of the open-sided draft tube (L_T=22 cm), and its entrainment height L_H is 7.5 cm. In order to study the effect of the aperture ratio, for now on, it will be assumed that the configuration without draft tube (WDT) is the same as a fully open tube configuration, ω_T=1, whereas the configuration with the solid draft tube (SDT) means no aperture, ω_T=0, leading to no solid incorporation through the wall of the draft tube, except at the bottom section through the entrainment zone.

In order to obtain a reasonable measurement of the whole solid velocity field, measurements have to be taken at varying positions throughout the bed. Taking an initial height of 22 cm in the 36^o conical spouted bed contactor with an inlet diameter (D_o) of 0.04 m, the measuring points shown in Table 2.2 have been chosen for each configuration. Note that the radial distance has been normalized so as r_i/r_{max} to be 0 at the center of the spout and 1 at the wall, which allows a comparison between different heights corresponding to various cross sectional areas in the bed.

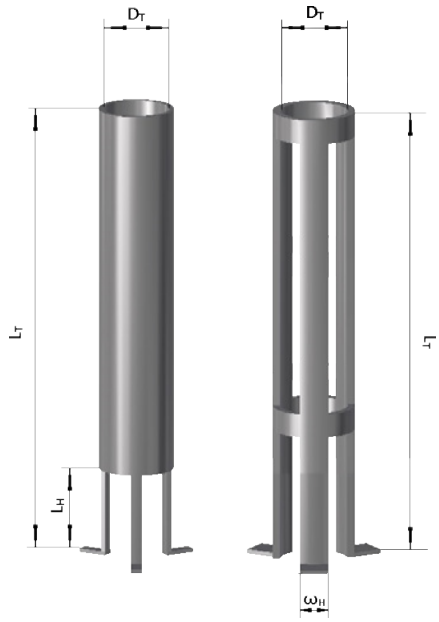

Figure 2.3. Diagram of a solid draft tube (on the left side) and an open-sided draft tube (on the right side) with their characteristic parameters.

Table 2.2. Measuring points for the configurations with different bed materials and operating conditions in the conical spouted bed

Conical Spouted bed	
H_i $[m]$	0.052, 0.113, 0.153, 0.203, 0.243, 0.30, 0.40
r_i/r_{max} $[-]$	0, 0.33, 0.66, 1
u_{ms} $[-]$	1.1, 1.25, 1.5
Bed Materials	Glass Beads, Lentils

2.2.2 Prismatic spouted bed

The set up of the prismatic spouted bed is shown in Figure 2.4a, and consists of a downstream pump whose air flow rate is controlled by a loop including a frequency variator, volumetric flow transmitter and computer. The blower sucks air from the spouted bed assembly in order to attain bed spouting based on the pressure difference created between the inlet and the outlet of the system. This particular setup, explained in detail elsewhere [110], creates a clear and ideal inlet of air, as no obstacles are present at the inlet of the contactor. During the experimentation, a pressure transducer (PD-23/8666.1, Keller, Germany) gathers pressure data at 300 Hz with a resolution of 10 Pa. The description of the main parameters of the contactor is shown in Figure 2.4b. The dimensions of the contactor used in this

study are as follows: height of the sloped wall H_c, 0.18 m; bottom depth L_c, 0.2m; contactor width L_T, 0.25 ; inlet width L_i, 0.8 cm and angle of the walls γ, 60^o. The measuring points for the configurations made up of different bed materials and operation conditions are summarized in Table 2.3.

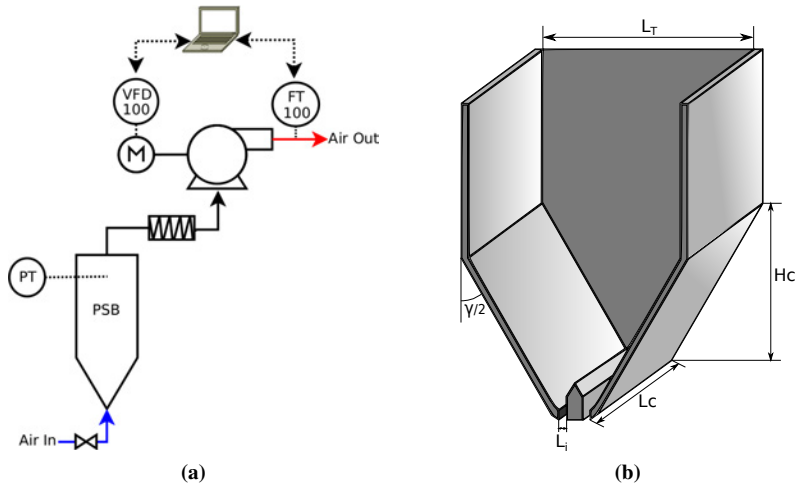

Figure 2.4. Simplified diagrams of (a) the experimental setup and (b) the prismatic spouted bed with its geometrical parameters.

PTV in the prismatic spouted bed has been conducted only on the lateral vertical wall, given that, unlike conical spouted beds, the vertical wall in these types of beds enables velocimetry measurements at different heights and radial locations with the capture of a single video. These measurements are assumed to be representative of the solid dynamic within the bed.

Table 2.3. Measuring points for the configurations with different bed materials and operating conditions in the prismatic spouted bed.

Prismatic spouted bed	
$\gamma\,[^o]$	60
$Z_i\,[m]$	0.0
$u_{ms}\,[-]$	1.0, 1.25, 1.5, 1.75, 2.0
Bed Materials	Glass Beads, Lentils, *ABS* Pellets

2.2.3 Optical system

The conical spouted bed has certain advantages over the prismatic one, such as better mixing and bed stability. However, the absence of a vertical wall does not

allow measuring the solid velocity within the bed, unless half columns are used. Therefore a way to access the bed is required in order to characterize it with negligible disturbances.

To that end, a borescope of $1.1\,cm$ in diameter and $15\,cm$ in length is employed, which has a very reduced footprint over the whole bed. This probe is inserted into the center of the bed and solid flow symmetry is assumed relative to the main axis. The borescope captures the light in front of its tip, decreasing even further the disturbance made to the measurement, as only solids around the device are expected to be disturbed, but not those in front of its tip. This light is transfered to the back of the borescope, where a gray scale (8 bits) high speed camera (S-PRI, AOS Technologies AG, Switzerland) is attached with a maximum recording speed of $2500\,fps$ at full resolution and $16000\,fps$ with a reduced window. As with any other high speed camera, the lighting is delivered from a high efficiency continuous light source (IntraLED5, Volpi, Switzerland) in order to reduce the flickering of the images when recording at high speed. In this case, a *LED* light source has been used with more than $700\,lm$, whose light is transmitted by an optical fiber to the tip of the borescope, as shown in Figure 2.5. The lighting level ought to be kept high when recording at high frame rates, given that the shutter speed, and hence the exposure of the objects to the sensors, is much shorter.

The whole borescope is a delicate piece of equipment that is intended to be inserted in a very abrasive and demanding environment with high speed solid particles passing by, and a resilient enough protection layer has to be used in order to increase the lifespan of the equipment. In order to protect the borescope and reduce the wearing off the borescope tip, a protective cartridge (shown in Figure 2.5) with a sapphire tip is employed to avoid scratching from glass beads or sand particles. The borescope is attached to the camera through a *C* type optical fitting, while the image is focused onto the *CMOS* camera sensor by a lens with an opening angle of 50^o and plane tuning physical dial to adjust the location of the object plane depending on the distance between the borescope and the protective cartridge.

The last component of the whole borescopic assembly is the tip spacer, which is used for regions where highly bubbling or very dilute regimes are expected. This tubular appendix has two big lateral openings in order to let solids freely flow, as shown in Figure 2.6. Once the openings have been aligned with the particle flow and the borescope to spacer relative distance has been set so as to minimize the distance while reducing disturbances, this device keeps a constant background color and increases the contrast of the particles. In addition, it removes particle projections that are far away from the depth of field of the camera, as they introduce noise in the solid detection algorithm. The spacer has been $3D$ printed with

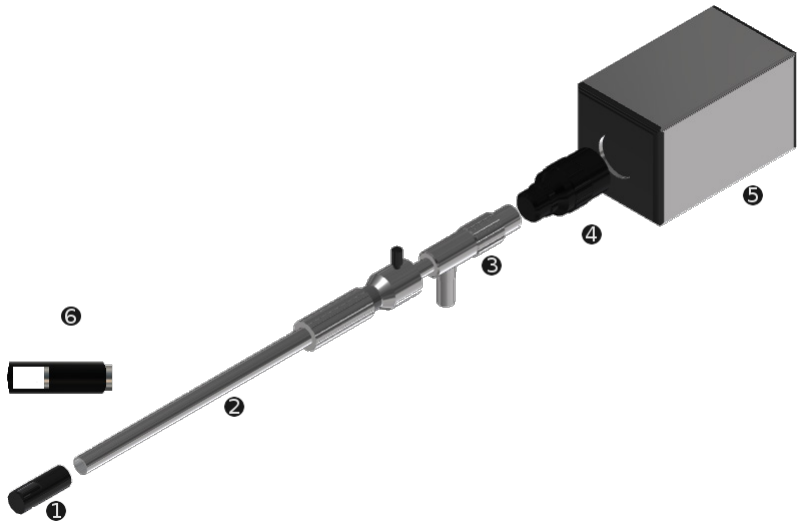

Figure 2.5. Borescope assembly: (1) Spacer, (2) cartridge protector, (3) borescope, (4) optical adapter, (5) camera and (6) enlarged image of the spacer.

black thermoplastic polyurethane (*TPU*) and the freshly printed device has been scraped in order to remove the glossy finish and scatter the incident light, thereby reducing the amount of light reflected back to the camera.

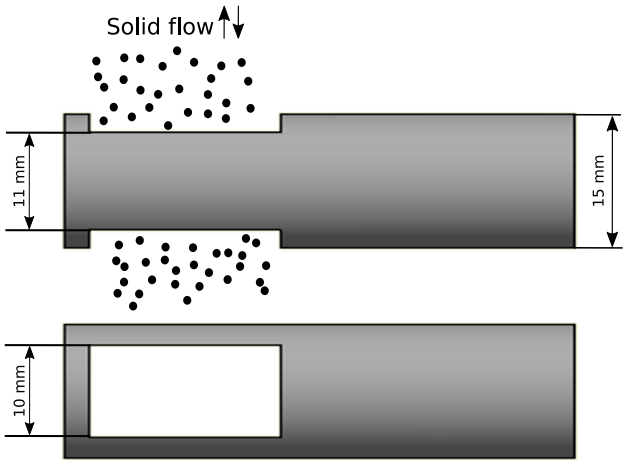

Figure 2.6. Diagram of the spacer with its main dimensions and direction of the solid flow.

As inferred from the length of the borescope and from the contactor diameter,

this optical system allows measuring at radial positions from the wall to the axis of the bed. In order to get a precise location and insertion of the borescope, a system of rails and sliders shown in Figure 2.7 has been mounted around the contactor. Firstly, a 180^o curved rail is placed around the bottom of the contactor and a horizontal slider is mounted on top of the curved rail. In addition, a set of two straight sliders are placed normal to each other and attached to the sliding platform. The camera is mounted to the last horizontal rail allowing for a primary radial positioning of the optical device and a subsequent movement along the other two axes in order to place the tip of the borescope anywhere in the contactor.

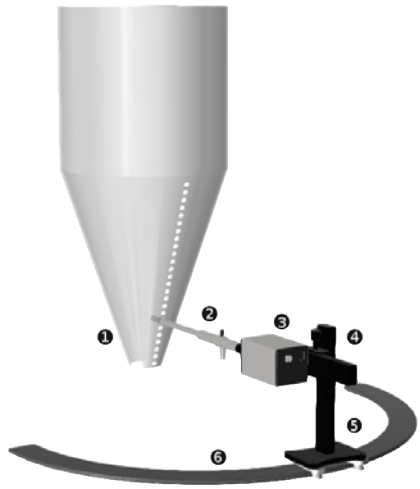

Figure 2.7. Image recording system: (1) Contactor, (2) borescope assembly, (3) camera, (4) straight sliders, (5) sliding platform and (6) perimeter slider.

In case the particles in the fountain are to be measured, instead of the optical system described above, the camera has been attached to a standard $12.5\,mm\ f/1.4$ C mounted lens (FLBC1214DVG, Ricoh, Japan) for a greater field of view than the previous configuration. The camera has been mounted and the focus adjusted for a correct detection of the fountain shape and height. All the calibration for the correction of the lens distortion has been based on a vertical reference scale placed beside the contactor in order to measure the local distance.

Once the optical system has been attached to the setup, a number of calibration steps have to be followed in order to ensure a correct detection of the images. The first step is to measure the radial and tangential distortion the lens and borescope introduce in the images. A printed $3.3\,mm$ black-white chessboard pattern is captured a number of times, as shown in Figure 2.8. Given that all lines in the chess board have to be either parallel or perpendicular to each other, the expected pat-

tern is checked against the one taken from the camera.

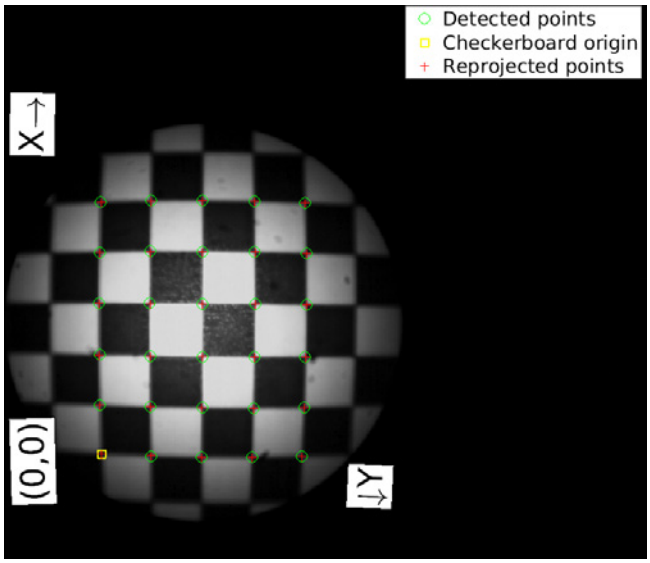

Figure 2.8. Chessboard calibration of the lens.

A common effect that must be avoided is the barrel effect, which occurs when a single lens is used in a borescope. To this end, the predicted positions of the cross points in Figure 2.8 are corrected based on those captured, by means of Equations 2.1-2.2.

$$x' = x(1 + k_1 r^2 + k_2 r^4 + k_3 r^6) \tag{2.1}$$
$$y' = y(1 + k_1 r^2 + k_2 r^4 + k_3 r^6) \tag{2.2}$$

where x and y are the normalized pixel positions in [-1,1] range and k_1, k_2 and k_3 are the fit parameters to correct the radial distortion.

The tangential distortion is generated by the misalignment of the sensor and the lens, giving as a result a plane object that is not completely aligned with the sensor. In case this distortion is significant, the chessboard pattern images are fitted to Equations 2.3-2.4

$$x' = x + (2p_1 xy + p_2(r^2 + 2x^2)) \tag{2.3}$$

$$y' = y + (p_1(r^2 + 2y^2) + 2p_2 xy) \tag{2.4}$$

where p_1 and p_2 are the fitting parameters for the tangential distortion.

In addition to the radial an tangential distortion, the intrinsic matrix must be obtained to account for possible pixel skew angles and camera aspect ratios. This matrix does not change with time and has to be obtained only once in order to make the required correction, where the radially corrected pixels from Equation 2.1-2.4 are transformed using Equation 2.5 to give the distortion free pixel projection.

$$\begin{bmatrix} x \\ y \\ 1 \end{bmatrix} = \begin{bmatrix} f_x & 1 & 1 \\ s & f_y & 1 \\ c_x & c_y & 1 \end{bmatrix} \begin{bmatrix} x' \\ y' \\ 1 \end{bmatrix} \tag{2.5}$$

where f_x and f_y are the projected center location of the camera in pixels, s is the skewness of the camera pixels and, finally, c_x and c_y are the field of view in relative pixels to the center in each of the axes. It is worth mentioning that only a single camera has been used in this work, and the extrinsic matrix of the camera is not therefore needed as no stereo *PTV* capabilities are used.

With the aim of obtaining the radial and tangential coefficients and the intrinsic matrix values, a number of captures have been taken to the mentioned chessboard pattern. Then, these figures haven been checked with the *Matlab* camera calibrator toolkit and with the *OpenCV* camera calibration function, thus obtaining the values shown in Table 2.4. As shown, the mean projection estimation error is below the single pixel value, which ensures a reliable measurement of particle position in the plane. Comparing the values from *Matlab* and *OpenCV*, the former performs slightly better with a greater consistency of the mean projection error. Therefore, these are the values that will be used in the image treatment algorithm.

2.3 Image processing

This section deals with the algorithm to convert the footage from the high speed camera to solid velocity, as this implementation determines the reliability of the experimental data, and therefore the validity of the subsequent simulations. The whole image treatment algorithm is written in *Matlab*2017*b* and is shortly described in Figure 2.9. The aim is to detect particle velocities for most materials commonly used in hydrodynamic studies and, specifically, those shown in Table 2.1. The detection range of the algorithm must cover spherical particles and slightly irregular materials, as well as a wide range of particle sizes; from a maxi-

Table 2.4. Main values for correcting the optical distortion of the used lenses.

Equation	Param.	Matlab [px]	OpenCV [px]	Matlab [px]	OpenCV[px]
2.1, 2.2	k_1	-0.615	-1.922	-0.0645	-0.049
	k_2	1.374	30.203	-0.2842	0.169
	k_3	-5.077	-145.45	0.6388	0.3736
2.3, 2.4	p_1	0.022	-0.0132	0.0024	0.0037
	p_2	-0.003	-0.0369	0.0032	-0.022
2.5	f_x	634.850	550.106	1339.72	1263.1
	f_y	632.75	551.45	1342.23	1275.2
	s	0.0	0.0	3.3521	0.0
	c_x	432.186	424.92	1009.1	927.11
	c_y	308.659	346.06	584.54	512.89
Projection error [px]		0.34	0.37	0.33	0.53

mum of $\bar{d}_p \sim 4\ mm$ to a minimum of $\bar{d}_p \sim 70\ \mu m$, as it is intended to also be valid for sand particles.

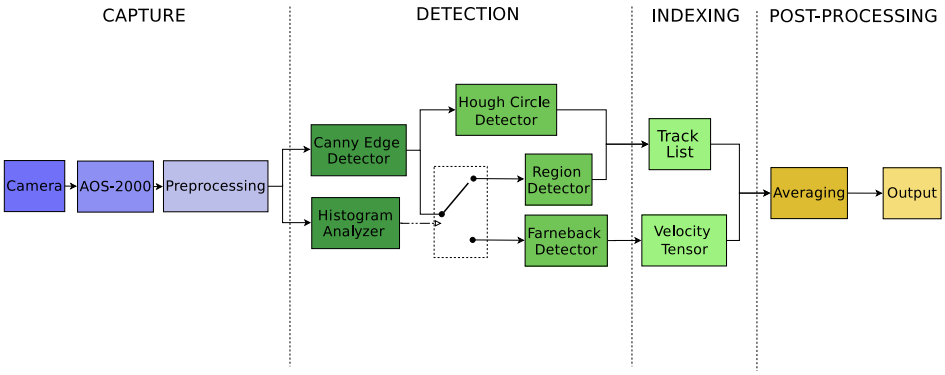

Figure 2.9. Flowchart of the algorithm for particle detection and image treatment.

Figure 2.9 displays the four main steps in which the image processing procedure is divided. The first one is the capture itself, which is the main step. Adequate lighting and camera parameters are set, as are recording time, recording speed and shutter time. The latter is specially influenced by the recording speed, as it conditions the minimum shutter speed that can be used at the current recording speed by exposing the sensor for the whole time a frame is being taken. This speed is rarely desired, as it reduces the sharpness of the image, which hinders the edge detection that will be applied in the following steps. Henceforth, a short shutter speed is desired, but the amount of light required increases as shutter speed is reduced, and therefore a balance should be struck between these factors. Once the camera is ready and stable fluidization or spouting takes place, the footage is taken for 2 s. Multiple recordings are taken at the same point in order to ensure

reproducible results.

The footage is fed in parallel to the algorithm and all the recordings follow the same path shown in Figure 2.9, which begins with the preprocessing of the image.

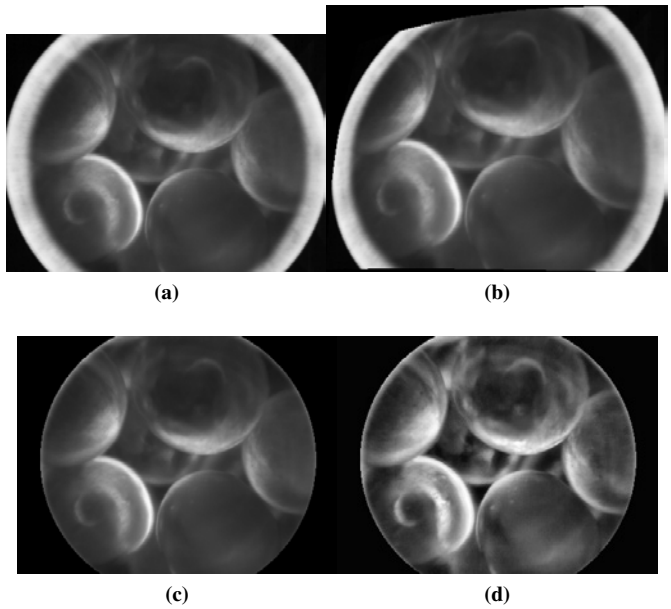

Figure 2.10. Preprocessing sequence: (a) Original image, (b) distortion free image, (c) cropped image and (d) dynamically equalized image.

As previously stated, the main distortion coming from the lens is of radial nature, due to the barrel effect in the input image (Figure 2.10a). In order to reduce the velocity estimation error this image is corrected using Equations 2.1-2.5, which provides a distortion free image shown in Figure 2.10b. As explained in the following paragraphs, the reflection of the sapphire needs to be removed as this would reduce the accuracy of the pixel motion estimation and the canny edge detector. Therefore, the image is cropped by removing the circle (Figure 2.10c) or cropping a rectangle inside the reflection circle, which in addition to reducing the error of the motion estimation also reduces the number of pixels per image to be processed. Once the desired window is obtained, the contrast of the particles shown in the image is increased by dynamically equalizing the grayscale histogram. In case the figure shows any kind of particle, the equalizer takes this brightness as a reference and increases the contrast accordingly, as shown in Figure 2.10d. However, in case no particles are present within the image, the equalization step raises the noise level of the sensor, a feature that will be useful in the following steps, specially when the solid packing is to be deduced from the grayscale histogram.

Once the capture and preprocessing step has been completed, the resulting image is fed to the solid detection step. Prior to that, the user must determine the type of solids to be detected, given that the detection approach differs depending on regularly or irregularly shaped particles.

In case the solid to be treated fits approximately the description of a sphere, the solid centroid detection becomes a circle detection problem. Firstly, the preprocessed image is fed into a canny edge detector that locates sharp and significant edges. The lower and upper threshold values are changed in an interactive manner until the user is satisfied with the resulting detected edges. After that, the algorithm requires the range of circle radii to be detected, which is a value readily available from the display of the first frame. Once the radii range is set for each radius value, a voting process as that shown in Figure 2.11 is applied, where, for every pixel coming from an edge detector, a vote is increased to those positions that fall within the corresponding radii range.

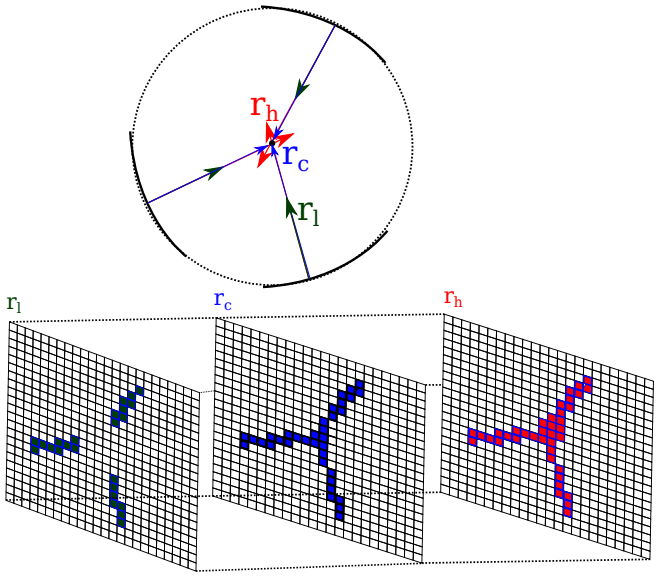

Figure 2.11. Hough circle detector voting process.

However, given the computation cost required to compute the overlapping radius positions for every edge pixel, its is more common to fit the aforementioned edges to polynomial equations and increase the votes only in the direction normal to the curve, as shown in Figure 2.11. Once all the voting matrixes have been calculated, the next step consists in a maximization problem where the objective function is the sum of all the votes for a particular radius. It is worth noting that radii values are mutually exclusive, and therefore once a radius has been chosen

for a location, the votes of the remaining radii for those pixels are removed. This introduces a problem when a particle is partially occluded behind another particle. Once a particle in the background has been detected, the chances of detecting a partially occluded particle are reduced, given that the votes in the centroid location of the latter have been reset to zero. However, this approach reduces the noise and false positives when multiple particles are detected for a single sphere. After the maximization process is concluded, the Hough detector gives the location of the most likely positions for centroids and their radii by choosing those locations with highest voting values.

Other materials under study in this work are ellipsoids, such as lentils or pills. The advantage of using such shapes is that these particles project either a circle or an ellipse on the sensor, and their detection is therefore reduced to the detection of ellipses. While the Hough circle detection is based on a voting process of three dimensions, i.e., circle centroid position (x_c and y_c) and particle radius (r_p), the detection of an ellipse can be describe as a five parameter voting process, given that, in addition to the centroid location, the main axis length, aspect ratio and orientation must be determined [111].

The procedure for detecting irregular particles, i.e., particles that are expected to be significantly far from a spherical representation, as is the case of *ABS* particles or sand, is shown in Figure 2.12. Firstly, the output of the canny edge detector is taken (Figure 2.12a) and a dilate erode routine is used with a stencil of $4x4\,px$ in order to close the edges into single regions (Figure 2.12b). Each region size is filtered based on the maximum surface that a given particle can have. This value, as in the case of the Hough detector, is derived from the first frame of the video. Finally, regions that fall under the area range being searched are indexed and their geometrical centroids found, and the spurious edges that are detected within the outer edge are removed, as shown in Figure 2.12c. Each centroid and particle surface is fed into the track list algorithm, whose objective is to pair subsequent detections of the same particle in a reliable fashion in order to infer the solid velocity.

However, the use of a region detection algorithm does not reliably work when particles are tightly packed. Under these conditions, as particle edges are too close to each other, the algorithm does not recognize individual grains. The problem gets worsened when considering that the whole annular region, except the annular-spout transition region, is expected to show this kind of behavior. In order to overcome this shortcoming, a pixel brightness displacement algorithm, as the one by Farnebäck, is used [112] with a multi-scale displacement motion estimation. Farnebäck algorithm requires the fitting of each pixel and a number of surrounding pixels to a polynomial expression, and provides as a result a three dimensional

(a) (b) (c)

Figure 2.12. Example of (a) original edge of the image, (b) dilate and erode routine and (c) region identification-indexing over the original frame.

tensor for the whole x and y direction of the image and the fitting coefficients for each pixel. Assuming that the lighting is constant and minimizing the change of said tensor between frames, the solid movement on each pixel is obtained. This algorithm however only works for small and packed solid displacement and cannot be used when the solids are in a lean phase. Therefore, a technique for bridging both techniques is required in order to detect irregular particles without a prior knowledge of the packing under study.

In order to switch from the region detection algorithm for the dilute packing regime to the pixel displacement algorithm for the densely packed regime, the gray scale histogram of each frame is analyzed. When solids are tightly packed, most solids reflect uniformly on the sensor, giving as a result a normal brightness distribution. When particles start to loosen, small gaps and holes appear in those regions and the distribution starts to show a tail. Based on this information, a two shape parameter distribution is fitted to the frame histogram. In this case, the β distribution has been chosen following

$$B_{\alpha,\beta} = \int_0^1 t^{\alpha-1}(1-t)^{\beta-1}dt \tag{2.6}$$

where α and β are the two shape variables of this distribution. Using Equation 2.6, the cumulative pixel brightness distribution is fitted as follows:

$$f(x) = \frac{1}{B_{\alpha,\beta}} x^{\alpha-1}(1-x)^{\beta-1} \tag{2.7}$$

where x are brightness values in a $[0-255]$ range. Thus, α and β values are fitted

to the gray scale histogram for each frame in order to obtain the shape values that best suits the distribution under study, resulting in values as the ones shown in Figure 2.13.

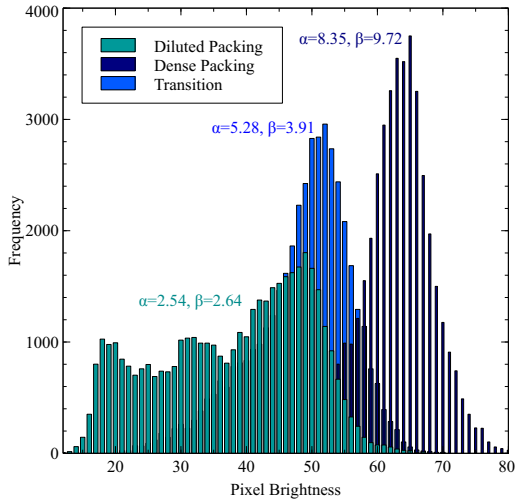

Figure 2.13. Gray scale histogram for different packing conditions and the values of best fit for the distribution shape coefficients.

When both parameters are away from values around 2 and are similar in magnitude, the distribution is assumed to be normal and the Farnebäck algorithm is used. When gaps appear between particles, shape parameters decrease in value due to the tail that starts to develop, and when any parameter decreases below a value of 3, the switch is activated because the distribution is getting skewed towards a flat distribution, characteristic of very dilute regimes.

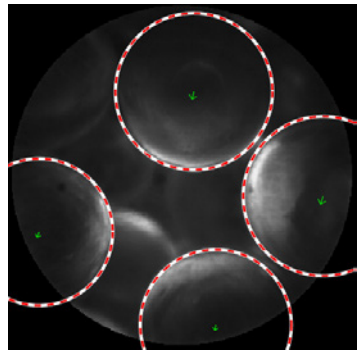

Figure 2.14. Result of the sphere tracking algorithm.

Once the solid centroid detection has been accomplished, the indexing step uses

this information to obtain the solid velocity for each frame, Figure 2.14. In the Farnebäck algorithm, the velocity tensor is given directly by the quadratic minimization routine. However, a velocity vector is given for each pixel, while the accuracy decreases towards the frame edges. Thus, a Gaussian weighting function is used in order to give more weight to those velocities closer to the center of the frame, resulting on the averaged frame solid velocity.

In order to perform the region detection algorithm or the circle detection, particles must be paired in subsequent frames. To that end, a track list class as the one shown in Figure 2.15 is built. The whole list is a collection of tracks (detected particles) represented by a structure that contains information about the current location P_0, future location P_1, velocity u_s, acceleration a_s, number of detected times n_d and number of frames in which the detection has been occluded n_o. Each one of the tracks are represented by a node, and their corresponding values are updated accordingly. In addition, this class is built with children and parent pointers in order to create hierarchical structures, if needed. Moreover, the paring between detections and tracks is done by the use of the hungarian algorithm [113] for the linear assignation problem [114], which consists on keeping the minimum of the summed distance differences between the predicted track ($P_{1,i}$) locations and those detected (C_i) by applying Equation 2.8 to the data in Table 2.5.

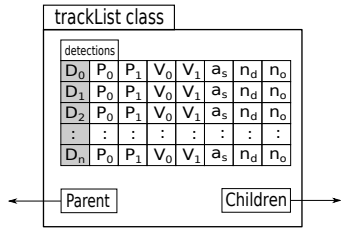

Figure 2.15. Graphical representation of the track list class.

Table 2.5. Hungarian algorithm assignation table.

	$P_{1,1}$	$P_{1,2}$	...	$P_{1,N}$
C_1	$(P_{1,1}-C_1)^2$	$(P_{1,2}-C_1)^2$	...	$(P_{1,N}-C_1)^2$
C_2	$(P_{1,1}-C_2)^2$	$(P_{1,2}-C_2)^2$	...	$(P_{1,N}-C_2)^2$
C_3	$(P_{1,1}-C_3)^2$	$(P_{1,2}-C_3)^2$	...	$(P_{1,N}-C_3)^2$
$\vdots$	$\vdots$	$\vdots$		$\vdots$
C_N	$(P_{1,1}-C_n)^2$	$(P_{1,2}-C_n)^2$	...	$(P_{1,N}-C_n)^2$

where the first term is the sum of the cost of all the assignments and the second term represents the cost of non assignments, in order to force Equation 2.8 to complete the detection-track pairing, while avoiding those distances that are

unreasonably high. Once the pair has been assigned and the velocity has been calculated, the next location of said particle is projected, not only to speed up the next pairing process, but also to make the algorithm somehow robust to a degree of occlusion between particles. For some cases, a single track list is enough to obtain a solid velocity signal, but, in other cases, some of the tracks have higher priority because they have been for longer in the image, and therefore a hierarchical track list data structure, such as the one shown in Figure 2.16, is built to single out only those velocities that have a higher degree of certainty.

$$MIN\left(\sum_{i=0}^{k}(P_{1,i}-D_l)^2+C_{na}N_{na}\right) \tag{2.8}$$

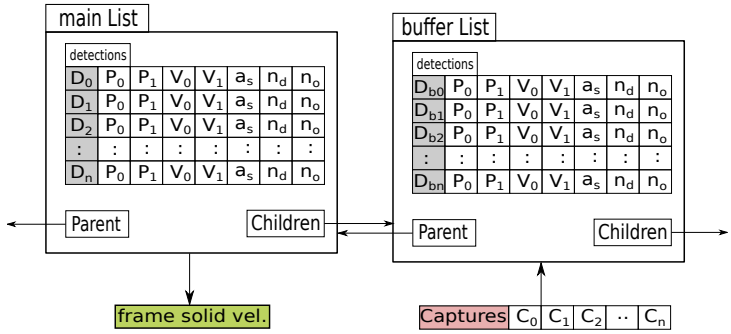

Figure 2.16. Data structure of the hierarchical tracking algorithm.

In this case, the fresh detections are first checked with the main track list for pairing, and the remaining detections are checked with the sub track list. Only when no pairs are found in any of the lists, a new track is created in the sub track list. At this point, those detections from the lower track list that have been paired and tracked for a number of frames are sent to the main list, where they are added to the final velocity vector. Hence, the lower track list behaves as a filter of detections in order to reduce the amount of spurious detections that get included in the final velocity vector.

The final step of the algorithm is the averaging of the signal, where each velocity tracked for every pair of frames gets indexed inside a velocity distribution, or in most cases velocities get averaged in order to obtain a dynamic time dependent solid velocity signal, as shown in Figure 2.17. As is readily clear, this signal is averaged in time in order to get the average solid velocity value for each location in the bed.

Algorithm validation is of uttermost importance in order to make sure that the data obtained through this technique are reliable enough to validate simulations.

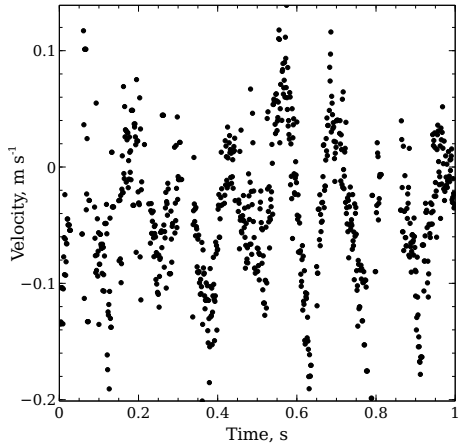

Figure 2.17. Time dependent solid velocity signal for a given spout location.

Taking into account the range of velocities expected inside the contactor along with the variety of packing regimes that are usually encountered in spouting regimes, a set of experiments have to be conducted.

In the first round, a low velocity high packing regime test has been run, where a vertical tube with an internal diameter of $4\,cm$ has been filled with spheres or sand. Subsequently, a hole has been opened in the lower end of the tube and let the solids fall under gravity, while the borescope is inserted in the tube perpendicularly to the flow. In each discharge, the solids accelerate until a steady state conveying velocity is achieved and at that moment the recording is started. The solid descend velocity has been varied by changing the diameter of the discharge hole.

The aforementioned technique is only valid for low velocity solids resembling the annular zone. For the remaining velocities, the spout is used for validation. Given that the spout axis is where high particle velocities are expected and no significant velocity changes occur at a single point when the bed is stable, it is reasonable to assume a constant velocity in the time range between two frames.

Once the footage for a range of velocities and solid types is obtained, randomly selected subsequent frame pairs are taken, to which their centroid detection and pair assignment process is carried out by hand. The resulting parity plot is shown in Figure 2.18. As shown in this image, the error between the values given by the algorithm and the optical flow is below 10% of the nominal value. The error increases as the velocity value increases, but the automatic detections are reasonable for the whole range of 0-8 $m\,s^{-1}$ velocities, and therefore these are suitable for

validating simulation data.

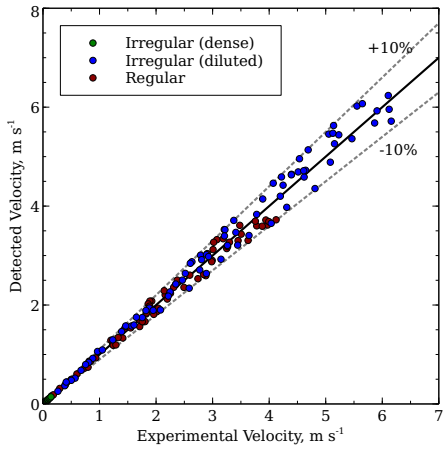

Figure 2.18. Parity chart of the visually detected velocities and those given by the algorithm.

In order to obtain *PTV* data in the prismatic spouted bed, a slightly different approach has to be used, as no endoscope has been used for velocity measurement at the lateral vertical wall. Thus, solid velocities in the different regions are captured on the same window. In order to obtain the local solid velocity, the raw image from Figure 2.19a has been split into sub-windows of interest with a uniform grid, as shown in Figure 2.19b, and the aforementioned image treatment algorithm has been applied.

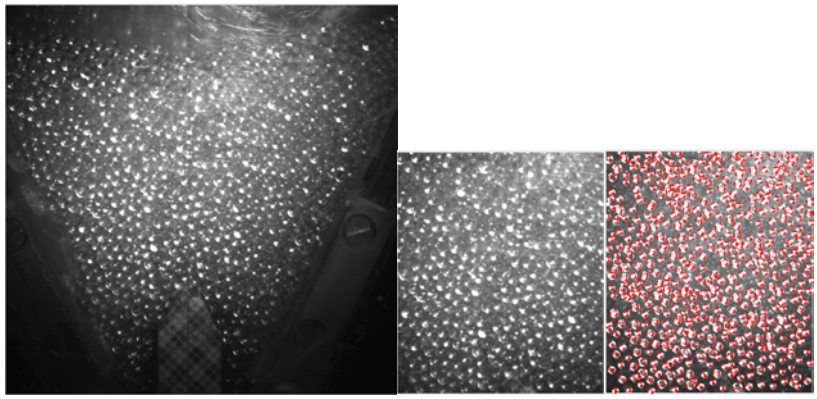

Figure 2.19. (a) Raw image of high speed capture with the solid velocity vectors, (b) a region of interest within the frame and (c) the resulting solid velocity vectors.

However, it should be noted that this velocity is heavily affected by the wall and do not necessarily represent the hydrodynamics of the whole bed, but gives an approximation of fluidization velocities.

2.4 Fountain height detection

As previously stated, the fountain height was measured with a single *AOS-SPRI* camera at 900x700 px resolution, at low framerate ($\sim$ 250 fps) and with a 12.5 mm lens. This set-up is enough for the capture of the fountain dynamics, as individual solids are not to be tracked, but rather the overall behavior and shape of the fountain particles. Each image has been corrected with the values shown in Table 2.4, with the pixel resolution being given by the black-white scale shown on the right in Figure 2.20a. After equalizing the grayscale histogram, each image has been binarized and the maximum height of the fountain region at each frame has been obtained (red dot in Figure 2.20a). Finally the time evolution shown in Figure 2.20b is averaged and the mean fountain height ($\bar{H}_f$) is registered.

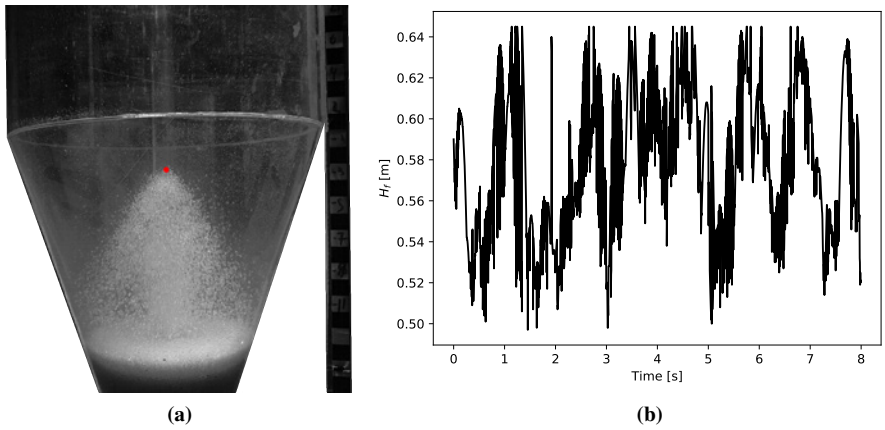

(a) **(b)**

Figure 2.20. (a) Experimental binarization for the fountain height detection and (b) resulting fountain height evolution.

Fountain height recordings resulting from this approach are somewhat dependent on local lighting conditions and local amount of contrast. Therefore the resulting signal has to be cleaned of outliers, thereby making the resulting signal reliable for any sort of dynamic analysis of the system. Thus, the average fountain height can be provided with an error of 1 mm (multiplication of pixel error from Table 2.4

by scale distance).

2.5 Pressure drop signal analysis

The pressure drop of the system is monitored with a sampling frequency of 1 kHz (ω) and a resolution of 0.1 Pa, which allows analyzing the main frequency components in any signal. This signal is related to the hydrodynamic regime present in the system and can be used to characterize the fluidization [115] and to validate the simulations by comparing the results with the experimental values.

A raw signal as the one shown in Figure 2.21 can be approximated to the addition of a number of sinusoidal functions of different frequencies ($f(k)$ in the figure). The tracing of a standard oscillatory signal given by Equation 2.9 can be reduced to Equation 2.10.

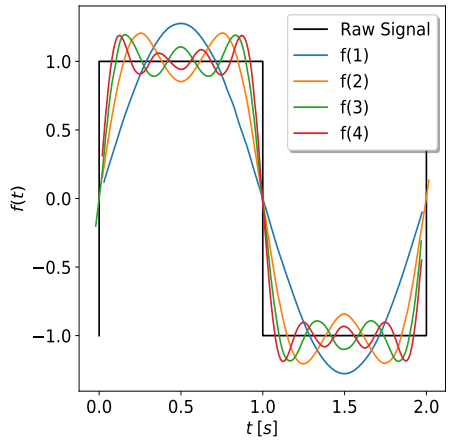

Figure 2.21. Fourier decomposition of a square signal with four k harmonics.

$$F(j\omega) = \int_{-\infty}^{\infty} f(t) \cdot e^{-j\omega t} dt \tag{2.9}$$

$$F(n) = \sum_{k=0}^{N-1} f(k) e^{-j\frac{2\pi}{N}nk} \tag{2.10}$$

where k is the harmonic number of each sinusoidal signal, which are added to approximate the original signal, Figure 2.21. The maximum number of frequencies is limited to $N-1$, where N is the number of sampled points, and care must be taken

in order to avoid a range of spurious effects, such as aliasing and leakage of the pressure spectra. All in all, the use of FFT in pressure signals allows determining the main harmonics that encompass the differential pressure signal through the reactor, Figure 2.22. Therefore, as shown in the example in the figure, the pressure signal can the decomposed into its main frequencies with clear harmonics in the 10 Hz range.

Even though different bed locations might have slightly different pressure fluctuations, this methodology provides a clear indication of the fluidization regime occurring in the bed [116]. In this case, the measuring point for fluidization monitoring is located at the outlet pipe, whereas solid velocity is used as a local property for model validation.

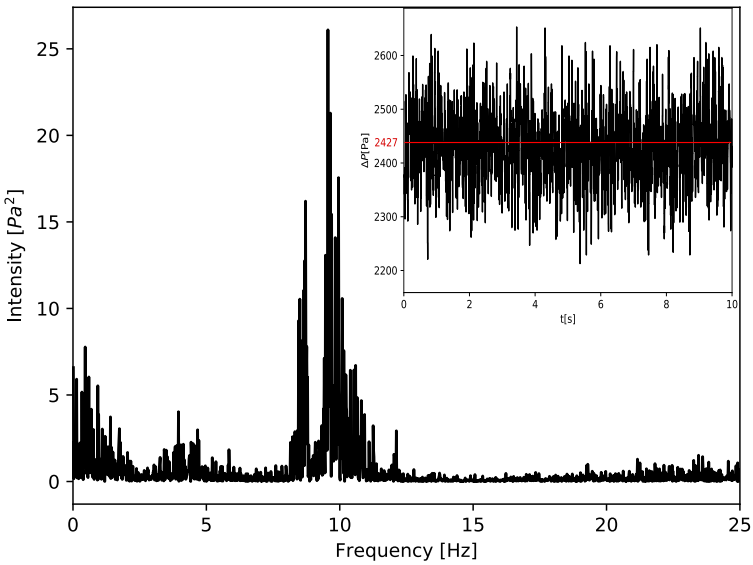

Figure 2.22. Discrete FFT analysis of the pressure signal for $1.1u_{ms}$ and $\bar{d}_p$=2 mm.

Given that the objective of this study is the analysis of the internal solid dynamics, the main signal components from the instrumentation, i.e., those from the pump, frequency variator and piping must be known beforehand. The power spectrum of the signal with an empty contactor is shown in Figure 2.23, where a wide distribution of components is detected around 50 Hz due to the blower and piping. Some authors have attributed this behavior in the signals to the pipping and inter-particle velocities [115], but no particles are present in the empty bed. For frequencies below 30 Hz, the instrumentation does not create significant dis-

turbance, and the 0-25 Hz range will therefore be closely studied, as it is believed to be created due to solid-solid and solid-wall interaction [117].

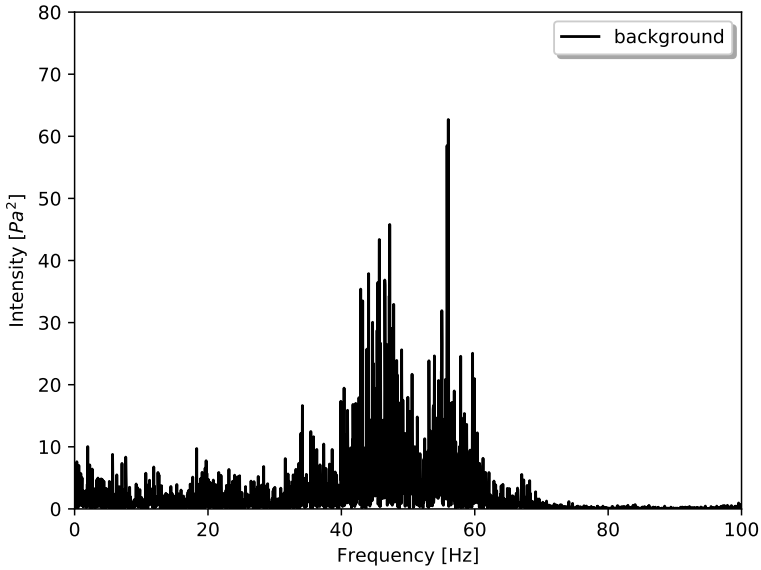

Figure 2.23. Power spectrum of the background pressure signal from the instrumentation.

Therefore, there is a reasonable degree of certainty that, under the experimental conditions in Figure 2.22, dominant 9.5 and 10Hz components coming from the solid-solid interaction are detected in the spouted bed.

3 Hydrodynamic analysis

A hydrodynamic study is the first step to characterize any system in a diverse set of operating conditions. In our case dealing with a spouted bed, two global parameters will be studied for any configuration, i.e., the minimum spouting velocity (u_{ms}) and the pressure drop under stable operation (ΔP_s), which allow setting the minimum operating requirements to operate in a spouting regime. In addition, u_{ms} will be used as the reference for setting each hydrodynamic regime and the resulting average fountain height $\bar{H}_f$ will be analyzed to determine the contactor volume for each configuration.

3.1 Minimum spouting velocity and pressure drop analysis

The minimum spouting velocity is defined as the one that achieves stable spouting with the lowest air flow rate. Stability varies depending on the material or configuration under study and, furthermore, no stagnant zones must be present under stable conditions. As widely reported in the literature, conical spouted beds have a significant hysteresis [118] regarding the evolution of pressure drop with air velocity, as higher flow rates are required to open the bed than those corresponding to collapse the spouting regime when air velocity is decreased. The minimum spouting velocity is obtained by first opening the bed and slowly reducing the air inlet until the spouting stops.The last velocity at witch the spouting is present in a stable manner is denoted as u_{ms}. There are numerous correlations in the literature to predict this parameter [11] for a wide range of spouted bed variants, but those by Altzibar et al. [119] are especially suitable for the presence

of draft tubes of varying aperture ratios. Thus, they have provided equations for predicting the minimum spouting velocity from zero aperture ratio (nonporous or solid draft tubes, for which ω_T=0) to full aperture ratio (for which ω_T=1). Figure 3.1 shows, as an example, some experimental values for three values of ω_T and the theoretical ones obtained using the correlations proposed by Altzibar et al. [119].

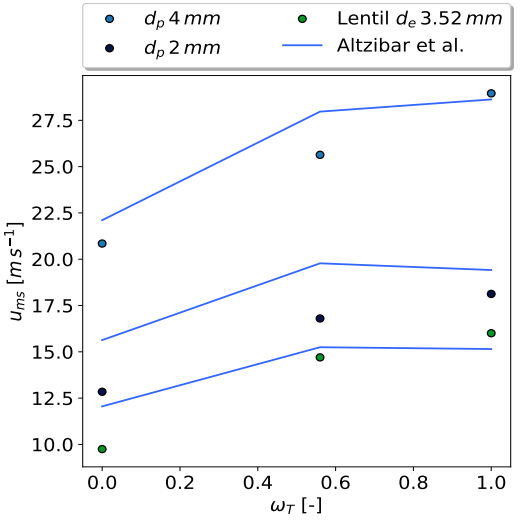

Figure 3.1. Evolution of experimental values of u_{ms} for different materials and aperture ratios, along with those predicted using the correlations of best fit by Altzibar et al. [119]. System: H_o=22 *cm*, D_o=4 *cm* and γ=36^o.

As observed in Figure 3.1, smaller particle diameters involve a lower u_{ms}. In addition, as particle density ρ_s is increased, gas flow rate requirements are also higher due to greater bed resistance. These trends are independent of the reactor configuration or shape and only depend on the solid features. Thus, they also apply to the prismatic spouted bed, Figure 3.2, in which the experimental values are shown for the system described in the experimental section. The comparison between experimental and correlation values are consistent for most of the points, with the maximum deviation being for the solid draft tube configuration (ω_H=0), which in this case is explained by the fact that the current draft tube design is slightly different to those used for the proposal of the mentioned correlations.

Pressure drop determines the amount of force the fluid has to overcome in order to go through the bed, which is directly related to operating costs when designing the pumping equipment of the apparatus. Several authors have studied and described pressure drop in conical spouted beds [120, 121] and provided empirical correlations for estimating operating pressure drop [104], ΔP_s, and peak pressure drop [102], ΔP_M.

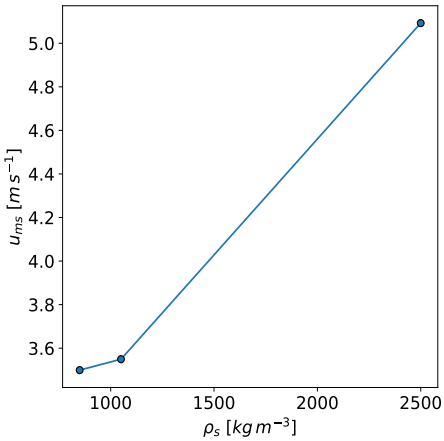

Figure 3.2. Minimum spouting velocities in a prismatic spouted bed.

Pressure signals have been obtained using a pressure transducer and, as already reported [102, 104], pressure drop increases with flow rate and aperture ratio ω_T. When the latter is increased, there is less draft tube wall surface to support the annulus, and therefore the pressure drop corresponding to spouting initiation is higher. In addition, a comparison of Figure 3.3a with Figure 3.3b allows concluding that a reduction in particle size reduces pressure drop, as permeability is lower (smaller voids for small particles), and therefore gas-solid momentum exchange decreases. When solid density ρ_s is reduced through the use of lentils, Figure 3.3c, pressure drop decreases as expected, as well as u_{ms}. However, at high flow rates there is a significant change in the trend of pressure drop evolution from that corresponding to *SDT* to those corresponding to *OSDT* and *WDT* configurations due to the solid transfer from the annulus into the spout. This behavior is attributed mainly to the particle shape, as irregular particles tend to interlace between each other [102] and the closing of the draft tube openings reduces this influence by increasing spouting stability and reducing pressure drop. By changing the spouted bed contactor geometry, the increase in pressure drop with flow rate and decrease by decreasing particle density is approximately linear, Figure 3.3d. However, a comparison of lentils and *ABS* pellets shows that shape influence counterbalances that of density, i.e., lentils have a lower particle density (850 $kg\ m^{-3}$) than *ABS* plastics (1200 $kg\ m^{-3}$), but the former show a slightly higher pressure drop over the whole range of flaw rates.

In order to analyze the fluidization stability, it is convenient to study the spectral distribution of pressure signals. Once the signal has been decomposed in its main components, the influence of each device on the fluidization stability, and hence on the pressure signal can be inferred, Figure 3.4. When solids are left to freely

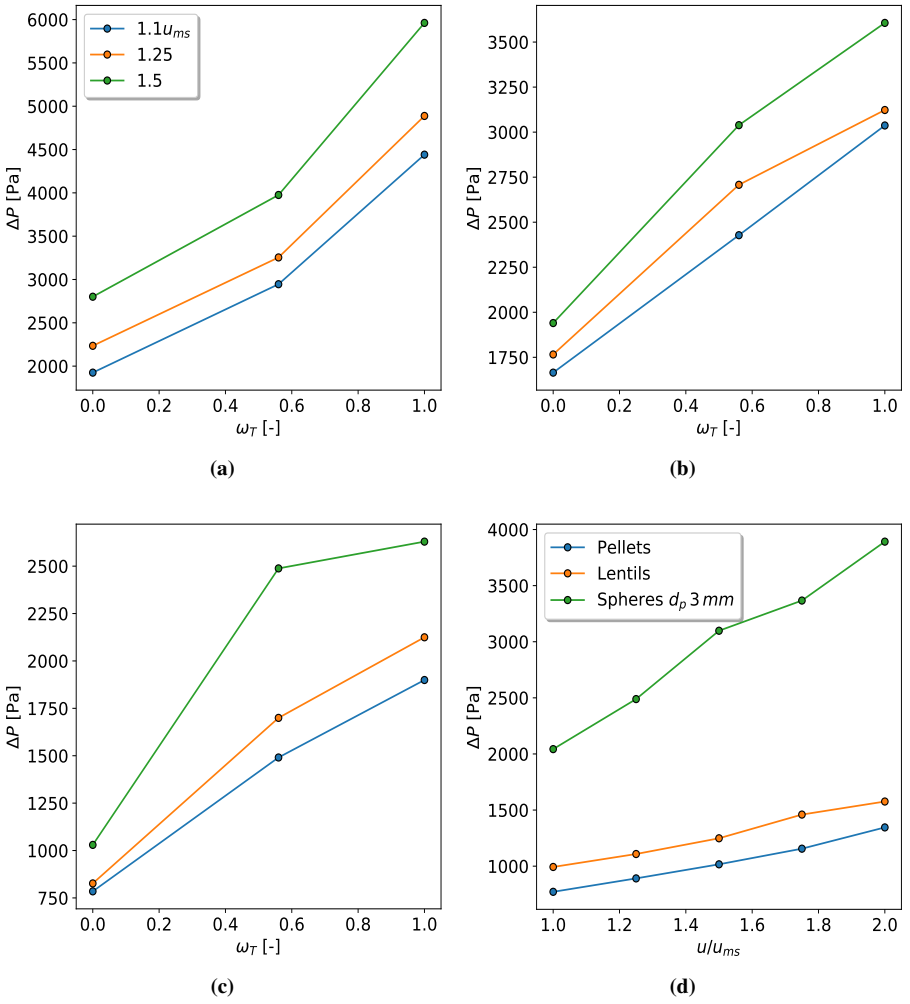

Figure 3.3. Operating pressure in a conical spouted bed of (a) $\bar{d}_p$=4 *mm*, (b) $\bar{d}_p$=2 *mm* and (c) lentils and (d) in a prismatic spouted (d).

transfer from the annular zone to the spout, such as in the WDT configuration, a main component at $5\,Hz$ is present due to stable fluidization. Concerning this configuration, low frequency components are noteworthy, which is due to a transport dominated by bulk solid transfer from the annular zone [122]. As the aperture ratio is decreased this trend is less significant, as the spout-annular transfer surface is lower and a main component around $10\,Hz$ begins to be evident, which has already been reported to be related to stable spouting. In fact this is a highly desirable property, since it allows monitoring the system without having to conduct

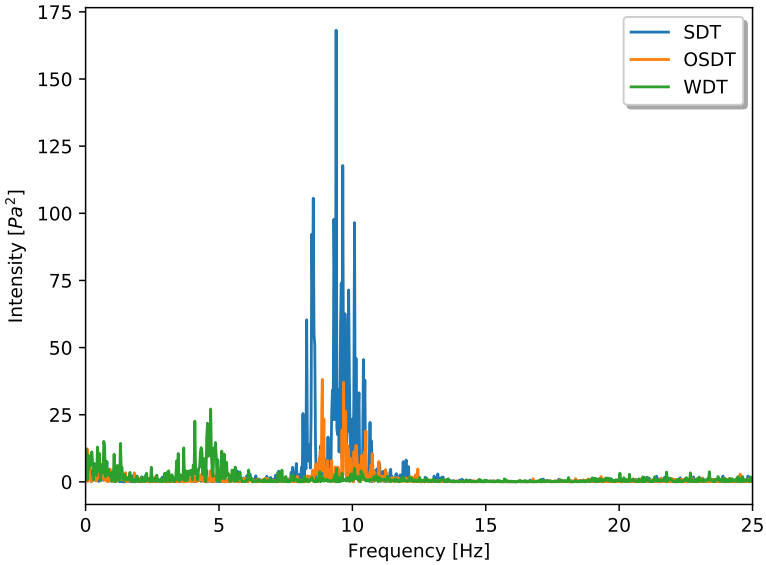

Figure 3.4. Comparison of pressure signals for the different configurations operating with $1.25u_{ms}$ and $\bar{d}_p$=2 mm.

any visual inspection. The appearance of higher frequency components is usually linked to a more stable spouting regime [122].

The main pressure fluctuation component not only varies with the configuration, but also with the material and the regime under study. Figure 3.5 shows the evolution of this value for each one of the materials and internal devices. These values are obtained by locating the maximum values in the spectra, as in Figure 3.4. In most cases, an increase in flow rate increases the dominant frequency, which means these systems are more stable at $1.5u_{ms}$ than at flow rates close to the minimum spouting velocity. This trend is consistent for the materials under study [123], but other authors have also noted a sharp change in frequency when there is a change in fluidization regime, as when passing from a bubbling spouting to a more dilute spouting regime[115].

Figure 3.5a shows that 4 mm particles tend to have a strong low frequency component, as big or irregular and coarse particles do not tend to roll and easily transfer from the annulus into the spout. At $1.5u_{ms}$ however, the flow rate is enough for the particles to fluidize in a more stable manner. As the internal device aperture is decreased, bed stability increases for glass beads of 2 mm and lentils. In the latter material (Figure 3.5c), a different main frequency is observed for the *SDT* configu-

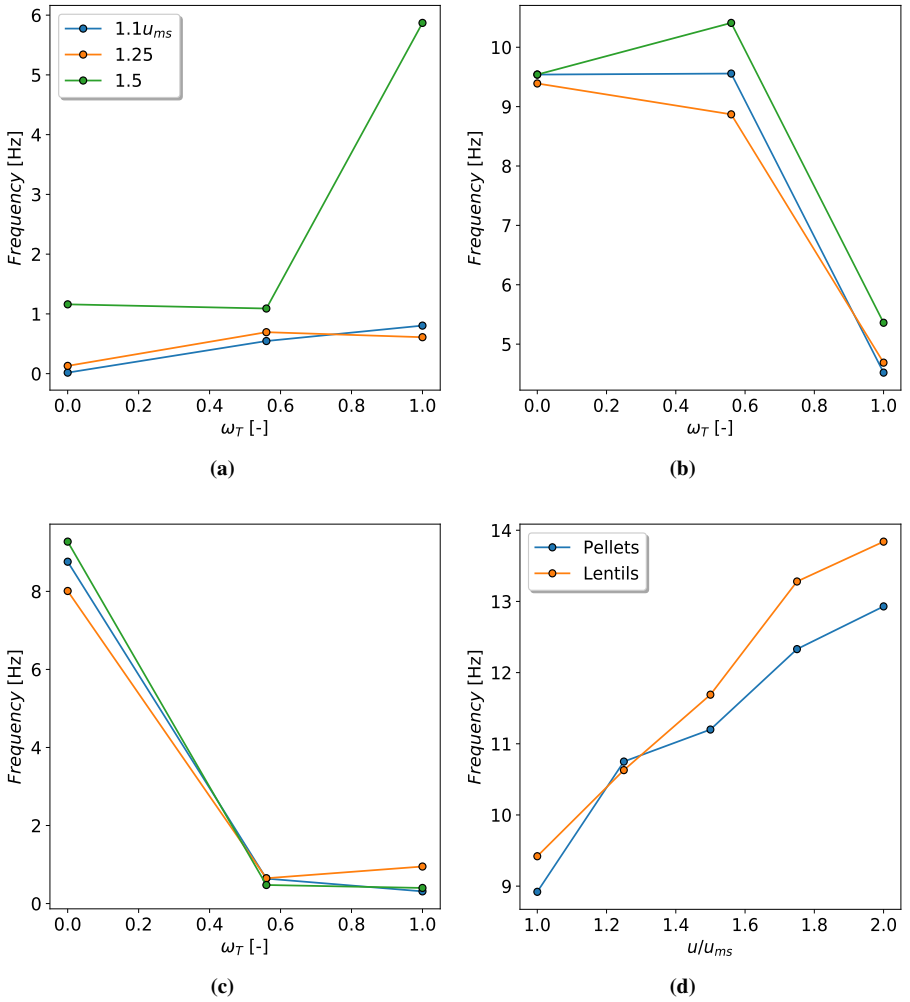

Figure 3.5. Comparison of the effect internal devices have on the main frequency component for glass beds of (a) $\bar{d_p}$=4 *mm*, (b) $\bar{d_p}$=2 *mm* and (c) lentils in the conical spouted bed, and (d) flow rate effect on the main fluctuation frequency in the prismatic spouted bed.

ration compared to those corresponding to the situations in which annular-spout solid transfer occurs easily due to the presence of irregularly shaped particles. In fact, these are more prone to undergo rotation, and therefore they transfer more easily from the annulus into the spout. The main frequency varies depending on whether the conical spouted bed, Figure 3.5a-3.5c, or a prismatic spouted bed is used Figure 3.5d, but the overall behavior of an increase in frequency as the flow rate increases is kept, as the underlying physics of fluidization do not change re-

gardless of the contactor geometry.

3.2 Fountain height

The fountain height determines the volume a given system takes within the reactor and given that most of the gas-solid contact happens in the spout and fountain region, this parameter heavily influences the gas-solid contact time. Following the procedure previously explained, the fountain height for each configuration has been obtained. The resulting values are displayed in Figure 3.6.

Figure 3.6a shows the fountain height for 4 *mm* glass bead particles. As observed, there is an increase in fountain height as flow rate is increased. Nevertheless, fountains are lower and denser as the aperture ratio of the draft tube is increased. Thus, the use of any draft tube leads to higher and more dilute fountains compared to the fountains without draft tube. In fact, the increment in the momentum available for particles reduces the likelihood of solid-solid perturbations as they rise through the bed.

This trend is inverted for small particles, Figure 3.6b. As particle size is decreased, permeability is lower, which leads to a decrease in u_{ms} when *OSDT* or *SDT* configurations are used. Lentils (Figure 3.6c) show a mixture of the previous two trends, which is evidence of the non-linear relationship among the parameters.

3.3 Solid velocity profiles

The behavior of spouted beds is greatly conditioned by the local solid velocity and packing conditions, giving rise to the formation of bubbles, instabilities or otherwise stable spouting. Hence, study of local solid velocities is of uttermost importance, as this data is essential for the validation of *CFD-DEM* models, and specifically of those used in the current work. This section will describe the axial and radial velocity profiles, with the former being especially dependent on the drag model, whereas the latter are more likely to depend on the material frictional properties.

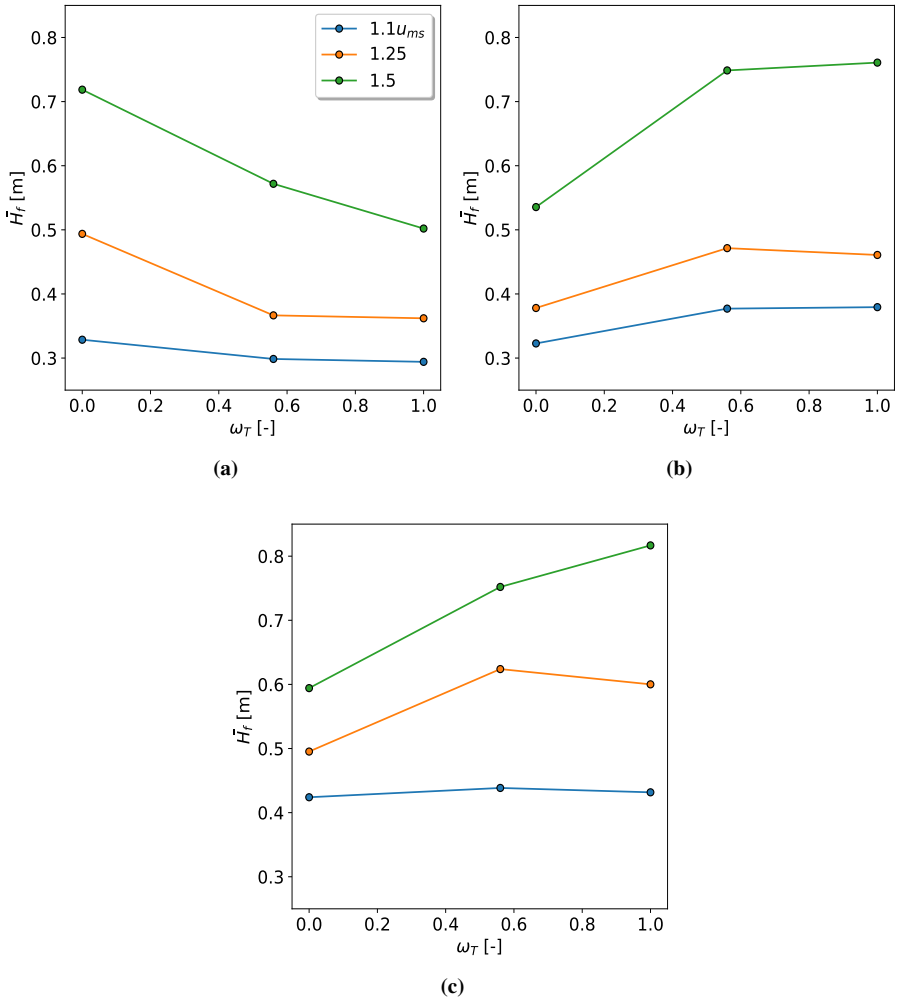

Figure 3.6. Fountain heights for beds made up of glass beads of (a) $\bar{d}_p$=4 *mm* and (b) 2 *mm*, and (c) lentils, for different aperture ratios.

3.3.1 Axial solid velocities

Axial velocity profiles allow estimating the overall solid circulation rate of a given system, and therefore inferring its capacity for processing materials. Axial measurements have been conducted at different levels along the axis from the inlet to the bed surface (5, 10, 15, 20 *cm*), with H_o=22 *cm* being the upper surface of the bed, and at another three points corresponding to the fountain region, i.e., 0.25, 0.30 and 0.40 *cm*. A detailed analysis of solid velocity has been conducted, espe-

cially in the bed, as it is where most of the solid-solid and solid-wall interactions occur.

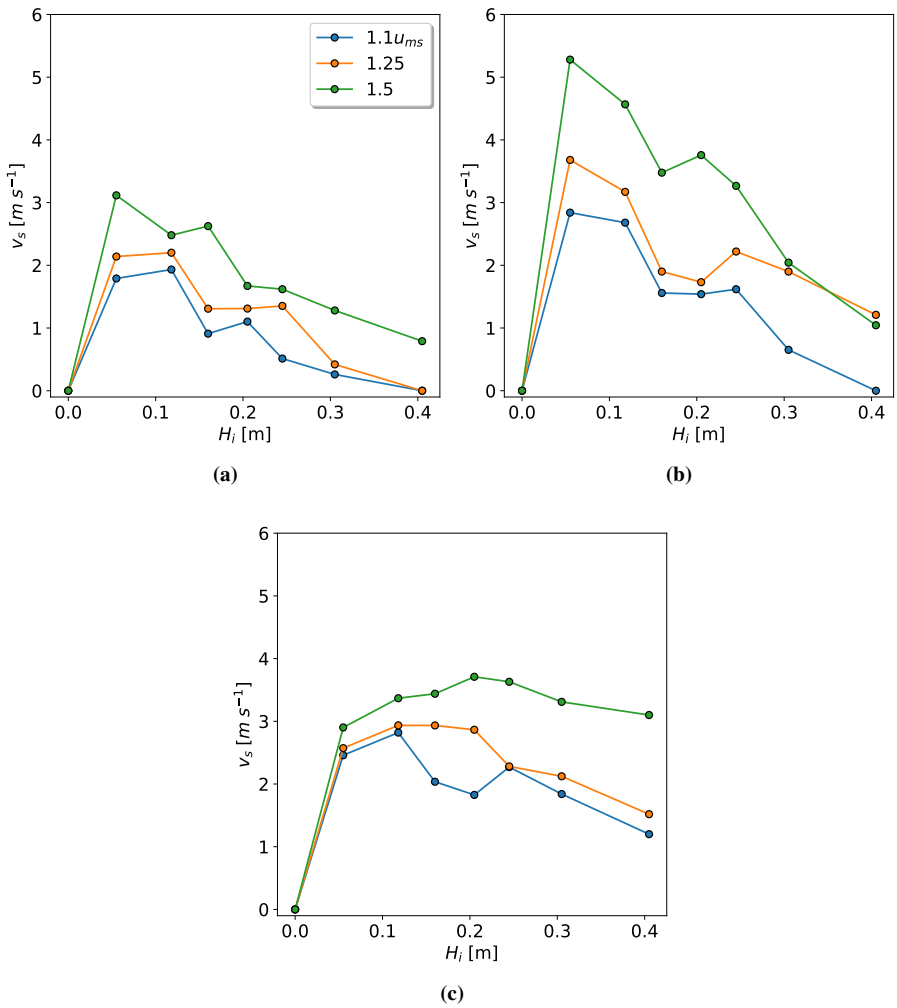

Figure 3.7. Comparison of the axial solid velocities for the *WDT* configuration under different air flow rates for glass beads of (a) $\bar{d}_p$=4 *mm* and (b) 2 *mm*, and (c) lentils, in the conical spouted bed.

Figure 3.7 shows the axial profiles of different materials without internal devices for a *WDT* configuration. For all flow rates and glass beads, the maximum solid velocity is achieved at the first measurement point, which is an indication that the maximum velocity is achieved somewhere close to the inlet. As the axial position is higher the velocity steadily decreases until the bed surface, where the

solids are transferred from the spout into the fountain. In this region, particles describe a parabolic path with a decreasing velocity. As the amount of momentum transferred to the particles increases (higher inlet air velocity), fountain particles keep enough momentum to rise further. Comparing Figure 3.7a with 3.7b, smaller particles reach higher velocities with maximum speeds near $5 m s^{-1}$. Such velocities enable these particles to keep rising after leaving the bed, which justifies the higher mean fountain height shown previously for the WDT configuration, (Figure 3.6). Figure 3.7c shows the axial profiles of lentils when a WDT configuration is used. The peak velocities are lower than those obtained with glass beads of 2 mm, but the profiles are flatter along most of the bed, as particles do not tend to slide or roll into the spout, and therefore solid-solid disturbances in the spout are lower.

When an open-sided configuration is used (Figure 3.8), axial solid velocity profiles peak at a location somewhere between 0.5 and 0.1 cm from the inlet. As expected, solid velocity increases as the regime is more vigorous (higher air velocity), but when big particles are used (Figure 3.8a) with low flow rates ($1.1 u_{ms}$) the solid velocity evolution gets closer to the WDT configuration. Smaller particle diameters lead to higher velocities in the spout and the fountain, Figure 3.8b. In the case of lentils, Figure 3.8c, velocity values are even higher due to the lower solid density, especially in the fountain, which in turn is higher.

Figure 3.9 shows the evolution of particle velocities for the configuration with solid (nonporous) draft tube. It is worth mentioning that this configuration is especially suitable for stabilizing the bed, as particles ascending through the spout do not have any disturbance from the solids crossing from the annulus into the spout. Therefore, solid velocity remains approximately constant from the first measuring height to the upper surface of the bed. In the case of vigorous regimes and small particles, the momentum of the air in the fountain is high enough to keep accelerating them, Figure 3.9b.

Even though lentils have an orientation dependent drag, the average velocity trend is similar to the mentioned ones, Figure 3.9c. However, it is worth mentioning that the solids show more angular momentum in lentils that in the remaining particles, given that their irregular shape make them prone to rotate under any collision, or orientate themselves in a particular way when descending along the annular zone.

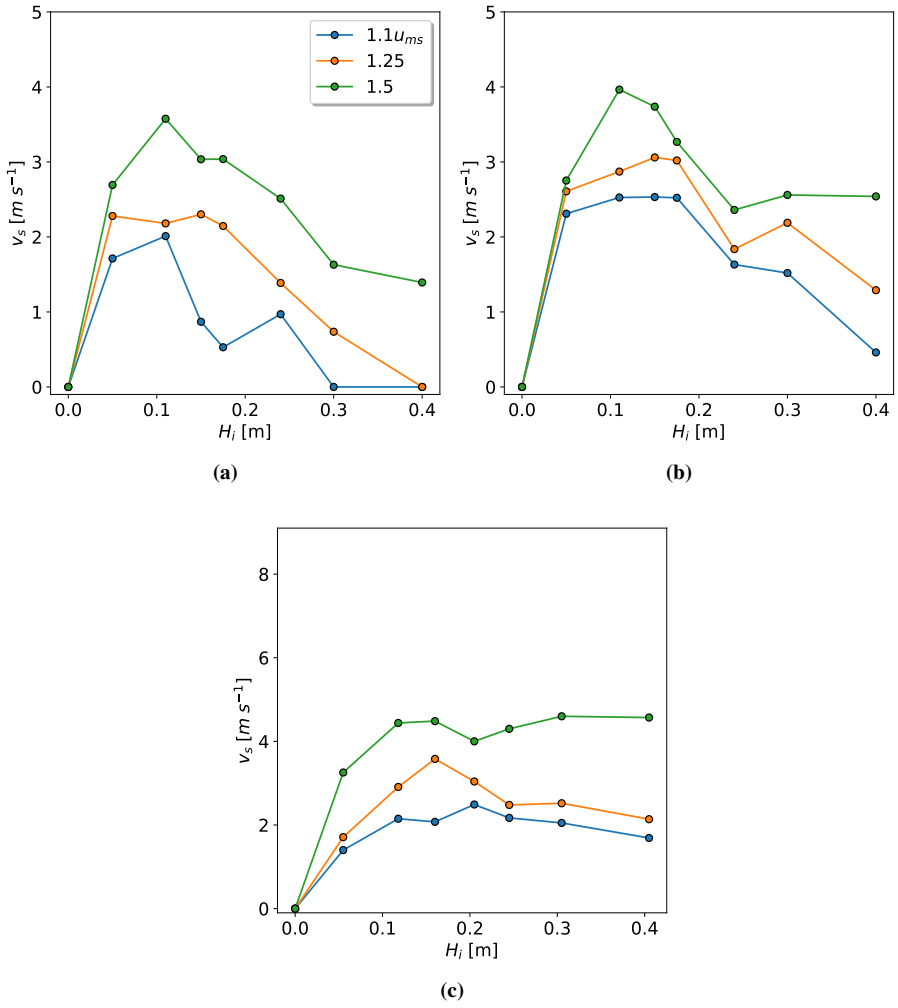

Figure 3.8. Comparison of the axial solid velocity for the *OSDT* configuration under different air flow rates for glass beads of (a) $\bar{d_p}$=4 *mm* and (b) 2 *mm* and (c) lentils in conical spouted beds.

3.3.2 Radial solid velocities

As previously explained, apart from the axial velocity profiles, the radial velocities affect the solid circulation, and must therefore be studied, as they are essential for predicting the correct solid cycle time as particles spend most of the time in the annular zone. Given the high number of data points for each configuration, heat-maps will also be used in order to show an overall trend of their evolution.

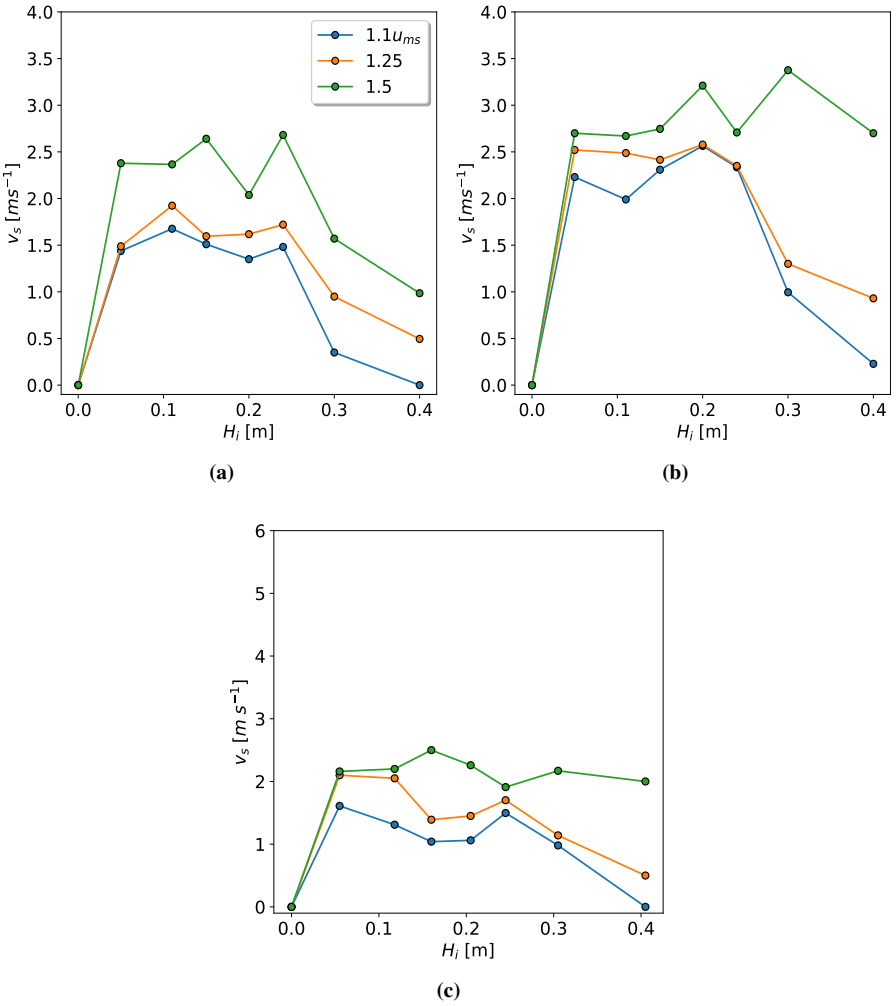

Figure 3.9. Comparison of the axial solid velocity for the *SDT* configuration under different air flow rates for glass beads of (a) $\bar{d}_p$=4 *mm* and (b) 2 *mm*, and (c) lentils.

Figure 3.10a shows the radial profiles for 4 *mm* particles and varying flow rates at 10 *cm* bed height. As expected, the maximum velocity is at the axis of the spout and decreases steadily, with a minimum at approximately the center of the annular section, i.e, maximum descending speed. At the wall, particles tend to descend more slowly due to the solid-wall interaction. In the case of 2 *mm* particles, Figure 3.10b, the same trend is observed, but with a steeper radial velocity gradient. This behavior is explained by the fact that smaller particles attain higher velocities in the spout due to their lower mass.

When lentils are used, their lower density, irregular shape and orientation dependent drag force cause an increase in the solid velocity gradient along the radial direction (Figure 3.10c). Consequently, the wall effect is more significant than in the previous material because lentils do not roll over the wall, and therefore sliding on the wall drains most of the momentum.

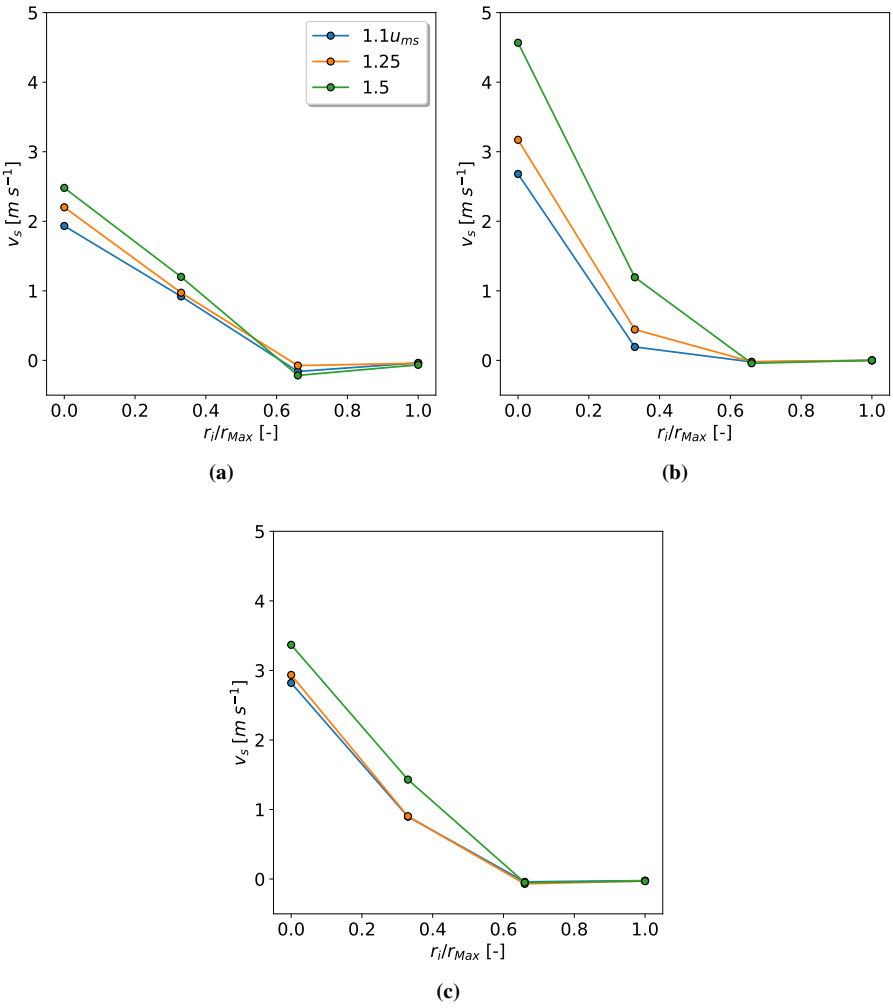

Figure 3.10. Radial solid velocity profiles at $H_i\,10\,cm$ in a WDT configuration under different air flow rates for glass beads of (a) $\bar{d}_p$=4 mm and (b) $\bar{d}_p$=2 mm, and (c) lentils in conical spouted beds.

When internal devices are used, velocity profiles are expected to be affected, as draft tubes disable annular-spout solid transfer by reducing the amount of air

percolating through the annular zone and, furthermore, friction occurs on the external walls of the device. Figure 3.11 shows the radial profiles when an *OSDT* is used. As expected, solid velocities are lower due to the aforementioned reasons, but also because the beds require lower flow rates for stable spouting. It is noteworthy that the evolution of the profiles for the different materials in a given configuration is consistent with those shown in Figure 3.10, which is explained by a significant wall effect on the draft tube external wall along with the previously mentioned contactor wall effect.

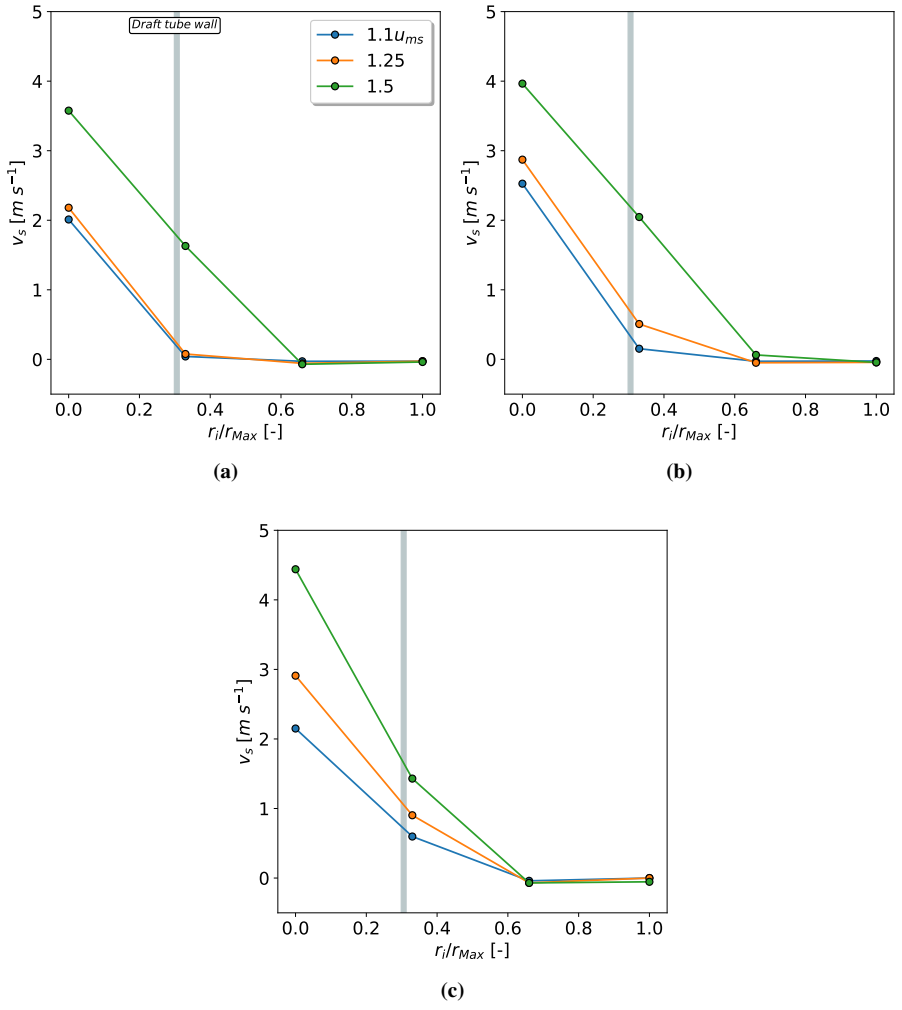

Figure 3.11. Radial solid velocity profiles at H_i 10 *cm* in a *OSDT* configuration and varying flow rates for glass beads of (a) $\bar{d}_p$=4 *mm* and (b) $\bar{d}_p$=2 *mm* and (c) lentils in conical spouted beds.

The radial solid velocity profiles in the *SDT* configuration, Figure 3.12, follow the trend already described for the previous two configurations, with a maximum at the axis of the contactor (spout region) and a sharp drop in the solid velocity in the annular zone. However given the presence of the draft tube wall (gray vertical line in Figure 3.12), solid velocities are kept at a minimum. The wall effect of both the draft tube and the contactor wall are apparent, as the maximum downward solid velocity is located at r_i/r_{Max}=0.6 for all solids, which suggest that the maximum solid circulation is somewhere in the middle region of the annular zone. Therefore, the solid circulation in the spouted beds with solid draft tube is obviously the smallest of the mentioned configurations due to the lack of annular-spout solid interaction, increased wall friction and the reduced air velocity required to open the bed.

In the previous figures, only the radial velocity at one height was displayed in order to clearly display the effect of each device and flow rate. However, these radial profiles change with height and material, Figure 3.13. The heat-map for 4 *mm* particles, Figure 3.13a, shows that at low and moderate flow rates (1.1-1.25u_{ms}) the spout takes most of the radial section at low heights as the solid velocities are in the positive direction. As the flow rate increases, the velocity at the spout (r/r_{Max}=0) gets understandably higher, but this also diminishes the radial section that the spout occupies in the lower regions. This is explained due to the spout expansion in the lower bed sections when the air encounters significant resistance to go through the bed [124]. At higher positions and radial locations significant descending solids are encountered, especially right above the initial bed height H_o=22 *cm*).

As previously shown, solid velocity gradients for all flow rates increase at all heights as particle size is decreased, (Figure 3.13b). In fact, the influence of the spout and the fountain zones on the annulus (velocities in this zone) is greatly reduced for small particle sizes, as most velocities in the annulus in Figure 3.13b are either negative or zero for all flow rates, while Figure 3.13a shows a more pronounced influence of the spout on the radial direction, which might indicate that the spout volume within the bed is bigger when 4 *mm* particles are used. This conclusion is consistent with data shown by San Jose et al. [125], who reported a greater spout volume when either the particle size or the irregularity of the material is increased [126].

3.3.3 Solid velocity profiles in prismatic spouted beds

In case of the prismatic spouted bed, the solid detection is similar to the one used previously, but each frame has been split into regions of interest (*ROI*) and the

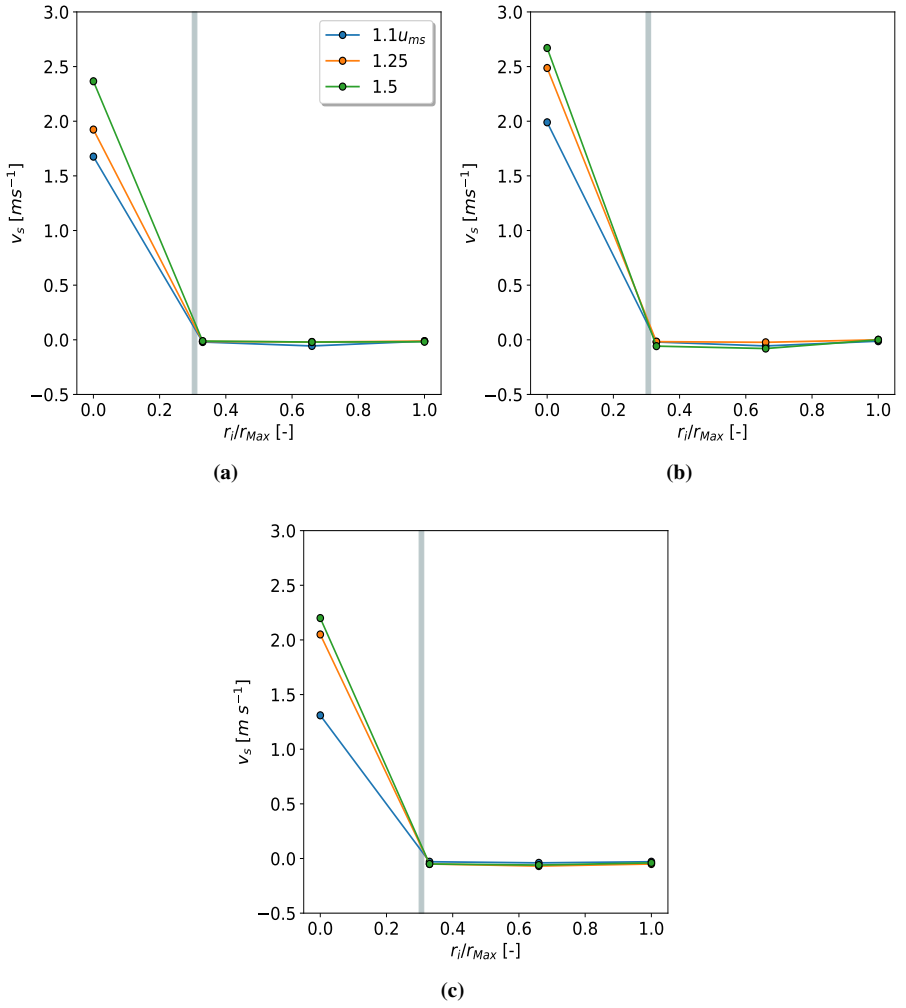

Figure 3.12. Radial solid velocity profiles at H_i 10 cm in a SDT configuration and varying flow rates for glass beads of (a) $\bar{d}_p$=4 mm and (b) $\bar{d}_p$=2 mm, and (c) lentils in conical spouted beds.

preceding solid detection algorithm has been used in a parallel fashion for each *ROI*. Thus, the velocity profiles for various materials can be studied, Figure 3.14.

Solid axial velocities, Figure 3.14a, follow a similar trend of the velocities to the conical spouted bed with an initial particle acceleration and a progressive descend of this value as particles rise through the spout. However, it is worth mentioning that particle velocity is lower in magnitude than in the conical spouted beds. It

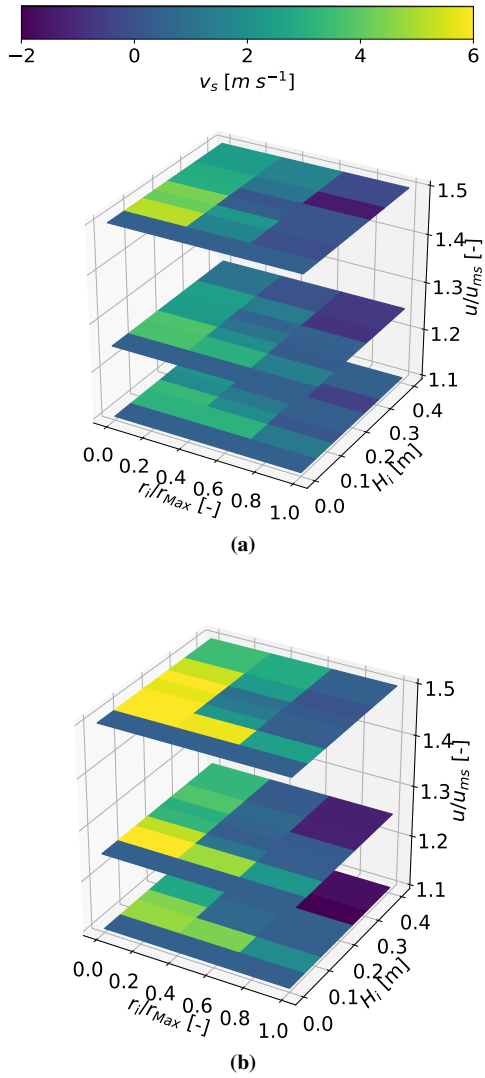

Figure 3.13. Heat maps of solid velocity in a WDT configuration for glass beads of (a) $\bar{d}_p$=4 *mm* and (b) $\bar{d}_p$=2 *mm* in conical spouted beds.

must be pointed out that this feature might be due to the location of the *PTV* measuring point, as the vertical wall exerts some friction to the particles, which might restrains solid movement. Figure 3.14a shows how low density solids such as lentils can be kept at a constant solid velocity for a reasonable section of the spout, while denser solids reduce their velocity faster once the inlet gas momentum has been drained. Regarding the radial solid velocities in Figure 3.14b, analogous trends to those shown in Section 3.3.2 are followed by the solids, with a maxi-

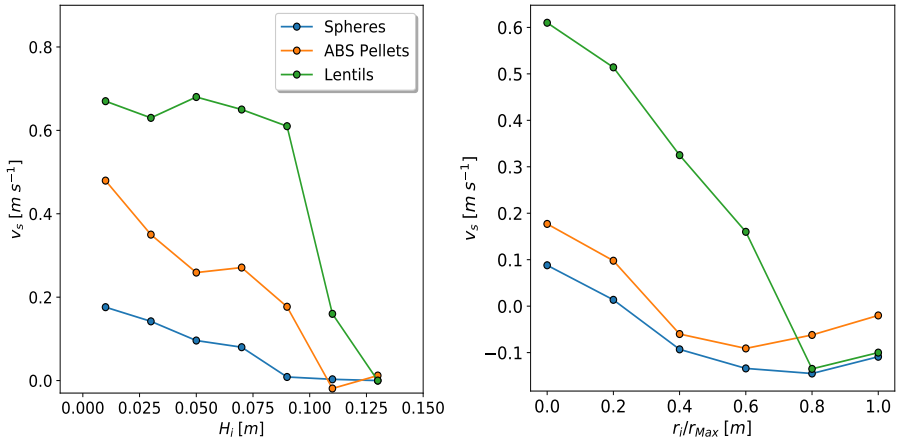

(a) **(b)**

Figure 3.14. Profiles for (a) axial velocity and (b) radial velocity using different materials in a WDT at $1.5u_{ms}$ in the prismatic spouted bed.

mum velocity at the spout axis, followed by a progressive solid descend towards the annular zone. In the annular zone, there is a local minimum of solid velocity, and close to the wall the particles have a lower descending velocity due to the wall friction. All in all, the prismatic spouted bed shows an analogous behavior to the conical spouted bed, albeit showing different solid velocity magnitudes that occur, understandably, from the change of the contactor geometry.

4 Regular material simulations

This chapter deals with the modeling and simulation of spherical particle fluidization in spouted beds, in order to ascertain the best force models to predict properties that are observed during the experimentation. Some properties require short simulations and are used to characterize the system and its internal behavior, such as particle velocities, pressure drop and minimum spouting velocity. Other properties, that are interesting from a reactor design perspective, require long simulations, as is the case of the pressure drop FFT analysis and particle cycle time distribution.

Spherical particles are the most studied shape in simulations, as they involve computational simplicity and good approximation for a variety of systems. Furthermore, a considerable number of correlations have been proposed throughout the years for the predictions of interactions involving exclusively spherical particles with surrounding fluids [1]. Regarding fluidized beds, a number of forces and interactions come into play when trying to model these processes. These systems are generally governed by the fluid-solid drag and solid-solid interactions, whereas lift and virtual mass play a significant role in some systems where the density of both phases is similar, as is the case of solid-liquid settling and liquid-solid fluidized beds [127, 128].

In the case of spouted beds, as with most gas-solid fluidized beds, the main interactions to take into account are the gravitational force, solid-solid collisions, solid-wall collisions and fluid-solid drag force. The last one has been the main force correlated by different authors to fit specific applications, defined as follows [129]:

$$F_D = \frac{1}{8} C_D \pi \rho_f d_p^2 \varepsilon_g^2 |u_i - v_i| (u_i - v_i) \varepsilon_g^{-\chi} \tag{4.1}$$

The most used expressions of the drag forces are summarized in Table 4.1. Syamlal and O'brien [130] defined the drag force on spherical particles based on liquid-solid fluidized beds, but subsequently extended the correlation for other gas-solid contacts [131]. A well-known correlation within chemical engineering community for quantifying this force is the Gidaspow drag model [80], Equations 4.7-4.10. It is a generalization of the Wen-Yu correlation [132], where the Ergun equation [133] is used for closely packed regions. This approach is a simple calculation that only requires knowing the void fraction ε_g and solid Reynolds number Re_s. However, given that a switching void fraction value is needed, a serious numerical instability is introduced when a common value (ε_s=0.2) is used, with no apparent reason. Some authors have later tried to smooth out this instability applying a transitional stitching technique by means of an inverse tangent [134] or a linear function [135], whose influence on the simulations has already been studied [136].

Di Felice noted [137] that the drag force shown in Equation 4.1 changes with the packing parameter (χ) depending on the Reynolds number, whereas other authors considered this term constant. However, in the range of intermediate and transitional Reynolds numbers, the packing function does not keep a constant value and, thus a *Re* dependent value was fitted to the experimental values in Equation 4.12 to take this effect into account.

Lately, some authors have proposed new correlations based on simulation approaches by using the Lattice Boltzmann (*LB*) method in order to understand the dynamics of a given particle configuration. Theses correlations do not rely on purely experimental data to calculate the drag coefficient (C_D). They calculate the drag created in a random assembly of spherical particles by calculating the inter-particle forces and relating them to the *Re* number (Equation 4.14). In a series of papers, Koch and Hill [138, 139] proposed Equations 4.13-4.16 for randomly packed spheres. Beetstra et al. [140] proposed an improved version of the drag model for those systems with intermediate *Re* numbers and polydispersed solid mixtures. Equation 4.17 shows the expression they obtained for monodispersed solids. More details about the methodology followed to obtain this equation are given elsewhere [138–140]. One of the main criticism about this technique for obtaining C_D correlations is the fact that it relies on uniformly packed particle assemblies, and therefore does not properly account for the drag coefficient in those specific regions where there is a high void fraction gradient [141].

Table 4.1. Drag models for single spherical particles.

Reference	Equation
	$C_D = \frac{4C_{D,s}}{\varepsilon_g v_t^2}$ (4.2)

Table 4.1. (continued)

Syamlal [130]	$C_{D,s} = (0.63 + 4.8\sqrt{v_t/Re})^2$ (4.3) $v_t = 0.5(A - 0.06Re + \sqrt{(0.06Re)^2 + 0.12Re(2B - A) + A^2}))$ (4.4) $A = \varepsilon_g^{4.14}$ (4.5) $B = \begin{cases} \varepsilon_g^{2.65}, & \varepsilon_s < 0.15 \\ 0.8\varepsilon_g^{1.28}, & \varepsilon_s \geq 0.15 \end{cases}$ (4.6)
Gidaspow [80]	$C_D = \begin{cases} C_{D,Wen\&Yu} & \varepsilon_s < 0.2 \\ C_{D,Ergun} & \varepsilon_s \geq 0.2 \end{cases}$ (4.7) $C_{D,Wen\&Yu} = C_{D\infty}\varepsilon_g^{-4.65}$ (4.8) $C_{D,Ergun} = 50\frac{\varepsilon_s}{\varepsilon_g^3 Re} + \frac{0.5833}{\varepsilon_g^2}$ (4.9) $C_{D\infty} = \begin{cases} \frac{6}{\varepsilon_g Re}(1 + 0.15(\varepsilon_g Re)^{0.687}) & \varepsilon_g Re \leq 1000 \\ 0.11 & \varepsilon_g Re > 1000 \end{cases}$ (4.10)
DiFelice [137]	$C_D = \left(0.63 + \frac{4.8}{\sqrt{Re}}\right)^2 \varepsilon_g^{2-\beta'}$ (4.11) $\beta' = 3.7 - 0.65e^{-\frac{(1.5 - log(Re))^2}{2}}$ (4.12)
Koch-Hill [138, 142]	$C_D = 18\frac{\mu_f \rho}{d_p^2}F$ (4.13) $F = \varepsilon_g(F_0 + 0.5F_3 Re_p)$ (4.14) $F_3 = 0.0673 + 0.212\varepsilon_s + 0.0232/(1 - \varepsilon_s)^5$ (4.15)

Table 4.1. (continued)

	$F_0 = \begin{cases} \frac{1+3\sqrt{\varepsilon_s/2}+(135/64)\varepsilon_s ln(\varepsilon_s)+17.14\varepsilon_s}{1+0.681\varepsilon_s-8.48\varepsilon_s^2+8.16\varepsilon_s^3} & \varepsilon_s < 0.4 \\ 10\frac{\varepsilon_s}{(1-\varepsilon_s)^3} & \varepsilon_s \geq 0.4 \end{cases}$	(4.16)
Beetstra[140]	$C_D = \frac{10\varepsilon_s}{(1-\varepsilon_s)^2} + (1-\varepsilon_s)^2(1+1.5\varepsilon_s^{0.5}) + \frac{0.413Re}{24(1-\varepsilon_s)^2}\left[\frac{(1-\varepsilon_s)^{-1}+3\varepsilon_s(1-\varepsilon_s)+8.4Re^{-0.343}}{1+10^{3\varepsilon_s}Re^{-(1+4\varepsilon_s)/2}}\right]$	(4.17)

In addition to the gas-solid interaction, particle-particle and particle-wall interactions require closure values for restitution, friction and damping coefficients, as explained in Section 1.2. A reasonable way to obtain these values is by beginning with literature values [143] for similar materials and adjusting them by calculating the angle of repose from a heap of the material under study [101, 144]. The experimental angle of repose is obtained by image treatment of a raw footage, Figure 4.1a, and subsequent binarization of the particles in order to distinguish particles from the dark background. Once the particle region has been extracted, the angle of the outer edge is fitted to a linear equation, which allows obtaining the experimental angle of repose.

In the simulation carried out in this thesis, the procedure is slightly changed in order to reduce any dependency of the angle of repose from the way particles are inserted into the domain. Thus, a number of particles are poured into a cylindrical vessel of $7\,cm$ in diameter and $5\,cm$ in height, Figure 4.1b, and some time is given for the particles to settle under gravity and dissipate the remaining kinetic energy. Once this stable state has been reached, the outer wall holding the particles in Figure 4.1b is lifted at a constant rate of $0.25\,cm/s$. As the wall is raised, particles slide through the opening between the wall and the base. Some particles roll over the edge of the base and leave the simulation domain, at which point they cease to exist in the simulation. The remaining particles form a heap on the base, whose angle of repose is measured by fitting a linear curve to the particles on the edge of the heap and this value is taken as the simulated angle of repose.

Even though the angle of repose, Figure 4.1b, may be calculated by averaging a single surface of the heap, two surfaces from two heaps have been taken and their averages have been calculated. For the sake of clarity, only the average of one surface is displayed in the aforementioned image. This procedure has been

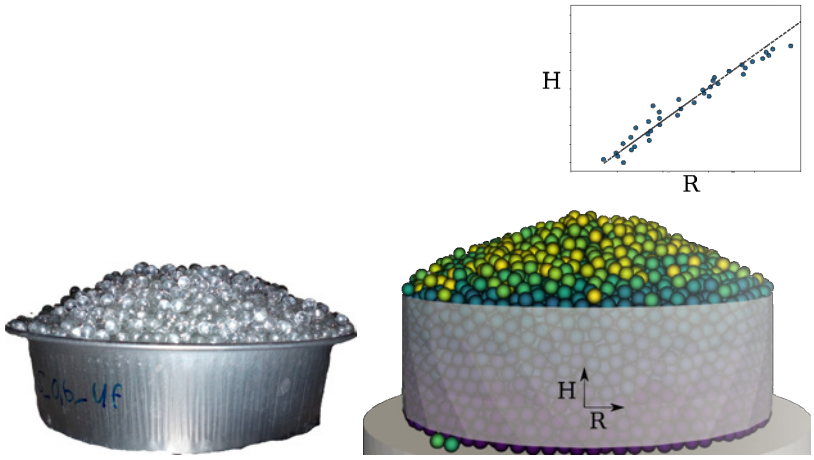

Figure 4.1. Simulation of the (a) heap formation and (b) the fitted linear equation to obtain the angle of repose.

Table 4.2. *CFD-DEM* simulation input parameters.

Parameter	Values	
$\bar{d_p}$ [m]	0.004	0.002
Particle-particle restitution coefficient, $k_{p,p}$	0.98	0.94
Particle-wall restitution coefficient, $p_{p,w}$	0.85	0.95
Particle-particle friction coefficient, $\gamma_{p,p}$	0.185	0.17
Particle-wall friction coefficient, $\gamma p, w$	0.45	0.45
Rolling friction, $\mu_{r,f}$	0.1	0.07
Rolling damping coefficient, $\gamma_{r,f}$	0.15	0.15
m_0 [kg]	4.5	4.53

repeated for all the materials and sizes, as $\bar{d_p}$ affects the angle of repose of a given material. The values obtained for each material are set out in Table 4.2.

Meshing of the fluid volume requires some explanation, as the complexity of the internal flow affects the way each configuration is meshed. At first, a tetrahedral mesh created by *SALOME-v.*1 and shown in Figure 4.2a was used. This cell shape allows describing intricate shapes without having to significantly reduce the mesh size. However, tetrahedral meshes tend to be more diffusive [145] and give non-smooth fields, which hinder long simulations around the internal devices. The use of a refining region around the internal devices, Figure 4.2b, reduces instabilities, but does not allow striking a suitable balance between cell volume and particle volume (V_C/V_p) in a non-resolved *CFD-DEM*.

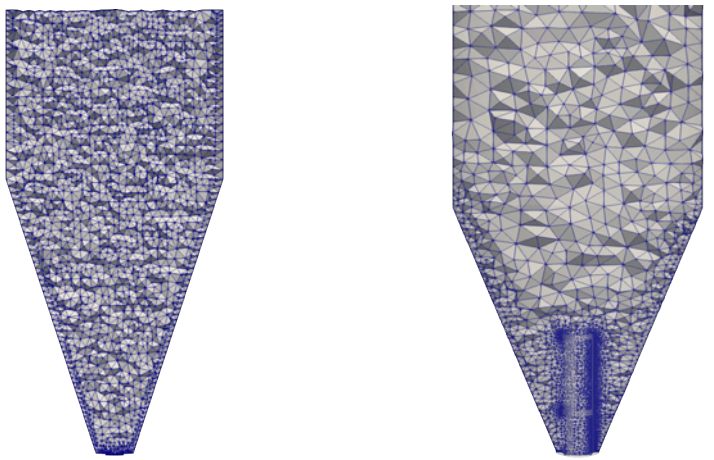

Figure 4.2. Tetrahedral meshing of the spouted bed volume for (a) WDT configuration and for (b) a configuration with internal device with the local refinement region around the device.

Given the difficulty in getting a reasonable tetrahedral mesh, when internal devices are particularly well orientated and no complex geometries are present, the use of a hexahedral mesh ($hex-mesh$) is plausible by only refining the sharp edges or regions where relatively omnidirectional solid and fluid movement is expected (mainly close to internal devices and inlet). Therefore, the mesh configuration shown in Figure 4.3 is employed.

The use of internal devices required a slight refinement in the spout region in order to accommodate the mesh for the draft tube, Figure 4.3b and Figure 4.3c. This refinement is needed in order to run the *snappyHexMesh* mesher and obtain a reasonable cell quality, specially in the regions surrounding the entrainment region and openings in the open-sided draft tube. Given that the cell size is reduced to $V_C/V_p < 3$, the use of a proper void fraction model is essential in order to assign the particle volume to the cells it overlaps. A more detailed explanation will be given when the void fraction model for the irregular particles is explained in Chapter 5. Accordingly, a divided void fraction model has been necessary for the internal device simulations, as some particles overlap more than one cell in the refined regions, as shown in Table 4.3 for the values of $V_C/V_P < 1$.

As particle size is decreased the number of required cells rises, but in order to reduce the computation time, the refining of cells has been specially applied in the lower section of the contactor, where most of the bed is located during the sim-

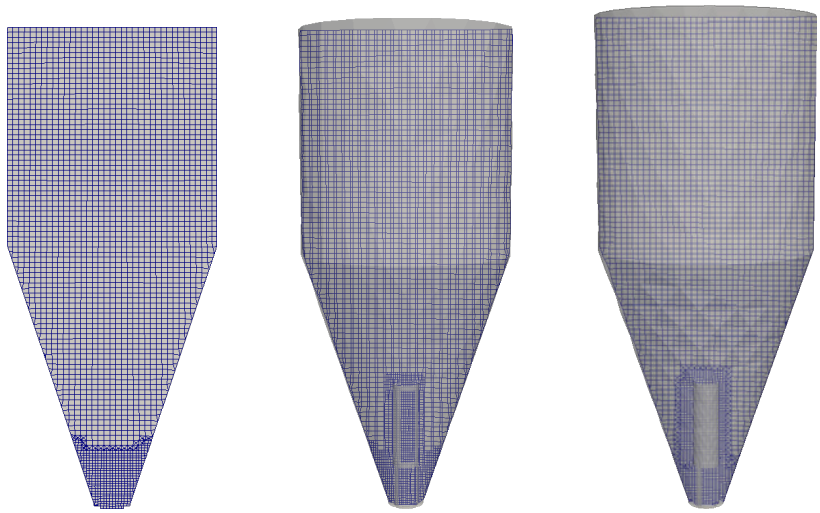

Figure 4.3. Cross section of the hexahedral mesh used for each configuration, i.e., (a) WDT, (b) $OSDT$ and (c) SDT for d_p=4 mm glass beads.

Table 4.3. Mesh size comparison for the different configurations in the conical spouted bed of regular materials.

Configuration	N. Elements	V_C/V_p		
		Min	Mean	Max
WDT, $\bar{d}_p$=4 mm	74018	0.77	3.06	4.72
$OSDT$, $\bar{d}_p$=4 mm	75627	0.84	2.85	4.87
SDT, $\bar{d}_p$=4 mm	77956	0.49	2.94	4.98
WDT, $\bar{d}_p$=2 mm	530581	0.65	3.42	4.87
$OSDT$, $\bar{d}_p$=2 mm	556270	0.45	3.13	5.17
SDT, $\bar{d}_p$=2 mm	601023	0.41	3.73	4.97

ulation and where most of the gas-solid momentum exchange takes place. Once the internal mesh for each particle type has been built, simulations are run with each of the gas-solid drag force correlations, Table 4.1, with the properties shown in Table 4.2 in order to assess the best model to reproduce the experimental data shown in Chapter 3.

4.1 Solid velocity profiles

The capacity of a conical spouted bed is strongly dependent on the axial solid velocity, especially in the spout, and therefore these profiles ought to be studied in detail. As already stated, a simulation has been run for each solid, configuration and drag model. Figure 4.4 shows the axial solid velocity profile predicted by each drag model and the experimental data, for a WDT configuration. All models predict a sudden acceleration of the particles until a height of around 5 cm is reached, where there is a massive solid incorporation. Once enough solids have been incorporated into the spout region, solid velocity decreases because the air momentum is drained by all the solids. This solid incorporation trend is evidenced by the decrease in the void fraction value, Figure 4.5. Solid velocities steadily decrease up to the bed surface (H_o=22 cm). Above this height, solid velocities decrease in a very pronounced way in the fountain .

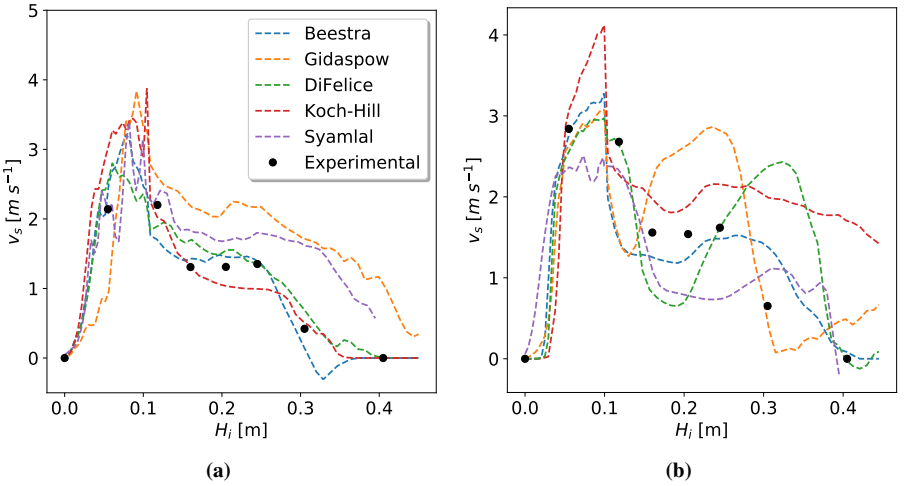

Figure 4.4. Comparison of the axial solid velocity profiles predicted using different drag models with the experimental ones for beds made up of glass beads of (a) 4 mm and (b) 2 mm, for WDT configuration at 1.25u_{ms}.

Gidaspow model [80] largely deviates in the prediction of solid velocities for the WDT configuration, over-predicting the velocities expected in the reactor, which leads to a higher fountain than what is experimentally observed. In some configurations, given the high solid velocity predicted, a crooked fountain is created, which is not observed experimentally for this configuration and bed material. In fact, glass beads of this size tend to create reasonably straight fountains. The correlation by Syamlal & O'brien [130] shows a better fit than Gidaspow model, but

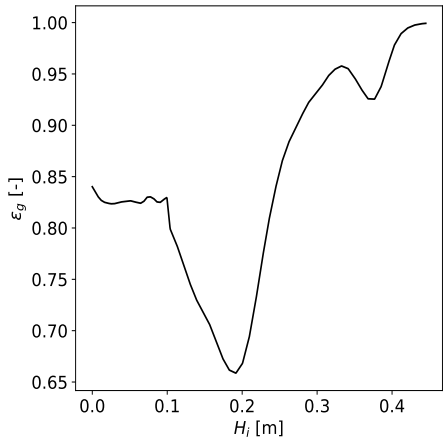

Figure 4.5. Void fraction axial profile in a WDT configuration at $1.25u_{ms}$.

still over-estimates the solid velocities, specially in the fountain region ($>$ 22 cm).

The remaining models predict a somehow similar trend close to the experimental values, and they therefore predict a reasonable fountain height. However, the model by Koch and Hill [139], over-predicts particle acceleration at the first measuring point ($H_i = 5\,cm$), which is then followed by a sharp decrease in solid velocity, i.e., the model under-predicts the experimental values at the end of the spout region. The models by Di Felice [137] and Beetstra [140] show a similar trend, with the latter leading to slightly better predictions of the experimental values.

In the case of 2 mm glass beads shown in Figure 4.4b, the solid velocity trend is similar to that shown for the previous case, with an initial sudden increase and a progressive deceleration as particles are dragged through the spout. When the trends of the simulated values are compared with the experimental ones, the models that best fit the data for this particular case are those proposed by Koch and Hill [139] and Beetstra [140]. The former model provides better prediction of solid velocity at heights above 20 cm, while the latter model follows the velocity trend with reasonable accuracy in the whole range of heights. In the case of Gidaspow [80] and Di Felice [137] models, the estimated values highly deviate from the expected trend, even though they are able to predict a sudden acceleration at the region of the bed surface (22 cm). This acceleration is observed in both simulation and experimental trends in the WDT configuration, and is attributed to the expansion of the spout at H_o and subsequent neck above this level, which leads to a slight increase in solid velocity at this height, specially if the mass of said particle is small. However, the acceleration values showed by the aforementioned models do not match the magnitude observed in the experimental runs.

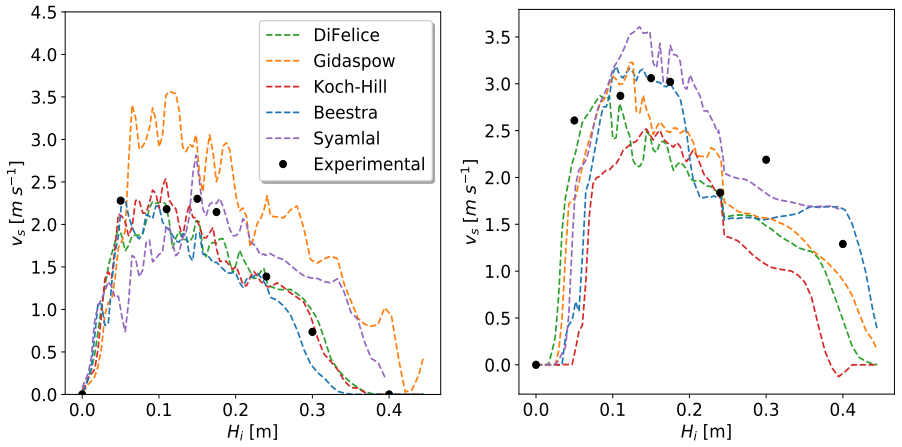

Figure 4.6. Comparison of the axial solid velocity profiles predicted using different drag models with the experimental ones for beds made up of glass beads of (a) 4 *mm* and (b) 2 *mm*, for *OSDT* configuration.

For the case of simulations with open-sided draft tube (*OSDT*), the simulated axial values follow a trend consistent with the experimental values (Figure 4.6), where particles are accelerated for a longer distance compared to the previous configuration, as solids rising through the spout have less disturbance from particles entering from the spout. As a consequence, the solid velocity at the surface of the bed and the fountain height are higher than when no draft tube is used.

Regarding the differences between the drag models, Gidaspow model [80] again over-predicts the drag coefficient, while the remaining models show a consistent trend with the experimental value. Syamlal & O'brien in turn underestimate the solid velocity in the first half of the bed height, but overestimate the value in the fountain region. Thus, Koch and Hill drag model [139] is consistent with the experimental values, (Figure 4.6a), with an error of around 5%. However, in the case of smaller glass bead particles, Figure 4.6b, this correlation heavily underestimates the solid velocity through the bed, and the correlation by Beetstra is the one providing the most reasonable fit for both sizes.

When the solid draft tube (*SDT*) is employed, spout-annular cross-flow is limited to the entrainment zone and the frequency at which clumps of solids are fed into the spout in the lower section of the contactor. Henceforth, particles rise in a relatively dilute manner with little or no momentum dissipation through solid-solid and solid-wall collisions. As a consequence, air leaves the height of the draft tube

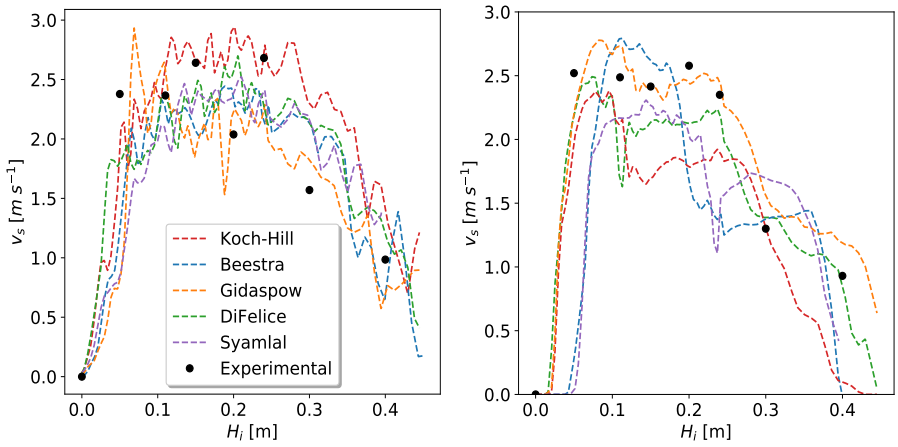

Figure 4.7. Comparison of the axial solid velocity profiles predicted using different drag models with the experimental ones for beds made up of glass beads of (a) 4 *mm* and (b) 2 *mm*, for *SDT* configuration.

with enough momentum to keep accelerating the particles until it is dissipated through momentum exchange and diffusion. Thus, Figure 4.7a shows that all models predict a flat solid velocity until the solids leave the spout with a smooth velocity decline. This flat velocity profile results from the balance between the mass of each solid and the momentum available. Thus, as solid size is decreased the solid acceleration becomes faster but again reaching a relatively stable solid velocity in the draft tube 4.7b.

As observed in Figures 4.4a-4.7b, the models that best fit the experimental data are those proposed by Beetstra [140] and Di Felice [137]. Between these two models, the former has been selected, given that it allows simulating particulate solids in a wider range of *Re* numbers and is able to include simulations of polydisperse solids [140]. Once the best fitting drag model has been chosen, all the simulations are run for all flow rates, and the experimental data are used to validate the robustness of the correlation.

Once all the simulations are run, the axial solid velocities can be compared wit the experimental data, Figure 4.8. As expected, the simulated profiles show a similar trend as the experimental data, with a sharp decrease in velocity in the *WDT* configuration for all flow rate due to the lack of draft tube to protect particles carried along the spout. These simulations slightly over estimate the solid velocity with an error of 6.2%. For the *OSDT* configuration, the prediction is slightly worse

for low flow rates, with a significant error for a few points, but it is acceptable in the fountain. When the *SDT* configuration is employed, the *CFD-DEM* profiles closely match those of the experimental data, with a much smoother solid velocity decreasing trend as the solids go up in the spout. The maximum error is obtained at the entrainment region, where an error of 22% is obtained, as the values predicted by simulation do not accelerate as much as the experimental data. In addition, the simulation shows a slightly higher velocity when particles leave the spout region, but they then match the experimental values at a height (H_i) of $40\,cm$.

Figure 4.9 shows the solid axial velocity profiles for 2 *mm* glass beads. They show a consistent trend with their specific configuration and flow rate, with the largest deviation being at $1.1u_{ms}$ in the *OSDT* configuration, (Figure 4.9b). In this case, no solid velocity has been recorded until a considerable height. The reason for this behavior is the fact that no solids are present in the spout until this height, and therefore no solid velocity has been recorded.

Once the axial profiles have been analyzed, attention will be paid to the radial profiles of velocity, as they provide an indication of solid incorporation into the spout. For the sake of clarity, Figures 4.10a-4.10c show the velocity values for all the configurations at $1.25u_{ms}$, whereas Figure 4.10d shows the parity plot for all the radial points.

When the *WDT* configuration is used, Figure 4.10a, the model correctly predicts the solid velocity at each radial position with the exception of the lowest height (H_i=5 *cm*) and radial position of r_i/r_M=0.6. At this point the spouted bed cross section is the smallest of the measured points, and hence the posible disturbance of the probe in the spouted bed is highest. In the case of the *OSDT* configuration, this height is also the one of largest deviation from the simulated values, Figure 4.10b, where the simulation predicts a wider spout at this height than what is experimentally observed. This may be corrected with an increase in the friction coefficient, but this would lead to an overall reduction in velocity values and a suitable compromise must be achieved in the fitting of all the data points. The profiles of radial velocity corresponding to the *SDT* configuration are slightly different to the previous cases. This configuration does not allow for a smooth transition of the velocity from the spout to the annulus due to the presence of the draft tube wall. As shown in Figure 4.10c, simulated solid velocity values match reasonably well with the experimental ones.

Figure 4.10d shows the parity plot for all the data shown in Figures 4.10a-4.10c. As observed, the model is able to fit reasonably well all the configurations, as is evidenced by the uniform spread of the data points around the diagonal line. Only a few outliers corresponding to *WDT* configuration are observed, and they

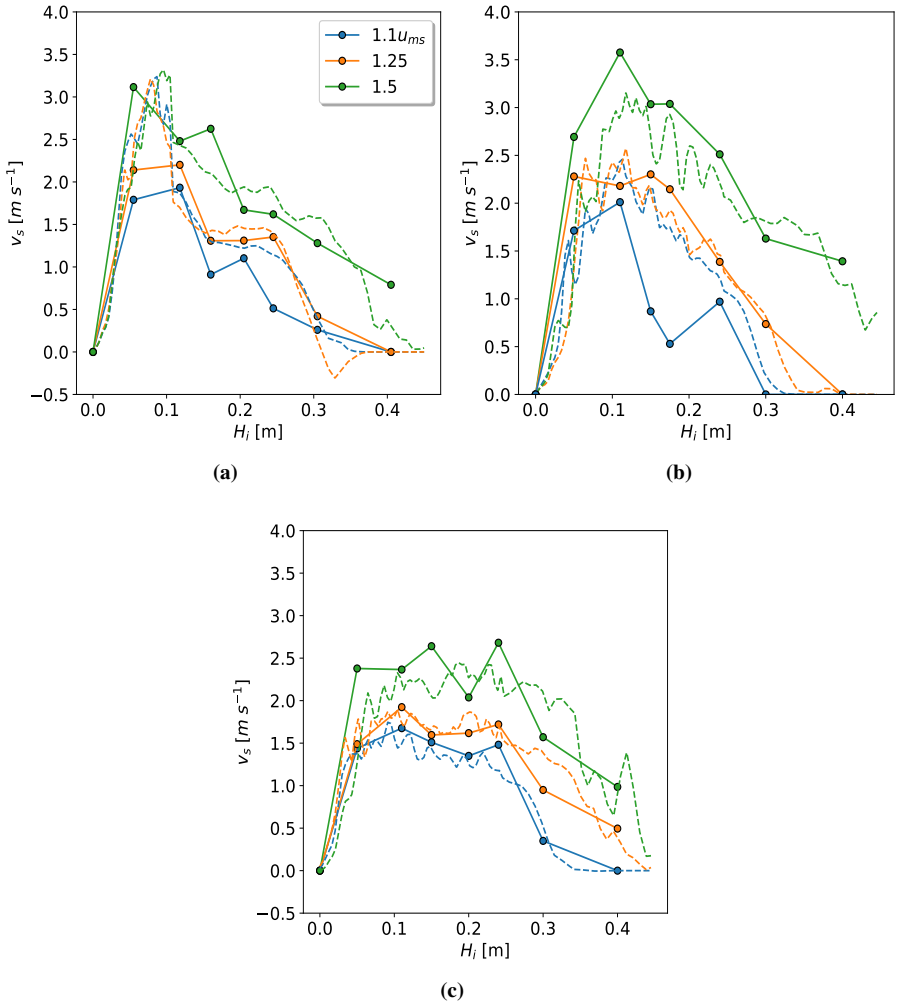

Figure 4.8. *CFD-DEM* (dashed lines) and experimental axial solid velocity profiles for 4 *mm* glass beads in the configurations of (a) *WDT*, (b) *OSDT* and (c) *SDT*, at the three flow rates studied.

are specifically derived from the already mentioned point at the lower end of the contactor (H_i=5 *cm*).

Once the axial and radial velocity profiles have been described for the different configurations, the effect of particle size may be ascertained by comparing the values for glass beads of 2 *mm* with those already shown above for 4 *mm*. The resulting radial profiles are displayed in Figure 4.11.

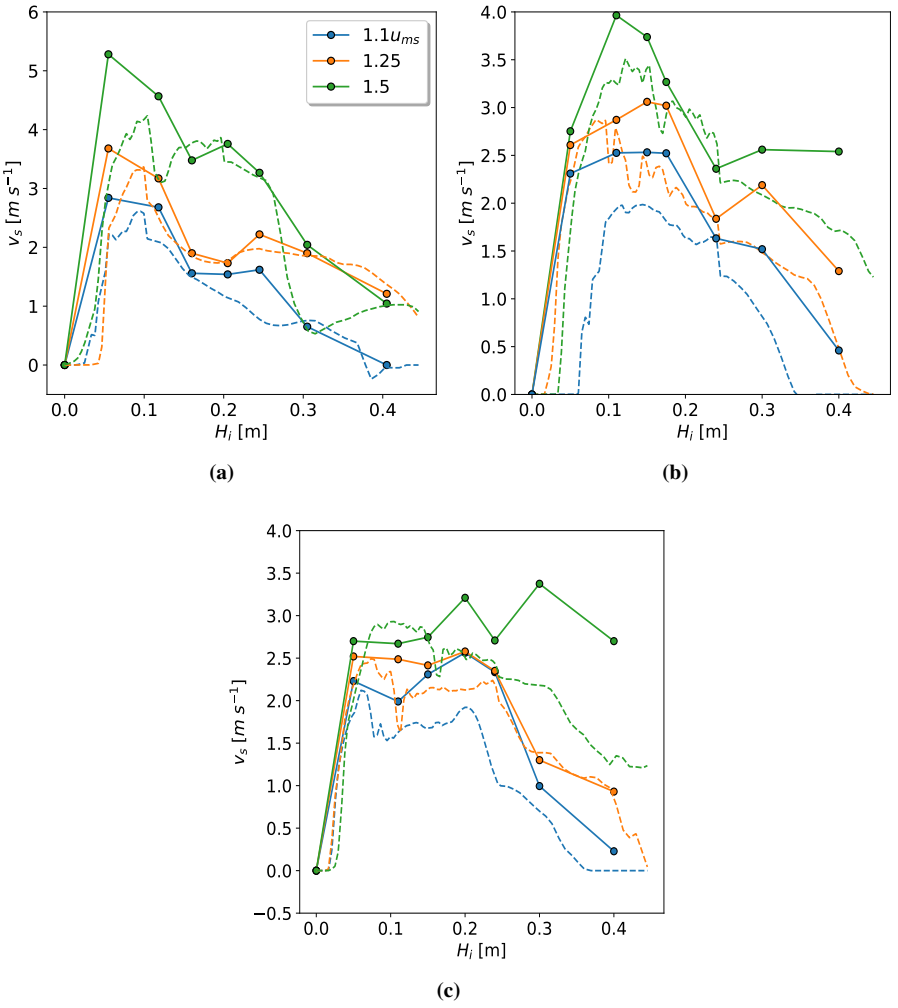

Figure 4.9. *CFD-DEM* (dashed lines) and experimental axial solid velocity profiles for 2 *mm* glass beads in the configurations of (a) *WDT*, (b) *OSDT* and (c) *SDT*,at the three flow rates studied.

As previously shown in the evolution of axial profiles, simulations slightly underestimate the solid velocity in the *WDT* configurations, and this mismatch is evident in the radial profiles shown in Figure 4.11a. The greatest disparity occurs at the lowest measurement point, as all the drag models predict a maximum solid velocity lower than the experimental value. When the draft tube lateral surface area is partially closed (Figure 4.11b) and the annular-spout solid cross-flow rate is therefore decreased, the fit gets better for most heights except for H_i=40 *cm*, where

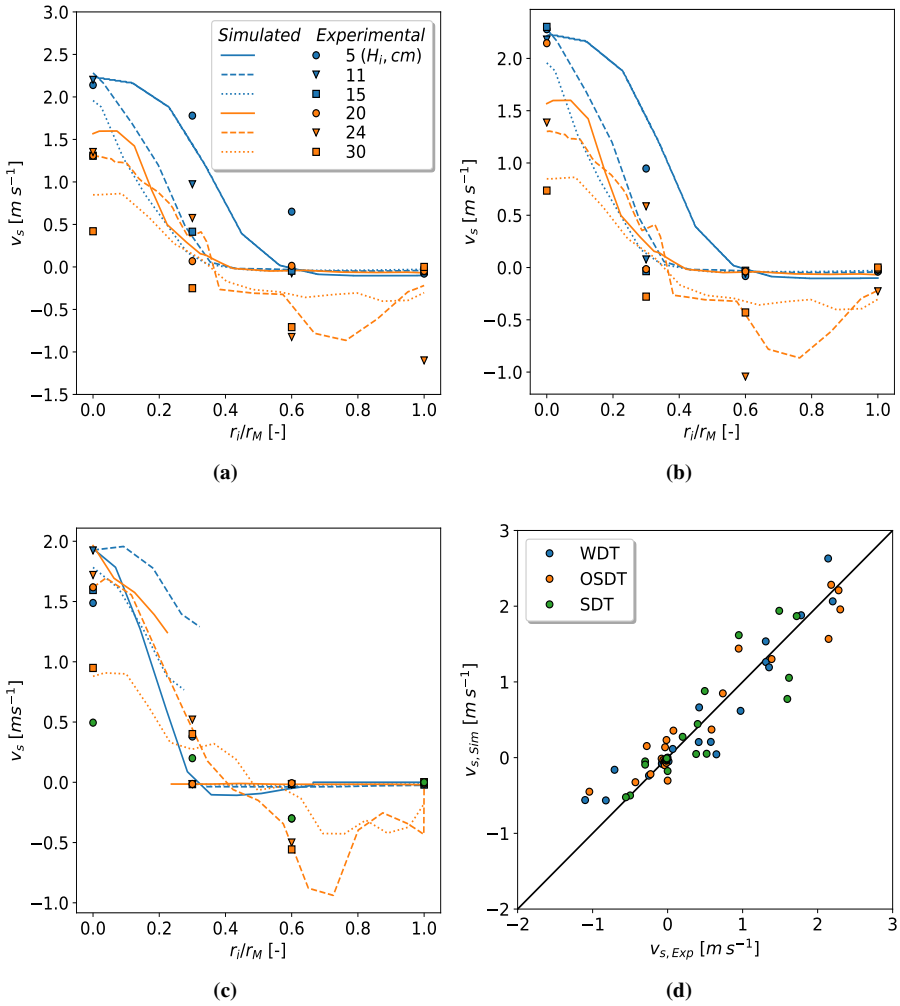

Figure 4.10. *CFD-DEM* (dashed lines) and experimental radial profiles of solid velocity for 4 *mm* glass beads in the configurations of (a) *WDT* , (b) *OSDT* and (c) *SDT*, and (d) their parity plot.

the predicted solid velocity is below the experimental value. In the case of the *SDT* configuration, simulated radial profiles follow a consistent and acceptable trend similar to the experimental one. The quality of the model for three configurations is shown again in Figure 4.11d, where the poorer prediction of the model for the *WDT* configuration is apparent, as is evident in view of several outliers and overall greater spread of the parity points from the perfect fit line. However, the model is suitable for overall prediction purposes.

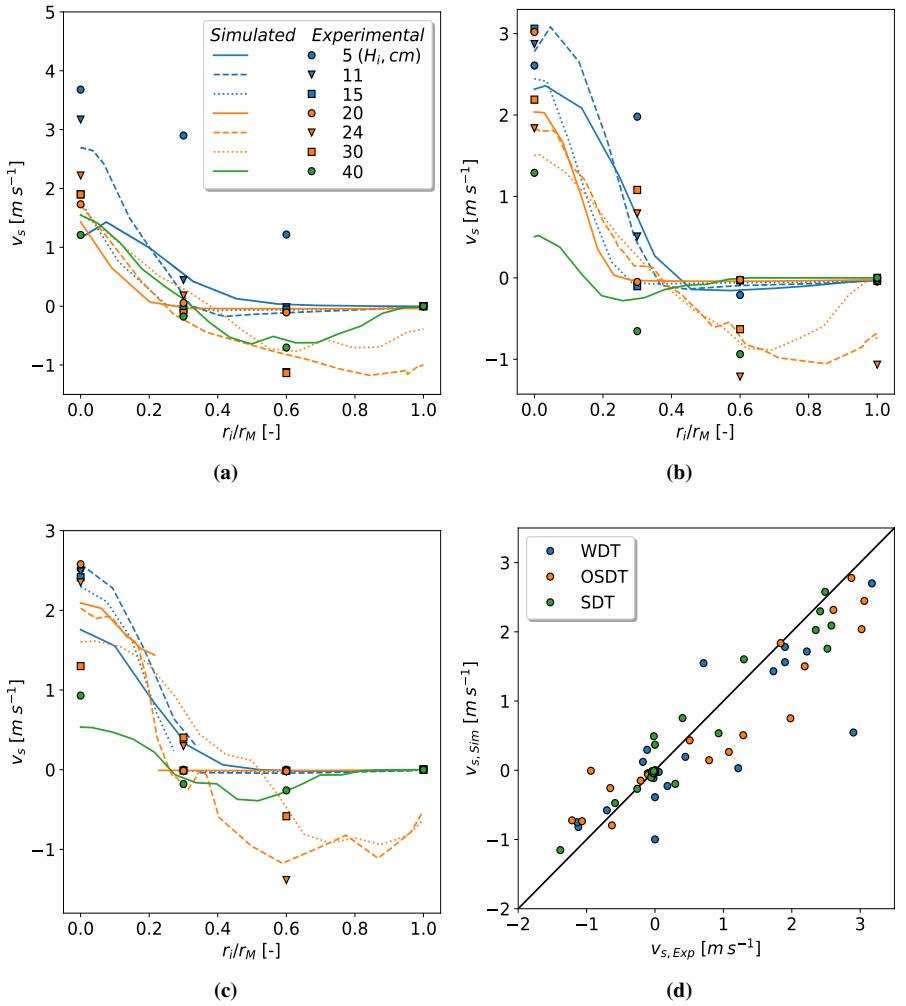

Figure 4.11. *CFD-DEM* (dashed lines) and experimental profiles of radial solid velocity profiles for 2 *mm* particles in the configurations of (a) *WDT* , (b) *OSDT*, (c) *SDT*, and (d) parity plot.

4.2 Minimum spouting velocity

In order to establish a simulation tool to determine the minimum spouting velocity, the experimentation procedure has been mirrored by steadily increasing the inlet air flow until the gas opens the central spout. Subsequently, the inlet air flow rate has been decreased in order to observe the well-known hysteresis in pressure

drop [119]. The minimum spouting velocity (u_{ms}) corresponds to the flow rate at which the spout collapses when decreasing air velocity. In order to stabilize the pressure field and hydrodynamic regime, $0.1\,s$ periods have been left between increasing steps in air flow rate. Defluidization is registered when the axial component of solid velocity at the top of the draft tube ($22\,cm$) is zero.

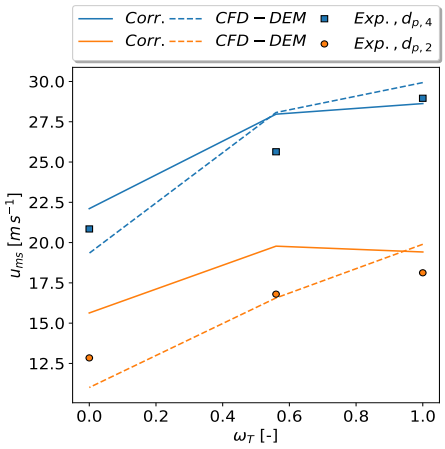

Figure 4.12. Comparison of experimental values (symbols) with those predicted by the correlations of best fit (solid lines) and by *CFD-DEM* (dashed lines) for the minimum spouting velocity of different configurations (aperture ratios) with two particle sizes.

Figure 4.12 shows the minimum spouting velocity for the three configurations and the values obtained with the correlations proposed in our group under similar operating conditions [146] (Equation 4.18) [105](Equation 4.19) [119](Equation 4.20), which are as follows:

$$Re_{o,ms} = 0.126 Ar^{0.5} \left(\frac{D_b}{D_0}\right)^{1.68} tan(\gamma/2)^{-0.57} \tag{4.18}$$

$$Re_{o,ms} = 0.126 Ar^{0.5} \left(\frac{D_b}{D_0}\right)^{1.68} tan(\gamma/2)^{-0.57} \omega_H^{0.3} \tag{4.19}$$

$$Re_{o,ms} = 0.126 Ar^{0.5} \left(\frac{H_0}{D_0}\right)^{1.2} \left(\frac{L_H}{D_0}\right)^{0.3} \tag{4.20}$$

where Archimedes number is defined by Equation 4.21 and Reynolds number (Re) for external flows is defined by Equation 4.22:

$$Ar = \frac{\bar{d_p}^3 g \rho_g (\rho_s - \rho_g)}{\mu_g^2} \tag{4.21}$$

$$Re_{ms} = \frac{\bar{d_p} \rho_g u_{ms}}{\mu_g} \tag{4.22}$$

As shown in Figure 4.12, the values obtained with the empirical correlations deviate from the experimental ones in a range from 0.7% for the *WDT* configuration to 6% for the *SDT* configuration, for both 2 and 4 *mm* glass beads. These error values are acceptable and comparable to the experimental ones in the pilot scale plat. Furthermore, Figure 4.12 shows the spouting velocities obtained by *CFD-DEM* simulations, whose error values are in the range from 3.3% for the *WDT* configuration to 7.2% for the *SDT* configuration when 4 *mm* glass beads are used. In the case of 2 *mm* particles, u_{ms} prediction error is in the 9-14% range, which is still an acceptable error level for an initial estimation when designing a new spouted bed reactor.

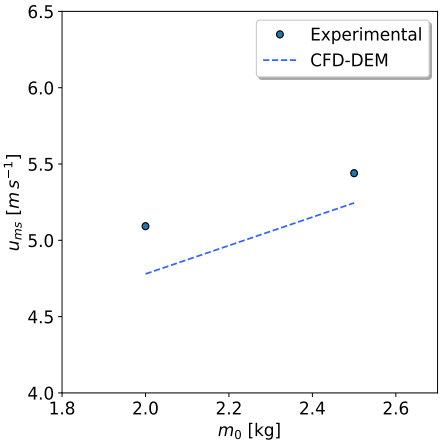

Figure 4.13. Experimental and simulated values of minimum spouting velocity for 3 *mm* glass beads in the prismatic spouted bed.

Additionally, Figure 4.13 shows the minimum spouting velocity values for the prismatic spouted bed with 3 *mm* glass beads and two static bed heights corresponding to 2 *kg* and 2.5 *kg* in the bed. The comparison shows a deviation of the simulated values from the experimental values by 5%, which corroborates the capability of *CFD-DEM* simulations to reasonably predict the u_{ms} values in various configurations, particle sizes and contactor designs.

4.3 Pressure drop simulations

Pressure drop is related to the operating cost of any configuration, and is therefore of uttermost relevance to determine its value through simulations. *CFD-DEM* hardly ever matches the experimental pressure drop values, partly due to the unresolved nature of the simulations and because of the piping and peripheral equipment (filters and valves) that are not taken into account. In order to increase the accuracy of the simulated pressure drop and consider the aforementioned effects, a Darcy-Forchheimer porous region is generally set at the inlet of the contactor following Equation 4.23:

$$\frac{\Delta P}{\Delta L} = \frac{\mu|\mathbf{u}|}{C_{1,d}} + \frac{1}{2}C_{2,d}\rho|\mathbf{u}^2| \tag{4.23}$$

where C_1 is the viscous constant and C_2 is the inertial constant, whose values are obtained through the pressure drop of the empty contactor at varying flow rates. The resulting pressure is added as a momentum sink at the reactor inlet and the simulated pressure drop is compared against the experimental values once the reactor is filled with particles, Figure 4.14.

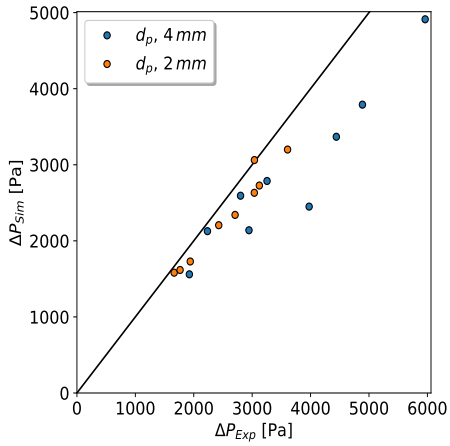

Figure 4.14. Parity plot of *CFD-DEM* simulated pressure drop values and the experimental ones.

Figure 4.14 shows a reasonable agreement between the experimental and simulated values. The greatest disparity is obtained at high pressures when *WDT* configuration is used with low flow rates ($1.1u_{ms}$) for spouting 4 *mm* glass beads.

As stated in the experimental section, the fluctuation of the pressure drop signal

gives hints about the stability of fluidization. First, it is important to observe the evolution of the spectrogram when the flow rate is increased. As more air is fed into the system, there is a higher solid circulation flow rate with more solid-solid collisions and annular-spout solid transfer, which leads to an increase in the main frequency in the spectrogram, Figure 4.15a. The same behavior is observed in the prismatic spouted bed, Figure 4.15b, where the main pressure component appears at $5\,Hz$, and progressively shifts towards higher frequencies as the air flow rate is increased. The regime might be identified by the shape of the pressure spectra dictribution [110]. A stable spouting in prismatic spouted beds is identified by a narrow distribution of the pressure harmonics, but, as readily seen in Figure 4.15a, this is not the case of the conical spouted beds composed of glass beads, as more collisions occur in these conical beds, which lead to fairly wide power distributions, even when a stable spouting regime is attained.

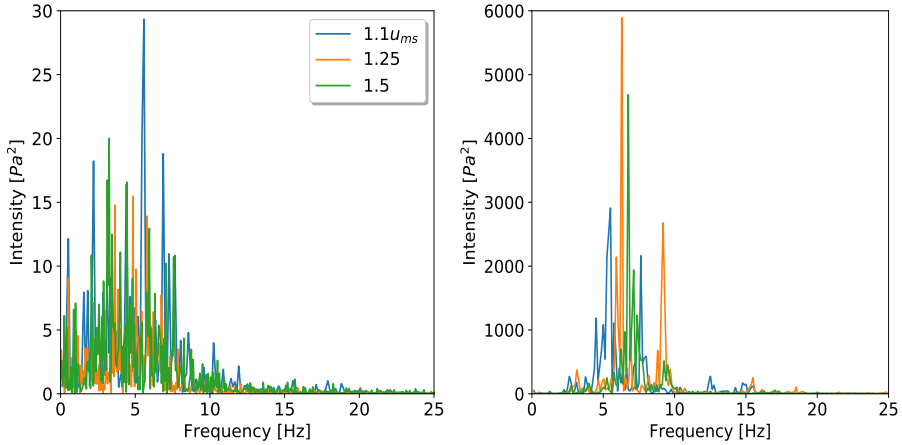

Figure 4.15. Evolution of the spectrogram with bed turbulence for (a) 4 *mm* glass beads in a conical spouted bed of *OSDT* configurations and (b) 3 *mm* glass beads in a prismatic spouted bed.

According to the experimental trend, as flow rate is increased the main frequency shifts towards higher frequencies for all configurations and particles sizes which has already been reported in literature[116]. Once the simulations have been run for a number of seconds in an steady fashion, the simulated pressure drop spectra can be compared with the experimental values shown in Figure 4.16.

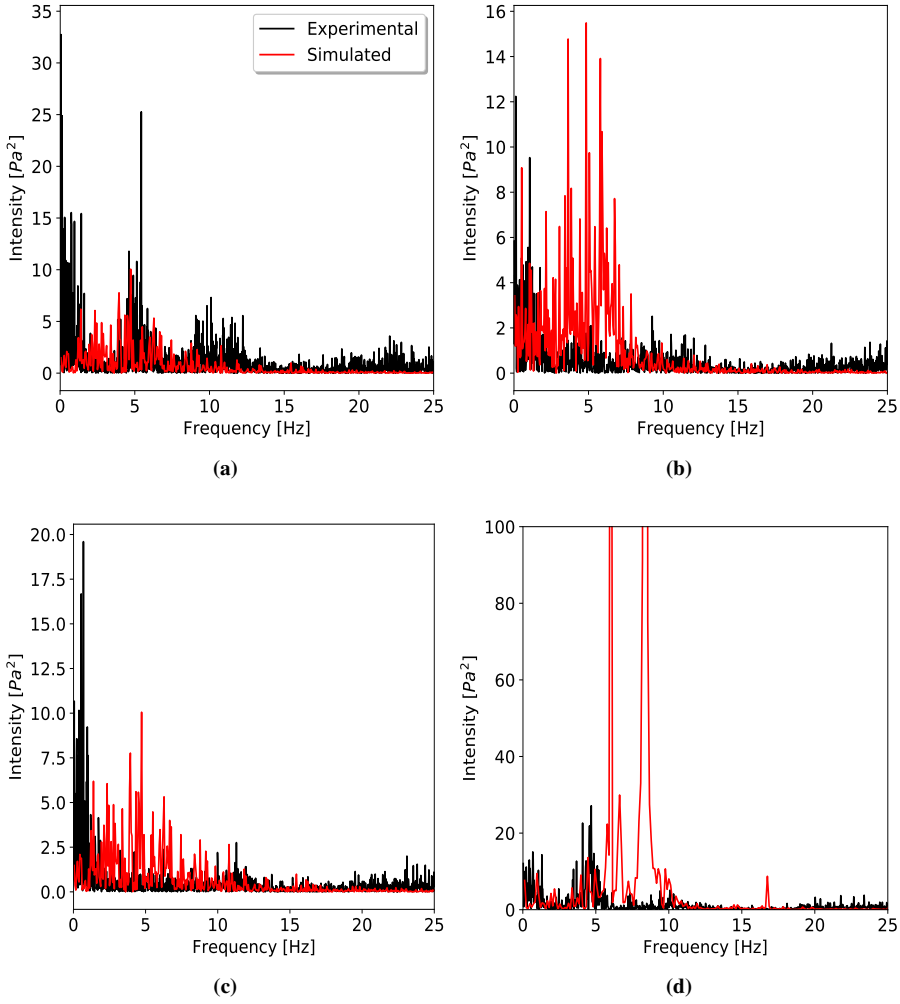

Figure 4.16. Experimental and simulated pressure drop spectra distribution for 4 *mm* glass beads in (a) WDT, (b) $OSDT$, (c) SDT configuration and (d) 2 *mm* glass beads in a WDT configuration.

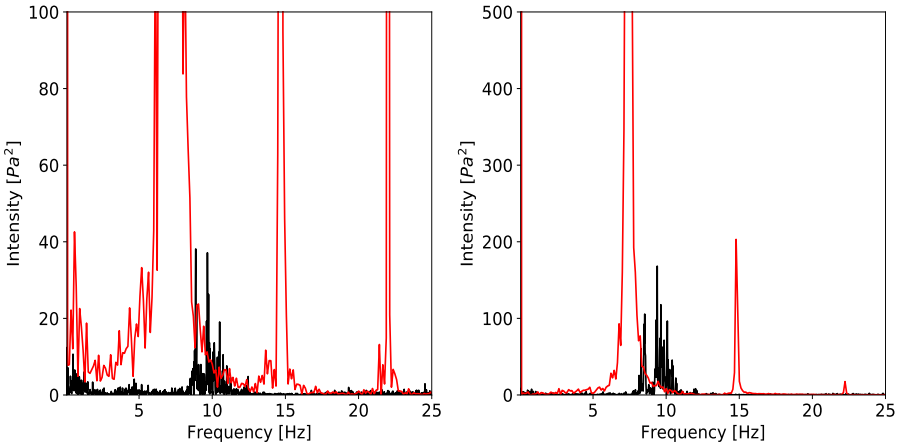

Figure 4.16. (continued) Experimental and simulated pressure drop spectra distribution for 2 *mm* glass beads in (e) *OSDT* and (f) *SDT* configurations.

As previously stated, the experimental power spectra distribution do not show a narrow distribution in a single frequency for the glass beads of $\bar{d}_p$=4 *mm*, Figures 4.16a-4.16c. For this material in *WDT* configuration, the simulation shows a clear distribution around the experimental values, even though the harmonics of low frequency in Figure 4.16a do no match up with the experimental values. In case of the *OSDT* configuration, the experimental value show more intense harmonics in the lower end of the frequency. This disparity suggests a more stable spouting been predicted by the simulation than observed in the experimental procedure. The same trend is observed for the *SDT* configuration with low frequency experimental harmonics not being present in the simulation.

The overall spouting of $\bar{d}_p$=2 *mm* glass bead particles is more stable than that of bigger 4 *mm* particles, and their simulated spectra fit better the experiment ones, Figures 4.16d-4.16f, with a single peak that is characteristic of stable spouting, as happens in prismatic spouted beds. The *WDT* configuration, Figure 4.16d, shows two main harmonics in the simulation in the regions corresponding to 5 and 10 Hz, while the experimental data show a wider distribution around 5 Hz. For all the internal devices used, Figures 4.16e-4.16f, the simulations slightly underestimate the frequency of the main harmonic and, furthermore, another component at 15 Hz is considerable, which is not significant in the experimental data. This suggests the possibility that solid-solids interactions should lead to a higher frequency, as particles have been slightly smoothened (lower Young modulus) in order to speed up simulation times. In most cases, the intensity of the pressure fluctuation dis-

tribution could not be reproduced, as it has been the case in other unresolved *CFD-DEM* simulations [92, 110].

4.4 Fountain height

Comparison of simulated values of fountain heights with those experimentally observed allows confirming the correct friction force established in the simulations. In addition, knowledge of the fountain height helps to determine the volume occupied by the solid phase, and therefore the contactor volume. Even though the fountain height does no greatly affect other important parameters, such as cycle time, it does have an affect on the time the gas phase is in contact with the solid, thereby playing a major role in certain reactions[147, 148]. In addition, given the importance of this parameter in process performance and product yields, efforts have been made to modify the fountain shape, specifically by confining it. This leads to higher product yields in processes such as gasification, as the gas phase spends more time in contact with the solid phase in a turbulent fashion [149].

The information about the fountain height is directly obtained in the simulation as a post-processing step, by calculating the maximum location of a particle in a cylinder around the main axis with a radius of $2\bar{d}_p$ (Figure 4.17a) in order to account for any slight inclination of the fountain. As a result, the maximum height of the fountain is registered each time a simulation file is dumped with a usual sampling frequency of $25Hz$. The evolution of the resulting values is plotted in Figure 4.17b. Finally, the time averaged value is taken as the average simulated fountain height $\bar{H_{f,sim}}$.

It is worth noting that, when the spout is opened, the simulations show a fountain height well above the average value corresponding to steady state, Figure 4.17b.

Once all the simulations are run with $\bar{d}_p$=2 and 4 *mm* particles, the experimental values shown in Section 3.2 are compared with the simulated ones, Figure 4.18. It is worth mentioning that frictional coefficients have not been changed when varying flow rates or configurations, but only the boundary condition values, mainly velocity and turbulence values at the inlet. Figure 4.18 shows a good agreement between experimental and simulated values, although there is a slight deviation for 2 *mm* particles, which may be due to the fact that slight velocity deviations lead to higher fountain deviations for the smaller particles (lower mass).

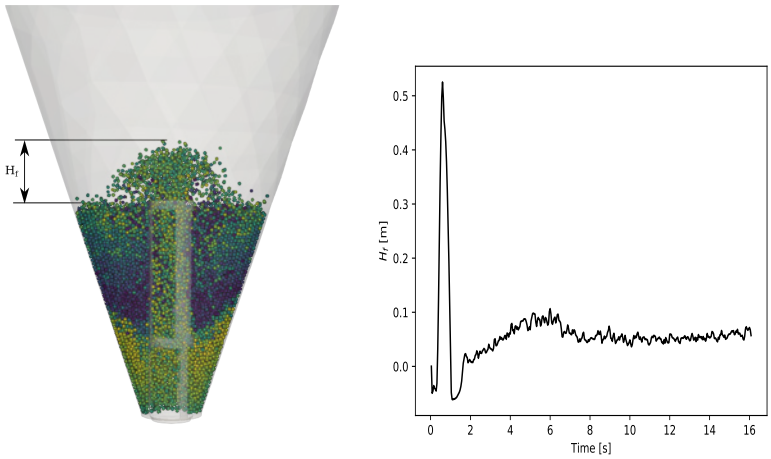

(a) (b)

Figure 4.17. Graphical representation of (a) the fountain height as a post-processing step in the simulation and (b) the resulting fountain height signal with time since process starts for a given air flow rate in the feed.

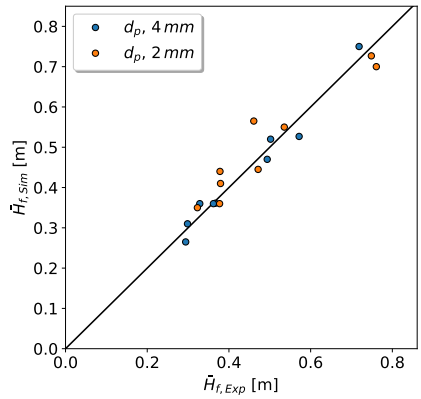

Figure 4.18. Parity plot of experimental fountain height values and those simulated for regular materials operated in the three configurations at varying flow rates.

4.5 Void fraction evolution

The assessment of void fraction from simulation runs requires some considerations to be introduced, given that, as shown in Table 4.1, all the drag models re-

quire including the void fraction field, which is also required in all the governing equations. Experimental data of void fraction have already been reported in the literature for this same system and certain materials through the use of a fiber optic probe [124, 150].

Following the same order as with the other parameters, the first configuration to be studied is the WDT one, as it is the most simple and widely used. Figure 4.19 shows the results obtained by simulating glass beads of $4\,mm$ and $2\,mm$. Each graph shows the influence of flow rate on the gas void fraction ε_g for a given particles size. Figure 4.19a, corresponding to $4\,mm$ glass beads, shows that the minimum void fraction values are achieved at low flow rates, and particles flow more loosely as the air flow rate is increased. With this solid size, the void fraction decreases until the bed surface is reached at $22\,cm$, as in the WDT configuration solid incorporation into the spout occurs along the whole bed length. Once this height is reached the fountain is formed and void fraction values go up due to the scattering of the solids.

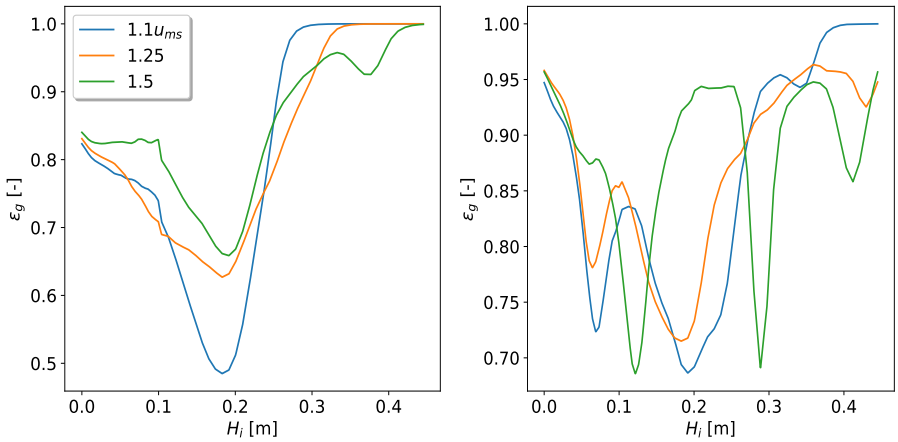

Figure 4.19. Void fraction distribution along the axis at different flow rates with (a) $4\,mm$ glass beads and (b) $2\,mm$ glass bead particles in the WDT configuration.

When $2\,mm$ solids are employed (Figure 4.19b), the void fraction value has a sudden decrease close to the bottom of the reactor due to a massive preferential incorporation of particles into the spout. Then, particles continue accelerating, but incorporation of the solids into the spout is not as significant at as in the previous position close to the bottom, and therefore void fraction increases for a length range. However, at positions of around H_i=20 cm there is again another decrease in void fraction due to particle deceleration. These inverse peaks shift to higher

longitudinal positions as the flow rate is higher. Another fact contributing to the different trend of this low size material lies in its tendency to move in clusters.

Figure 4.20 shows the void fraction evolution in the *OSDT* configuration. The influence of internal devices can be observed when comparing Figure 4.19 with Figure 4.20. Comparing the inverse peaks achieved at low flow rates in both cases, it is deduced that the use of an internal device like the *OSDT* dilutes the spout even at low air velocities. This conclusion is consistent with the fact that internal devices reduce the number of collisions with particles coming from the annular zone, and therefore lead to more dilute spout zones.

Regarding the evolution of the profile as the flow rate is increased, a similar trend as the one shown in *WDT* configuration is observed, with a flatter void fraction distribution as more air is fed into the spout. Furthermore, the presence of the internal device makes the location of the minimum value (inverse peak) to be at lower longitudinal positions. The same applies as the flow rate is increased.

When the particle size is decreased, there is a sharp decrease in void fraction for low flow rates, with the minimum value close to the surface of the bed. However, when the inlet flow rate is increased, this void fraction reduction is less significant and another minimum value appears close to the bottom of the contactor ($\sim 7\ cm$), which is approximately at the upper position in the entrainment zone of the *OSDT*. In addition, at low flow rates there is another void fraction minimum close to the top of the fountain, as the particles do not acquire enough momentum to disperse and fall back onto the annulus surface. At high flow rates particles are more scattered and acquire enough momentum to flatten the void fraction profile.

When Figure 4.20a and Figure 4.20b are compared, it is evident that void fraction does not decrease sharply close to the inlet (in the first couple of centimeters) for $2\ mm$ glass beads Figure 4.6b. This means that there is hardly any particle at the axis of the bed in this initial stretch of the bed.

The radial profiles of the void fraction are important in order to understand the level of gas-solid mixing that takes place within the reactor at different heights. Figure 4.21 shows the void fractions in cross sections at varying heights. At the entrainment height of the *OSDT* in Figure 4.21a, the spout and spout-annulus interface region take a significant fraction of the bed, with air trickling from the spout region towards the wall. In addition, it is evident that the the draft tube legs have an influence at this height, as they do not let air pass through their lateral surface. At higher bed positions in Figure 4.21b, the influence of the legs in the overall section of the bed (overall radial profile) gets reduced, but there is still a significant dilute region covering the cross sectional area. At a height of $15\,cm$ (Figure 4.21c), corresponding to the minimum void fraction along the axis, there

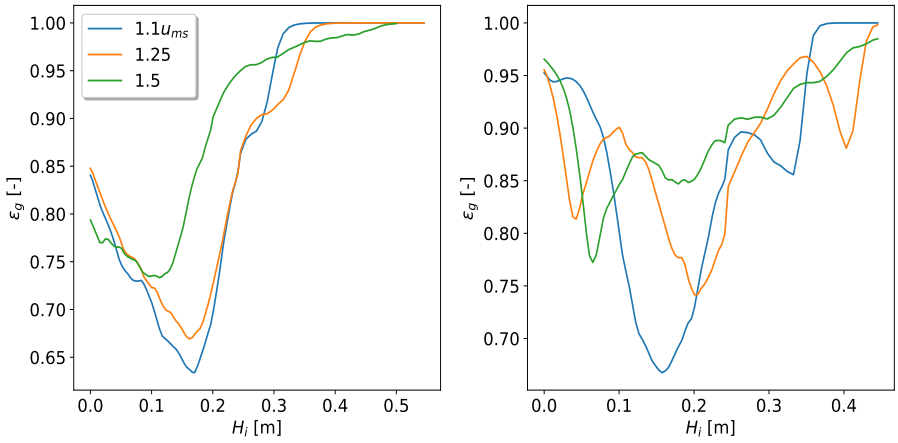

Figure 4.20. Void fraction distribution in the axial direction at different flow rates with (a) 4 *mm* and (b) 2 *mm* glass bead particles with the *OSDT* configuration.

is clearly a significant solid incorporation into the spout, which in turn leaves air gaps behind. This might be a good reason to use *OSDT* configurations to improve the gas-solid contact, especially in applications that require high heat and mass transfer rates, as is the case of oxidative pyrolysis or combustion [3]. At higher positions corresponding to the fountain, Figure 4.21d, there is a central dense region and a dilute region around it formed by particles falling back onto the annulus of the bed.

As the aperture ratio (ω_T) is decreased down to the *SDT* configuration, the location of the minimum void fraction is at a lower level in the bed. As the level of the bed is higher, the void fraction increases, as this configuration leads to the most dilute spouting regimes of the systems studied. Figure 4.22 shows the void fraction profile at different heights for the inlet air flow rate corresponding to $1.1u_{ms}$. As observed, the presence of the solid draft tube makes the minimum void fraction value to be below the entrainment height (L_H=7.5 *cm*, *i* in Figure 4.22). Above the entrainment zone, the spout keeps a consistent void fraction value of 0.9 (*ii-iii* Figure 4.22). This is an indication of how dilute the spout is when a *SDT* is used. When particles leave the spout, the void fraction shows a steady increase until the end of the fountain is achieved (0.33 *cm*, *iv* in Figure 4.22).

When the smaller particle size of $\bar{d_p}$=2 *mm* and high flow rates are used in the *SDT* configuration(Figure 4.23a), the solid profile keeps a similar trend as the one already mentioned for the bigger particle , even though the spout void fraction

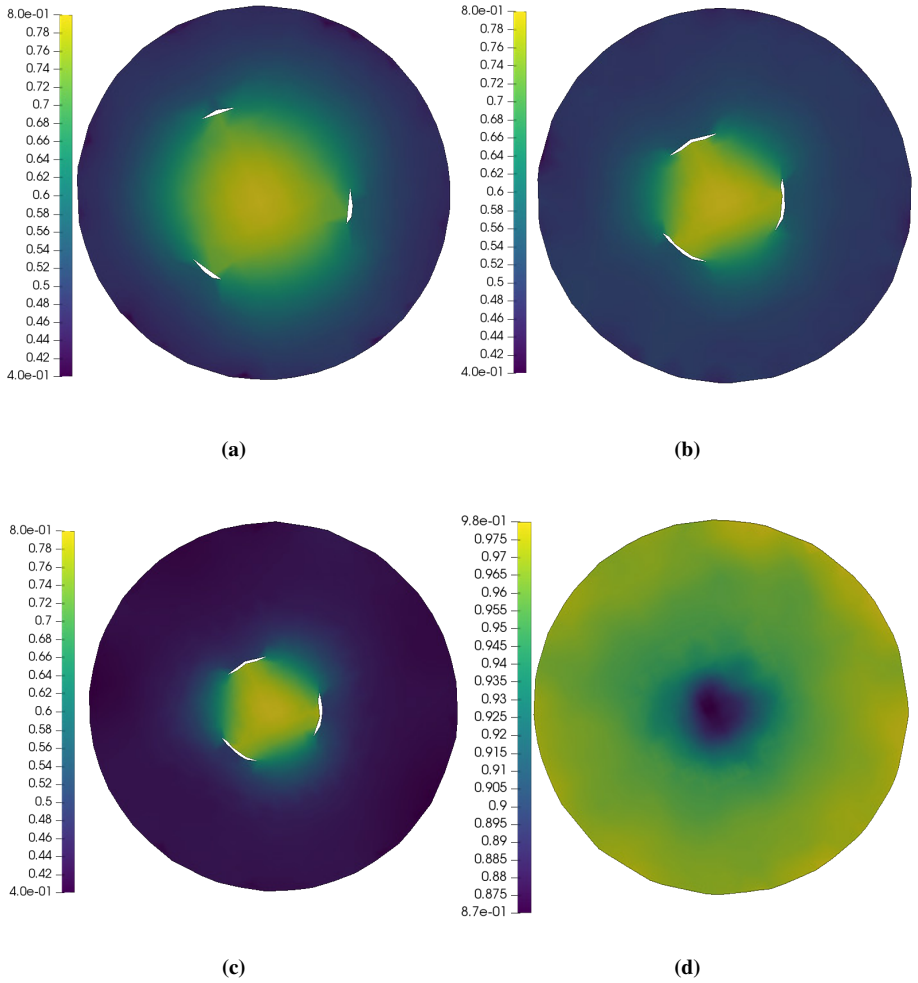

Figure 4.21. Void fraction fields in radial cross sections at the heights of (a) 5 *cm*, (b) 11 *cm*, (c) 15 *cm* and (d) 24 *cm* in the *OSDT* configuration for 4 *mm* glass beads.

(ε_g) is slightly lower due to a better packing of the particles in the spout under these conditions. However, when a lower flow rate is employed ($1.1u_{ms}$), solids barely have enough momentum to overcome solid-solid and solid-wall friction forces just at the upper end of the draft tube, and therefore accumulate at this upper position in the draft tube, attaining the minimum void fraction of 0.7 at H_O, shown in Figure 4.23a, which is also shown in the color scaled cross section of the contactor in Figure 4.23b. In addition, as the spout is expanded above H_O and the fountain is formed, another minimum is achieved around the maximum fountain

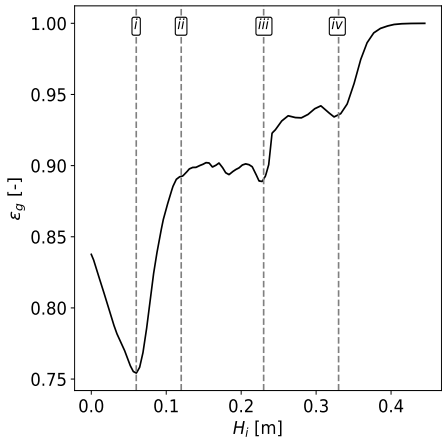

Figure 4.22. Gas void fraction distribution along the axis of the contactor at $1.1u_{ms}$ when the *SDT* is used with 4 *mm* glass beads.

height, at the same time as the particles start to fall back onto the bed surface at 0.34 *cm*.

As the flow rate is increased the local void fraction minima are less significant (Figure 4.23c-4.23d) due to the higher momentum exchange to the particles and a more dilute fountain, which leads to a profile similar to the one in Figure 4.22 for coarser particles.

In addition to the axial profile of the void fraction, the radial profiles shown in Figure 4.24 deserve attention. Thus, Figure 4.24a shows that, in addition to the minimum void fraction in the axial direction, there is a reduced value even outside the device, as particles flowing into the spout leave dilute regions behind with a similar trend to that shown in the *OSDT* configuration, with solid trickling depending on the flow rate and the aperture ratio of the entrainment zone. For low flow rates the void fraction behind the legs of the draft tube is low, but an increase in flow rate makes the air overcome this situation and dilute even the regions behind the legs, Figure 4.25. Furthermore, Figures 4.24b and 4.24c show certain wall effect on the cone inner and draft tube outer walls.

Figure 4.24d shows the radial cross section at the fountain height of H_i=24 *cm*, where the presence of the central fountain is evident, as it takes most of the contactor section, which is consistent with that experimentally observed.

As previously mentioned, the presence of the legs in the design of the draft tube has a great influence on the local void fraction values, and hence on the drag force on the particles in these regions. Figure 4.25 shows the influence the flow rate and

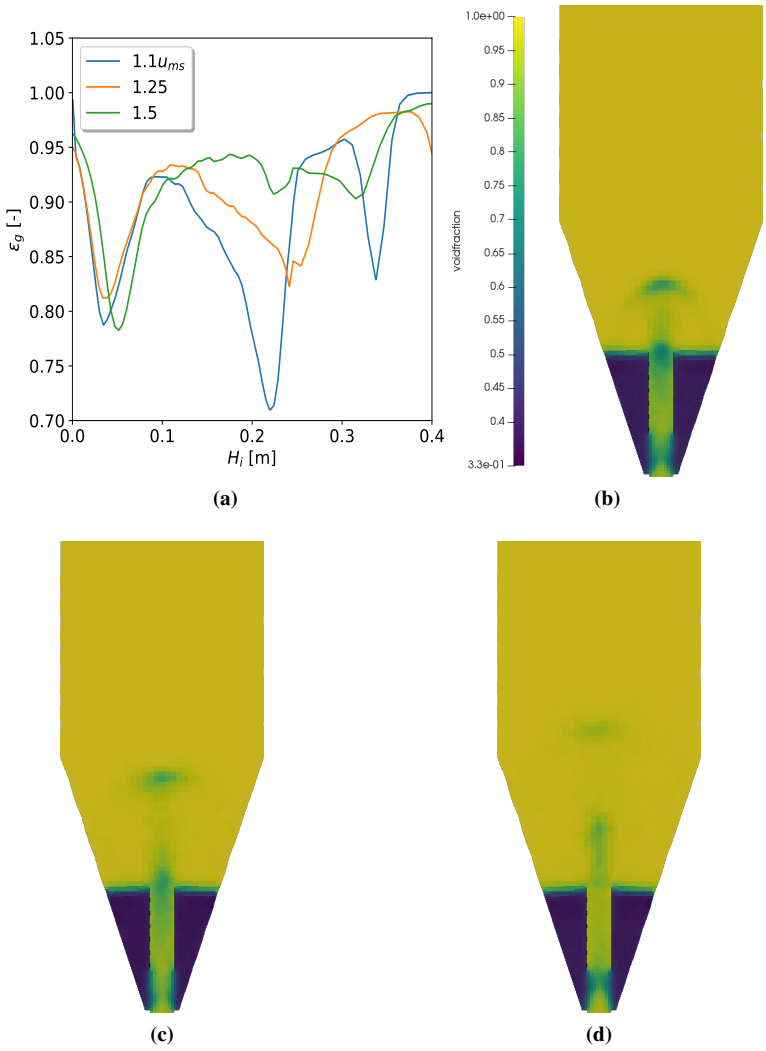

Figure 4.23. Evolution of (a) void fraction along the axis for the three flow rates studied and snapshots for (b) $1.1u_{ms}$, (c) $1.25u_{ms}$ and (d) $1.5u_{ms}$, when a *SDT* is used with 2 *mm* glass beads.

solid size have on the void fraction profiles in the entrainment zone of a *SDT*. As the flow rate is increased (Figures 4.25a and 4.25b), both the void fraction and the spout radius increase, and the death zones behind the draft tube legs decrease, as more air trickles into the annular zone. When smaller particles are used, Figure 4.25c, the death zones behind the draft tube legs are more severe due to the higher number of particles retained in the death zone.

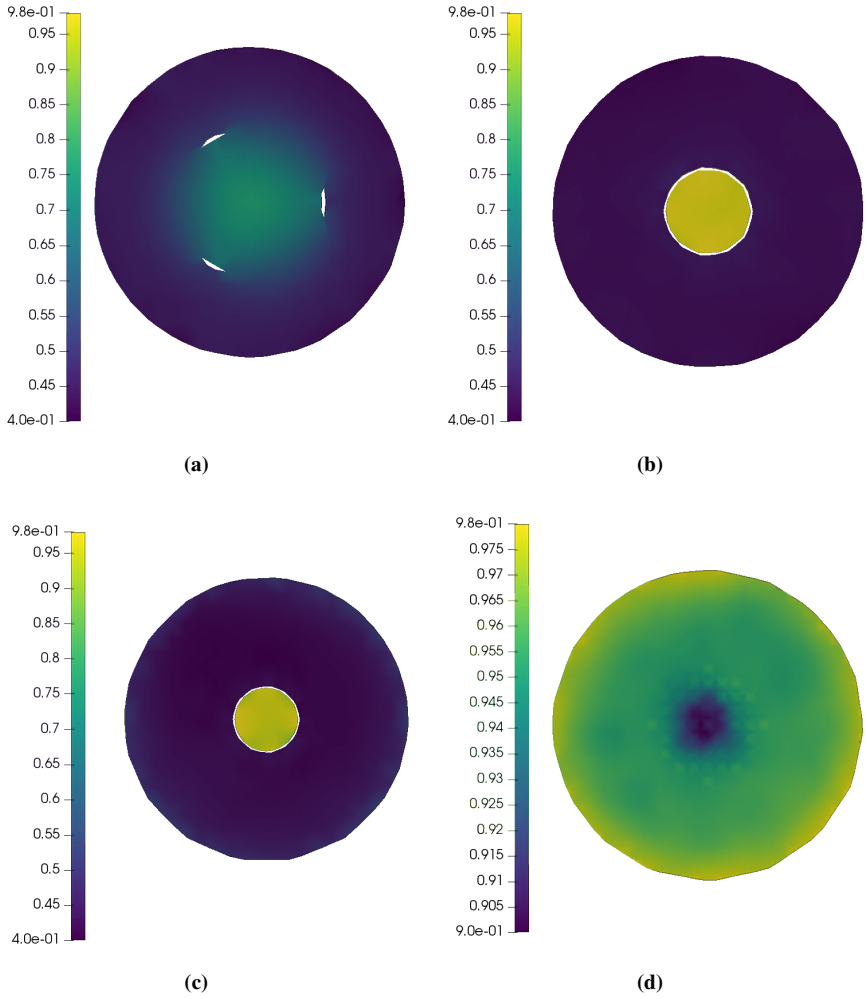

Figure 4.24. Void fraction fields in radial cross sections at the heights of (a) 5 *cm*, (b) 11 *cm*, (c) 15 *cm* and (d) 24 *cm* for a *SDT* configuration and $\bar{d_p}$=2 *mm* glass beads.

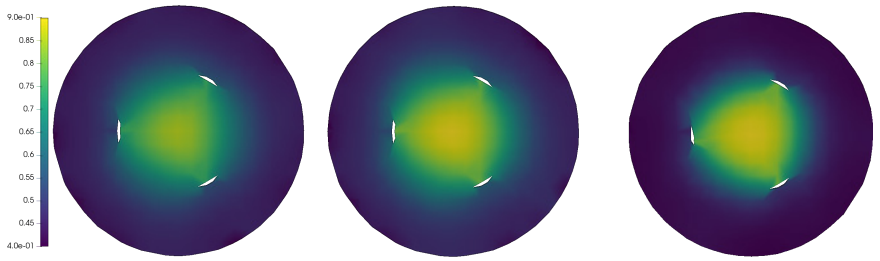

Figure 4.25. Void fraction evolution when the flow rate is increased to (a) $1.25u_{ms}$ and (b) $1.5u_{ms}$ with $\bar{d}_p$=4 *mm* particles, and (c) the solid size is reduced to $\bar{d}_p$=2 *mm* at $1.5u_{ms}$, in the *OSDT* configuration.

4.6 Cycle time analysis

The solid cycle time is determined by the time a particle takes to go through the annular, spout and fountain zones to finally land back on the annular zone. As particles follow paths that are influenced by the internal dynamics of the contactor, there is a distribution of said cycle times, which are comprised of different solid populations. This distributions allow calculating the average cycle time, which is a highly relevant parameter to assess the solid circulation flow rate. Furthermore, the average cycle time determines the time particles have to withstand the operating conditions from a mechanical and chemical standpoint. Thus, it defines the minimum requirements for the bed material in order to operate under stable conditions. This fact is essential in systems where fast reactions happen or severe deactivation is present [151]. The experimental cycle time values for the conical spouted bed have already been published for $1.1u_{ms}$ [103, 151], as well as the relevant correlations for the three configurations, given by Equations 4.24-4.26, corresponding to *WDT*, *OSDT* and *SDT*, respectively. The experimental setting used for the proposal of these correlations is the same as in this study, which is a great advantage, as it allows comparing both the experimental and simulated values.

$$\bar{t_c} = 33.51Ar^{-0.12}\left(\frac{H_O}{D_O}\right)^{0.13} tan(\gamma)^{0.78} \tag{4.24}$$

$$\bar{t_c} = 101.82Ar^{-0.18}\left(\frac{H_O}{D_O}\right)^{0.48}\left(\frac{\omega_H}{D_O}\right)^{0.31} tan(\gamma)^{0.87} \tag{4.25}$$

$$\bar{t_c} = 4.08Ar^{-0.06}\left(\frac{H_O}{D_O}\right)^{1.71}\left(\frac{L_H}{D_O}\right)^{-0.79}tan(\gamma)^{0.94} \tag{4.26}$$

Cycle times were obtained by tracking the time needed for a colored particle to appear two consecutive times on the bed surface, as it has completed a cycle in this time range. The average cycle time changes with operating conditions and, specially, with the internal device employed, with the minimum average cycle time being for the systems without any internal device and the maximum one for systems using a solid draft tube (*SDT*). In addition to the average cycle time, the shape of said time distribution provides crucial information for certain applications, in which the solid cycle time must be kept within a preset cycle time range.

In order to obtain the cycle time distribution of each simulation, the location of each particle is post-processed. Thus, the cycle time of each particle has been taken as the time required for a given particle to reach consecutively a given height, which has been set just below the initial stagnant bed height (H_o) at $21\,cm$. The time resolution for the cycle time is proportional to the sampling frequency, which in most cases has been set at $16K\ \Delta t_{DEM}$ or $0.04\,s$. The resulting time distribution frequency is generally normalized in order to compare systems with different particle numbers. The final distributions obtained for the three configurations at the conditions studied are shown in Figure 4.26.

Figure 4.26a shows the solid cycle time for a system without any internal device. The average cycle time is close to the value reported in previous studies, i.e., $5\,s$ [103]. Furthermore, the simulation shows the shape of the particle cycle time distribution, with a very wide distribution ranging from the minimum to the maximum cycles times, $t_{c,min} = 0.5\,s$ to $t_{c,max} = 15\,s$. Thus, there is a population of particles with very short cycles, which is characteristic of a *WDT* configuration, as a particle on the top of the bed falls back onto a point that is very close to the spout region. In addition, very long cycles are also present, as some particles describe a cycle from the top of the bed to the bottom of the contactor, following a path along the wall.

However, when an *OSDT* is used, Figure 4.26b, the distribution is bimodal with a first narrow peak for short cycles, whose average value is $3.5\,s$ and a second population of particles completing longer cycles with an average of $14\,s$. Finally, those particles that follow the wall make up the tail of the distribution with a maximum cycle time value of $30\,s$. The second population of particles is linked to the decrease in the void fraction profile shown in Figure 4.20a, i.e., a sharp decrease in void fraction up to a height of $7\ cm$. The remaining population is related to the solid incorporation into the spout along its length, and therefore to the decrease in void fraction from the mentioned position to the bed surface ($22\ cm$). This trend

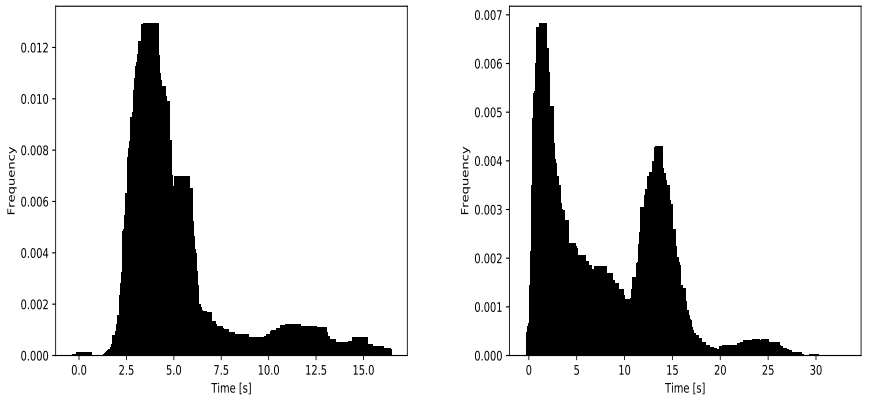

(a) **(b)**

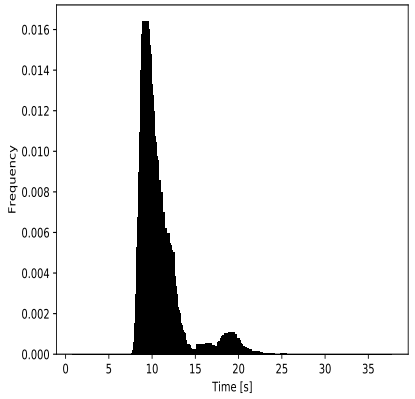

(c)

Figure 4.26. Cycle time distributions at $1.1u_{ms}$ with $4\,mm$ glass beads for the configurations of (a) WDT, (b) $OSDT$ and (c) SDT.

accounts also for a slight influence of the structural ring contained in the $OSDT$ when low flow rates are used.

The SDT forces the particles to complete long cycles, Figure 4.26c. It is similar to the one obtained with WDT configuration, but narrower and shifted towards longer times. Thus, solids have no way to get into the spout, but through the entrainment region and the minimum spouting velocity leads to the minimum solid circulation flow rate. The average cycle times simulated for the three configura-

tions and the values obtained by Estiati et al. [151] are compared in Figure 4.27, with the maximum error being 20 % for the *SDT* configuration.

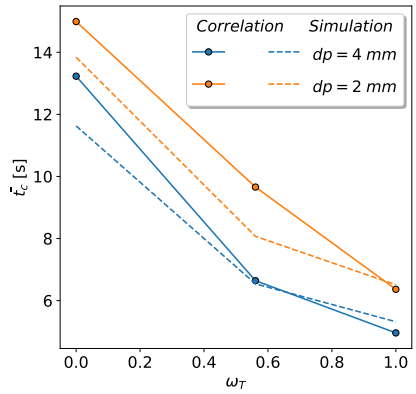

Figure 4.27. Comparison between the simulated and correlated [151] cycle times for the three configurations studied.

The average cycle time decreases slightly with an increase in flow rate in the range studied, which leads to an increase in the overall solid circulation flow rate in the bed. Figure 4.28 shows this trend in all configurations for both glass bead sizes. As previously stated in Figure 4.27, the *WDT* configuration shows the shortest cycle time distribution, as solids are free to flow from the annulus into the spout and the spouting flow rate required for this configuration is the highest. As the air velocity is increased, the fountain expands, and therefore the cycle time slightly increases when transitioning from 1.1 to 1.25 times the minimum spouting velocity u_{ms}. However, as the flow rate is further increased the enhanced solid circulation rate makes the average cycle time to drop sharply. Nevertheless, *OSDT* and *SDT* configurations do not show this sharp decrease in cycle time with air flow rate, but follow an approximately linear trend.

As solid size is decreased, the average cycle time increases due to the lower minimum spouting velocity required for operation, but overall the same trends as with 4 *mm* particles are observed.

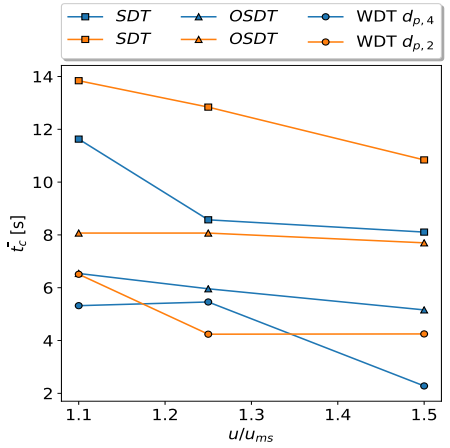

Figure 4.28. Evolution of the average cycle time with flow rate and particle diameter ($\bar{d}_p$=2,4 *mm*).

4.7 Gas residence time

Gas residence time distribution or *RTD* provides information of the time fluid volume elements stay inside the bed, which is of great relevance in those applications heavily dependent on particular gas-solid contacts [152]. Thus, significant deviations from the ideal *RTD* might incur in penalties in either the volume of the reactor to be built or the capacity of the system [153, 154].

The *RTD* has been obtained by introducing a pulse of a passive scalar, in which the scalar (θ) is being transported along the fluid. Once the transport equation has been divided by ε_g, the governing equation is as follows:

$$\frac{\partial \theta}{\partial t} + \nabla \cdot (\mathbf{u}\theta) - \nabla^2 \left(\frac{\mu_f}{\rho_f} \theta \right) = 0 \tag{4.27}$$

The most common ways to conduct simulations to determine *RTD* are based on injecting a tracer as a pulse or step [1]. The ideal pulse has the limitation of needing to integrate the amount of tracer over a very short period of time. The step approach simplifies the data treatment and increases reproducibility, as the injected quantities are known. A step experiment as the one shown in Figure 4.29 has been run for each simulation and flow rate under study. As spouted beds tend to have short residence times, the injection has been kept during a preset amount of time (relatively short) depending on the inlet flow rate, i.e., until the output concentration is stable for all configurations. Once this time has elapsed, the inlet

passive scalar value has been dropped to 0 again, and a second RTD curve (inverse step) has been obtained as the scalar is leaving the reactor. Given that the inlet passive scalar injection is 1 unit, the output concentration is directly the $F(t)$ curve, which can be transformed through Equation 4.28 to obtain the $E(t)$ curve shown in Figure 4.30.

$$F(t) = \frac{C(t)}{C_0} = \int_0^t E(t)dt \tag{4.28}$$

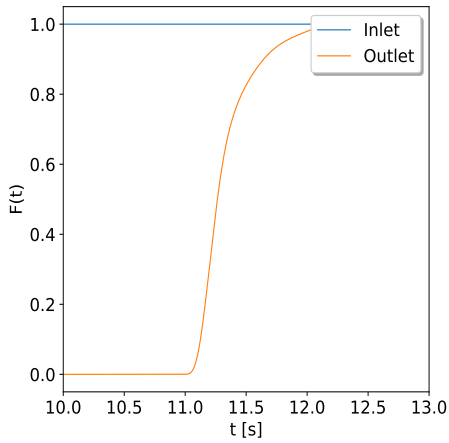

Figure 4.29. Simulated passive scalar step experiment to obtain the $F(t)$ curve.

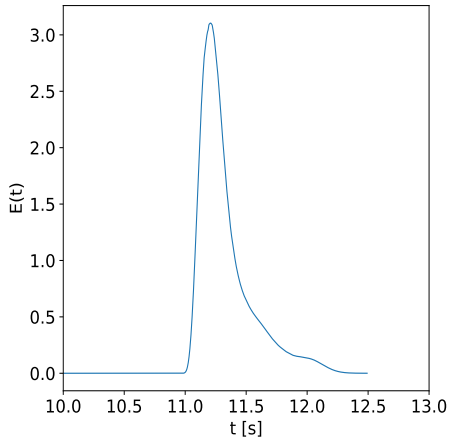

Figure 4.30. Simulated passive scalar $E(t)$ curve at the reactor outlet.

In order for the solution of the passive scalar to be bounded in the $[0-1]$ range, a linear discretization scheme has not been applied, but $\nabla \cdot (\phi\theta)$ has been treated

by a limited van Leer discretization scheme [155], which gives a second order accurate solution while maintaining a bounded solution by applying a flux limiter [156, 157]. This way, the F curves shown in Figure 4.31 can be obtained and, by deriving these curves, also the more useful E curves are obtained. Given that these curves are dependent on the specific flow rate applied to the system, they have been plotted against the dimensionless time Θ defined as follows:

$$\Theta = \frac{tV_r}{Q_i} \tag{4.29}$$

where V_r is the reactor volume and Q_i the volumetric inlet flow rate. This definition allows comparing F and E curves from different configurations and flow rates.

The RTD are only displayed to a maximum of 5Θ in Figure 4.31, as this has been considered a reasonable time to reach steady state, with the gas having enough time to disperse and mix. The first thing to notice is that some F curves at high flow rates in the $OSDT$ configuration and all flow rates in the SDT configuration do not reach the inlet tracer concentration of 1 for the reasonable time assumed. This behavior is believed to be related to the use of draft tubes, which, at these flow rates, increase shear force in the spout region, thus hindering the radial distribution and trickling of the gas through the annular section. In the WDT configuration, Figure 4.31a, the use of low and moderate flow rates 1.1-1.25u_m creates a single distribution of the gas phase, but, as the flow rate is increased, a second population of gas volume elements appears. When particle size is decreased, the same trend is observed, Figure 4.31b, with a bi-modal distribution of the gas E curve suggesting two distinctive populations at the outlet of the reactor. When the $OSDT$ configuration is used at low flow rates, a similar single gas residence time is observed, but high flow rates lead to gas bypassing through the spout, which is clearly evidenced by the first peak of the E curve, Figure 4.31c. This latter behavior is observed for all flow rates in the SDT configuration, Figure 4.31d, with almost no effect of the flow rate on the E curve other than reducing the outlet tracer concentration as the flow rate is increased.

Once the E curves have been obtained for all configurations, the mean gas residence times ($\bar{\Theta}$) are calculated as follows:

$$\bar{\Theta} = \frac{\int_0^\infty \Theta E(t)dt}{\int_0^\infty E(t)dt} \tag{4.30}$$

In addition, the variance (σ_t^2) can be obtained from the aforementioned RTD functions through Equation 4.31. These parameters give an idea of the deviation of the

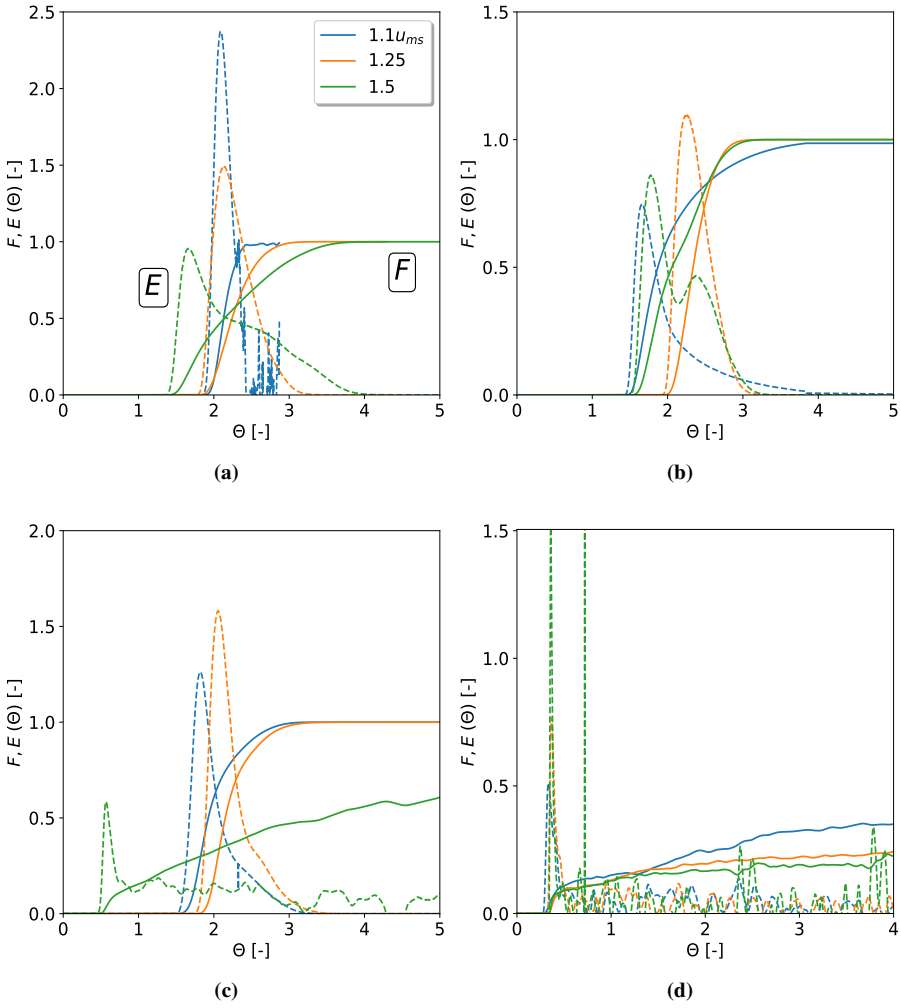

Figure 4.31. RTD evolution for the *WDT* configuration with (a) $\bar{d}_p$=4 *mm* and (b) $\bar{d}_p$=2 *mm* glass beads, and for (c) *OSDT* and (d) *SDT* configurations with $\bar{d}_p$=4 *mm* glass beads, in the conical spouted bed at different flow rates.

system from the ideal models of plug flow or ideal mixing regime and, furthermore, give hints of dead zones and gas back-mixing [158]

$$\bar{\sigma_g^2} = \frac{\int_0^\infty \Theta^2 E(t)dt}{\int_0^\infty E(t)dt} - \bar{\Theta}^2 \tag{4.31}$$

Figure 4.32a shows the evolution of $\bar{\Theta}$ with the type of configuration and flow rate.

As expected, as the input flow rate is increased, the mean residence time decreases for most configurations, except for $\bar{d}_p$=4*mm* glass beads in the *WDT* configuration, where the gas phase is able to trickle through the bed (specifically the annulus) as the air flow rate is increased, thus creating a wide distribution leading to an increase in the average residence time. This increase in the distribution width is shown in the evolution of the variance in Figure 4.32b, where the *WDT* configuration with 4 *mm* glass beads starts with a very narrow *E* curve (small variance) and widens as the flow rate is increased. Overall, 4 *mm* particles tend to have a lower mean dimensionless residence time than the 2 *mm* ones and, as the flow rate is increased, this value steadily drops. However, this drop in the mean residence time is accompanied by a widening in the distribution, as some portion of the gas entirely by-passes the bed through the spout, while the remaining fraction takes the tedious path through the annular zone.

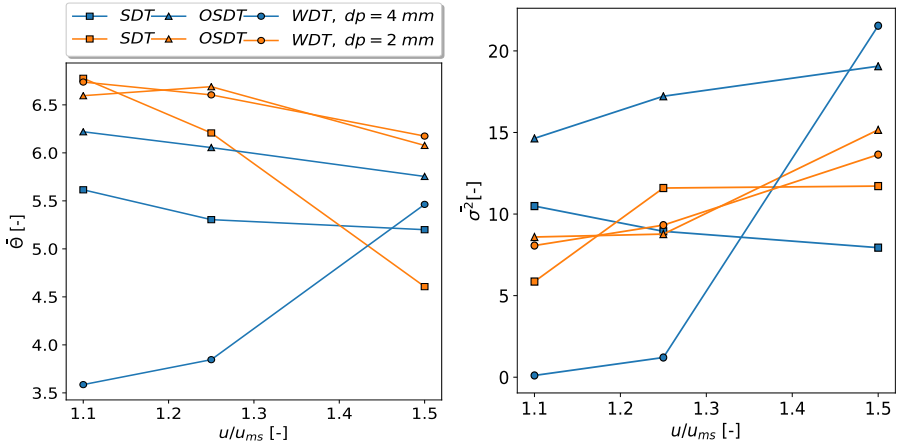

(a) **(b)**

Figure 4.32. Change in the (a) mean residence time and (b) variance with gas flow rate and configuration for $\bar{d}_p$=4 *mm* and $\bar{d}_p$=2 *mm* particles.

5 Simulation of superquadrics in spouted beds

Conducting simulations in industrial applications sometimes requires the shape of the particles to be taken into account, as irregular particles cover most of the applications of reasonable significance in the pharmaceutical [159], petrochemical [84], exploration-mining [160] and energy industries [5, 161]. Some authors have made significant strides in the description of these systems based on multi-sphere [129] and polyhedral approaches [58]. However, the solid description through a continuous function like a superquadric equation has some advantages, such as great shape flexibility and computational speed. Considering these advantages, the superquadric approach will therefore be used in this chapter to study the behavior of irregular solids in spouted beds.

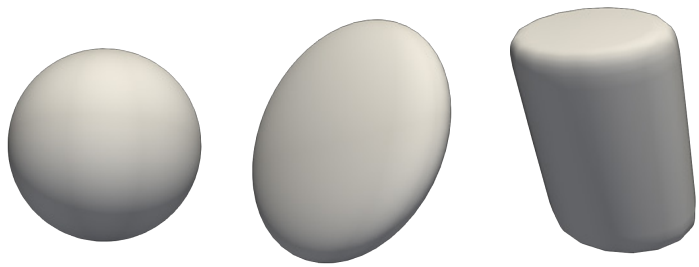

(a) (b) (c)

Figure 5.1. Superquadric representation of a (a) sphere, (b) ellipsoid and (c) pellet.

As shown in Figure 5.1, superquadric (SQ) particles cover a wide range of solids [99] from spheres (Figure 5.1a) to ellipsoids (Figure 5.1b) and pellets (Figure 5.1c).

5.1 Obtaining DEM parameters

Unlike spherical particles, studies dealing with *SQ* particles are rather scarce in the literature. Therefore, *DEM* parameters need to be carefully calibrated for each particle shape and size under study. The usual ways to calibrate these parameters are through bulk calibration approaches, such as penetration tests, static angle of repose, dynamic angle of repose in a hoper/silo discharge, load displacement test, in-situ shear test and artificial neural networks with angle of repose and shear test [97, 162].

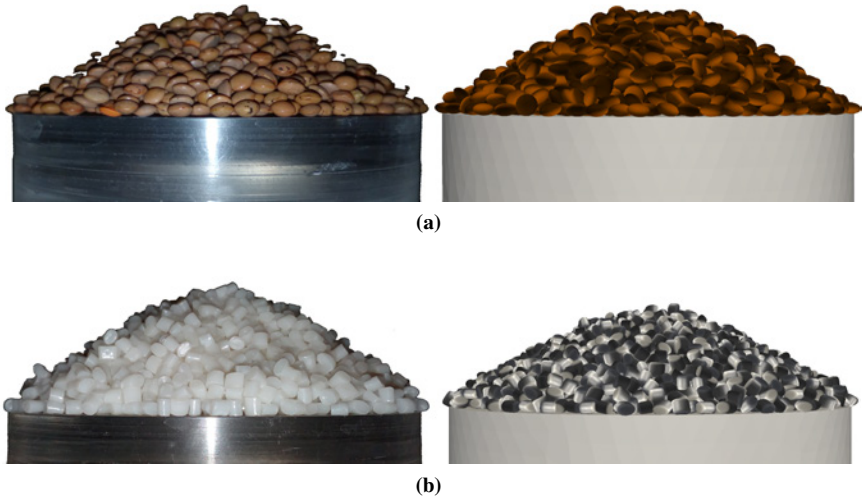

Figure 5.2. Comparison between experimental and simulated heap formation of lentils (a) and ABS pellets (b).

The static angle of repose test is the most straightforward method for the particle sizes under study. In the case of lentils, the blockiness values are kept at spherical values, whereas the main dimensions (r_x, r_y, r_z) are set to the average particle size. As shown in Table 5.1, the blockiness values for *ABS* pellets are set as $n_1 = 2$ and $n_2 = 8$ in order to capture the relatively sharp edges of pellets that affect the rolling and packing of particles. The relevant literature shows that values of $n_2 > 8$ do not have significant effect on the packing and rheological properties of *SQ* particles [99]. Furthermore, in order to accelerate simulation times, the particle stiffness

Table 5.1. Particle physical properties and *SQ* representation.

Parameter	Lentils	ABS Pellets
Particle density, ρ_s [$kg\ m^{-3}$]	850	1120
Young Modulus, E [MPa]	75	60
Poisson's Ratio, ν [-]	0.22	0.22
$\bar{r_x}$ [m]	0.00225	0.0011
$\bar{r_y}$ [m]	0.00127	0.0017
$\bar{r_z}$ [m]	0.00225	0.00135
Blockiness, n_1 [-]	2	2
Blockiness, n_2 [-]	2	8

defined by Young modulus (E) is reduced a couple of orders of magnitude below the real one, as this hardly changes particle behavior and allows for higher time steps [163]. The experiments to determine static angle of repose are run in triplicate and the resulting values are compared with those obtained in the simulations (heaps formed by the angle of repose), Figure 5.2. The angles of repose that best fit the experimental heaps are determined, and they are used to determine the *DEM* parameters, Table 5.2, which are taken as inputs for the *CFD-DEM* simulations.

Table 5.2. *DEM* parameters for *SQ* particles.

Parameter	Lentils	ABS Pellets
Particle-particle restitution coefficient, $k_{p,p}$	0.91	0.9
Particle-wall restitution coefficient, $k_{p,w}$	0.95	0.92
Particle-particle friction coefficient, $\gamma_{p,p}$	0.31	0.36
Particle-wall friction coefficient, $\gamma_{p,w}$	0.4	0.45
Rolling friction, $\mu_{r,f}$	0.05	0.06
Damping coefficient of rolling friction, $\gamma_{r,f}$	0.1	0.1

5.2 Drag models for irregular particles

As already shown for spherical particles, the drag force plays a major role in fluid-particle contact, and hence must be taken into account when simulating the spouting of irregular particles. In addition, the use of irregular particles introduces shape anisotropy, which leads to greater pressure drop than their spherical counterparts, as elongated biomass particles, such as straw or rice husk, lace with each other, and therefore increase bed resistance [102]. This increase in pressure drop due to particle shape is partially responsible for the unstable fluidization of irregular and elongated materials, specially when low density particles are handled. Spouted beds, however, have the advantage of relying on a central preferential

path to operate, and therefore are relatively impervious to particle shape, with slight to moderate changes in operating regimes and characteristics of the spouting behavior when irregular particles are used.

This change in bed behavior is derived from the solid-solid interlocking related to particle shape and, especially, from the deviation of gas-solid drag models from the experimental trend for irregular particles. In order to fill this gap, a number of correlations have been proposed, albeit fewer and only applicable in narrower Reynolds ranges than those for spherical counterparts. One of the first correlations for slightly irregular particles was proposed by Haider & Levenspiel [164], with corrections based on sphericity (ϕ), which were obtained for a limited number of shapes-regimes, with low accuracy, specially for particles of low sphericity [165].

An overview of the most common and recent drag models for irregular particles has been published by Ullah et al. [166]. Most correlations account for the shape of the particles by either the previously mentioned sphericity or by parameters dependent on the main shape dimensions, i.e., length (L), height (I) and width (S), which are used to compute the flatness value (f) by Equation 5.1 or elongation value (e) by Equation 5.2 [167].

$$f = \frac{S}{I} \tag{5.1}$$

$$e = \frac{I}{L} \tag{5.2}$$

The drag models used in this study for irregular particle simulations are shown in Table 5.3.

Table 5.3. Gas-solid drag models for irregular shaped particles.

Reference	Equation
Hölzer and Sommerfeld [168]	$C_D = \frac{8}{Re\sqrt{\phi_{\parallel}}} + \frac{16}{Re\sqrt{\phi}} + \frac{3}{\sqrt{Re}\phi^{3/4}} + 0.421^{0.4(-log\phi)^{0.2}} \frac{1}{\phi_{\perp}}$ (5.3) $\phi = \frac{\pi d_{eq}^2}{\frac{8 r_x r_y r_z}{n_1 n_2} B\left(\frac{1}{n_1}, \frac{2}{n_1}+1\right) B\left(\frac{1}{n_2}, \frac{1}{n_2}+1\right)}$ (5.4) $\phi_{\perp} = \frac{\pi d_{eq}^2}{4\Psi_{\perp}}$ (5.5)

Table 5.3. (continued)

	$\phi_{\parallel} = \frac{\pi d_{eq}^2}{4\left(\frac{4r_x r_y r_z}{n_1 n_2} B\left(\frac{1}{n_1}, \frac{2}{n_1}+1\right) B\left(\frac{1}{n_2}, \frac{1}{n_2}+1\right) - \Psi_{\parallel}\right)}$ (5.6)
Sanjeevi [169]	$C_{D,\lambda} = C_{D,\lambda=0^o} + (C_{D,\lambda=90^o} - C_{D,\lambda=0^o}) sin^2\lambda$ (5.7) $C_{D,0^o,90^o} = \left(\frac{a_1}{Re} + \frac{a_2}{Re^{a_3}}\right) e^{-a_4 Re} + a_5(1 - e^{-a_4 Re})$ (5.8)
Diouguardi et al. [170]	$C_D = \frac{24}{Re_t}\left(\frac{1-\psi}{2}+1\right)^{0.24} + \frac{24}{Re_t}(0.1806 Re_t^{0.6459})\psi^{0.08 Re_t} + \frac{0.4251}{1+\frac{6880.95}{Re_t}\psi^{5.05}}$ (5.9) $Re_t = \frac{u_t \rho d_p}{\mu}$ (5.10)
Bagheri & Bonadonna [171]	$C_D = \frac{24\kappa_S}{Re_s}[1 + 0.125(Re\kappa_N/\kappa_S)] + \frac{0.46\kappa_N}{1+\frac{5330}{Re_s\kappa_N/\kappa_S}}$ (5.11) $\kappa_S = (F_S^{1/3} + F_S^{-1/3})/2$ (5.12) $\kappa_N = 10^{\alpha_2[-log(F_N)]^{\beta_2}}$ (5.13) $\alpha_2 = 0.45 + 10/(e^{(2.5 log\rho')} + 30)$ (5.14) $\beta_2 = 1 - 37/(e^{(3 log\rho')} + 100)$ (5.15) $F_S = f e^{1.3}(d_{eq}/LIS)$ (5.16)

Table 5.3. (continued)

	$F_N = f^2 e(d_{eq}^3/LIS)$	(5.17)

Hölzer and Sommerfeld [168] developed a drag model that takes into account the shape and the fluid-solid relative orientation along the longitudinal and parallel projected surfaces. There is no limitation in the application of this correlation in terms of shape or *Re* number, and has been widely used in the literature. However, it has been reported that this correlation, shown in Equation 5.3, tends to under-predict the influence of the orientation, along with over-predicting the drag force when particles are aligned with the flow [172].

Sanjeevi et al. [169] developed a drag model based on Lattice-Boltzman *LB* simulations giving as a result Equation 5.7, following the expression proposed by Zastawny et al. [172], Equation 5.8, in which a_i parameters are fitting parameters corresponding to the shapes taken into account in each particular case.

Finally, the last type of irregular shape solid drag force is the one by Diauguardi et al. [170], who improved the correlation given by Bagheri et al. [171] shown in Equation 5.11. Even though some authors [173] have raised doubts about the methodology proposed by Diauguardi et al. [170], their drag model shown in Equation 5.9 is reported to give comparable results to the one by Bagheri et al. [171], and has therefore been implemented in this study. This correlation requires an iterative calculation of the particle terminal velocity (u_t), which has been carried out following the information supported by Diauguardi et al. [170]. In addition to the terminal velocity, particle shape factor (ψ) must be obtained based on the followings equations:

$$\psi = \frac{\phi}{\xi} \tag{5.18}$$

$$\xi = \frac{P_{mp}}{P_c} \tag{5.19}$$

where ϕ is the particle sphericity and *xi* is the circularity coefficient defined following Equation 5.19, whilst P_{mp} is the maximum projection perimeter and P_c the perimeter of the circle equivalent to the maximum projection area of the particle [170].

All these correlations lead to different drag coefficients at varying flow-rates, as

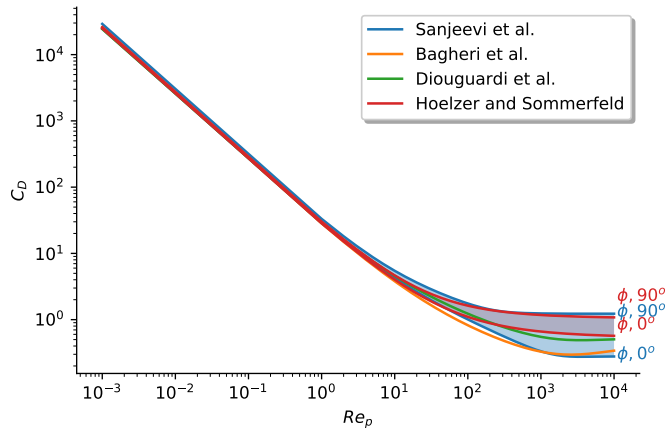

Figure 5.3. Evolution of the drag coefficient, C_D, at varying Re numbers for each drag model.

shown in Figure 5.3 for the ellipsoidal particles shown in Table 5.1. Depending on the orientation of each particle, drag values change, with the maximum drag values in the correlations by Sanjeevi et al. [169] and Hölzer and Sommerfeld [168] being when particles biggest face is normal to the flow. Furthermore, the range of drag coefficients predicted varies depending on the correlation under study, with the correlation by Hölzer and Sommerfeld predicting a narrower drag coefficient range than the one by Sanjeevi et al. The differences are greatest for $Re_p > 3000$. As shown in Figure 5.3, the models by Bagheri et. al [171] and Diouguardi et al. [170] do not depend on any orientation dependent variables, as they assume the most likely orientation a given particle is prone to have, and therefore develop a shape dependent C_D value at different Re_p values. These values fall closer to the correlation by Sanjeevi et al. than to the one by Hölzer & Sommerfeld at 0^o attack angle. Once these forces have been properly implemented, the drag model that best fits the simulation of irregular solids in conical spouted beds must be chosen.

5.2.1 Implementation of drag models

Although this section is mainly devoted to the selection of the drag force model of best fit for irregular material systems, and that most of the computational time is usually spent in the solid-solid collision algorithm, attention should also be paid to the implementation of solid-fluid forces in order to further reduce the computational overhead of the implemented models.

The first problem to be tackled is the fact that the information of solids is stored

within LIGGGHTS®memory space, whereas the drag force calculation is done by the *CFD* side. Thus, the communication has to optimized in order to minimize verbosity and excessive data transfer. Most drag models shown in Table 5.3 make use of solid properties, such as shape, size and blockiness. However, no changes in shape or size in a given particle are considered in these simulations. Implementation of these simulations may only be carried out by communicating all the dynamic data, such as velocity, location and angular momentum of each particle, along with the tag of the particle type (shape and size). At the first coupling step, all the shape and blockiness properties are communicated to the *CFD* domain and indexed in a particle type based index. After this first coupling has been accomplish, and unless another information is explicitly requested, only dynamic data and particle type are exchanged between LIGGGHTS®and OpenFOAM® . When forces are to be computed, the shape and blockiness values are obtained in a per type basis, which are readily available through the look-up table.

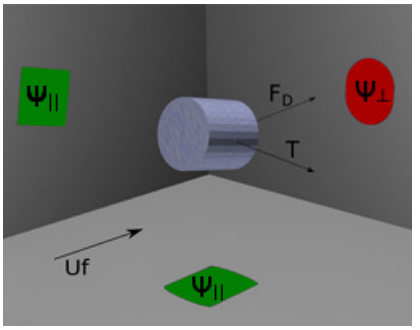

Figure 5.4. Shadow projection for a relative velocity vector.

When the model by Hölzer and Sommerfeld [168] is to be implemented, in addition to the shape of each of the particles already mentioned, the perpendicular ($\phi_{||}$) and parallel sphericities ($\phi_{||}$) have to be efficiently calculated. In the *CFD-DEM* coupling, only the final sphericities are transferred for each particle, and only three scalars must therefore be transferred, i.e., ϕ, $\phi_{||}$ and $\phi_{\perp}$. However, the calculation of each projected surface takes considerable time and is dependent on the orientation of the fluid velocity vector. In order to reduce computation time and enable constant computation time, each particle type is pre-processed before the *CFD-DEM* simulation begins. To that end, all the available particle types are checked throughout the domain and a look-up table of all the projection surfaces is created with the different particle types, following the procedure shown in Figure 5.4. These projections are stored in a two-dimensional table indexed by the first two angles (α_e and β_e) of the relative particle-velocity vector orientation Euler angles. This procedure is repeated for a [0-360^o] rotation of the particle along the first two axes, registering their projected areas. The tabulation of the third

Euler angle is not needed in these types of solids, as the surface projected by a superquadric particle does not change when the particle rotates along the third axis. Once the tables have been built for each particle type, they are broadcasted to all processors. This final step is crucial, as particles move through domains and processors when the simulation proceeds, and a particle type that might not have been initially present in a particular domain might be requested as it enters the domain from other processor.

At run time, a procedure is followed for each particle. Thus, the cell at which the particle is located is determined, after which the fluid velocity vector for this cell is stored and the relative quaternion between this vector and the particle is computed. After the particle-vector relative quaternion has been computed, the Euler angles corresponding to this quaternion are obtained. After which, a search is done in the table corresponding to its particle type and relative orientation, thus obtaining $\Psi_{\perp}$ and $\Psi_{\parallel}$. This procedure is conducted for all particles in each processor using Equations 5.4- 5.5. These three values will be the only additional data communicated to the CFD domain in order to obtain the drag force applying Equation 5.3 to each particle.

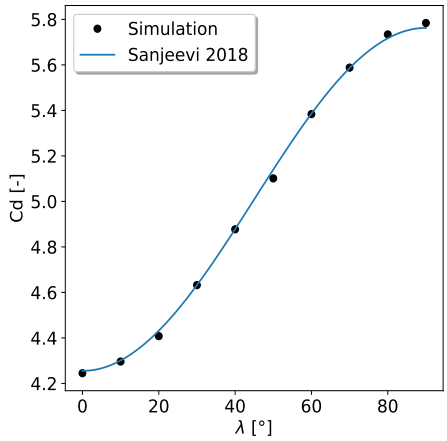

Figure 5.5. Drag coefficient of the model by Sanjeevi et al. for different attack angles.

In the model by Sanjeevi et al. [169], only the solid relative orientation is computed, which results in the drag profile shown in Figure 5.5. This Figure shows that for 0^o attack angle, for which the solid exposed surface is the lowest, the drag coefficient C_D is the lowest and increases in a sigmoid fashion until an attack angle of 90^o is reached, for which the maximum surface is exposed normal to the fluid. This relative orientation is obtained by computing the relative quaternion [174] between the solid and the fluid velocity vector. Finally, it is straightforward to infer that the implementation of the models by Bagheri & Bonadonna [171] and

Diouguardi et al. [170] only requires shape dependent values that can be computed at the first *CFD-DEM* coupling step and the stored values are subsequently used to set the final drag coefficient (C_D).

5.3 Implementation of additional forces

In addition to the drag force, other less influential forces have to be implemented in order to simulate the solid translational and rotational behavior.

5.3.1 Lift force

When an irregular particle is not completely aligned with the fluid flow direction, a lift force that has a perpendicular direction to the fluid velocity vector appears. Thus, when the fluid interacts with an irregular shaped solid, slight pressure differences are created normal to the air flow direction, giving as a result a lift force that does not require any specific fluid-solid relative orientation. The total lift force is determined by the following equation:

$$\mathbf{F_L} = \frac{1}{8}\pi C_L \rho_f |\mathbf{u_r}|^2 d_{eq}^2 \tag{5.20}$$

5.3.2 Pitching torque

Another force that is present when irregular solids are simulated is the pitching torque [172] derived from imbalances in the surface exposure of the solid relative to the fluid vector and to its center of mass [175]. This pitching torque is proportional to the angle at which the particle is orientated towards the flow. Furthermore, it has to decrease to zero at every multiple of $\pi/2$, as the surface exposed to the flow is the same at these angles, Figure 5.6.

The angle ϕ in Figure 5.6 refers to the angle of attack of the particle towards the fluid. It is calculated by computing the relative quaternion [161] between the relative fluid velocity vector ($\mathbf{u} - \mathbf{v_i}$) and the solid quaternion. This value is then used in Equation 5.21 [169] in order to obtain the pitching torque coefficient shown in Figure 5.7. The force magnitude is obtained based on Equation 5.22, in which the superquadric volume is used [176] to obtain the equivalent sphere diameter (d_{eq}).

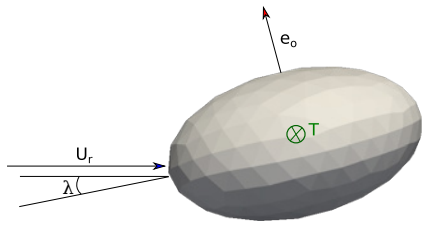

Figure 5.6. Graphical representation of the pitching torque in a spheroid and the relationship between vectors.

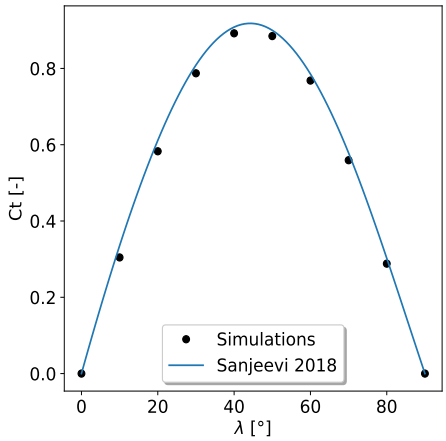

Figure 5.7. Torque coefficient at different angles of attack.

$$C_{T,\lambda} = \left(\frac{c_1}{Re^{c_2}} + \frac{c_3}{Re^{c_4}}\right) sin\lambda^{(1+c_5 Re^{c_6})} cos\lambda^{(1+c_7 Re^{c_8})} \tag{5.21}$$

$$\mathbf{F_T} = \frac{1}{16}\pi C_T \rho_f |\mathbf{u_r}|^2 d_{eq}^3 \tag{5.22}$$

However, the direction of the pitching torque can have multiple possible outcomes, as it only has to be normal to the relative velocity vector ($\mathbf{u_r}$). This way, a preferential orientation and rotation plane must be chosen in order to remove this restriction. In the current approach, a specific surface vector ($\mathbf{e_o}$) is chosen at the maximum surface projection direction and the particle orientates itself with the fluid in order for this vector to be normal to the fluid force. This behavior is accomplished by using Equation 5.23 to align the rotation vector towards this preferential orientation.

$$\mathbf{T} = |\mathbf{F_T}| \frac{(\mathbf{u_r} \cdot \mathbf{e_o})}{\|\mathbf{u_r} \cdot \mathbf{e_o}\|} \frac{(\mathbf{u_r} \times \mathbf{e_o})}{\|\mathbf{u_r} \times \mathbf{e_o}\|} \tag{5.23}$$

5.3.3 Void fraction treatment

The correct description of the void fraction is essential for an accurate representation of the force a fluid volume exerts on a particle, as local deviations from the experimental values of void fraction induce unrealistic over-packing of the bed, and hence deviation of the drag force from real values [177]. In regular materials, the divided void fraction model for spherical particles is used in order to split each particle into 29 slices of the same volume. The computation is run in order to determine the location of each particle slice, and the resulting particle volume is added to the cell [178].

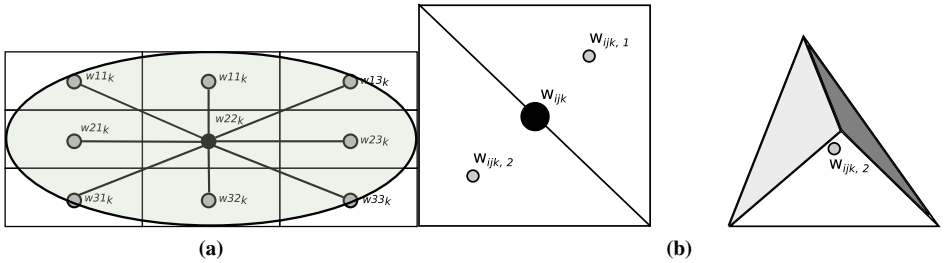

Figure 5.8. Ellipsoidal particle with (a) the superimposed volume stencil and (b) the tetrahedral weighting decomposition of each node.

In order to compute the void fraction for superquadric particles, a simplified shape void fraction model has been implemented in this work [179, 180]. To that end, the default void fraction model has been overloaded with a model that precomputes a stencil like that shown in Figure 5.8a, which is a generalization of the approach taken by Liu et al. [98] for convex superquadrics of varying blockiness values. This stencil is kept in relative dimensions ([0-1]) in case a particle of the same type but different scale enters the domain and is able to use the same stencil. The stencil is represented in $3D$ by 27 nodes in the current implementation and the local superquadric equation is computed (Equation 1.28) at every point. Each node in turn is split into a number of sub-nodes (Figure 5.8b). At the beginning of each simulation, the weight of the node $W_{i,j,k}$ is computed through $W_{i,j,k,1}$ and $W_{i,j,k,2}$ tetrahedral centroids, where the superquadric local equation is computed and the weights of the nodes are determined. Once the weight of every node has been computed for each particle type, this weighted-stencil is used at run time for the void fraction calculation.

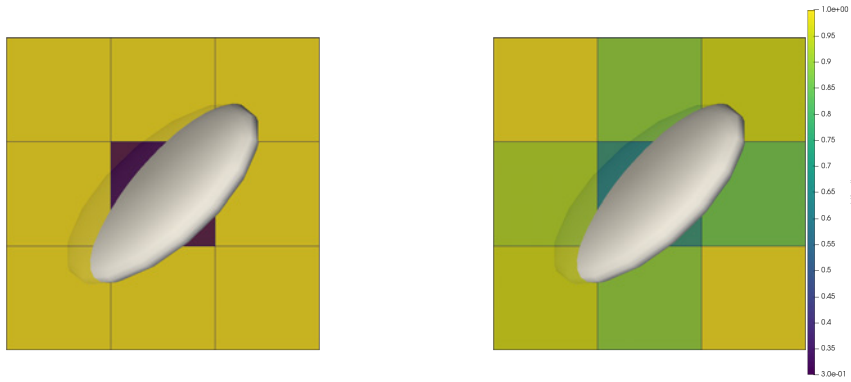

(a) **(b)**

Figure 5.9. Particle volume distribution according to (a) center void fraction model and (b) divided void fraction model.

At run-time, each stencil is translated and rotated according to the particle under study. A hierarchical approach is taken for the void fraction computation, where the eight outermost node locations are computed first and, if any of them happens to fall in a different cell, all the remaining 17 stencil points are checked in order to add their volumes to the corresponding cells. In case all the outermost particles fall in the same *CFD* cell, the remaining nodes do not need to be computed and are assigned to the same cell. This way, a void fraction as the one shown in Figure 5.9a is spread through the neighboring cells according to the particle orientation and size in order to obtain the void fraction field shown in Figure 5.9b.

5.4 Solid velocity profiles of superquadrics

The fist comparison to be made is between the drag model by Beetstra [140], based on the equivalent volume model, and orientation dependent drag models shown in Table 5.3. Figure 5.10 compares the experimental velocity profiles and those obtained with the different drag models, for all the different configurations used in the conical spouted bed.

As shown in 5.10a, corresponding to the *WDT* configuration, as expected, all the models predict a sudden acceleration of the particles with a maximum value at a position close to the surface of the bed. However, given that the accuracy in the prediction is different depending on the model, the most suitable drag model

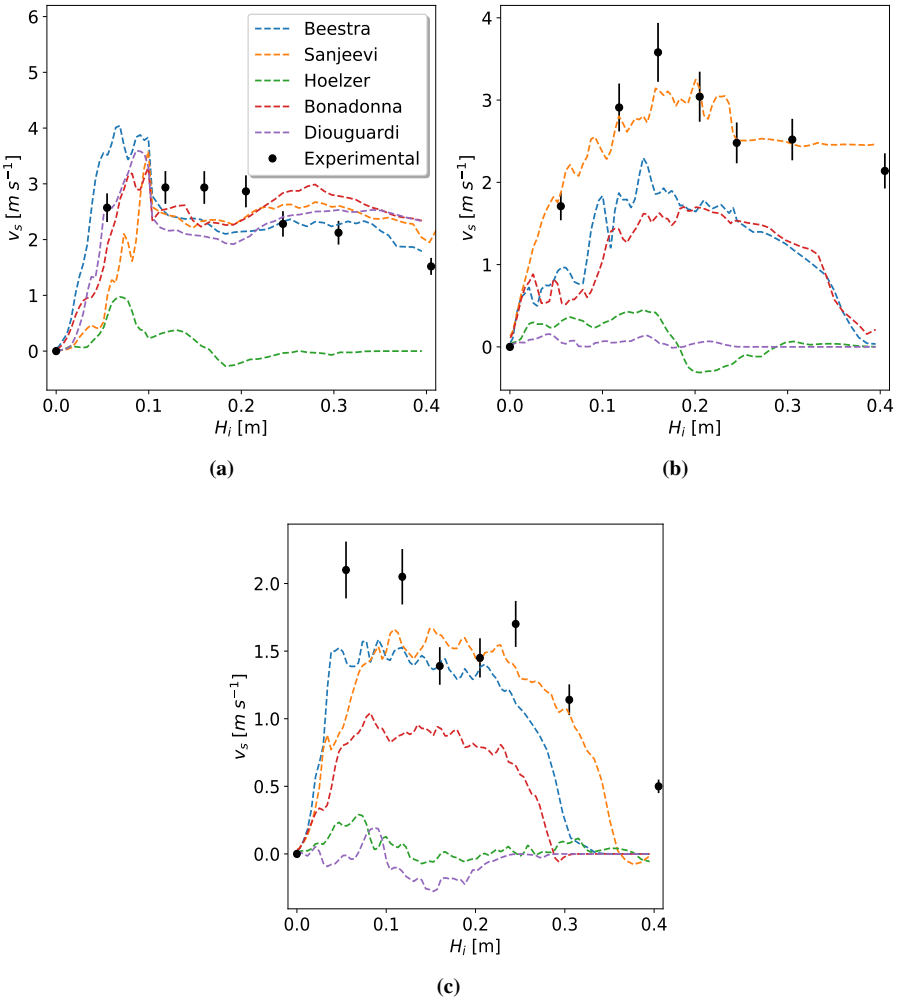

Figure 5.10. Comparison of drag models for irregular particles in conical spouted beds for the configurations of (a) WDT, (b) $OSDT$ and (c) SDT, at $1.25u_{ms}$.

for this particular application should be chosen. The model by Beetstra [140], based on the volume equivalent diameter, shows a significant deviation from the experimental data, over-predicting the solid velocity of particles at the lower end of the spout. This trend is reduced when internal devices are used, as they need lower fluid flow rates for operation, which leads to flatter solid velocity profiles, Figures 5.10b-5.10c. In fact, this deviation is significant enough to make use of irregular solid drag models in every configuration under study.

Although the model by Höelzer et al. [168] has been widely used with no theoretical shape limitations, it does not correctly predict solid velocity, as it clearly underpredicts velocity values. When the *OSDT* configuration is used, Figure 5.10b, the model of best fit is clearly the one by Sanjeevi et al. [169]. The model by Beetstra [140] gives similar results to those by Bagheria & Bonadonna [171], i.e., with a slight under prediction of solid velocity in the whole axial length. In the case of the *SDT* configuration, Figure 5.10c shows that similar results are again obtained with the models by Sanjeevi et al. [169] and Beetstra [140], and the former may therefore again be considered as the model of best fit. Bagheri & Bonaddona model again underpredicts the solid velocity for this configuration. In short, Figures 5.10a-5.10c show that the model by Sanjeevi et al. provides the best predictions, which is cosistent with the fact that this correlation was obtained for fibers and ellipsoids.

Once the irregular particle drag model has been chosen, it has been used with all the configurations and all flow rates in order to asses the prediction capabilities when different flow rates are employed. Figure 5.11 shows the fitting of each configuration. When the *WDT* configuration is used, the axial velocity at low flow rates is slightly under-predicted, which leads to lower fountain heights than the experimental ones. However, at higher flow rates (1.25-1.5u_{ms}), predictions are considerably better, which might be due to the influence of frictional coefficients at low flow rates, whose influence is reduced as the air velocity is increased. Considering the low particle density of lentils (850 $kg\ m^{-3}$), the simulated profiles resemble those of the *SDT* configuration for glass beads. However, the value at the first height (5 cm) in Figure 5.11a is not properly predicted, as experimental particles accelerate at a higher rate than the simulated ones, and the experimental velocity values at $\sim 5\ cm$ are therefore higher than those expected.

Figure 5.11b compares experimental and simulated axial velocity values for *OSDT* configuration. As observed, low flow rates are much better predicted than in the *WDT* configuration. In addition, the first measurement point is properly predicted, which is evidence of a correct particle acceleration in the simulations. However, at high flow rates particle velocity is slightly under-predicted at the lowest measurement points, but overall acceptable solid velocity profiles are obtained.

For the *SDT* configuration shown in Figure 5.11c, the simulated profiles are slightly over-predicted, which considering the whole trend observed in Figures 5.11a-5.11c might be due to a deviation in the estimation of the draft tube frictional coefficient.

Along with the axial profiles, the radial profiles complement information about particle circulation rate. Furthermore, in the case of irregular materials, these pro-

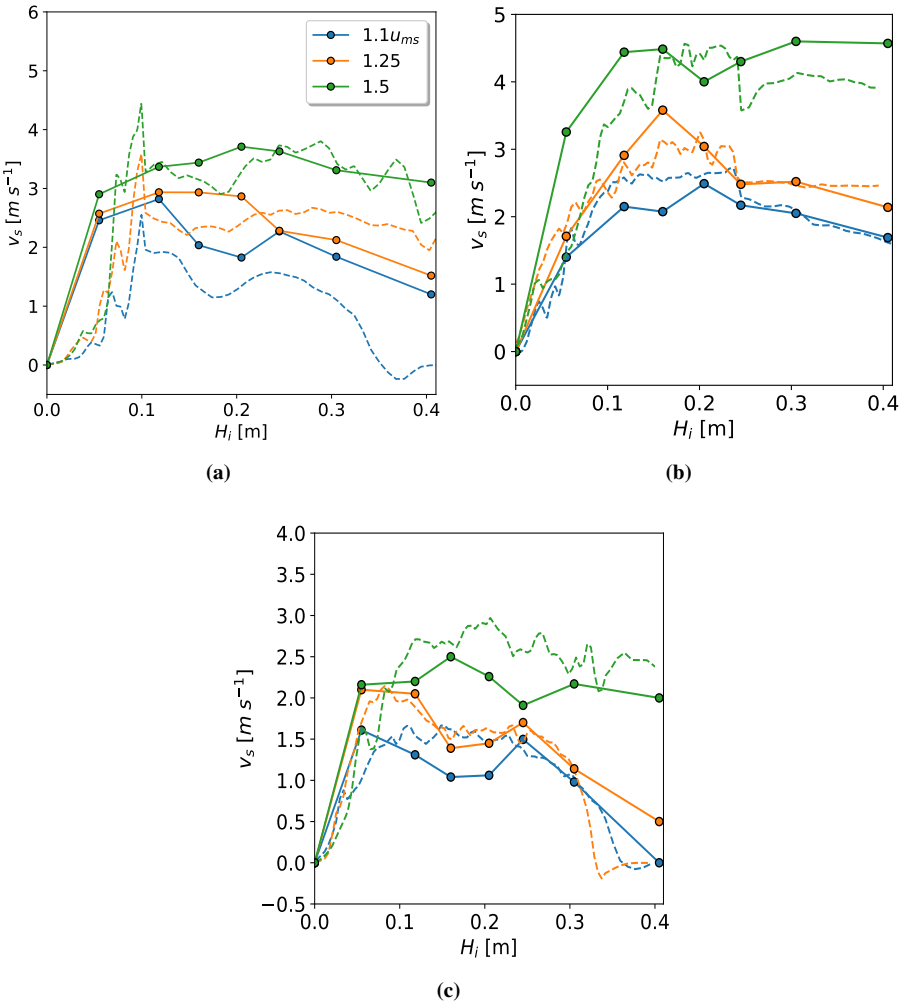

Figure 5.11. Comparison of *CFD-DEM* (dashed lines) and experimental data under different hydrodynamic regimes (u_{ms}) for lentils in the configurations of (a) *WDT*, (b) *OSDT* and (c) *SDT*.

files become especially important, as irregular particles do roll when descending, and therefore result from a balance between the convective movement and friction of solids with walls. To that end, Figure 5.12 shows the radial profiles determined using Sanjeevi et al. [169] drag model and the friction values shown in Table 5.1.

Radial models follow the trend shown for regular particles with the maximum solid velocity being located at the axis of the reactor (r_i/r_{Max}=0). Similarly as in

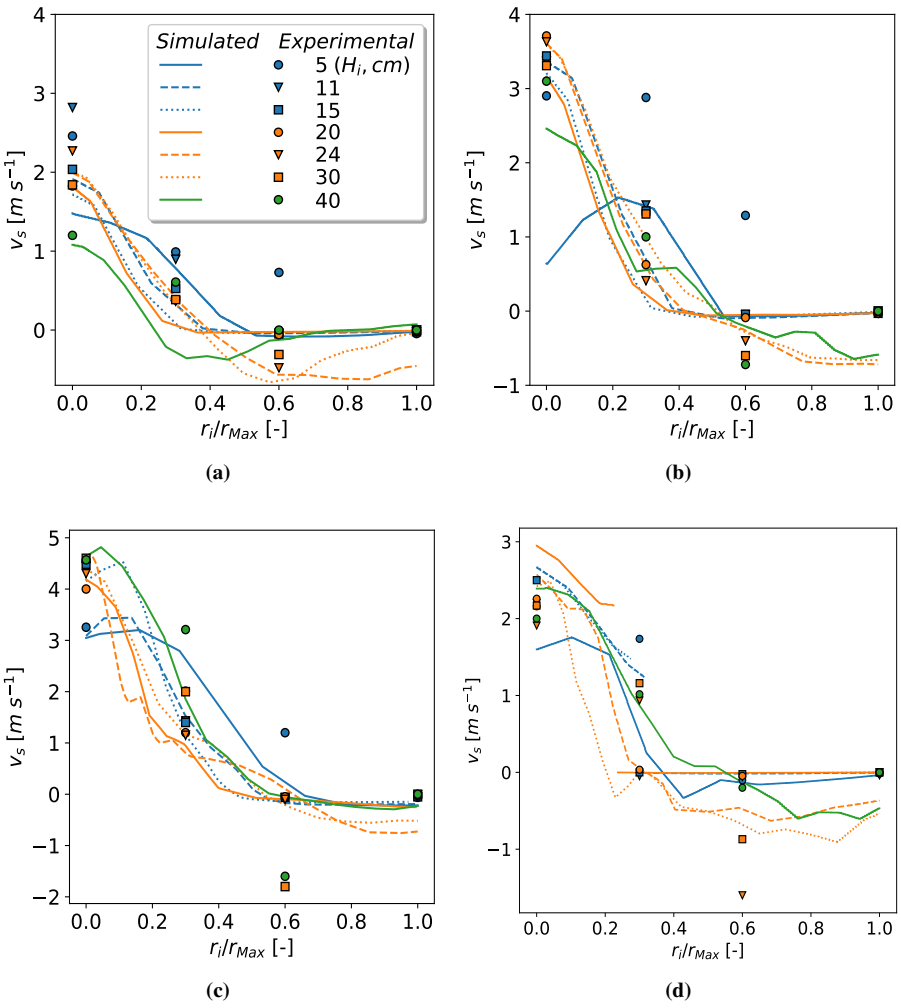

Figure 5.12. Radial *CFD-DEM* (dashed-lines) and experimental solid velocity profiles for lentils in conical spouted beds, for the systems (a) *WDT* ($1.1u_{ms}$), (b) *WDT* ($1.5u_{ms}$), (c) *OSDT* ($1.5u_{ms}$) and (d) *SDT* ($1.5u_{ms}$).

the case of axial profiles, the radial profiles also evidence a lower accuracy of the models at low flow rates for *WDT* configuration, Figure 5.12a. For this configuration and low flow rates, the model by Sanjeevi et al. provides a rather poor prediction in the spout zone, while those points at further radial positions fall close to the experimental values, except those at the height of H_i=5 *cm*, where the model predicts a narrower spout section than the one observed in the experiments. As the flow rate is increased, Figure 5.12b ($1.5u_{ms}$), the model consistently follows the

trend observed in the experimentation, with a correct prediction of the spout size.

In the case of the *OSDT* configuration, the radial solid velocity profiles at ($1.5u_{ms}$), Figure 5.12c, are reasonably close to the experimental values, including those at 5 cm, which suggests that the presence of a draft tube heavily influences the spout shape, as the experimental and simulated trends locate the beginning os the spout around the draft tube diameter at this height. The effect of the internal device is more noticeable in the *STD* configuration, Figure 5.12d, with the draft tube wall clearly limiting the spout expansion, and therefore the solid velocity. In this configuration, the model follows the experimental data reasonably well, with a few outliers in the fountain solid descend velocity (H_i=24 cm, r_i/r_M=0.6).

In the case of the prismatic spouted bed, the simulated values follow the trend of the experimental values, Figure 5.13. The greatest deviation in the axial profiles, Figure 5.13a is encountered for pellets, as the simulated values predict a maximum velocity at a higher height than what is seen in the *PTV* data. In the case of the spheres, the simulation shows a good agreement with the experimental data, albeit there is a slight over-prediction of solid velocities at H_i=0.075 m. The *CFD-DEM* simulations follow roughly the experimental trend for lentils, with velocity being approximately constant for a considerable height range, and then decreasing due to the their loss of momentum by various dissipation methods.

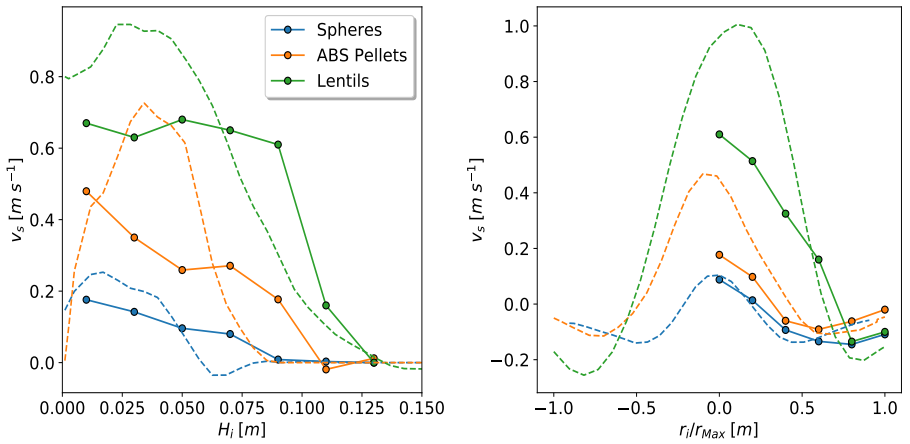

Figure 5.13. Comparison of experimental solid velocities (solid points) and simulated data (dashed lines) for the (a) axial and (b) radial solid velocities in the prismatic spouted bed for various materials at $1.5u_{ms}$.

The simulated radial solid velocity profiles, Figure 5.13b, show the same wall ef-

fect observed in the experimental observation for the three materials. However, as observed in the axial profiles, the velocity magnitudes are considerably higher than the experimental values in the spout.

5.5 Minimum spouting velocity of irregular particles

Minimum spouting velocity, as previously stated, is used as a reference for the minimum operation requirements and base operating cost of a given spouting process. However, in the case of irregular particles, this parameter is of especial relevance, as these particles and, specially those of high aspect ratio, have a much higher minimum spouting velocity than their spherical counterparts [109]. Accordingly, the experimental minimum spouting velocity values are compared with the values obtained through the simulations in Figure 5.14.

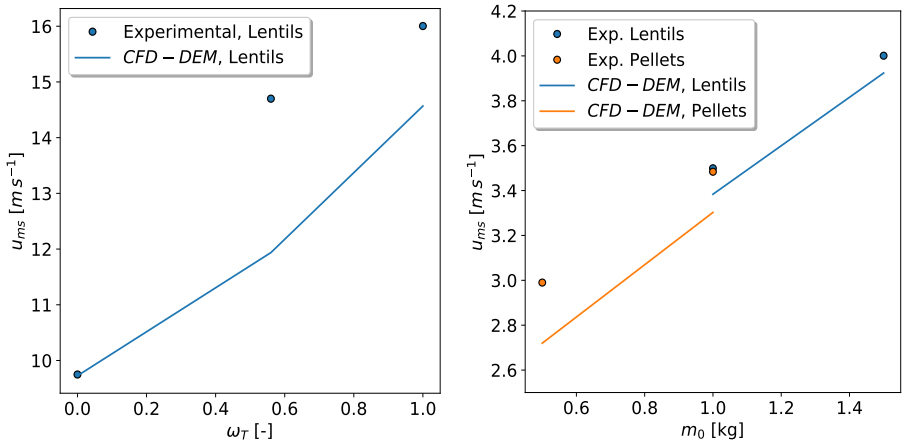

Figure 5.14. Experimental vs. *CFD-DEM* simulation values for the minimum spouting velocities of lentils in the (a) conical and (b) prismatic spouted bed.

Figure 5.14a shows the evolution of the experimental u_{ms} values for lentil beds when changing the internal device (aperture ratio), and compares their trend with those obtained through simulations. The error falls below 10% with the maximum deviation encountered at the *WDT* configuration, as the bed is more influenced by the particle-particle internal friction and the spouting regime is not improved by

any internal device. When these particles are put into a prismatic spouted bed, Figure 5.14b, the simulation results accurately fit the experimental ones.

5.6 Pressure spectral analysis for superquadrics

The pressure drop of a bed is directly related to the operating cost of the unit. Biomass in general tends to have a lower particle density, and hence a lower pressure drop across the bed. However, the irregular shape of such materials requires the correction of pressure drop equation by accounting for this irregularity in the simulation, which leads to the fit shown in Figure 5.15a for the conical spouted bed. The non-resolve nature of the current *CFD-DEM* make pressure drop values slightly differ from the experimental values. Overall, there is an acceptable deviation between simulation and experimental values, even when the contactor geometry is changed and a prismatic spouted bed is used, Figure 5.15b.

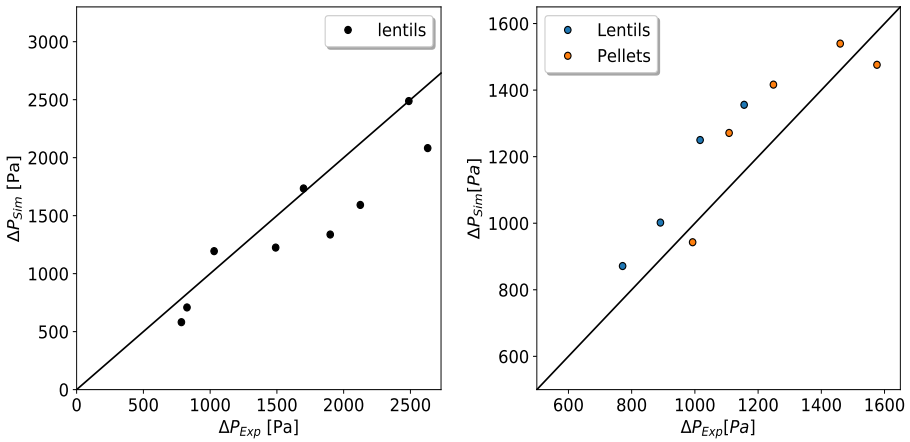

(a) **(b)**

Figure 5.15. Parity plot of the experimental and simulated values of the nominal pressure drop for the (a) conical spouted bed and (b) prismatic spouted bed.

The use of these models allows for the simulation of the prismatic spouted bed for lentils and pellets, with pressure drop falling again within acceptable values for both materials. In addition to the average pressure drop values, the FFT analysis of these signals, Figure 5.16, may give some insight into the spouting stability and on the use of this technique in order to simulate the process at various flow rates and configurations.

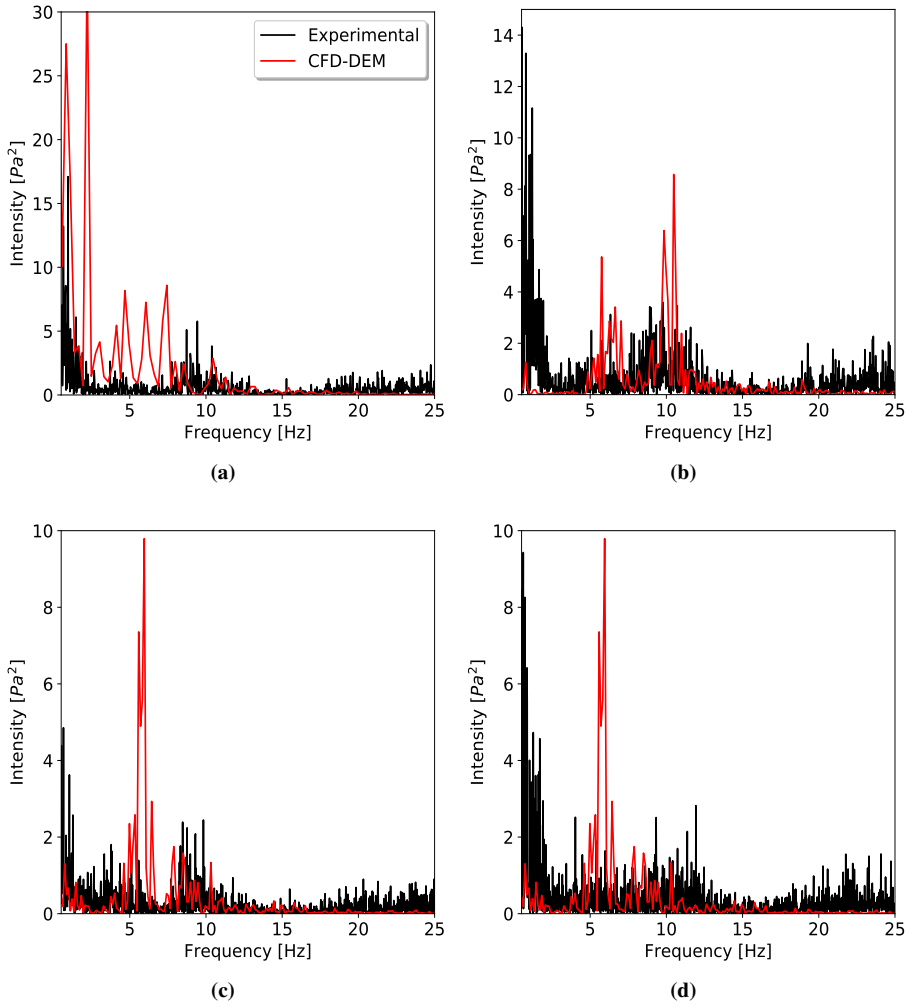

Figure 5.16. Experimental and simulated FFT spectra of pressure drop fluctuations of lentil beds in the WDT configuration at the flow rates of (a) $1.25u_{ms}$, (b) $1.5u_{ms}$ and in the $OSDT$ configuration at the flow rates of (c) $1.25u_{ms}$ and (d) $1.5u_{ms}$.

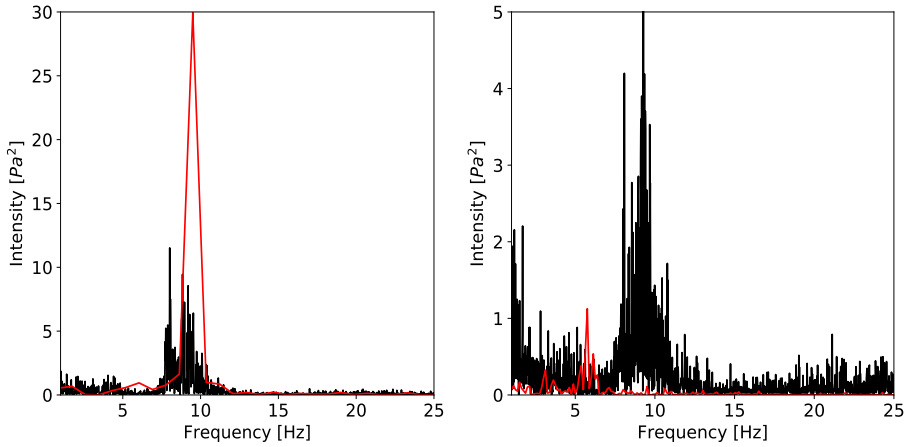

Figure 5.16. (continued) Experimental and simulated FFT spectra of pressure drop fluctuations of lentil beds in the the SDT configuration at the flow rates of (e) $1.25u_{ms}$ and (f) $1.5u_{ms}$.

In the case of the WDT configuration, Figures 5.16a-5.16b, the experimental FFT spectra show a high component for low frequencies, while the simulations only predict such behavior at $1.25u_{ms}$. In the case of $1.5u_{ms}$ flow rate, the simulation shows a moderate component at 10 Hz, which is consistent with the experimental trend, albeit a poor prediction of the low frequency component. Therefore, simulation results have a more stable behavior than the experimental ones. In the case of the $OSDT$ configuration with lentils, 5 and 10 Hz harmonics prevail in the spectra, Figures 5.16c-5.16d. However, it should be noted that, similarly to the regular material case, the simulated intensities do not match with the experimental values, which was also reported in other studies [181]. When a completely closed internal device is used, i.e., the SDT configuration, a dominant 10 Hz is clearly visible in both the experimental and simulated spectra, Figure 5.16e, albeit signal intensities do not match. However, as the flow rate is increased the simulated spectra shifts towards the 5 Hz range which is a clear deviation from the experimental values, Figure 5.16f.

This analysis can also be conducted for prismatic spouted beds at the same hydrodynamic conditions for lentils and pellets, Figure 5.17. Even though this analysis is purely limited to the WDT configuration because no internal devices were used in the prismatic spouted bed.

Although beds of the same material are used in Figure 5.16a and Figure 5.17a, the use of a prismatic spouted bed removes the low frequency components from the

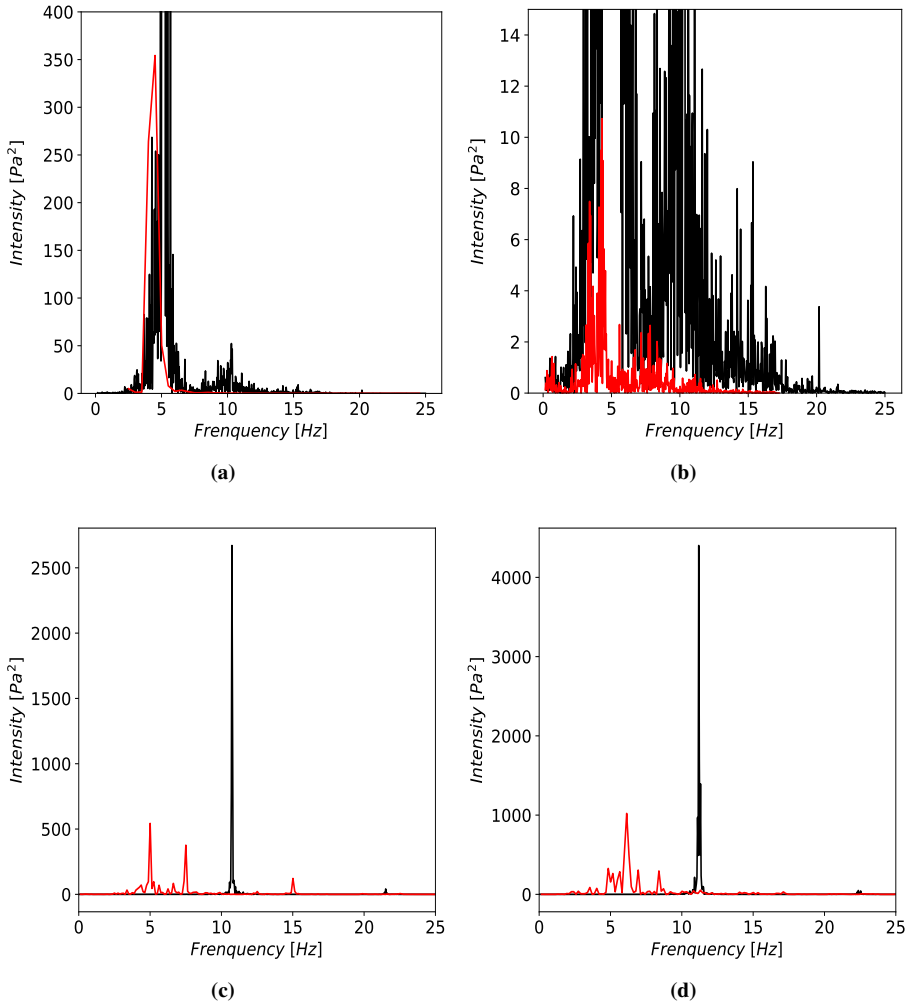

Figure 5.17. Experimental and simulated FFT spectra of pressure drop fluctuation in prismatic spouted beds of lentil beds at the flow rates of (a) $1.25u_{ms}$ and (b) $1.5u_{ms}$, and pellet beds at the flow rates of (c) $1.25u_{ms}$ and (d) $1.5u_{ms}$.

pressure signal, with this trend being observed in both the experimental data and the simulated signals in Figures 5.17a-5.17b. In both cases, the simulation successfully predicts the pressure component around 5 Hz, but fails to detect a proper 10 Hz component, which is clearly present in the experimentation. Figure 5.17b reveals the presence of this component in the simulation at high flow rates, $1.5u_{ms}$, but it is located at ~ 8 Hz. The shape of the experimental spectra is evidence of a bubbly spouting regime according to the classification shown in the literature

[92], i.e., the presence of the spout leads to a dominant frequency, but there is a wide distribution of frequencies. This behavior results from the fact that, even though the spout has already been opened, some particles fall down to the gas inlet slits, partially blocking the gas entrance, and therefore increasing bed pressure drop. This transient behavior adds more components to the main pressure fluctuation, which is evidenced by the experimental and simulated results in Figures 5.17a-5.17b

The use of pellets, clearly changes the FFT distribution in Figures 5.17c-5.17d, with a dominant component above 10 Hz and a smaller one at 22 Hz, which consistently shifts towards higher frequencies as the flow rate is increased. The presence of a single narrow FFT signal component has been linked to a stable spouting, in which the spout is relatively attached to the central axis without any significant bubbling or slugging of the bed [181]. Regarding the comparison between the simulated FFT spectra and the experimental values, it is clear that the *CFD-DEM* simulations under-predict the frequencies of the main harmonics at which the bed fluidizes. Thus, the simulation predicts the main harmonics at 15 Hz and 5 Hz, which in the experimentation are detected at 22 Hz and 10 Hz, respectively, Figures 5.17c-5.17d. Similarly as displayed in the velocimetry analysis, the simulation of pellets considerably deviates from the experimental ones in the prismatic spouted bed.

5.7 Void fraction in irregular particles

The void fraction in spouted beds of irregular particles is a crucial information for process optimization, as their preferential orientation and interlocking tendency greatly influence bed packing, and therefore the resulting spouting behavior [182]. Some experimental data of void fraction have already been reported by San Jose et al. [124] for a narrow distribution of pseudo-spherical particles. They reported that a reduction in particle sphericity leads to an increase in the overall void fraction of the bed. This only holds true for a mono-disperse solid mixture, as the addition of fine particles to a bed of coarse ones fills the inter-particle gaps, thereby reducing void fraction. In order to understand the effect particle irregularity has on the void fraction in spouted beds, simulations have been conducted for various materials and flow rates.

Figure 5.18 shows the profiles of void fraction along the axis of the contactor at each configuration and spouting velocity studied. As already shown in Chapter 4, the use of a internal device considerably affects the void fraction profile due to the draft tube disturbance and the lower flow rate required to attain a stable

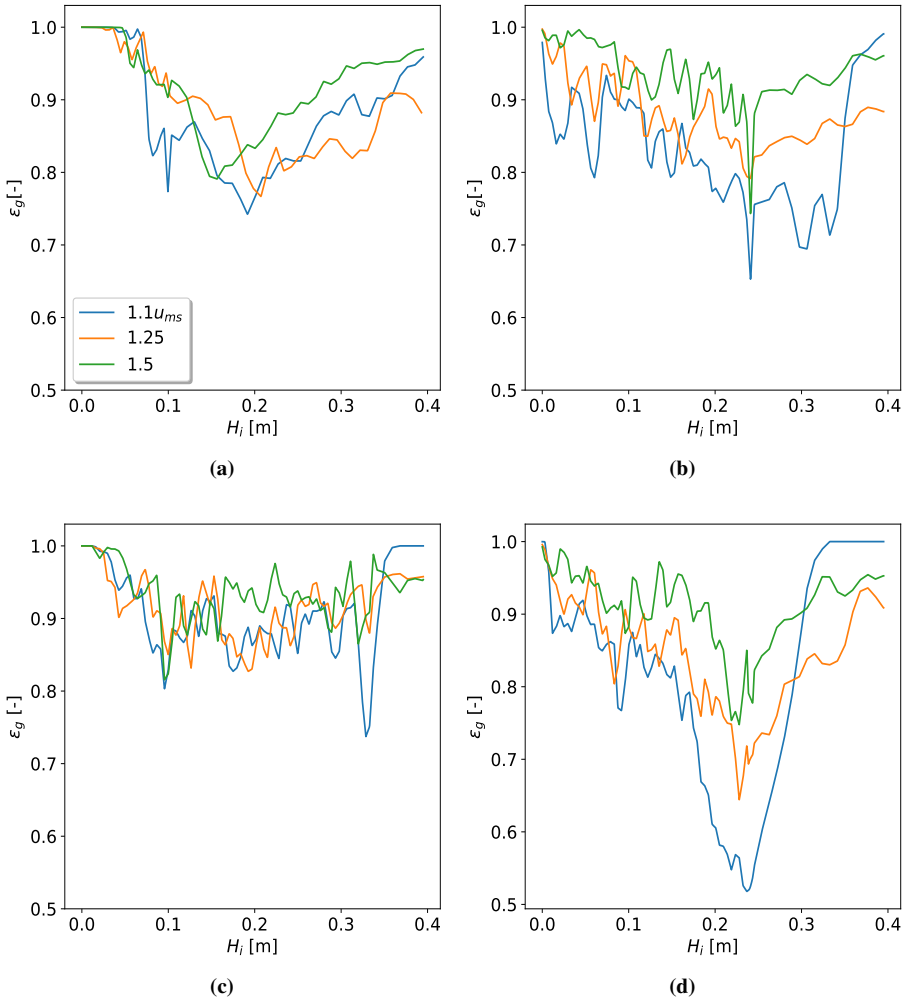

Figure 5.18. Void fraction profiles along the contactor axis at the three spouting velocities for lentils in (a) *WDT*, (b) *OSDT* and (c) *SDT* configurations, and (d) for pellets in the *OSDT* configuration.

spouting. Furthermore, the irregular shape of the particles leads to a much greater heterogeneity in void fraction profiles, which applies to all the systems analyzed, Figures 5.18a-5.18d. Given that the particles do not easily roll over their neighbors, they incorporate into the spout in clumps, Figure 5.19, and lead to uneven void fraction along the spout.

Figure 5.18a shows the evolution of void fraction as the inlet flow rate is increased

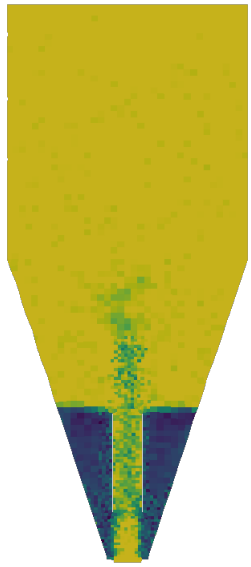

Figure 5.19. Cross section of the void fraction field in the *SDT* configuration of lentils spouted at $1.25u_{ms}$.

for the *WDT* configuration. Following the same trend already shown for regular materials, particles get dragged into the spout all along the bed, hence a descending void fraction trend is observed through the bed until the bed surface is reached (H_o). The fountain region shows a progressive evolution of the void fraction field towards more diluted mixtures with height. As the inlet flow rate is increased, the location of the void fraction inverse peak shifts to lower positions at the axis, and the whole profile gets flattened as a result of a more dilute spouting regime. The use of irregular particles leads to more dilute regimes than those shown in Chapter 4 for regular ones.

When the draft tube opening ratio is slightly reduced in the *OSDT* configuration displayed in Figure 5.18b, the descending slope of the void fraction is significantly reduced, as the solid transfer from the annular zone to the spout is hindered by the draft tube walls. It is worth noting that, at low flow rates ($1.1u_{ms}$) the *OSDT* configuration shows a lower minimum void fraction than the *WDT* configuration, Figure 5.18a, given that, although a lower solid transfer rate is allowed from the annululs into the spout, the minimum spouting velocity is also reduced when an *OSDT* is used, and therefore a greater amount of solids are present in the spout due to the lower air momentum. Apart from that fact, the effect of flow rate is consistent with that shown in Figure 5.18a, with the spout being more dilute as

the air flow rate is increased.

Figure 5.18c shows the same non-smooth void fraction profile as in the other configurations for the *SDT* configuration. Nevertheless, similarly to the spherical particles, a rather uniform mean void fraction is observed in the bed, which results from the protection the solid draft tube provides to the rising particles. As flow rate is increased, there is an increase of the void fraction profile as a more diluted spouting regime is achieved.

Therefore, the use of a completely closed draft tube, i.e., *SDT* configuration, leads to the axial void profiles shown in Figure 5.18c, in which void fraction only descends during the first third of the bed where the entrainment zone (L_H=7.5 cm) enables solid cross-flow from the annulus into the spout. At positions above the the entrainment height, void fraction is kept at an average constant value, as particles are not disturbed by the incorporation of other ones. Even though this configuration requires the lowest minimum spouting velocity (u_{ms}), the choking effect the entrainment has on the solid transfer to the spout makes this configuration inherently the most dilute of all. Therefore, an increase in flow rate results in a negligible effect on void fraction and the resulting additional air momentum is then used to increase the fountain height and particle velocity.

The effect of shape on void fraction profiles is clear, as the higher blockiness value for *ABS* pellets leads to a more densely packed spout (Figures 5.18b and 5.18d); that is, blocky particles leave smaller gaps than their ellipsoidal counterparts.

Non-spherical particles also change the radial void fraction profiles in all configurations (Figure 5.20), specially close to the wall, where non-uniform packing results in slightly higher values than in the bulk of the annulus. Regarding the void fraction profiles for each configuration, those for the *WDT* configuration are considerably smoother than the remaining configurations, Figure 5.20a. In this configuration the maximum void fraction is located at the center of the spout, whose values increases with the flow rate as a more diluted regime is achieved.

When internal devices are employed, the coarse nature of the bed material makes particle rolling difficult, thus creating a more heterogeneous void fraction in the spout region (Figure 5.20c) for the *OSDT* configuration. In this figure, it is apparent how the particles flow in a non-uniform fashion from the annular into the spout region, which leave behind dilute regions in the draft tube openings. This result greatly differs from the trend of smooth profiles shown for spherical particles. This particle flow heterogeneity, makes radial profiles (Figure 5.20d) slightly differ from those for the *WDT* configuration, with the maximum void fraction shifted from the spout center, as clusters of particles may flow at any radial position in the spout. The fact that particles can only flow though the openings makes

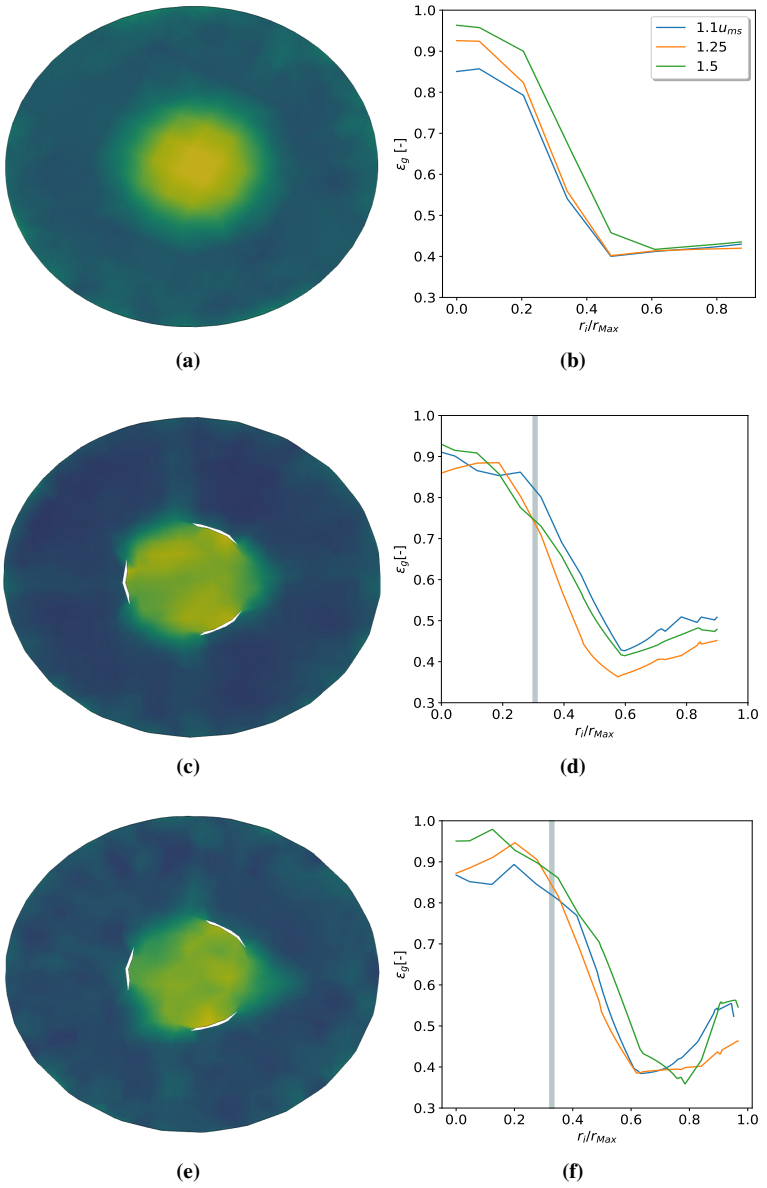

Figure 5.20. Evolution of the void fraction profiles at H_i=11 cm in conical spouted bed with the three flow rates in (a-b) WDT and (c-d) $OSDT$ configurations for lentils and (e-f) for pellets in the $OSDT$ configuration. The shaded vertical line is the location of the draft tube wall.

radial profiles decrease to local minima at $r_i/r_{Max} \sim 0.6$, and then progressively increase to the corresponding values on the wall, rather than an almost flat void fraction profile as in the WDT configuration. The use of pellets in Figure 5.20e-5.20f shows a more tightly packed bed, with a sharp decrease of the void fraction values in the annular regions in comparison to ellipsoids in Figure 5.20d.

5.8 Particle cycle times for superquadrics

Solid cycle time, $\bar{t}_c$, is defined as the average time a particle takes from the moment it lands onto the bed annulus, descends through this zone to a given position in the bed, in which it incorporates into the spout and goes up to the fountain, finally landing onto the annulus. As previously stated, this parameter, as well as the cycle time distribution, are of special significance in those applications that require a fine control of the solid residence time, such as catalytic cracking and coating. The chemical industry hardly ever employs completely spherical particles, with pelletization and compaction being common methods to increase the mechanical integrity of a catalyst. As a result, the shape of some materials employed in large scale plants follows a superquadric description and their cycle time ought to be studied. The addition of different internal devices and changes in flow rate are well known strategies for modifying both the average cycle time and the cycle time distribution in order to tailor the optimal configuration to a particular application or process. The effect of the configurations studied on the average particle cycle time of lentils is shown in Figure 5.21 for the conical spouted bed.

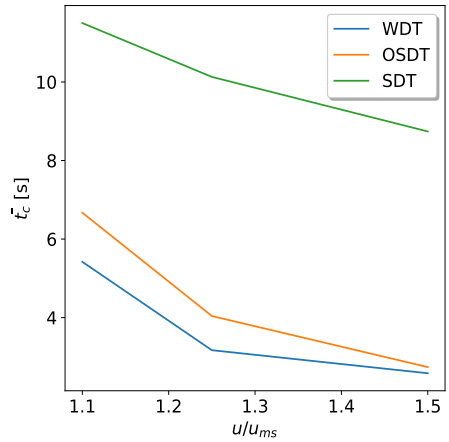

Figure 5.21. Mean solid cycle time in the three configurations under different flow rates for lentils in a conical spouted bed.

The average cycle time is used as a guiding parameter to ascertain the solid circulation flow rate and bed turbulence, that are related to heat and mass transfer rates. Nevertheless, cycle time distribution provides an indication of the percentage of material that must be replenished or remove from the reactor once every given number of cycles have been completed. Given that long and short cycles are linked to the most likely paths, the cycle time distribution gives an idea of the best location for the outlet pipe to remove the spent solid from the reactor. The simulation of the whole process allows locating every particle at each time step, and hence calculating the resulting cycle time distribution in each configuration under different operating flow rates.

Figure 5.22 shows the cycle time distribution of lentils and pellets in the three configurations studied under the three flow rates. Figure 5.22a shows how the cycle time distribution evolves with flow rate in the WDT configuration for lentils. This configuration is especially suitable for attaining a distribution with very short cycle times, as any particle has a chance of getting into the spout and completing a cycle without having to descend through the whole bed. As the flow rate is increased, the peak of the distribution shifts towards shorter cycles due to higher particle circulation rate. However, a long tail of those particles that stay close to the wall in their descending path is always present. In the $OSDT$ configuration, Figure 5.22b, the cycle time distribution is more skewed towards higher cycle times, with a considerable particle population completing short cycles as in the previous configuration, given that they have a chance of falling into the spout through the openings of the draft tube. This likelihood of completing short cycles is progressively reduced as the opening ratio, ω_T, of the draft tube is decreased.

At the limit where no openings are available for the solids to cross in the SDT configuration , Figure 5.22c, the cycle time distribution shows no sign of short cycles and the whole distribution is shifted towards higher cycle times. In the case of this configuration at $1.1u_{ms}$, every particle is guarantied to stay in the bed for more than 6 s, while particles with high cycle times may stay even up to $\sim$ 30 s. Furthermore, the minimum cycle time can be tailored by changing the draft tube entrainment height. The gas flow rate can also be used as another degree of freedom, with the maximum mean particle cycle time corresponding to the minimum spouting velocity.

The use of the superquadric description for the solid shape allows for simulating pellets and their cycle time in order to study the effect of shape on the cycle time distribution, Figure 5.22d. When particles are changed from an ellipsoidal shape (lentils) to a cylindrical one (pellets) in the $OSDT$ configuration, the distribution shifts towards shorter times, especially for low inlet flow rates. As shown in this section each configuration and flow rate affect differently to the cycle time, which

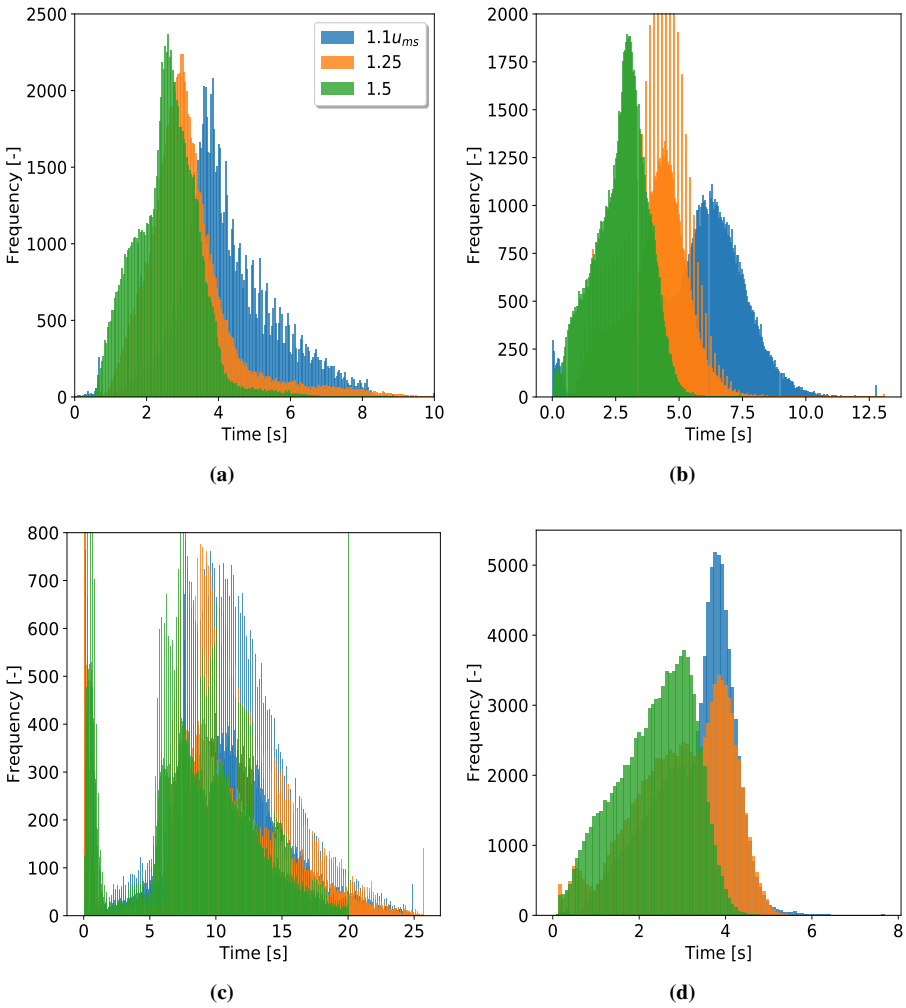

Figure 5.22. Solid cycle time distribution under different flow rates for lentils used in the configurations of (a) *WDT*, (b) *OSDT*, (c) *SDT*, and (d) pellets in the *OSDT* configuration.

allows tailoring the system to specific cycle time requirements. However, changing any of these parameters will also modify the gas residence time, which will be studied in the following section.

5.9 Gas RTDs for irregular particles

The gas residence time distribution (RTD) is closely related to process efficiency, such as in drying and chemical reactions [152], where the main phenomena depend on the time particles are in contact with the gas. In addition, the RTD gives information about possible inefficiencies due to stagnant gas pockets and dead zones. A number of models have been proposed in the literature to describe the gas behavior in the bed [183, 184], such as a plug flow vessel followed by a well mixed tank with by-pass. However, these models simplify most of the solid movement and gas-solid momentum exchange. Thus, CFD-DEM models can be employed for the simulation of the gas dispersion, and therefore obtain the average and the distribution of residence time for different materials, configurations and operating conditions, Figure 5.23.

In order to enable the comparison between hydrodynamic regimes the widely accepted dimensionless time has been used. This, enables straightforward comparison of F curves, Figure 5.23. The WDT configuration shows the greatest delay in the tracer concentration, which suggests that, for the same contactor volume, this configurations leads to better mixing and higher residence time than the remaining configurations. At low flow rates, the E curve, Figure 5.23a, shows a reasonably uniform population of gas residence times, but as the flow rate is increased a separation of the population is observed, leading to bi-modal E curves. This difference in residence time is likely due to the different times the gas takes to go through the spout and the annular zone. As the flow rate is increased, these two populations get further separated. Furthermore, both gas populations should be considered when designing the reactor for a given mean gas residence time.

In the case a draft tube is used, Figures 5.23b-5.23c, the concentration of the tracer at the outlet is significantly lower than the inlet concentration, even when reasonable time is given for the tracer to disperse. In addition, an increase in flow rate worsens this trend, with the concentration of the tracer at the contactor outlet being lower. This behavior is attributed to a significant fraction of the gas stream by-passing most of the contactor volume, which is worsen as flow rate is increased due to the increased shear force in the spout, hindering the radial dispersion of the gas. Furthermore, the use of a SDT exacerbates this effect, as almost no radial dispersion is observed in this type of configuration, with most of the air stream being driven through the spout. This latter configuration results in a gas RTD configuration that approaches a plug-flow regime of very low residence time, which is not always desirable in spouted bed applications, as most of the solid inventory in the contactor is not in contact with the gas phase. Albeit the shortcoming caused by using configurations with apparent dead zones, the average residence time of

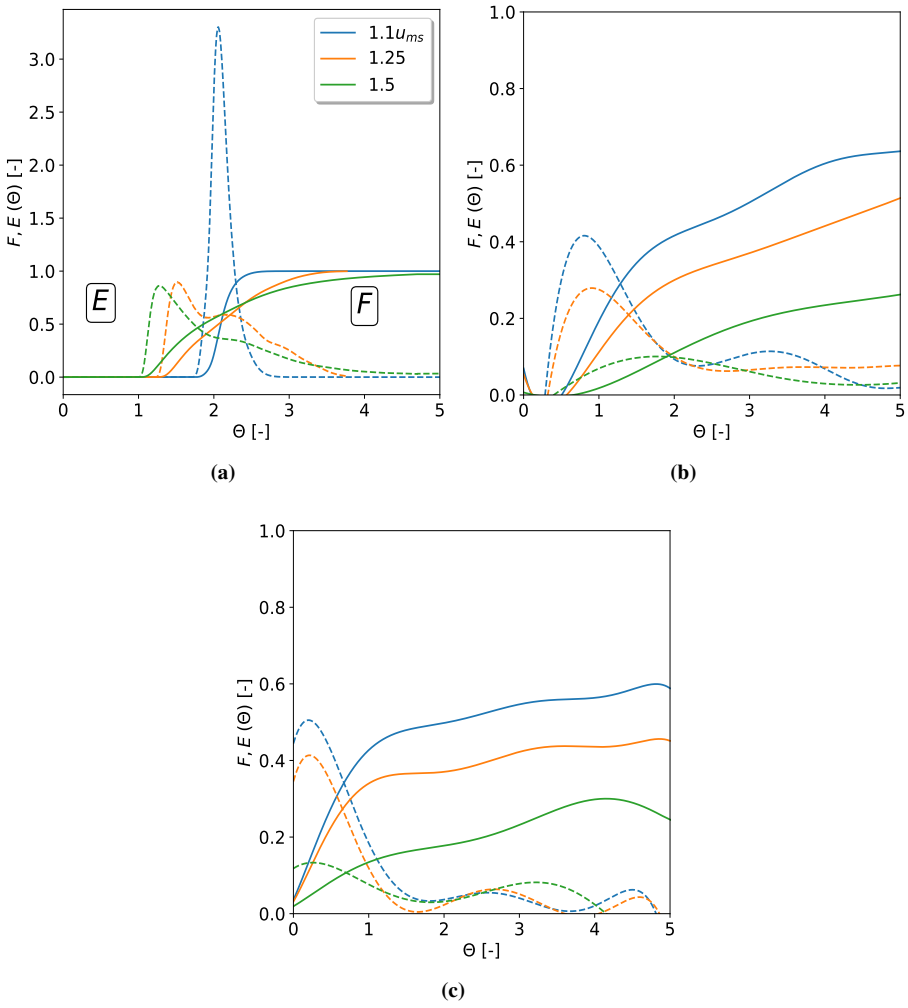

Figure 5.23. Evolution of F and E curves for the gas in (a) WDT, (b) $OSDT$ and (c) SDT configurations with lentils in a conical spouted bed at varying flow rates.

almost the whole gas stream can be predicted for the aforementioned configurations, Figure 5.24.

As observed in this figure, the dimensionless residence time decreases with flow rate for all configurations, with $OSDT$ leading to the maximum adimensional residence time, which results from the lower air flow rate and increased gas-solid contact in the annular section in comparison to the SDT configuration. The minimum residence time corresponds to the SDT configuration, in which almost the

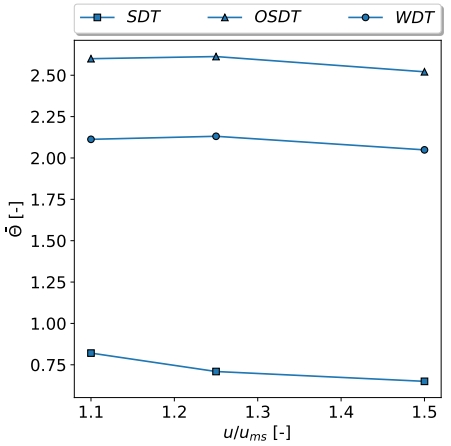

(a)

Figure 5.24. Change in the mean residence time depending on the configuration and flow rate.

whole air stream is directed through the spout.

As previously mentioned, most configurations and flow rates do not reach the inlet concentration, even when the simulations are run for considerably long times (5Θ). The lowest flow rate in the system leads to the highest outlet concentration, as a weak spout creates low shear forces to be overcome by the injected air in order to radially disperse. Even in this case, in which there is some radial dispersion driven by the turbulence model, most of the upper section of the contactor remains unused. This feature evidences the presence of significant death zones, in which the tracer remains for long time until taking the path to the contactor outlet, as shown in Figure 5.25.

In the best case scenario in which the gas residence time is not a critical operating condition, such as in drying or non-catalytic gas-solid reactions, these dead pockets mean a non-efficient use of the contactor volume resulting in a poor use of the energy put into the system. However, in the cases in which the gas residence time crucially determines the final product quality, such as in catalytic gas-solid reactions, the presence of these gas pockets may lead to not only a loss of product quality, but also could accelerate catalyst deactivation, as reaction products stay for a long time in the reactor [185]. Thus, the fountain confiner is proposed as a means to alleviate some of the shortcomings of using spouted beds at high flow rates and allow an easy control of the gas phase residence time and mixing.

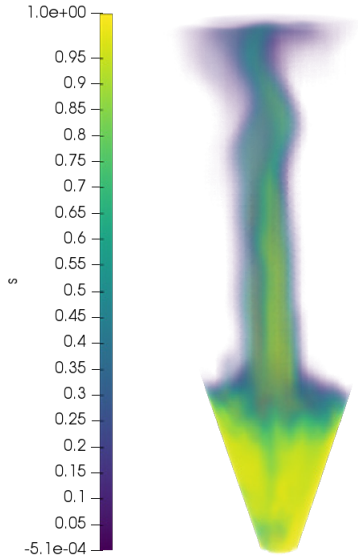

Figure 5.25. Tracer concentration in the *OSDT* configuration at $1.5u_{ms}$ showing the presence of gas dead zones around the central jet above the bed surface.

5.9.0.1 Fountain confiner as a gas mixing device

Fountain confiners were originally designed to reduce the elutriation problem spouted beds encounter when high inlet flow rates and fine particles are employed [107]. In addition, given that biomass particles, such as sawdust or rice husk, have an elongated shape and low density, they tend to create a rotary fountain with a characteristic bed crater over the annular region, Figure 5.26a. When a fountain confiner is used, this crater is removed, as particles descend to annular positions around the inner section of this region, Figure 5.26b. This fact changes the particle cycle time distribution and shortens the average particle cycle time, as particles coming from the fountain are fed closer to the spout region. However, the way cycle time is affected by each parameter has not been reported yet.

The use of a confiner has already been reported to improve some processes, such as drying [108] and pyrolisis of biomass [149]. In order to study the effect the confiner has on the spouted bed dynamics, a bed-to-confiner distance, H_f, of 0.07 *cm* has been used, which was reported by Tellabide et al. [186] to be optimum for bed stabilization, and also for avoiding clogging of the outlet air, as this leads to a slugging bed. In this study, the confiner used has a diameter of 15 *cm*, and has

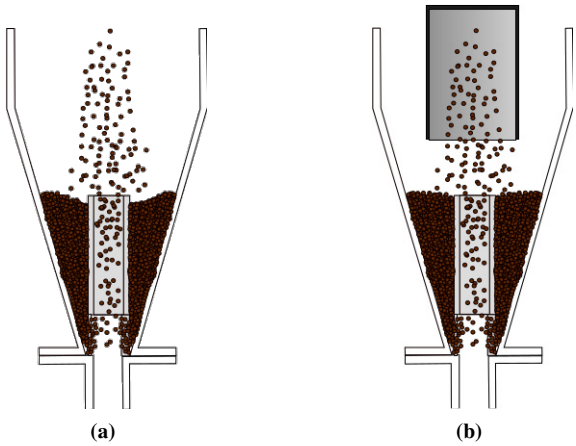

Figure 5.26. Upper surface of the bed (a) without confiner and (b) with confiner.

been inserted in the conical spouted bed with the open-sided draft tube, i.e., the *OSDT* configuration has been used. Thus, the effect of this device on the solid cycle time distribution is showed in Figure 5.27, in which the cycles times with and without confiner are shown at each simulated flow rates.

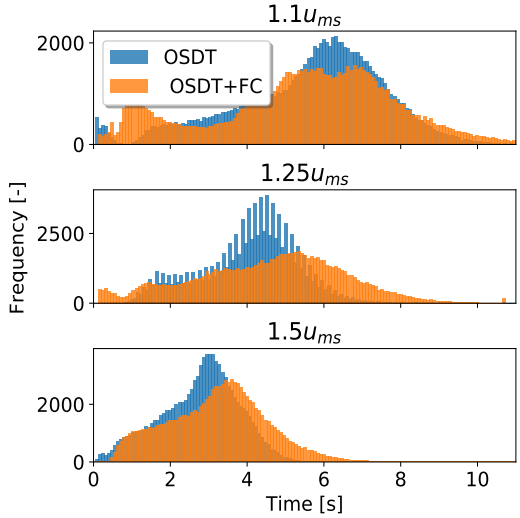

Figure 5.27. Effect of the confiner on the solid cycle time in a conical spouted bed equipped with an *OSDT* at various flow rates.

As expected, when low flow rates are used ($1.1u_{ms}$), the solid cycle time is shortened with the addition of the fountain confiner (*FC*). The use of this device, in

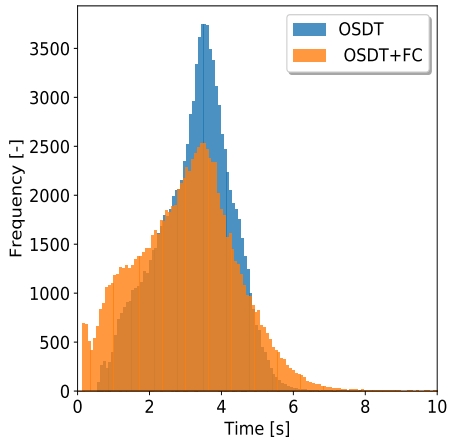

Figure 5.28. Effect of the confiner on the particle cycle time distribution for a confiner-to bed distance of H_f=14 cm at 1.5u_{ms} in the $OSDT$ configuration.

addition to slightly displacing the solid cycle distribution to the left, it also creates a new solid population that completes short cycles ($< 2\ s$), as particles coming from the confiner are directly fed into the inner section of the annular region. When the flow rate is increased to 1.25u_{ms}, there is hardly any difference in the average cycle time with and without confiner. Finally, when the highest flow rate is used (1.5u_{ms}), the average cycle time increases with the presence of the fountain confiner. After studying the solid flow pattern, it is concluded that an increase in flow rate in this configuration leads to a higher radial gas velocity in the confiner-to-bed range (H_f), which in this case is 7 cm. This radial gas velocity at the top of the bed makes a significant amount of particles coming down from the confiner to be thrown against the contactor wall, balancing off the effect the fountain confiner has on the particle cycle time shortening. The easiest way to alleviate this behavior is by rising the fountain confiner, i.e., increasing H_f. Thus, Figure 5.28 shows the effect of placing the confiner at H_f=14 cm on the cycle time.

Unlike Figure 5.27, high flow rates do not have any influence on the cycle time when the confiner is located sufficiently high, Figure 5.28. This is likely due to the increased cross sectional area available for the air to leave the confiner, resulting in lower solid radial velocities, which would otherwise drag some particles in the horizontal direction on the upper side of the bed. With the addition of this internal device, the overall use of the contactor volume significantly improves, Figure 5.29, as all F curves reach values close to the injection concentration of 1 within a reasonable time. Figure 5.29 shows how the gas flow rate influence on the dimensionless residence time is significantly diminished compared to the same configuration without the fountain confiner, Figure 5.23b.

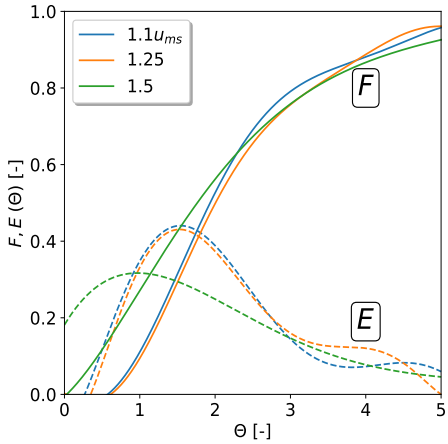

Figure 5.29. Effect of the fountain confiner on the gas residence time distribution in the *OSDT* configuration and lentil bed.

Therefore, it may concluded that the fountain confiner can be used as an effective device for controlling the gas residence time, which is of great significance for the design of spouted beds, even in these cases where there is not a significant elutriation problem or bed stabilization requirement.

6 Coating of irregular particles in spouted beds

Spray coating requires the addition of a third phase in addition to the fluid and solid phases described in the previous chapters, and their interactions must be characterized in order to obtain a realistic and reliable behavior of the real system, Figure 6.1. Some authors include the third phase as a discrete fluid phase interpenetrating with the gas phase in a *TFM* approach [187], while keeping the solid phase in a Lagrangian reference frame. Other authors neglected the disturbance of the coating agent in the medium and integrated the fluid fields, and post-processed the deposition values in a further step [6].

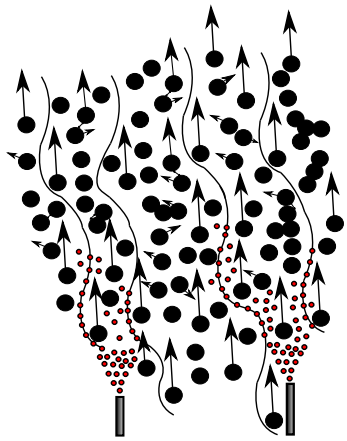

Figure 6.1. Addition of the droplet phase (red dots) to a four-way coupled gas-solid media.

However, this approach does not take into account the discrete nature of the coat-

ing agent droplets and the dependency of the droplets on droplet-solid relative orientation [188]. The use of droplets in a Lagrangian framework is an alternative to the diffusive nature of TFM models, but at the expense of computational resources. Therefore, the way contact detection is implemented must be carefully considered in order to avoid unreasonable computational cost for this additional information on granularity that the Lagrangian approach provides.

In addition to simulating which particle is hit by a droplet, the approximate surface location coated by this droplet plays a mayor role in processes, in which the homogeneity of the coating layer is essential, such as: film coating [189], nuclear fuel coating [93] and catalyst production [190]. This additional modeling requirement increases computational cost, and therefore arises the need for an optimal implementation.

The *CFD-droplet* coupling is achieved by a cloud of droplets injected through an opening, where the outer cone angles have to be set to form a cone as shown in Figure 6.2a. The nozzle type will determine the geometrical factors of the resulting spray, as well as the droplet size distribution, for which the Rosin-Rammler size distribution is commonly used [191]:

$$F(x) = 1 - e^{ln(0.2)\left(\frac{x}{d'}\right)^n} \tag{6.1}$$

where $F(x)$ is the value of the cumulative function of the distribution, n is the spread of the distribution and d' the mean droplet size of the distribution.

Droplets are injected into the *CFD* domain with a velocity defined by the nozzle diameter and the mass flow rate set by the user. As the particles come in contact with air and start to diverge from each other, the droplets break up depending on the hydrodynamic forces they encounter. There are a number of secondary break-up models that take into account the internal droplet oscillations, such as *TAB* (Taylor Analogy Breakup) [192] or *LISA* (Linearized Instability Jet Atomization) [193], but, in this work, only the *KH-RT* (Kelvin-Helmholtz Rayleigh-Taylor) model developed by Reitz & Diwakar (break-up model) [194, 195] is going to be used, as it allows a simple and fast computation of the droplet size distribution based on the following Equation:

$$\frac{d(d_i)}{dt} = \frac{-(d_i - d_{st,bg})}{\tau_{st,bg}} \tag{6.2}$$

where d_i is the droplet diameter, $d_{st,bg}$ is the pseudo-stable droplet size and $\tau_{st,bg}$ is the characteristic break-up time. In this case, only two break-up mechanisms are considered, namely, bagging and striping break up mechanisms defined by the

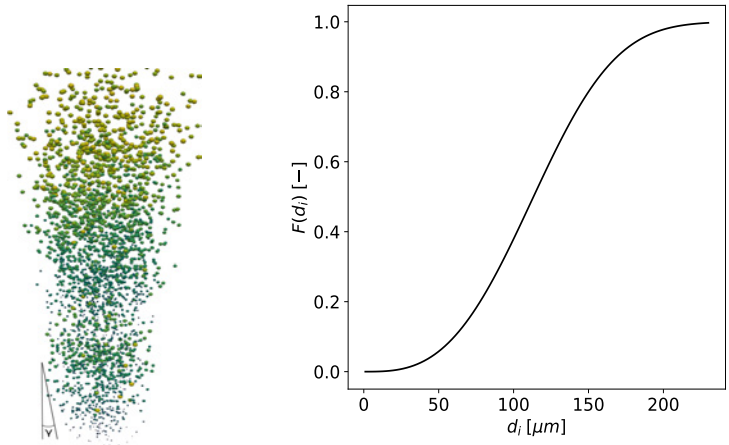

(a) (b)

Figure 6.2. Representation of the (a) physical shape and external angle of the spray and (b) size distribution of a given spray.

following Equations 6.3 and 6.4, respectively:

$$d_{st,bg} = \begin{cases} \frac{2C_{bg}\sigma}{\rho|u_r|^2} & \text{We} \geq 6.0 \\ \frac{(2C_{st}\sigma)^2}{\rho|u_r|^3\mu} & We/\sqrt{Re} \geq 0.5 \end{cases} \tag{6.3}$$

$$\tau_{st,bg} = \begin{cases} \frac{C_{sd}\sqrt{\frac{\rho_d}{\rho}}}{|u_r|} & \text{We} \geq 6.0 \\ C_{bd}\sqrt{\frac{\rho_d d}{\sigma}} & We/\sqrt{Re} \geq 0.5 \end{cases} \tag{6.4}$$

The dominant mechanism is determined based on the Weber number (We) defined by Equation 6.5, which provides the relative significance of inertial forces against the liquid surface tension

$$We = \frac{\rho|\mathbf{u_r}|^2 d_i}{\sigma} \tag{6.5}$$

where σ is the liquid surface tension at the droplet temperature.

The coupling between the gas phase and liquid phase is again accomplished through the drag force by using the default Weng-Yu [132] model. However, given the size and volume taken by each droplet, the void fraction effect of the droplets within the cell void fraction has not been considered, completing this way a one-way

coupling of the gas-droplet interaction.

6.1 Implementation of the contact detection

As already mentioned, there is a growing need to identify the location and relative orientation when a droplet hits a particle in order to control and avoid spurious effects, such as twining and layer breakage, derived from a non-uniform distribution of the coating agent [189, 196]. This uniformity is a key factor in the diffusion of the pharmaceutical agent through the coating layer [197].

To that end, a way of efficiently discretizing the surface of the particle must be accomplished and the quantity deposited on each surface cell must be tracked.

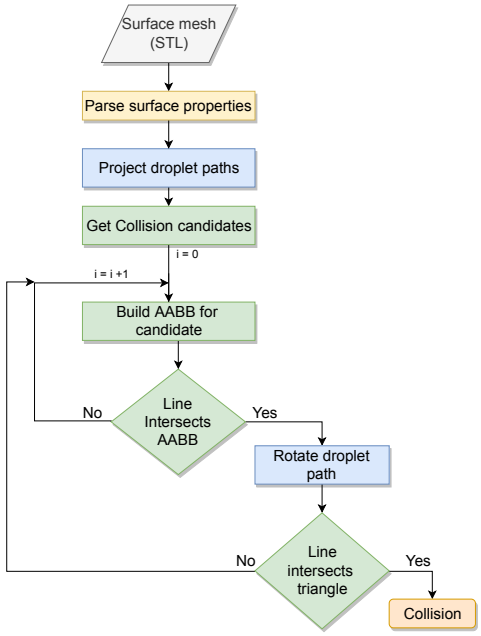

Figure 6.3. Flow chart of the hierarchical contact detection algorithm.

The collision algorithm is briefly described in Figure 6.3, where the user needs to input a *STL* file of the surface mesh attached to the particles to be coated. This procedure gives flexibility to the user to decide the granularity of the final coating based on available computational resources and requirements. At the beginning of each simulation, the algorithm reads the surface mesh file and stores the location and relative positions of all the vertices for each particle type, Figure 6.4.

In addition, all the information, such as cell normal area and centroid location, is parsed into their corresponding variables for later use. By keeping all the geometrical factors relative to the main shape parameters (r_x, r_y and r_z), the same data can be used for particles of the same blockiness, but different shape values.

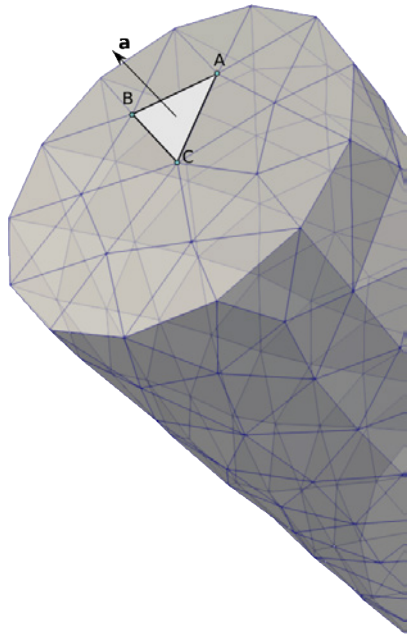

Figure 6.4. Superquadric particle surface tessellation storing its surface data.

In order to make a contact detection efficient, a hierarchical contact detection approach is taken, as shown in Figure 6.3. Firstly the droplet location is projected along a time step by connecting the current location and the location expected in the next time step if no collision happen, thus creating a line. Subsequently, the contact detection of lines with geometrical shapes, derived from computer graphic approaches [198], can be used . Secondly, the particle *Id* of all the granular particles located within the same *CFD* cell and adjacent cells are pulled from the search tree. For every particle, starting with the particle whose centroid is closest to the droplet, an axis aligned bounding box (*AABB*) is computed and the primitive line-*AABB* contact detection is computed. This approach greatly reduces the number of contact candidates and speeds up the contact detection process. Once a line-*AABB* intersection has been detected, the fine contact detection is executed.

The fine contact detection, shown in Figure 6.5, is the most expensive part of the computation, as a search has to be done with the tessellation triangles. In order to reduce the number of required computations, some calculations only related to the relative positioning of the particle vertices are computed prior to the beginning of

the simulation. However, the vectors related to the triangle-line relative position have to be computed at run-time, requiring five dot products and one cross vector multiplication per triangle element. When the condition described in Equation 6.6 is met for the three edge-line combinations, the line intersects the triangle and the contact point is obtained as barycentric coordinates [198]. When the contact is registered, the droplet is removed from the droplet cloud and its mass is added to the particle surface element.

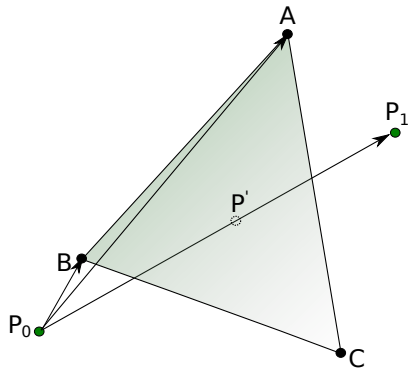

Figure 6.5. Primitive line triangle contact detection.

$$(\vec{P_0P_1} \times \vec{P_0B}) \cdot \vec{P_0A} \geq 0 \tag{6.6}$$

Once all the droplet-particle collisions are computed, the deposited mass must be communicated to the *DEM* side in order to be taken into account for those applications where the solid-solid contact is influenced by coating layer and its homogeneity. Thus, at every *CFD-DEM* coupling step, all the droplet deposition is compressed into a single vector, where the vector magnitude accounts for the deposited mass, while its direction gives information about the particle face covered. The main drawback of this approach is that some droplet-particle collision granularity is lost, as some triangles will get coated even when they have not been hit by a droplet, because of their orientation facing stream wise. In addition, in case a particle is hit from more than one direction, the vector communication would not be mass conservative and another more granular communication scheme would have to be implemented. However, the current implementation gives reasonable results for the applications that are intended, as only a single nozzle is going to be used.

This way, at the coupling step, the deposition is updated uniformly distributing the mass between all the faces that are exposed to the spray. The mass that each exposed face receives is proportional to the angle between the deposition vector and each face normal vector, obtaining coating profiles as the ones shown in Fig-

ure 6.6.

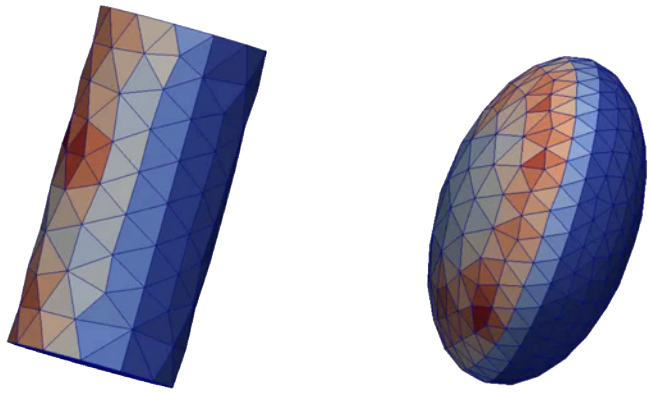

(a) (b)

Figure 6.6. Representation of non-uniform coating for (a) pellet and (b) ellipsoidal particle.

This figure shows the area covered by the coating agent on a pellet (Figure 6.6a) and on an ellipsoid (Figure 6.6b). As a result, the deposition coming from the left in Figure 6.6 show a greater deposited mass in the left of the cylinder as their faces are almost perpendicular to the deposited droplets. It is worth noting that the greater area deposition in the edges in Figure 6.6b is due to the smaller tessellation cells in this region, as the coating agent is stored in a per area basis (kg/m^2).

6.1.1 Additional liquid-solid forces

Given the speed at which droplets leave a regular nozzle [199] , inclusion of the drag and torque droplets exert on a particular solid particle has been considered, as they can be significant in the spraying area and can significantly affect the covering of particles. Luckily enough, the location and mass of each droplet is known after the contact detection is run. A conservation of momentum equation is solved by applying a torque according to Figure 6.7.

In order to determine the force exchanged between the droplet and the solid, the mean contact time has to be defined based on the following equation [200]:

$$\tau_0 = \sqrt{\frac{r_d^3 \rho_d}{\sigma}} \tag{6.7}$$

Once the contact time is determined at the particle temperature, the total torque

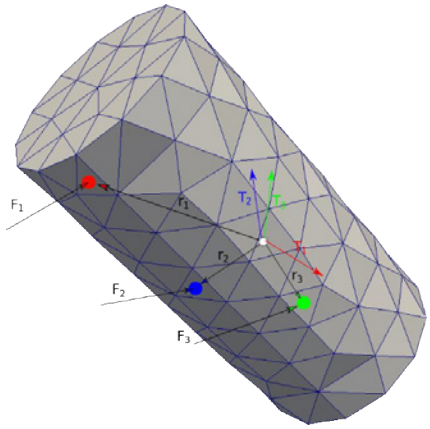

Figure 6.7. Graphical representation of the torque applied around a particle center of mass due to various collisions.

exerted by all droplets is computed by the following equation:

$$\mathbf{T_d} = \sum_{i=1}^{n} (\mathbf{r_i} \times \mathbf{F_i}) \tag{6.8}$$

where $\mathbf{r_i}$ is the vector from the center of mass to the collision point and $\mathbf{T_d}$ is the total torque exerted on the particle by the coating agent.

6.2 Test cases for the coating of particles in the spouted bed

When designing a coating reactor, there are some design considerations to be taken into account in order to choose the most efficient configuration for a particular product. For example, in the case of spouted beds, the first thing to be considered is the geometry and configuration of the contactor. The injector design and properties are usually given by its manufacturer (spread angle, operating pressure and flow rate), but its location and interaction with the spouting air, as well as the changes caused in process efficiency, are interesting facts to be studied. The first thing that is to be determined in a potential particle coater is the geometry of the spouted bed to be used. To that end, some test cases are run in both a prismatic spouted bed, in which the coating agent is sprayed from the top (Figure 6.8a) and in a conical spouted bed, in which the coating agent is sprayed from the

bottom (Figure 6.8b). The aim is to assess their coating capabilities.

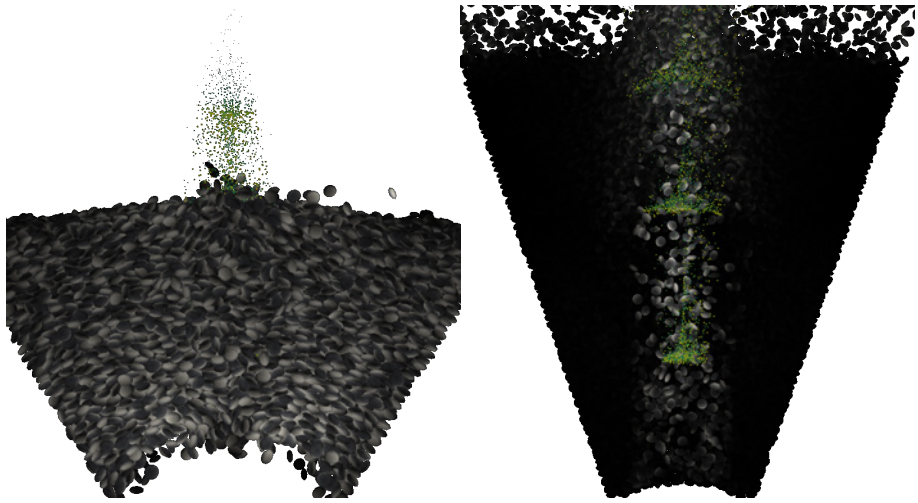

(a) (b)

Figure 6.8. Examples of the location of the injection point in (a) top-down spraying prismatic spouted bed and (b) bottom-up spraying conical spouted bed.

The simulations are run for 20 s of coating time by feeding 10 ml/min of spraying agent flow rate under moderate turbulence ($1.25u_{ms}$) in both geometries. In all simulations, the injection cone is located at the axis of the contactor and the coating agent is sprayed along the axis. As previously stated, each particle surface is discretized into a number of tessellation cells and the average of the mass deposited on these cells is determined, which allows calculating the distribution of the coating agent on the particles, as shown in Figure 6.9 for three spraying times. This distribution allows determining the average coating attained for given spraying times. Usually, each particle is required to be coated with a pre-determined quantity or thickness. Therefore, this simulation allows the time required to coat a number of particles.

Figure 6.9a shows the evolution of coating load distribution in a conical spouted bed sprayed from the bottom. At 1 s, some particles have not reached the spout region, as the average cycle time is higher than 1 s. Therefore some non-coated particles are apparent in the distribution. Once 10 s have elapsed, all particles have been passed through the spout and have received some fraction of the sprayed content. From this point onward, the distribution only shifts to the right, as more mass is added into the system. In the case of the prismatic spouted bed sprayed from the top (Figure 6.9b), the distribution is significantly different, which is a consequence of the cycle time distribution in this type of spouted bed. Further-

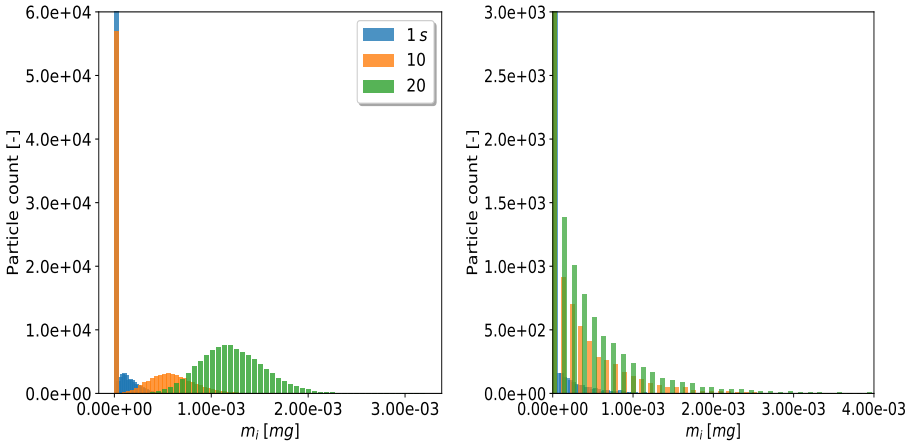

(a) **(b)**

Figure 6.9. Coating agent coverage distribution in a bed of lentils for different spraying times in (a) conical spouted bed and (b) prismatic spouted bed.

more, the specific design of this type of bed, especially the inlet section (geometry of the inlet), is responsible for this very skewed distribution.

However, the average of the coated surface does not indicate how uniformly a given particle surface has been coated. Given that the total agent content in each triangle of each particle is available, the coating variance on the surface can be computed, Figure 6.10. This metric can be used to avoid configurations where a number of particles are being coated only in specific faces. However, as seen in the figure the variance only start to be representative of the population once all particles have been been slightly coated and thus, Figure 6.10b can not be used to identify the homogenous coating of particles as Figure 6.9b still shows a significant population of particles that have not passed in front of the spray nozzle.

To alleviate that problem, the intra-particle coating variability is defined following Freireich et al., who used a similar surface discretization approach for a Monte Carlo-*DEM* simulation of a perforated drum coating process [159]. This parameter determines the coating variability between particles, and is defined as follows:

$$CoV_{intra} = \frac{\sqrt{\frac{1}{N}\sum \sigma_i^2}}{\frac{1}{N}\sum \mu_i} \tag{6.9}$$

By monitoring this parameter during the simulation, an estimation of the time re-

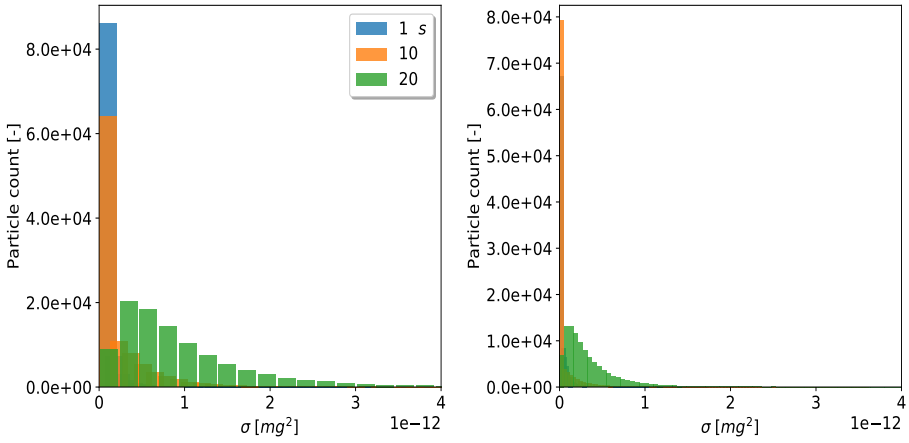

Figure 6.10. Variance of the surface coating of (a) lentils and (b) pellets in the conical spouted bed.

quired for a uniform and acceptable quality coating process can be ascertained. In addition, the inclusion of the coating algorithm within superquadric particle framework enables the analysis of the coating process using different shapes, such as pills, pellets and tablets, which are widely used shapes in the coating process in the pharmaceutical and food industry [201]. In the current study, only the aforementioned lentils and pellets are used in order to see the coating time requirements for each shape in a conical spouted bed, Figure 6.11.

When the particles in the bed are homogeneously coated, Freireich et al. [188] show that Co_V parameter reaches an asymptotic value once a particular number of turns in the coater are completed. In this case, no asymptotic trend has been reached, which suggests that the conical coater requires rather long times ($> 1\ min$) to reach a uniformly distributed coating distribution. However, there is a clear difference when comparing the evolution of CoV parameter for lentils and pellets, Figure 6.11. The former are more uniformly coated at every time. Nevertheless, the blocky nature of the latter requires their axes to have a given orientation with the nozzle (the lowest cross section area perpendicular to the injection nozzle) in order to achieve a uniform distribution. These pellets tend to rotate preferentially around their major axis, while ellipsoidal particles are more likely to expose all their faces with similar probability. On the whole, the descending trend observed in Figure 6.11 is consistent with the trends reported in the literature [202], and they provide estimations of batch time requirements for each type of tablet coating.

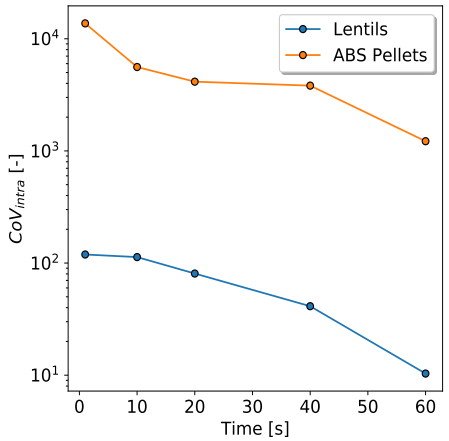

Figure 6.11. Evolution of the intra-tablet variation parameter as the coating process evolves for lentils and pellets.

6.3 Performance and scaling

Code performance is defined as the way computational resources are employed in order to complete a specific task. Concerning computational simulation, and specifically *CFD-DEM* simulation, code performance must strike a balance between the available computational resources and the scale and result granularity that the industry demands. However, the use of a distributed computation to conduct these simulations involves inter-processor communication and latency problems that may hinder the overall performance of the simulation model.

When implementing pieces of *CFD-DEM* coupling or a coating algorithm, special care must be taken in order to avoid penalties in the code performance and keep an acceptable scaling level in the successive simulations. Thus, an scaling study is conducted at *Arina, Scientific Computational Services (IZO-SGI SGIker)*, which consists of dual socket *Xeon* 2680*v*4 processor nodes that are linked through a InfiniBand *FDR* interconnection.

In order to study how the code scales, firstly, the scaling performance when the surface resolution is changed has been conducted. Figure 6.12 shown the results when the particle surface resolution is increased and the collision algorithm is subsequently run.

As the number of surface cells is increased, the computational cost of the droplet collision detection algorithm increases, although with a lower slope ($O(0.8\,n)$) than

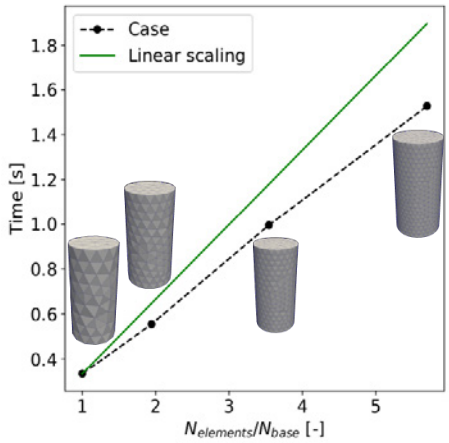

Figure 6.12. Influence of the surface refinement level in the timing of the collision detection algorithm.

the linear one. The difference between the linear scaling of the computation time and the trend shown in Figure 6.12 is explained by the fact that, when jumping from a coarse to a fine discretization, most of the added cells are included in regions away from the collision path.

In addition to the scaling of the algorithm occurring when the tessellation resolution is changed, the scaling when the number of particles is changed has to be studied. Therefore, a set of simulation runs are conducted with a bottom-up coating spray. Firstly, the number of particles to be coated with a given number of droplets has been considered, and the time required to solve each submodel (flow model and deposition model) and the whole CFD model have been calculated, Figure 6.13a. The calculation is run at $10K\ particles/core$ and for $1\ s$ (simulated time) in order to obtain comparable results. This figure shows that a rather high penalty is paid for an injection of $2M$ droplets into the system, but the total computation time (denoted CFD in the figure) is approximately constant with the number of particles, as observed in Figure 6.13a, given that collision detection is mainly a single threaded workload.

An analysis of the second case, in which the number of droplets is increased, the solution of the flow model does not depend on the number of droplets. However, as shown in Figure 6.13b, collision detection increases the computation time significantly, as this algorithm takes a significant time in comparison to the solution of the fluid fields, specifically when the number of droplets is high. This, problem should be addressed in order to run simulations in which there are multiple sprays or a high number of droplets are involved.

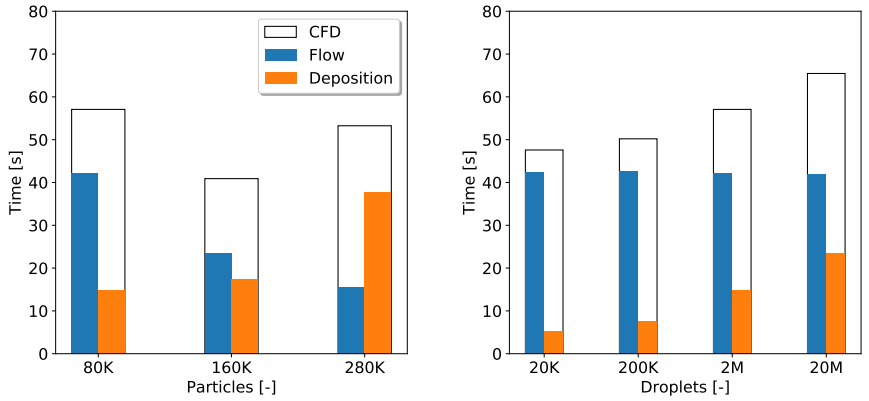

Figure 6.13. Code profiling considering the droplet contact detection, for the cases: (a) number of particles coated with an injection of $2M$ droplets, (b) droplets injected to coat $80K$ particles.

As already explained, the scaling of the droplet-solid collision algorithm, Figure 6.13b, needs improving, as the number of droplets that might be involved in a simulation of considerable size is very high. In order to improve upon this issue, the fine collision detection must be modified. In the original algorithm, the line joining the current (P_0) and projected positions (P_1) has to be computed with all the triangles imported from the surface tessellation of the particle, that are stored in an array. This data structure forces the algorithm to run trough all the triangles until the correct one is found, which is efficient if the required triangle is stored close to the beginning of the array, but costly in the remaining cases. To improve upon this, the imported triangles are stored in a tree data structure [203], instead of a regular list of triangles. This data structure stores the triangle nodes by proximity and allows for a more efficient search of intersecting line-triangles by running the parent or child of a particular node. The times required to solve the two submodels and the whole CFD model are shown Figure 6.14.

This figure shows the scaling of the collision algorithm with the number of particles injected in the domain. As readily obvious, this approach significantly improves the scaling features of the droplet-solid collision detection, which enables running cases in which there are a large number of droplets in the system.

The final variable to study from a performance standpoint is the spatial core decomposition that is more favorable to achieve an efficient use of the computational

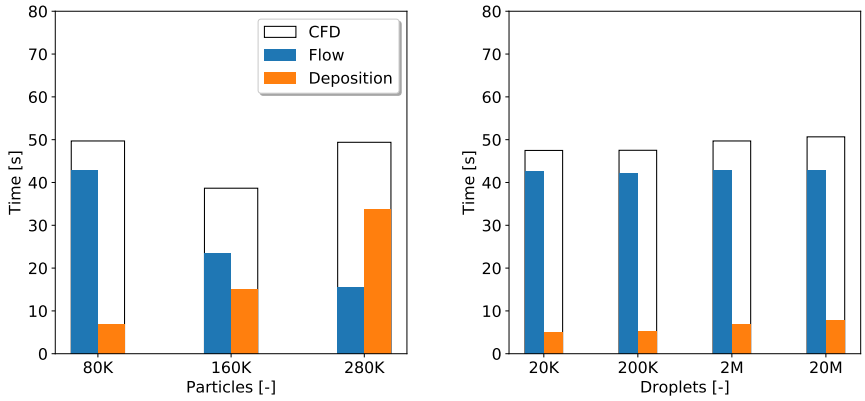

Figure 6.14. Code profiling considering the tree-based droplet contact detection, for the cases: (a) number of particles coated with an injection of $2M$ droplets, (b) droplets injected to coat $80K$ particles.

resources. This spatial decomposition determines the number or cores that are given to solve each dimension, Figure 6.15a. When a node of 24 cores is used to solve $240K$ particles, a number of core combinations can be proposed and each of them lead to a slightly different timing, Figure 6.15b. In every case, the *DEM* side of the simulation takes orders of magnitude longer than the solution of the *CFD* side, as the neighbor list building and solid-solid contact detection takes most of the time. However, the relative timing for each decomposition into *CFD* and *DEM* sides is approximately constant. The $2x2x6$ decomposition (see axis reference frame in Figure 6.15a) offers the fastest solution, while the $1x1x24$ resulting in the worst performance of the tested combinations. In the case of LIGGGHTS®, the spatial decomposition is not static, but changes throughout the simulation, as particles move by expanding or contracting the bounding boxes of each of the processors in all dimensions. Therefore, as the fountain gets expanded and particles are shot up, the spout algorithm acts upon the z dimension in order to accommodate the new particle distribution location. In addition, the location of neighboring particles gets significantly faster if each particle contains all its neighbors within the same processor. However, when too many slabs of particles are introduced in a single dimension ($1x1x24$ decomposition), the neighbor list building routine has to retrieve considerable information from the other processors, which severely hinders the overall performance of the code.

Regarding the $3x2x4$ decomposition, the performance is increased as the number

of slabs are reduced in the z dimension. However, the use of a $3x2$ decomposition in the conical section seems to require some communication, thus suggesting the use of a $2x2$ base for an efficient DEM solution. In the case of the CFD algorithm, Figure 6.15b, a similar trend to the one already explained is shown. In this case however, OpenFOAM® does not dynamically balance the cells by default, as these simulations use static meshes. The increased performance shown in the CFD side is thus attributed to a more balance distribution of the number of cells. Therefore, in order to achieve a sensible performance for n cores, a decomposition of $2x2x\frac{n}{4}$ is recommended for both CFD and DEM sides.

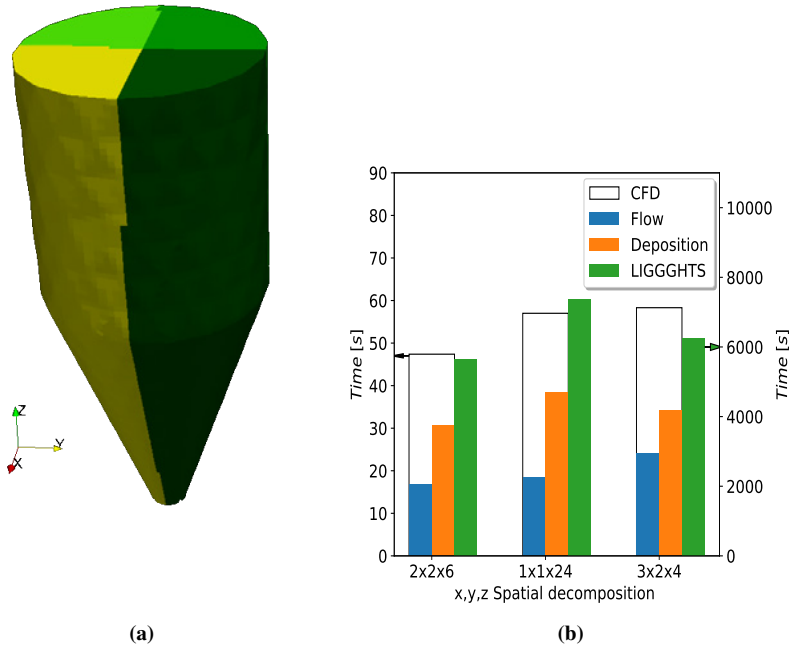

(a) **(b)**

Figure 6.15. Graphical representation of (a) $2x2x1$ spatial decompositions and (b) performance of different spatial decomposition when coating $240K$ particles with $2M$ droplets in the conical spouted bed.

7 Conclusions

The studies carried out in this thesis allowed obtaining results on the hydrodynamic performance of different configuration spouted beds and on the subsequent simulation of these beds made up with regular and irregular particles of various shapes. The overall study was carried out using different internal devices and operating conditions. The main conclusions drawn concerning the different aspects analyzed are as follows:

Hydrodynamic analysis of spouted beds

The hydrodynamic performance of the conical spouted has been characterized based on the analysis of nominal pressure drop fluctuations in both time and power (FFT) domain, and the monitoring of the minimum spouting velocity and fountain height. Bed materials, internal devices and operating flow rates significantly affect the mentioned parameters.

Pressure fluctuations show dominant frequencies at 5 Hz and 10 Hz when internal devices are used with flow rates close to the minimum one required for spouting, and they shift to higher values as the air flow rate is increased. The minimum spouting velocities are reasonably well predicted by the correlations published by Altzibar et al. [103].

A technique based on Particle Tracking Velocimetry (PTV) specifically set up and tuned for these types of systems has been proven to accurately monitor particle tracking with an error well below 10%. The equipment and the codes built on purpose allow obtaining solid velocity profiles within the different zones in the spouted bed, which are required for validating the simulation model.

The shape of the axial profiles of solid velocity along the contactor axis is influenced by the presence and type of draft tube. Thus, axial profiles are flatter (less pronounced peak velocity close to the bottom) as the draft tube aperture ratio is decreased, which is basically due to a more dilute spout zone. Regarding the effect of the internal devices on the radial profiles, as the aperture ratio of the draft tubes is smaller, the solid velocities along the radial direction in the annular zone are lower due to the lower transfer rate from the annulus into the spout, and therefore the lower u_{ms} required for operation. The same trends apply for the prismatic spouted bed, albeit only the configuration without tube (WDT) has been employed.

Modeling and simulation of regular and irregular particles

The methodology based on the angle of repose of the heap is suitable for obtaining *DEM* frictional coefficients for lentils, *ABS* pellets and $2,3$ and 4 *mm* glass beads. These values perform well in the *CFD-DEM* simulations for the configurations studied, namely, without draft tube (WDT), with opened-sided draft tube ($OSDT$) and with solid draft tube (SDT), in a considerable range of air flow rates, 1.1, 1.25 and 1.5 u_{ms}.

Validation of the drag models in the literature for regular materials using the axial and radial *PTV* data has proven that the one by Beetstra et al. [140] is that of best fit. In the case of irregular particles, the best overall fit is obtained by Sanjeevi et al. model [169], which provides good predictions for almost all configurations and flow rates. However, this model is not able to predict the correct trends for *ABS* pellets in prismatic spouted beds, as it is not meant for other particles than ellipsoids. For this case, the correlation by Bagheri & Bonadonna [173] has proven to be the most suitable, which, although under-estimates drag force for ellipsoids, provides reasonable values for even high aspect ratio particles. In addition to the drag force, lift and pitching torque forces are also required for superquadric particles in order to account for the rotation caused by their irregular shape.

The *CFD-DEM* model based on mass, momentum and force balances allows calculating gas and particles velocity profiles, void fraction profiles, particle cycle times and gas residence times. Particle velocity profiles have been used for model validation and gas velocity profiles are the basis for determining the residence time of the gas.

The void fraction in the spout shows a descending trend with bed height from the inlet to the upper surface of the bed, which is explained by particle incorporation from the annulus into the spout along its whole length. As the flow rate is in-

creased or the draft tube aperture ratio is reduced, this trend gets flatter, as a more dilute spout is formed.

The simulated mean cycle times closely follow the values given by a previous correlation by our research team, with the maximum deviation being in the *SDT* configuration, which is explained by a slight change in this configuration from the one corresponding to the correlation. In addition to the mean cycle time, these simulations allow obtaining the whole cycle time distribution, which is a highly interesting information in these applications in which a rigorous control of the cycle time is required. The WDT configuration shows a time distribution skewed towards short cycle times, as particles can enter the spout at any height of the reactor and there is a fraction that makes short cycles close to the bed surface. The *SDT* configuration leads to a similar distribution as the one for the WDT configuration, but shifted to higher cycle times, as particles cannot enter the spout in any other place but the entrainment zone. Finally, the distribution for the *OSDT* configuration is somewhat intermediate between the other two, although it is closer to the one for WDT.

The *CFD-DEM* model allows an accurate estimation of the average residence time of the gas through the RTD curve determined by conducting a step injection in the simulation. The presence of the draft tube, specially at high flow rates, has a great impact on the residence time. Thus, their presence creates enough shear in the spout region to by-pass a great fraction of the inlet air through this zone.

The insertion of the fountain confiner enhances gas mixing, and therefore is a highly interesting device for this purpose. Thus, it removes all the dead zones over the annular zone, which means this device is also useful for controlling the average residence time. Moreover, this device shortens the particle cycle time, with this reduction being strongly influenced by the bed-to-confiner (H_f) distance. This parameter along with the flow rate are crucial parameters for attaining a good gas mixing regime and the desired distribution of the particle cycle time for a given solid and design requirements.

Spray coating of irregular particles in spouted beds

A novel spray coating algorithm has been built, which allows running the direct droplet-solid contact detection in a scalable manner through the use of a surface tessellation of varying resolutions. In addition, droplet-particle torque has been implemented so as to capture particle increased rotation when being hit by the spray at high velocities, as the angular velocity increases the number of faces that can be hit by the coating agent.

The surface tessellation developed allows determining not only the particles that are being coated, but also the locations on their surfaces that are being coated. Therefore, the model may predict particle coating irregularities, as well as the inter tablet coating variation or variance. These features enable to determine the time required to coat uniformly a batch of particles and the effect tablet shape, contactor geometry and nozzle location have on this time. The coating uniformity suggest that pellets are difficult to coat due to their flat faces and that an ellipsoid is more suited for this process.

An analysis of the the scaling up of the algorithm for the coating process has proven that the best spatial decomposition for conical spouted beds with a given number of droplets is achieved through the 2x2xn decomposition and the use of an octree mesh for the tessellation. The scaling up by increasing the number of particles is considerably worse, but the resulting algorithm may still cope with reasonably sized problems (300K particles with 20 M droplets) to be solved at high surface tessellation resolutions.

List of Tables

List of Figures

Nomenclature

Acronyms

AABB	Axis Aligned Bounding Box
ABS	Acrylonitrile Butadiene Styrene
CFD	Computational Fluid Dynamics
CMOS	Complementary Metal-Oxide Semiconductor
CN	Common Normal
CPU	Central Processing Unit
DEM	Discrete Element Method
FC	Fountain Confiner
FDR	Fourteen Data Rate
FFT	Fast Fourier Transform
GAMP	Geometric Agglomerated Algebraic Multigrid
GJK	Gilbert–Johnson–Keerthi Distance algorithm
GP	Geometric Potential
KH-RT	Kelvin-Helmholtz Rayleigh-Taylor
KTGF	Kinetic Theory of Granular Flows
LAMMPS	Large Atomic Model Massively Parallel Simulator
LB	Lattice Boltzmann
LES	Large Eddy Simulation
LIGGGHTS	*LAMMPS* Improved for General Granular and Granular Heat Transfer Simulations
LISA	Linearized Instability Jet Atomization

MPI	Message Passing Interface
MPPIC	Multiple Particle Parcels In Cell
MS	Multi-Sphere
MUSCL	Monotonic Upstream-centered Scheme for Conservation Laws
NVE	Constant atom Number, Volume and Energy
OSDT	Open-Sided Draft Tube
PET	Polyethylene Terephtalate
PISO	Pressure Implicit with Split Operator
PIV	Particle Image Velocimetry
PLC	Programmable Locic Controler
PTV	Particle Tracking Velocimetry
QUICK	Quadratic Upstream Interpolation for Convective Kinematics
ROI	Region Of Interest
RSC	Recursive Coordinate Bisection
RSM	Reynolds Stress Model
RTD	Residence Time Distribution
SDT	Solid Draft Tube
SIMPLE	Semi-Implicit Method for Pressure-Linked Equations
SQ	Superquadric
TAB	Taylor Analogy Breakup
TFM	Two Fluid Model
TPU	Thermoplastic Polyurethane
WDT	Without Draft Tube

Dimensionless Numbers

Ar	Archimedes number
Pe	Péclet adimensional number
Re	Reynolds number
We	Weber number

Greek Symbols

α, β	Probability distribution shape factors

α_2	Empirical value	
β'	Swarm packing correction	
β_2	Empirical value	
$\beta_{f,s}$	Gas-Solid momentum exchange term	$kg\ m^{-3}\ s^{-1}$
χ	Void fraction function correction	
$\delta_t,\ \delta_n$	Tangential and normal overlapping distance	m
ΔL	Width of the porous media	m
ΔP_M	Peak pressure drop	Pa
ΔP_s	Stable pressure drop	Pa
Δt	Time step	s
ε_i	Volumetric void fraction of i-th phase	px
ε_t	Turbulence dissipation term	$J\ kg^{-1}\ s^{-1}$
γ	Contactor angle	^{o}
Γ_i	Potential distance to superquadric surface of i-th particle	m
$\gamma_n,\ \gamma_t$	Tangential and normal dash-pot coefficient	$kg\ m^{-1}$
κ	Turbulent kinetic energy	$J\ kg^{-1}$
κ_N	Newton drag correction	
κ_S	Stoke drag correction	
λ	Particle angle of attack	^{o}
$\rho_\mathbf{i}$	Density of i-th phase	$kg\ m^{-3}$
μ	Fluid kinematic viscosity	$Pa\ s$
μ_t	Turbulent viscosity	$kg\ m^{-1}\ s^{-1}$
ν_i	Poisson ratio of i-th particle	
ω_g^2	Gas residence time variance	s^2
ω_H	Draft tube leg width	m
ω_i	Angular velocity of i-th particle	s^{-1}
ω_T	Draft tube opening ratio	
ϕ	Sphericity	
$\phi_\parallel$	Ratio between the cross-sectional area of the volume equivalent sphere and the difference between half the surface area	
$\phi_\perp$	Ratio between the cross-sectional area of the volume equivalent sphere and the projected cross-sectional area	

ψ	Particle shape factor	
$\Psi_{\parallel}$	Stream wise particle projected area	m^2
$\Psi_{\perp}$	Stream perpendicular particle projected area	m^2
σ	Liquid surface tension	$J\,m^{-2}$
$\sigma_{\varepsilon_t}, \sigma_{\kappa}$	k-ε turbulence model constants	
τ_0	Droplet collision contact time	s
$\tau_{st},\ \tau_{bg}$	Striping and bagging characteristic break-up time	s
θ	Scalar field	
ξ	Circularity	

Latin Symbols

A	Syamlal A coefficient	
a_i	Linear acceleration of i-th particle	$m\,s^{-2}$
a_{1-5}	Sanjeevi coefficient for the drag or lift force	
B	Syamlal B coefficient	
$B_{\alpha,\beta}$	Beta probability distribution	m
$C(t)$	Tracer concentration at time t	
C_0	Inlet tracer concentration	
C_1, C_2	k-ε turbulence model constants	
C_D	Drag coefficient	
C_L	Lift coefficient	m
$C_o V_{intra}$	Inter tablet coating variation	
$C_{1,d}, D_{2,d}$	Darcy kinematic and viscous coefficients	
$C_{D,s}$	Drag coefficient of a single sphere	
C_{na}	Non assignment cost	
$c_{x,y}$	Field of view in x and y directions	px
D_b	Diameter of the bed surface	m
D_c	Diameter of the cylindrical section	m
D_i	Conical base diameter	m
D_i	Detection of i-th posible particle	px
D_o	Inlet spouted bed diameter	m
D_T	Draft tube diameter	m
$d_{st},\ d_{bg}$	Striping and bagging characteristic pseudo stable droplet size	m

d_0	Minimum size of the droplet distribution	m
d_1	Maximum size of the droplet distribution	m
$\bar{d_p}$	Mean particle Shauter diameter	m
E_{ij}	Shear Reynolds stress	$kg\ m^{-1}\ s^{-2}$
E_i	Young modulus of i-th particle	$kg\ m^{-1}\ s^{-2}$
e	Elongation shape value	
e_r	Rolling friction	
F_N	Newton shape descriptor	
F_S	Stoke form factor	
$F_{1,3}$	Koch-Hill coefficients	
f	Flatness shape value	
H_c	Conical section height	m
H_f	Bed to confiner relative distance	m
H_i	Location height in the contactor	m
H_o	Initial bed height	m
$\bar{H_f}$	Average fountain height	m
I	Particle height	m
k	Harmonic number of sin function	
k_n, k_t	Tangential and normal spring coefficient	$kg\ m^{-2}$
$k_{1,2,3}$	Fitting radial distortion correction coefficients	
L	Particle length	m
L_c	Inlet slit length in prismatic spouted beds	m
L_H	Draft tube entrainment height	m
L_i	Inlet slit width in prismatic spouted beds	m
L_T	Draft tube total length	m
m_0	Initial mass load of the bed	kg
m_i	Mass of i-th phase	kg
n	Droplet distribution order	
$n_1,\ n_2$	Superquadric blockiness coefficient	
P_c	Perimeter of equivalent to the maximum projection area of the particle	m
P_i	Projected position of i-th track	px
P_{mp}	Maximum projection perimeter	m

p	Static pressure	Pa
p_p	Particle-Particle restitution coefficient	
$p_{1,2}$	Fitting tangential distortion correction coefficients	
q_i	Quaternion of i-th particle	
r_{Max}	Maximum radial position at a given contactor height	m
r_i	Radius of i-th particle	m
$r_{x,y,z}$	Superquadric shape value	m
S	Particle width	m
s	Skewness of the sensor pixels	
t	Time	s
$\bar{t_c}$	Average particle cycle time	s
$\bar{t_g}$	Average gas residence time	s
V	Volume	m^3
v_t	Terminal velocity of the particle in the medium	$m\,s^{-1}$
$w_{i,j}$	Weight of the i, j cell of the irregular particle void fraction	

Matrices and Vectors

$\mathbf{c_i}$	Vector to centroid of i-th particle	m
$\mathbf{e_o}$	Normal vector of the maximum area orientation	
$\mathbf{F_i}$	Flux through face i	$kg\,m^{-2}s^{-1}$
$\mathbf{F_T}$	Exerted torque force	$N\,m$
$\mathbf{g}$	Gravitational acceleration vector	$m\,s^{-2}$
$\mathbf{I_i}$	Moment of inertia of i-th particle	$kg\,m^{-2}$
$\mathbf{n}$	Face normal vector	
$\mathbf{S_i}$	Area vector of face i	m^2
$\mathbf{T_i}$	Torque of i-th particle	$N\,m$
$\mathbf{u_r}$	Gas-Solid relative velocity vector	$m\,s^{-1}$
$\mathbf{u}$	Fluid velocity vector	$m\,s^{-1}$
$\mathbf{v_i}$	Solid velocity vector	$m\,s^{-1}$

Superscript

$''$	Guessed field
n	Previous time step

$n+1$	Current time step

Subscript

C	Cell
$Corr$	Correlated
c	Centroid
Exp	Experimental
eq	Equivalent volume
ms	Minimum spouting
p	Particle
Sim	Simulated
t	Terminal

Mathematical Symbols

$\mathbf{O}$	Time complexity
∇	Nabla operator
∇^2	Laplacian operator

Bibliography

[1] O. Levenspiel. *Chemical reaction engineering*. Wiley, 1999, p. 668.

[2] M. Saidi et al. "A review on pulsed flow in gas-solid fluidized beds and spouted beds: Recent work and future outlook". In: *Advanced Powder Technology* 30.6 (2019), pp. 1121–1130.

[3] R. Aguado et al. "Influence of the kinetic scheme and heat balance on the modelling of biomass combustion in a conical spouted bed". In: *Energy* 175 (2019), pp. 758–767.

[4] M. Artetxe et al. "Styrene recovery from polystyrene by flash pyrolysis in a conical spouted bed reactor". In: *Waste Management* 45 (2015), pp. 126–133.

[5] J. Alvarez et al. "Evolution of biomass char features and their role in the reactivity during steam gasification in a conical spouted bed reactor". In: *Energy Conversion and Management* 181 (2019), pp. 214–222.

[6] P. Kieckhefen et al. "Simulation of spray coating in a spouted bed using recurrence CFD". In: *Particuology* 42 (2019), pp. 92–103.

[7] M. Olazar et al. "Design and Operation of a Catalytic Polymerization Reactor in a Dilute Spouted Bed Regime". In: (1997).

[8] P. Mollick et al. "Deposition of diversely textured buffer pyrolytic carbon layer in TRISO coated particle by controlled manipulation of spouted bed hydrodynamics". In: *Chemical Engineering Science* 128 (2015), pp. 44–53.

[9] D. Geldart. "Types of gas fluidization". In: *Powder Technology* 7.5 (1973), pp. 285–292.

[10] Z. Rahimi-Ahar and M. S. Hatamipour. "Hydrodynamics, numerical study and application of spouted bed". In: *Reviews in Chemical Engineering* 34.6 (2018), pp. 743–766.

[11] M. Olazar et al. "Solid Flow in Jet Spouted Beds". In: *Industrial & Engineering Chemistry Research* 35.8 (1996), pp. 2716–2724.

[12] X. Yang et al. “Time-resolved characterization of a flat-base spouted bed with a high speed X-ray system”. In: *Chemical Engineering Journal* 254 (2014), pp. 143–152.

[13] X. Chen et al. “Using stereo XPTV to determine cylindrical particle distribution and velocity in a binary fluidized bed”. In: *AIChE Journal* 65.2 (2018), aic.16485.

[14] H. C. Park and H. S. Choi. “Visualization of flow structures inside a conical spouted bed by electrical capacitance volume tomography”. In: *Particuology* 42 (2019), pp. 15–25.

[15] M. Bieberle and F. Barthel. “Combined phase distribution and particle velocity measurement in spout fluidized beds by ultrafast X-ray computed tomography”. In: *Chemical Engineering Journal* 285 (2016), pp. 218–227.

[16] T. Al-Juwaya et al. “Investigation of cross-sectional gas-solid distributions in spouted beds using advanced non-invasive gamma-ray computed tomography (CT)”. In: *Experimental Thermal and Fluid Science* 86 (2017), pp. 37–53.

[17] N. Ali et al. “An advanced evaluation of spouted beds scale-up for coating TRISO nuclear fuel particles using Radioactive Particle Tracking (RPT)”. In: *Experimental Thermal and Fluid Science* 80 (2017), pp. 90–104.

[18] L. Spreutels et al. “Experimental investigation of solid particles flow in a conical spouted bed using radioactive particle tracking”. In: *AIChE Journal* 62.1 (2016), pp. 26–37.

[19] G. Mohs et al. “Magnetic monitoring of a single particle in a prismatic spouted bed”. In: *Chemical Engineering Science* 64.23 (2009), pp. 4811–4825.

[20] E. E. Patterson et al. “Innovative Method Using Magnetic Particle Tracking to Measure Solids Circulation in a Spouted Fluidized Bed”. In: *Industrial & Engineering Chemistry Research* 49.11 (2010), pp. 5037–5043.

[21] D. A. Santos et al. “Disturbances in the Hydrodynamic Behavior of a Spouted Bed Caused by an Optical Fiber Probe: Experimental and CFD Study”. In: *Industrial & Engineering Chemistry Research* 51.9 (2012), pp. 3801–3810.

[22] M. J. San José et al. “Local Bed Voidage in Conical Spouted Beds”. In: *Industrial & Engineering Chemistry Research* 37.6 (1998), pp. 2553–2558.

[23] L. Qian et al. “Developing a High Speed Fiber-optic Endoscopic Technique for Statistical Analysis of Particle Phase Velocity”. In: *Procedia Engineering* 102.423 (2015), p. 423.

[24] J. Yang et al. “Determination of flow patterns by a novel image analysis technique in a rectangular spouted bed”. In: *Powder Technology* 334 (2018), pp. 151–162.

[25] T. Dracos. “Particle Tracking Velocimetry (PTV)”. In: Springer, Dordrecht, 1996, pp. 155–160.

[26] A. H. Thaker et al. “PIV measurements and CFD simulations of the particle-scale flow distribution in a packed bed”. In: *Chemical Engineering Journal* 374 (2019), pp. 189–200.

[27] M. Dudukovic. “Trends in catalytic reaction engineering”. In: *Catalysis Today* 48.1-4 (1999), pp. 5–15.

[28] H. Jakobsen. *Chemical Reactor Modeling*. 2014.

[29] Y. Gao et al. “On lumped-reduced reaction model for combustion of liquid fuels”. In: *Combustion and Flame* 163 (2016), pp. 437–446.

[30] F. Cavalcanti et al. “A catalyst selection method for hydrogen production through Water-Gas Shift Reaction using artificial neural networks”. In: *Journal of Environmental Management* 237 (2019), pp. 585–594.

[31] J. Thybaut and G. Marin. “Single-Event MicroKinetics: Catalyst design for complex reaction networks”. In: *Journal of Catalysis* 308 (2013), pp. 352–362.

[32] G. Kimaev and L. A. Ricardez-Sandoval. “Multilevel Monte Carlo for noise estimation in stochastic multiscale systems”. In: *Chemical Engineering Research and Design* 140 (2018), pp. 33–43.

[33] N. Deen et al. “Review of discrete particle modeling of fluidized beds”. In: *Chemical Engineering Science* 62.1-2 (2007), pp. 28–44.

[34] J. Solsvik et al. “Modeling and simulation of bubbling fluidized bed reactors using a dynamic one-dimensional two-fluid model: The sorption-enhanced steam–methane reforming process”. In: *Advances in Engineering Software* 80.C (2015), pp. 156–173.

[35] M. Andrews and P. O’Rourke. “The multiphase particle-in-cell (MP-PIC) method for dense particulate flows”. In: *International Journal of Multiphase Flow* 22.2 (1996), pp. 379–402.

[36] B. W. Fitzgerald et al. “Multiscale simulation of elongated particles in fluidised beds”. In: *Chemical Engineering Science: X* 2 (2019), p. 100019.

[37] A. Amsden and F. Harlow. “The SMAC Method: A numerical Technique for Calculating Incompressible Fluid Flows”. In: *Journal of Computational Physics* 6.2 (1970), pp. 322–325.

[38] T. Anderson and R. Jackson. “Fluid Mechanical Description of Fluidized Beds. Equations of Motion”. In: *Industrial & Engineering Chemistry Fundamentals* 6.4 (1967), pp. 527–539.

[39] D. A. Drew. “Averaged Field Equations for Two-Phase Media”. In: *Studies in Applied Mathematics* 50.2 (1971), pp. 133–166.

[40] Message Passing Interface Forum. *A Message-Passing Interface Standard*. Tech. rep. 2015.

[41] F. Moukalled et al. *The Finite Volume Method in Computational Fluid Dynamics*. Vol. 113. Fluid Mechanics and Its Applications. Cham: Springer International Publishing, 2016.

[42] H. R. Norouzi et al. *Coupled CFD-DEM Modeling : Formulation, Implementation and Application to Multiphase Flows.* P. 433.

[43] E. Robertson et al. “Validation of OpenFOAM numerical methods and turbulence models for incompressible bluff body flows”. In: *Computers & Fluids* 123 (2015), pp. 122–145.

[44] X. Loyseau et al. “Scale-up and turbulence modelling in pipes”. In: *Journal of Petroleum Science and Engineering* 162 (2018), pp. 1–11.

[45] K. Stüben. “A review of algebraic multigrid”. In: *Journal of Computational and Applied Mathematics* 128.1-2 (2001), pp. 281–309.

[46] N. Brilliantov et al. “A model for collisions in granular gases”. In: *Physical Review E* 53.5 (1996), pp. 5382–5392.

[47] H. Chen et al. “Effect of Young’s modulus on DEM results regarding transverse mixing of particles within a rotating drum”. In: *Powder Technology* 318 (2017), pp. 507–517.

[48] J. Ai et al. “Assessment of rolling resistance models in discrete element simulations”. In: *Powder Technology* 206.3 (2011), pp. 269–282.

[49] Y. Zhou et al. “Rolling friction in the dynamic simulation of sandpile formation”. In: *Physica A: Statistical Mechanics and its Applications* 269.2-4 (1999), pp. 536–553.

[50] P. Gopalakrishnan and D. Tafti. “Development of parallel DEM for the open source code MFIX”. In: *Powder Technology* 235 (2013), pp. 33–41.

[51] P. J. in ’t Veld et al. “Accurate and efficient methods for modeling colloidal mixtures in an explicit solvent using molecular dynamics”. In: *Computer Physics Communications* 179.5 (2008), pp. 320–329.

[52] M. Kodam et al. “Cylindrical object contact detection for use in discrete element method simulations. Part I – Contact detection algorithms”. In: *Chemical Engineering Science* 65.22 (2010), pp. 5852–5862.

[53] G. Lu et al. “Discrete element models for non-spherical particle systems: From theoretical developments to applications”. In: *Chemical Engineering Science* 127 (2015), pp. 425–465.

[54] Y. Guo et al. “Some computational considerations associated with discrete element modeling of cylindrical particles”. In: *Powder Technology* 228 (2012), pp. 193–198.

[55] A. Podlozhnyuk et al. “Efficient implementation of superquadric particles in Discrete Element Method within an open-source framework”. In: *Computational Particle Mechanics* 4.1 (2017), pp. 101–118.

[56] E. G. Gilbert and C. P. Foo. *Computing the Distance Between General Convex Objects in Three-Dimensional Space*. 1990.

[57] A. D. Rakotonirina and A. Wachs. “Grains3D, a flexible DEM approach for particles of arbitrary convex shape - Part II: Parallel implementation and scalable performance”. In: *Powder Technology* 324 (2018), pp. 18–35.

[58] A. Wachs et al. “Grains3D, a flexible DEM approach for particles of arbitrary convex shape - Part I: Numerical model and validations”. In: *Powder Technology* 224 (2012), pp. 374–389.

[59] Barr. “Superquadrics and Angle-Preserving Transformations”. In: *IEEE Computer Graphics and Applications* 1.1 (1981), pp. 11–23.

[60] W. Zhou et al. “A geometric potential-based contact detection algorithm for egg-shaped particles in discrete element modeling”. In: *Powder Technology* 327 (2018), pp. 152–162.

[61] W. Xu et al. “An overlapping detection algorithm for random sequential packing of elliptical particles”. In: *Physica A: Statistical Mechanics and its Applications* 390.13 (2011), pp. 2452–2467.

[62] K. Kildashti et al. “Evaluation of contact force models for discrete modelling of ellipsoidal particles”. In: *Chemical Engineering Science* 177.November 2018 (2018), pp. 1–17.

[63] S. Plimpton. “Fast Parallel Algorithms for Short-Range Molecular Dynamics”. In: *Journal of Computational Physics* 117.1 (1995), pp. 1–19.

[64] M. Uhlmann. “An immersed boundary method with direct forcing for the simulation of particulate flows”. In: *Journal of Computational Physics* 209.2 (2005), pp. 448–476.

[65] K. Walayat et al. “Dynamics of elliptic particle sedimentation with thermal convection”. In: *Physics of Fluids* 30.10 (2018), p. 103301.

[66] M. Trofa et al. “CFD-DEM simulations of particulate fouling in microchannels”. In: *Chemical Engineering Journal* 358 (2019), pp. 91–100.

[67] R. Berger et al. “Hybrid parallelization of the LIGGGHTS open-source DEM code”. In: *Powder Technology* 278 (2015), pp. 234–247.

[68] S. G. Srinivasan et al. “Dynamic-domain-decomposition parallel molecular dynamics”. In: *Computer Physics Communications* 102.1-3 (1997), pp. 44–58.

[69] T. Lichtenegger et al. “Dynamics and long-time behavior of gas–solid flows on recurrent-transient backgrounds”. In: *Chemical Engineering Journal* 364 (2019), pp. 562–577.

[70] S. H. Hosseini et al. “CFD simulation of cylindrical spouted beds by the kinetic theory of granular flow”. In: *Powder Technology* 246 (2013), pp. 303–316.

[71] C. R. Duarte et al. “A study of the fluid dynamics of the spouted bed using CFD”. In: *Brazilian Journal of Chemical Engineering* 22.2 (2005), pp. 263–270.

[72] A. Nikolopoulos et al. “Numerical investigation and comparison of coarse grain CFD – DEM and TFM in the case of a 1 MWth fluidized bed carbonator simulation”. In: *Chemical Engineering Science* 163 (2017), pp. 189–205.

[73] M. Fattahi et al. “CFD simulation of transient gas to particle heat transfer for fluidized and spouted regimes”. In: *Applied Thermal Engineering* 105 (2016), pp. 385–396.

[74] S. Golshan et al. “Hydrodynamics of slot-rectangular spouted beds: Process intensification”. In: *Chemical Engineering Research and Design* 121 (2017), pp. 315–328.

[75] J. Melo et al. “CFD modeling of conical spouted beds for processing LDPE/Al composite”. In: *Chemical Engineering and Processing: Process Intensification* 108 (2016), pp. 93–108.

[76] S. H. Hosseini et al. “CFD Study of hydrodynamic and heat transfer in a 2D spouted bed: Assessment of radial distribution function”. In: *Journal of the Taiwan Institute of Chemical Engineers* 58 (2016), pp. 107–116.

[77] S. H. Hosseini et al. “CFD simulation of gas–solid flow in a spouted bed with a non-porous draft tube”. In: *Chemical Engineering and Processing: Process Intensification* 48.11-12 (2009), pp. 1539–1548.

[78] J. L. V. Neto et al. “Effect of a Draft Tube on the Fluid Dynamics of a Spouted Bed: Experimental and CFD Studies”. In: *Drying Technology* 26.3 (2008), pp. 299–307.

[79] S. Azizi et al. “CFD modeling of a spouted bed with a porous draft tube”. In: *Particuology* 8.5 (2010), pp. 415–424.

[80] D. Gidaspow. *Multiphase flow and fluidization : continuum and kinetic theory descriptions*. Academic Press, 1994, p. 467.

[81] B. Hooshdaran et al. “CFD modeling of heat transfer and hydrodynamics in a draft tube conical spouted bed reactor under pyrolysis conditions: Impact of wall boundary condition”. In: *Applied Thermal Engineering* 127 (2017), pp. 224–232.

[82] R. Walpot. *3D particle tracking velocimetry and statistical analysis of turbulent pipe flow*. april. 2007.

[83] D. Snider. “An Incompressible Three-Dimensional Multiphase Particle-in-Cell Model for Dense Particle Flows”. In: *Journal of Computational Physics* 170.2 (2001), pp. 523–549.

[84] J. Li et al. “Investigation of a bubbling fluidized bed methanation reactor by using CFD-DEM and approximate image processing method”. In: *Chemical Engineering Science* 207 (2019), pp. 1107–1120.

[85] B. Mahmoodi et al. “CFD-DEM simulation of a conical spouted bed with open-sided draft tube containing fine particles”. In: *Journal of the Taiwan Institute of Chemical Engineers* 81 (2017), pp. 275–287.

[86] S. Pietsch et al. “CFD-DEM modeling of a three-dimensional prismatic spouted bed”. In: *Powder Technology* 316 (2017), pp. 245–255.

[87] F. Marchelli et al. “Discrete element method for the prediction of the onset velocity in a spouted bed”. In: *Powder Technology* 321 (2017), pp. 119–131.

[88] C. Moliner et al. “CFD simulation of a spouted bed: Comparison between the Discrete Element Method (DEM) and the Two Fluid Model (TFM)”. In: *Chemical Engineering Journal* (2018), p. 120466.

[89] Y. Liang et al. “A critical validation study on CPFD model in simulating gas–solid bubbling fluidized beds”. In: *Powder Technology* 263 (2014), pp. 121–134.

[90] Y. Tsuji et al. “Discrete particle simulation of two-dimensional fluidized bed”. In: *Powder Technology* 77.1 (1993), pp. 79–87.

[91] S. Yang et al. “Numerical investigation on the effect of draft plates on spouting stability and gas–solid characteristics in a spout-fluid bed”. In: *Chemical Engineering Science* 148 (2016), pp. 108–125.

[92] P. Kieckhefen et al. “Influence of gas inflow modelling on CFD-DEM simulations of three-dimensional prismatic spouted beds”. In: *Powder Technology* 329 (2018), pp. 167–180.

[93] M. Liu et al. “CFD–DEM–CVD multi-physical field coupling model for simulating particle coating process in spout bed”. In: *Particuology* 42 (2019), pp. 67–78.

[94] H. Boujjat et al. “Numerical simulation of reactive gas-particle flow in a solar jet spouted bed reactor for continuous biomass gasification”. In: *International Journal of Heat and Mass Transfer* 144 (2019), p. 118572.

[95] D. Liu et al. “Simulation of char and propane combustion in a fluidized bed by extending DEM–CFD approach”. In: *Proceedings of the Combustion Institute* 33.2 (2011), pp. 2701–2708.

[96] L. Li et al. “Modeling of spout-fluidized beds and investigation of drag closures using OpenFOAM”. In: *Powder Technology* 305 (2017), pp. 364–376.

[97] C. Coetzee. “Review: Calibration of the discrete element method”. In: *Powder Technology* 310 (2017), pp. 104–142.

[98] X. Liu et al. “Particle shape effects on dynamic behaviors in a spouted bed: CFD-DEM study”. In: *Powder Technology* (2019).

[99] W. Zhong et al. “DEM/CFD-DEM Modelling of Non-spherical Particulate Systems: Theoretical Developments and Applications”. In: *Powder Technology* 302 (2016), pp. 108–152.

[100] X. Zhao et al. “Flow patterns of solids in a two-dimensional spouted bed with draft plates: PIV measurement and DEM simulations”. In: *Powder Technology* 183.1 (2008), pp. 79–87.

[101] M. Rackl and K. J. Hanley. “A methodical calibration procedure for discrete element models”. In: *Powder Technology* 307 (2017), pp. 73–83.

[102] J. Saldarriaga et al. “Correlations for calculating peak and spouting pressure drops in conical spouted beds of biomass”. In: *Journal of the Taiwan Institute of Chemical Engineers* 80 (2017), pp. 678–685.

[103] H. Altzibar et al. “Particle Cycle Times and Solid Circulation Rates in Conical Spouted Beds with Draft Tubes of Different Configuration”. In: *Industrial & Engineering Chemistry Research* 52.45 (2013), pp. 15959–15967.

[104] M. Olazar et al. “Design factors of conical spouted beds and jet spouted beds”. In: *Industrial & Engineering Chemistry Research* 32.6 (1993), pp. 1245–1250.

[105] M. J. San José et al. “Operating Conditions of Conical Spouted Beds with a Draft Tube. Effect of the Diameter of the Draft Tube and of the Height of Entrainment Zone”. In: *Industrial & Engineering Chemistry Research* 46.9 (2007), pp. 2877–2884.

[106] H. Altzibar et al. “Fountain confined conical spouted beds”. In: *Powder Technology* 312 (2017), pp. 334–346.

[107] I. Estiati et al. “Fine particle entrainment in fountain confined conical spouted beds”. In: *Powder Technology* 344 (2019), pp. 278–285.

[108] I. Estiati et al. “Influence of the fountain confiner in a conical spouted bed dryer”. In: *Powder Technology* 356 (2019), pp. 193–199.

[109] J. Saldarriaga et al. “Minimum spouting velocity for conical spouted beds of vegetable waste biomasses”. In: *Journal of the Taiwan Institute of Chemical Engineers* 60 (2016), pp. 509–519.

[110] V. Salikov et al. “Characterization and CFD-DEM modelling of a prismatic spouted bed”. In: *Powder Technology* 270 (2015), pp. 622–636.

[111] Y. X. Qiang et al. “A New Efficient Ellipse Detection Method”. In: *International Conference On Pattern Recognition 2002* 2 (2002), p. 20957.

[112] G. Farnebäck and G. Farnebäck. “Two-Frame Motion Estimation Based on Polynomial Expansion”. In: *Scandinavian Conference on Image Analysis*. Vol. 2749. 2003.

[113] J. Munkres. “Algorithms for the Assignment and Transportation Problems”. In: *Journal of the Society for Industrial and Applied Mathematics* 5.1 (1957), pp. 32–38.

[114] K. Date and R. Nagi. “GPU-accelerated Hungarian algorithms for the Linear Assignment Problem”. In: *Parallel Computing* 57 (2016), pp. 52–72.

[115] N. Mostoufi et al. “Flow structure characterization in conical spouted beds using pressure fluctuation signals”. In: *Powder Technology* 269 (2015), pp. 392–400.

[116] J. Xu et al. “Statistical and frequency analysis of pressure fluctuations in spouted beds”. In: *Powder Technology* 140.1-2 (2004), pp. 141–154.

[117] Y. Chen et al. “Characterization of pressure fluctuations from a gas-solid fluidized bed by structure density function analysis”. In: *Chemical Engineering Science* 129 (2015), pp. 156–167.

[118] M. Olazar et al. “Pressure drop in conical spouted beds”. In: *The Chemical Engineering Journal* 51.1 (1993), pp. 53–60.

[119] H. Altzibar et al. “Hydrodynamics of Conical Spouted Beds Using Different Types of Internal Devices”. In: *Chemical Engineering & Technology* 32.3 (2009), pp. 463–469.

[120] A. Markowski and W. Kaminski. “Hydrodynamic characteristics of jet-spouted beds”. In: *The Canadian Journal of Chemical Engineering* 61.3 (1983), pp. 377–381.

[121] A. G. I. Mukhlenov. “Hydraulic resistance of a fluidized bed in a cyclone without a grate. II. Critical gas rate corresponding to the beginning of jet formation”. In: *Zh Prikl Khim* 37 (1964), pp. 1887–1893.

[122] H. Gao et al. “Statistical and frequency analysis of pressure fluctuation in an annular spouted bed of coarse particles”. In: *Powder Technology* 317 (2017), pp. 216–223.

[123] W. Zhong and M. Zhang. “Pressure fluctuation frequency characteristics in a spout-fluid bed by modern ARM power spectrum analysis”. In: *Powder Technology* 152.1-3 (2005), pp. 52–61.

[124] M. J. San José et al. “Local porosity in conical spouted beds consisting of solids of varying density”. In: *Chemical Engineering Science* 60.7 (2005), pp. 2017–2025.

[125] M. J. San José et al. “Spout and fountain geometry in conical spouted beds consisting of solids of varying density”. In: *Industrial and Engineering Chemistry Research* 44.1 (2005), pp. 193–200.

[126] M. J. San José et al. “Solid Cross-Flow into the Spout and Particle Trajectories in Conical Spouted Beds Consisting of Solids of Different Density and Shape”. In: *Chemical Engineering Research and Design* 84.6 (2006), pp. 487–494.

[127] S. Wang et al. “Numerical simulation of flow behavior of particles in an inverse liquid–solid fluidized bed with a jet using CFD-DEM”. In: *Journal of the Taiwan Institute of Chemical Engineers* 82 (2018), pp. 214–225.

[128] P. G. Saffman. “The lift on a small sphere in a slow shear flow”. In: *Journal of Fluid Mechanics* 22.2 (1965), pp. 385–400.

[129] F. Farivar et al. “CFD-DEM simulation of fluidization of multisphere- modelled cylindrical particles”. In: *Powder Technology* (2019).

[130] M. Syamlal and T. O’Brien. “Simulation of granular layer inversion in liquid fluidized beds”. In: *International Journal of Multiphase Flow* 14.4 (1988), pp. 473–481.

[131] M. Syamlal et al. *MFIX Documentation Theory Guide Technical Note*. Tech. rep. 1993.

[132] C. Y. Wen and Y. H. Yu. “A generalized method for predicting the minimum fluidization velocity”. In: *AIChE Journal* 12.3 (1966), pp. 610–612.

[133] S. Ergun and A. A. Orning. “Fluid Flow through Randomly Packed Columns and Fluidized Beds”. In: *Industrial & Engineering Chemistry* 41.6 (1949), pp. 1179–1184.

[134] L. Huilin et al. “Hydrodynamic simulation of gas–solid flow in a riser using kinetic theory of granular flow”. In: *Chemical Engineering Journal* 95.1-3 (2003), pp. 1–13.

[135] S. Dahl and C. Hrenya. “Size segregation in gas–solid fluidized beds with continuous size distributions”. In: *Chemical Engineering Science* 60.23 (2005), pp. 6658–6673.

[136] J. Leboreiro et al. “Revisiting the standard drag law for bubbling, gas-fluidized beds”. In: *Powder Technology* 183.3 (2008), pp. 385–400.

[137] R. Di Felice. “The voidage function for fluid-particle interaction systems”. In: *International Journal of Multiphase Flow* 20.1 (1994), pp. 153–159.

[138] R. J. Hill et al. “The first effects of fluid inertia on flows in ordered and random arrays of spheres”. In: *Journal of Fluid Mechanics* 448 (2001), pp. 213–241.

[139] R. J. Hill et al. “Moderate-Reynolds-number flows in ordered and random arrays of spheres”. In: *Journal of Fluid Mechanics* 448 (2001), pp. 243–278.

[140] R. Beetstra et al. “Drag force of intermediate Reynolds number flow past mono- and bidisperse arrays of spheres”. In: *AIChE Journal* 53.2 (2007), pp. 489–501.

[141] J. S. Marshall et al. “Fluid Forces on Particles”. In: *Adhesive Particle Flows*. Cambridge University Press, 2014, pp. 130–181.

[142] D. L. Koch and R. J. Hill. *Inertial Effects In Suspension And Porous-Media Flows*. Tech. rep. 2000.

[143] R. L. Brown and J. C. Richards. “Principles of powder mechanics : essays on the packing and flow of powders and bulk solids”. In: (), p. 221.

[144] A. Chi-Ying Wong. “Characterisation of the flowability of glass beads by bulk densities ratio”. In: *Chemical Engineering Science* 55.18 (2000), pp. 3855–3859.

[145] S. C. Tadepalli et al. “Comparison of hexahedral and tetrahedral elements in finite element analysis of the foot and footwear”. In: *Journal of Biomechanics* 44.12 (2011), pp. 2337–2343.

[146] M. Olazar et al. “Hydrodynamics of Sawdust and Mixtures of Wood Residues in Conical Spouted Beds”. In: *Industrial & Engineering Chemistry Research* 33.4 (1994), pp. 993–1000.

[147] J. Yang et al. “Experimental investigation of fountain height in a shallow rectangular spouted bed using digital image analysis”. In: *Chemical Engineering Journal* 380 (2020), p. 122467.

[148] J. R. Grace and K. B. Mathur. “Height and structure of the fountain region above spouted beds”. In: *The Canadian Journal of Chemical Engineering* 56.5 (1978), pp. 533–537.

[149] M. Cortazar et al. “Advantages of confining the fountain in a conical spouted bed reactor for biomass steam gasification”. In: *Energy* 153 (2018), pp. 455–463.

[150] M. Olazar et al. “Local Bed Voidage in Spouted Beds”. In: *Industrial & Engineering Chemistry Research* 40.1 (2001), pp. 427–433.

[151] I. Estiati et al. “Comparison of artificial neural networks with empirical correlations for estimating the average cycle time in conical spouted beds”. In: *Particuology* 42 (2019), pp. 48–57.

[152] L. Spreutels et al. “Gas residence time distribution in a conical spouted bed”. In: *Powder Technology* 290 (2016), pp. 62–71.

[153] K. Chen et al. “CFD simulation of particle residence time distribution in industrial scale horizontal fluidized bed”. In: *Powder Technology* 345 (2019), pp. 129–139.

[154] S. Geng et al. “Conditioning micro fluidized bed for maximal approach of gas plug flow”. In: *Chemical Engineering Journal* 351 (2018), pp. 110–118.

[155] B. van Leer. “Towards the ultimate conservative difference scheme. II. Monotonicity and conservation combined in a second-order scheme”. In: *Journal of Computational Physics* 14.4 (1974), pp. 361–370.

[156] D. Zhang et al. “A review on TVD schemes and a refined flux-limiter for steady-state calculations”. In: *Journal of Computational Physics* 302 (2015), pp. 114–154.

[157] E. F. Toro. “High–Order and TVD Methods for Scalar Equations”. In: *Riemann Solvers and Numerical Methods for Fluid Dynamics*. Berlin, Heidelberg: Springer Berlin Heidelberg, 2009, pp. 413–492.

[158] X. Yu and Y. Shen. “Model analysis of gas residence time in an ironmaking blast furnace”. In: *Chemical Engineering Science* 199 (2019), pp. 50–63.

[159] B. Freireich et al. “Comparisons of intra-tablet coating variability using DEM simulations, asymptotic limit models, and experiments”. In: *Chemical Engineering Science* 131 (2015), pp. 197–212.

[160] J.-P. Latham et al. “Three-dimensional particle shape acquisition and use of shape library for DEM and FEM/DEM simulation”. In: *Minerals Engineering* 21.11 (2008), pp. 797–805.

[161] A. Džiugys and B. Peters. “An approach to simulate the motion of spherical and non-spherical fuel particles in combustion chambers”. In: *Granular Matter* 3.4 (2001), pp. 231–266.

[162] M. Marigo and E. H. Stitt. “Discrete element method (DEM) for industrial applications: Comments on calibration and validation for the modelling of cylindrical pellets”. In: *KONA Powder and Particle Journal* 32.32 (2015), pp. 236–252.

[163] J. Härtl and J. Y. Ooi. “Experiments and simulations of direct shear tests: Porosity, contact friction and bulk friction”. In: *Granular Matter* 10.4 (2008), pp. 263–271.

[164] A. Haider and O. Levenspiel. “Drag coefficient and terminal velocity of spherical and nonspherical particles”. In: *Powder Technology* 58.1 (1989), pp. 63–70.

[165] B. van Wachem et al. “Modelling of gas–solid turbulent channel flow with non-spherical particles with large Stokes numbers”. In: *International Journal of Multiphase Flow* 68 (2015), pp. 80–92.

[166] A. Ullah et al. “An overview of Eulerian CFD modeling and simulation of non-spherical biomass particles”. In: *Renewable Energy* 141 (2019), pp. 1054–1066.

[167] G. Bagheri et al. “On the characterization of size and shape of irregular particles”. In: *Powder Technology* 270 (2015), pp. 141–153.

[168] A. Hölzer and M. Sommerfeld. “New simple correlation formula for the drag coefficient of non-spherical particles”. In: *Powder Technology* 184.3 (2008), pp. 361–365.

[169] S. K. Sanjeevi et al. “Drag, lift and torque correlations for non-spherical particles from Stokes limit to high Reynolds numbers”. In: *International Journal of Multiphase Flow* 106 (2018), pp. 325–337.

[170] F. Dioguardi et al. “A New One-Equation Model of Fluid Drag for Irregularly Shaped Particles Valid Over a Wide Range of Reynolds Number”. In: *Journal of Geophysical Research: Solid Earth* 123.1 (2018), pp. 144–156.

[171] G. Bagheri and C. Bonadonna. “Erratum to “On the drag of freely falling non-spherical particles”". In: *Powder Technology* 349 (2019), p. 108.

[172] M. Zastawny et al. “Derivation of drag and lift force and torque coefficients for non-spherical particles in flows”. In: *International Journal of Multiphase Flow* 39 (2012), pp. 227–239.

[173] G. Bagheri and C. Bonadonna. “Comment on “A New One-Equation Model of Fluid Drag for Irregularly Shaped Particles Valid Over a Wide Range of Reynolds Number” by F. Dioguardi et al.” In: *Journal of Geophysical Research: Solid Earth* 124.10 (2019), pp. 10261–10264.

[174] W. R. Hamilton. “II. On quaternions; or on a new system of imaginaries in algebra”. In: *The London, Edinburgh, and Dublin Philosophical Magazine and Journal of Science* 25.163 (1844), pp. 10–13.

[175] X. Wu et al. “Experimental study of particle rotation characteristics with high-speed digital imaging system”. In: *Powder Technology* 181.1 (2008), pp. 21–30.

[176] A. Jaklič et al. “Superquadrics and Their Geometric Properties”. In: Springer, Dordrecht, 2000, pp. 13–39.

[177] D. Clarke et al. “Investigation of Void Fraction Schemes for Use with CFD-DEM Simulations of Fluidized Beds”. In: *Industrial & Engineering Chemistry Research* 57.8 (2018), pp. 3002–3013.

[178] Z. Peng et al. “Influence of void fraction calculation on fidelity of CFD-DEM simulation of gas-solid bubbling fluidized beds”. In: *AIChE Journal* 60.6 (2014), pp. 2000–2018.

[179] L. Fries et al. “DEM–CFD modeling of a fluidized bed spray granulator”. In: *Chemical Engineering Science* 66.11 (2011), pp. 2340–2355.

[180] H. P. Zhu and A. B. Yu. “Averaging method of granular materials”. In: *Physical Review E* 66.2 (2002), p. 021302.

[181] V. Salikov et al. “Investigations on the spouting stability in a prismatic spouted bed and apparatus optimization”. In: *Advanced Powder Technology* 26.3 (2015), pp. 718–733.

[182] C. E. Agu et al. “Prediction of void fraction and minimum fluidization velocity of a binary mixture of particles: Bed material and fuel particles”. In: *Powder Technology* 349 (2019), pp. 99–107.

[183] M. Olazar et al. “A simplified model for gas flow in conical spouted beds”. In: *Chemical Engineering Journal and the Biochemical Engineering Journal* 56.2 (1995), pp. 19–26.

[184] M. Olazar et al. “One-dimensional modelling of conical spouted beds”. In: *Chemical Engineering and Processing: Process Intensification* 48.7 (2009), pp. 1264–1269.

[185] P. Tian et al. “Methanol to olefins (MTO): From fundamentals to commercialization”. In: *ACS Catalysis* 5.3 (2015), pp. 1922–1938.

[186] M. Tellabide et al. “New operation regimes in fountain confined conical spouted beds”. In: *Chemical Engineering Science* 211 (2020).

[187] M. Askarishahi et al. “Full-physics simulations of spray-particle interaction in a bubbling fluidized bed”. In: *AIChE Journal* 63.7 (2017), pp. 2569–2587.

[188] B. Freireich et al. “Intra-tablet coating variability for several pharmaceutical tablet shapes”. In: *Chemical Engineering Science* 66.12 (2011), pp. 2535–2544.

[189] W. R. Ketterhagen. “Modeling the motion and orientation of various pharmaceutical tablet shapes in a film coating pan using DEM”. In: *International Journal of Pharmaceutics* 409.1-2 (2011), pp. 137–149.

[190] R. Xiang et al. “Spray coating as a simple method to prepare catalyst for growth of diameter-tunable single-walled carbon nanotubes”. In: *Carbon* 64 (2013), pp. 537–540.

[191] M. Shafaee and S. Mahmoudzadeh. “Numerical investigation of spray characteristics of an air-blast atomizer with dynamic mesh”. In: *Aerospace Science and Technology* 70 (2017), pp. 351–358.

[192] P. J. O’Rourke and A. A. Amsden. “The Tab Method for Numerical Calculation of Spray Droplet Breakup”. In: 1987.

[193] D. P. Schmidt et al. “Pressure-Swirl Atomization in the Near Field”. In: 1999.

[194] R. D. Reitz and R. Diwakar. “Structure of High-Pressure Fuel Sprays”. In: *Society of Automotive Engineers international congress and expo*. 1987.

[195] R. D. Reitz and R. Diwakar. “Effect of Drop Breakup on Fuel Sprays”. In: *SAE Transactions*. 1986.

[196] G. W. Smith et al. *Mixing Efficiency in Side-Vented Coating Equipment*. Tech. rep. 3. 2003, p. 37.

[197] K. E. Wilson and E. Crossman. “The influence of tablet shape and pan speed on intra-tablet film coating uniformity”. In: *Drug Development and Industrial Pharmacy* 23.12 (1997), pp. 1239–1243.

[198] C. Ericson. *Real-time collision detection*. Elsevier, 2005, p. 593.

[199] B. K. Fritz et al. “Measuring droplet size of agricultural spray noozles-measurement distance and airspeed effects”. In: *Atomization and Sprays* 24.9 (2014), pp. 747–760.

[200] L. Rayleigh. “VI. On the capillary phenomena of jets”. In: *Proceedings of the Royal Society of London* 29.196-199 (1879), pp. 71–97.

[201] D. Brock et al. “Evaluation of critical process parameters for intra-tablet coating uniformity using terahertz pulsed imaging”. In: *European Journal of Pharmaceutics and Biopharmaceutics* 85.3 Part B (2013), pp. 1122–1129.

[202] A. Kalbag et al. “Inter-tablet coating variability: Residence times in a horizontal pan coater”. In: *Chemical Engineering Science* 63.11 (2008), pp. 2881–2894.

[203] C. A. Shaffer. *A Practical Introduction to Data Structures and Algorithm Analysis Third Edition (C++ Version)*. Tech. rep. 2010.